

SYNTHESIS AND APPLICATIONS OF METAL OXIDE NANOWIRES

By

LI-CHIA TIEN

A DISSERTATION PRESENTED TO THE GRADUATE SCHOOL  
OF THE UNIVERSITY OF FLORIDA IN PARTIAL FULFILLMENT  
OF THE REQUIREMENTS FOR THE DEGREE OF  
DOCTOR OF PHILOSOPHY

UNIVERSITY OF FLORIDA

2008

© 2008 Li-Chia Tien

To my family

## ACKNOWLEDGMENTS

Many people have inspired, guided, helped, and laughed with during the 5 years I spent at the University of Florida, and I would like to thank them all for a great graduate school experience. First, I would like to thank my advisor Dr. David Norton for his guidance, both personally and professionally. His positive attitude, enthusiasm and patience inspired me during different research projects. Throughout my doctoral work he encouraged me to develop independent thinking and research skills. He continually stimulated my analytical thinking and greatly assisted me with scientific writing. It has been a great pleasure to work with him. Also I thank Dr. Steve Pearton and Dr. Fan Ren's guidance and support during these years. I would also like to thank the members of my committee, Dr. Cammy Abernathy and Dr. Simon Phillpot for their valuable advice.

Special thanks go to Young-Woo for teaching me and fitting me into the lab when I first joined the group. He is always nice, patient and a pleasure to work with. Thank to Hung-Ta and Sam for performing measurements and help in hydrogen sensor project. Also thank Hyun-Sik's help in PL measurements. Mat's dedication on PPMS is greatly appreciated. I thank Kerry Siebein from MAIC for her generous help in HR-TEM. I also thank Dr. John Budai for performing HR-XRD on tin oxide thin film samples.

Finally, I thank all the members in Dr. Norton's research group, especially those who helped and taught me when I was here in University of Florida. I really enjoy having small talk with Patrick, it always enlighten me on American culture. I'll remember the great time sharing laser, chambers, targets, experience and jokes. Finally, I would like to thank my parents and my brother for their understanding, unconditional support and dedication throughout the years. A special congratulation goes to Tze-Ning, my nephew born just before my final defense. I also want thank my best friend Shih-Ying's support these years.

# TABLE OF CONTENTS

	<u>page</u>
ACKNOWLEDGMENTS .....	4
LIST OF TABLES .....	8
LIST OF FIGURES .....	9
ABSTRACT.....	14
CHAPTER	
1 INTRODUCTION .....	16
2 LITERATURE REVIEW .....	19
2.1 Introduction.....	19
2.2 Material Properties.....	20
2.2.1 Properties of ZnO.....	20
2.2.2 Properties of ZnMgO .....	22
2.2.3 Properties of SnO <sub>2</sub> .....	22
2.2.4 Properties of VO <sub>2</sub> .....	23
2.3 Synthesis of One-Dimensional Nanostructures .....	24
2.3.1 Vapor-liquid-solid mechanism.....	24
2.3.2 Vapor-solid mechanism .....	26
2.3.3 Laser ablation.....	26
2.3.4 Thermal evaporation .....	26
2.3.5 Solution-based chemistry.....	27
2.4 Applications of Nanowires .....	28
2.4.1 Electrical applications .....	28
2.4.2 Optical applications.....	29
2.4.3 Chemical and biochemical sensing.....	30
3 EXPERIMENTAL DETAILS AND CHARACTERIZATION .....	37
3.1 Materials Synthesis Techniques .....	37
3.1.1 Molecular beam epitaxy.....	37
3.1.2 Pulsed laser deposition.....	38
3.2 Characterization Techniques .....	39
3.2.1 Scanning electron microscope .....	40
3.2.2 Atomic force microscopy.....	40
3.2.3 X-ray diffraction.....	41
3.2.4 Transmission electron microscope.....	42
3.2.5 Photoluminescence.....	43
3.2.6 Energy-Dispersive X-ray spectroscopy .....	44

3.2.7	Hall measurement .....	44
3.3	Processing and Device Fabrication .....	45
3.3.1	Electron beam lithography .....	45
3.3.2	Sputter deposition .....	46
3.3.3	Fabrication of multiple nanowire devices .....	47
3.3.4	Fabrication of single nanowire devices .....	47
3.3.5	Gas sensing measurement .....	47
4	NUCLEATION CONTROL AND SELECTIVE GROWTH OF ZNO NANOWIRES .....	54
4.1	Introduction .....	54
4.2	Experimental Methods .....	55
4.3	Results and Discussion .....	56
4.3.1	Structural and optical properties of ZnO nanorods grown on Si .....	56
4.3.2	Growth mechanism .....	57
4.3.3	Nucleation control and site-selective growth .....	58
4.3.4	Structural and optical properties of ZnO nanowires grown on sapphire .....	59
4.4	Summary and Conclusions .....	61
5	ZNO NANOWIRES FOR HYDROGEN SENSING APPLICATIONS .....	74
5.1	Introduction .....	74
5.2	Experimental Methods .....	76
5.2.1	Synthesis and fabrication of ZnO nanowires sensors .....	76
5.2.2	Synthesis and fabrication of ZnO thin films sensors .....	77
5.2.3	Synthesis and fabrication of single ZnO nanowire sensors .....	77
5.2.4	Synthesis and fabrication of SnO <sub>2</sub> -ZnO nanowire sensors .....	78
5.3	Results and Discussion .....	78
5.3.1	Catalyst functionalized ZnO nanowires .....	78
5.3.2	Room temperature hydrogen selective sensing with ZnO nanowires .....	80
5.3.3	Single ZnO nanowire sensors .....	82
5.3.4	A comparison of ZnO thin film and nanowire sensors .....	85
5.3.5	Surface functionalized SnO <sub>2</sub> -ZnO nanowire sensors .....	87
5.4	Summary and Conclusions .....	89
6	CATALYST-FREE GROWTH OF METAL OXIDE NANOWIRES .....	109
6.1	Introduction .....	109
6.2	Experimental Methods .....	112
6.2.1	ZnO nanowires growth .....	112
6.2.2	ZnMgO nanowires growth .....	113
6.2.3	SnO <sub>2</sub> nanorods growth .....	114
6.2.4	VO <sub>2</sub> nanowires growth .....	115
6.3	Results and Discussion .....	115
6.3.1	Synthesis and characterization of vertical-aligned ZnO nanowires .....	115
6.3.2	Synthesis and characterization of ZnMgO nanowires .....	119
6.3.3	Synthesis and characterization of SnO <sub>2</sub> nanorods .....	121

6.3.4	Synthesis and characterization of VO <sub>2</sub> nanowires .....	123
6.4	Summary and Conclusions .....	125
7	EPITAXIAL GROWTH OF TRANSPARENT TIN OXIDE THIN FILMS.....	151
7.1	Introduction .....	151
7.2	Experimental Methods .....	153
7.3	Results and Discussion.....	154
7.3.1	Properties of undoped SnO <sub>2</sub> thin films .....	154
7.3.1	Properties of gallium-doped SnO <sub>2</sub> thin films .....	157
7.4	Summary and Conclusions.....	160
8	CONCLUSION.....	174
	LIST OF REFERENCES.....	176
	BIOGRAPHICAL SKETCH .....	189

## LIST OF TABLES

<u>Table</u>		<u>page</u>
2-1	Properties of ZnO.....	32
5-1	Relative resistance response of metal-coated multiple nanowires.....	91
5-2	Relative resistance response of Pd and Pt coated multiple nanowires.....	91
7-1	Candidate dopant atoms for SnO <sub>2</sub> .....	161
7-2	Hall data of SnO <sub>2</sub> thin films grown at different temperature.....	161
7-3	Hall data of Ga-doped SnO <sub>2</sub> films grown at different temperature. ....	161
7-4	Hall data of Ga-doped SnO <sub>2</sub> films grown at different oxygen pressure. ....	161

## LIST OF FIGURES

<u>Figure</u>	<u>page</u>
2-1 Electronic, chemical and optical processes occurring on metal oxides that can benefit from reduction in size to the nanometer range.....	33
2-2 Crystal structure of wurtzite ZnO.....	34
2-3 Unit cell of rutile SnO <sub>2</sub> .....	34
2-4 Vapor-Solid-Liquid (VLS) process.....	35
2-5 Vapor-Solid (VS) process.....	35
2-6 The energy band diagram of oxide thin film materials.....	36
2-7 Gas sensing mechanism of ZnO nanowire.....	36
3-1 Molecule beam epitaxy chamber.....	49
3-2 Pulsed laser deposition chamber.....	50
3-3 Typical Hall measurement setup and Van der Paul sample geometry.....	51
3-4 Photograph of gas sensor device.....	52
3-5 Gas sensing measurement system.....	52
3-6 Process sketch for the fabrication of single ZnO nanowire devices.....	53
4-1 Scanning electron microscope images of ZnO nanorods on a Ag coated silicon grew at 400°C.....	62
4-2 X-ray diffraction pattern of ZnO nanorods grown on a 20Å Ag coated SiO <sub>2</sub> /Si substrate at 400°C.....	63
4-3 High resolution TEM image of a single ZnO nanorod and room temperature PL spectra.....	64
4-4 25Å Ag on SiO <sub>2</sub> /Si with different annealing temperature and time.....	65
4-5 25Å Ag on Si <sub>3</sub> N <sub>4</sub> /Si with different annealing temperature and time.....	66
4-6 Density and average size of the resulting Ag clusters on SiO <sub>2</sub> .....	67
4-7 Density and average size of the resulting Ag clusters on Si <sub>3</sub> N <sub>4</sub> .....	68

4-8	Scanning electron microscope images of selectively grown ZnO nanorods on 25 Å Ag/SiO <sub>2</sub> .....	69
4-9	Scanning electron microscope images of 200–650 nm of Au clusters on sapphire.....	70
4-10	Scanning electron microscope images of 50–150 nm of Au clusters on sapphire.....	71
4-11	Scanning electron microscope images of ZnO nanowires on an Au coated <i>c</i> -sapphire. ...	72
4-12	X-ray diffraction pattern of ZnO nanowires. ....	73
4-13	Room temperature photoluminescence spectra of ZnO nanowires .....	73
5-1	Metal catalysts decorated ZnO nanowires. ....	92
5-2	Time dependence of relative resistance response of metal-coated multiple nanowires ....	93
5-3	Time dependence of resistance change of Pt-coated multiple ZnO nanowires .....	93
5-4	Time dependence of resistance change of Pd-coated multiple ZnO nanowires.....	94
5-5	Time dependence of resistance of either Pd-coated or uncoated multiple ZnO nanowires .....	94
5-6	Relative response of Pd-coated nanowires as a function of H <sub>2</sub> concentration in N <sub>2</sub> . ....	95
5-7	Time dependence of resistance change of Pd-coated multiple ZnO nanowires .....	95
5-8	Rate of resistance change after exposure to 500 ppm H <sub>2</sub> in N <sub>2</sub> was measured at different temperatures. ....	96
5-9	Arrhenius plot of rate of resistance change after exposure to 500 ppm H <sub>2</sub> in N <sub>2</sub> . ....	96
5-10	Current-voltage (I-V) plot of uncoated or Pt-coated single ZnO nanowires measured at room temperature in pure N <sub>2</sub> .....	97
5-11	Current-voltage (I-V) characteristics of Pt-coated ZnO single nanowires measured in vacuum, air, N <sub>2</sub> or 500ppm H <sub>2</sub> in N <sub>2</sub> ambients. ....	97
5-12	Current versus time plot for single ZnO nanowires either with or without Pt coatings and corresponding $ \Delta R /R(\%)$ -time plots .....	98
5-13	Room temperature I-V characteristics from ZnO thin films of thickness 20 or 350 nm measured in air before and after coating with Pt. ....	99
5-14	Current as a function of time for Pt-coated ZnO thin films of different thickness. ....	100
5-15	Time dependence of current from Pt-coated ZnO nanowires and thin films.....	101

5-16	Change in current at fixed bias (0.5V) when switching to the H <sub>2</sub> -containing ambient of either Pt-coated ZnO nanowires or thin films. ....	101
5-17	Scanning electron microscopy micrographs of SnO <sub>2</sub> -coated ZnO nanowires and EDX spectrum. ....	102
5-18	X-ray diffraction pattern from SnO <sub>2</sub> -coated ZnO nanowires. ....	103
5-19	High resolution transmission electron microscope images of SnO <sub>2</sub> /ZnO nanowires. ....	104
5-20	High resolution transmission electron microscope image of SnO <sub>2</sub> -coated ZnO nanowire. ....	104
5-21	Energy-Dispersive X-ray Spectroscopy analysis of SnO <sub>2</sub> /ZnO nanowires. ....	105
5-22	Current-voltage (I-V) characteristics from SnO <sub>2</sub> -coated ZnO nanowires for two different deposition times. ....	106
5-23	Current-voltage (I-V) characteristics from SnO <sub>2</sub> -coated ZnO nanowires at room temperature or 400°C ....	107
5-24	Current at fixed bias of -0.5 V and temperature of 400°C as a function of time. ....	108
6-1	Scanning electron microscope images of well-aligned ZnO nanowires grown on a ZnO thin film template. ....	127
6-2	X-ray diffraction $\theta$ -2 $\theta$ scan of ZnO nanowires grown at 800°C in 500 mTorr Ar. ....	128
6-3	High resolution transmission electron microscope images of ZnO nanowires grown on a ZnO thin film. ....	129
6-4	Scanning electron microscope images of the ZnO nanowires grown at 800°C ....	130
6-5	Scanning electron microscope images of the ZnO nanowires. ....	131
6-6	Room temperature PL spectra of ZnO nanowires and near-band-edge-emission of ZnO thin film and ZnO nanowires grown under different background ambient. ....	132
6-7	Scanning electron microscope images of the ZnMgO nanowires grown at 800°C in 500 mTorr Ar. ....	133
6-8	Energy-dispersive spectroscopy spectra for ZnMgO nanowires grown on sapphire at 800°C in 500 mTorr Ar. ....	134
6-9	X-ray diffraction $\theta$ -2 $\theta$ scan of ZnMgO nanowires grown on sapphire at 800°C in 500 mTorr Ar. ....	135
6-10	High resolution transmission electron microscope image of single ZnMgO nanowire. ....	136

6-11	Scanning electron microscope images of the cored ZnMgO nanowires grown on sapphire at 800°C in 500 mTorr Ar.....	137
6-12	X-ray diffraction $\theta$ -2 $\theta$ scan of cored ZnMgO nanowires grown on sapphire on sapphire at 800°C in 500 mTorr Ar.....	138
6-13	Transmission electron microscope image of single cored ZnO/ZnMgO nanowire.....	139
6-14	X-ray diffraction patterns of SnO <sub>2</sub> nanorods grown at 800°C in 500 mTorr oxygen. ....	140
6-15	Energy-dispersive spectroscopy spectra of SnO <sub>2</sub> nanorods grown on sapphire at 800°C.....	141
6-16	Scanning electron microscope morphologies of SnO <sub>2</sub> nanorods grown on silicon .....	142
6-17	Scanning electron microscope images showing the surface morphology and cross-section of SnO <sub>2</sub> nanorods deposited by pulsed laser deposition.....	143
6-18	High resolution transmission electron microscope image of SnO <sub>2</sub> nanorods.....	144
6-19	X-ray diffraction patterns of VO <sub>2</sub> nanowires grown at 600°C in 500 mTorr oxygen.....	145
6-20	Energy-dispersive spectroscopy spectra for VO <sub>2</sub> nanowires grown on silicon at 600°C.....	146
6-21	Scanning electron microscope images of VO <sub>2</sub> nanowires on silicon grew at 600°C.....	147
6-22	High resolution transmission electron microscope image of VO <sub>2</sub> nanowires .....	148
6-23	The photoluminescence spectra of VO <sub>2</sub> thin film and nanowires grew at different oxygen pressure. ....	149
6-24	Scanning electron microscope images of fabricated single nanowire device and I-V characteristics of the individual VO <sub>2</sub> nanowire .....	150
7-1	X-ray diffraction patterns of SnO <sub>2</sub> films deposited on (0001) Al <sub>2</sub> O <sub>3</sub> at different temperature. ....	162
7-2	<i>a</i> -axis constant as a function of growth temperature. ....	162
7-3	Rocking curve of (200) reflection of SnO <sub>2</sub> films grown at 700°C.....	163
7-5	The SnO <sub>2</sub> crystal structure projection on the (100) plane, and in-plane epitaxial growth orientations. ....	165
7-6	Growth rate of SnO <sub>2</sub> films on (0001) Al <sub>2</sub> O <sub>3</sub> as a function of temperature. ....	165
7-7	Atomic force microscope images of SnO <sub>2</sub> thin film grown at 700°C.....	166

7-8	Resistivity and carrier density of SnO <sub>2</sub> films grown at different temperatures. ....	166
7-9	Transmission spectra of the SnO <sub>2</sub> film. ....	167
7-10	Energy-Dispersive X-ray Spectroscopy analysis of Ga-doped SnO <sub>2</sub> thin film ....	168
7-11	Comparison of <i>a</i> -axis constant as a function of growth temperature. ....	168
7-12	X-ray diffraction patterns of Ga-doped SnO <sub>2</sub> films deposited on (0001) Al <sub>2</sub> O <sub>3</sub> at different oxygen pressure.....	169
7-13	<i>a</i> -axis constant of Ga-doped SnO <sub>2</sub> films as a function of growth pressure. ....	169
7-14	Transmission spectra of the Ga-doped SnO <sub>2</sub> film.....	170
7-15	Hall plot ( $B \cdot R_H - B$ ) of Ga-doped SnO <sub>2</sub> film grew at 400°C in 50 mTorr oxygen.....	171
7-16	Hall plot ( $B \cdot R_H - B$ ) of Ga-doped SnO <sub>2</sub> film grew at 400°C in 50 mTorr oxygen.....	172
7-17	Hall plot ( $B \cdot R_H - B$ ) of Ga-doped SnO <sub>2</sub> film grew at 400°C in 20 mTorr oxygen and annealed at 800°C in oxygen for 1h.....	173

Abstract of Dissertation Presented to the Graduate School  
of the University of Florida in Partial Fulfillment of the  
Requirements for the Degree of Doctor of Philosophy

SYNTHESIS AND APPLICATIONS OF METAL OXIDE NANOWIRES

By

Li-Chia Tien

May 2008

Chair: David P. Norton  
Major: Materials Science and Engineering

The one-dimensional nanostructured materials have attracted much attention because of their superior properties from the deducing size in the nanometer range. Among them, metal oxide materials provide a wide diversity and functionality in both theoretical study and applications. This work focused on the synthesis of metal oxide nanowires, and further investigated possible applications of nanostructured metal oxide materials.

High quality ZnO nanowires have been synthesized by catalyst-assisted molecular beam epitaxy. The control of initial Au or Ag film thickness and subsequent annealing conditions is shown to provide an effective method for controlling the size and density of nucleation sites for catalyst-driven growth of ZnO nanowires. For gas sensing applications, it is found that the sensitivity for detecting hydrogen is greatly enhanced by sputter-depositing metal catalysts (Pt and Ag) on surface. The sensors are shown to detect ppm hydrogen at room temperature using  $<0.4$  mW of power when using multiple nanowires. A comparison study of the hydrogen-sensing characteristics of ZnO thin films with different thickness and ZnO nanowires was studied. The Pt-coated single nanowires show a current response by approximately a factor of 3 larger at room temperature. Both types of sensors are shown to be capable of the detection of ppm hydrogen at

room temperature with nW power levels, but the nanowires show different recovery characteristics, consistent with the expected higher surface coverage of adsorbed hydrogen.

The feasibility of a number of metal oxide nanowires has been synthesized by a high-pressure assisted pulsed laser deposition. The high density well-aligned metal oxide nanowires can be directly grown on substrate without metal catalysts. The results suggest the possibility of growing complex metal oxide nanostructures, including tailored heterostructures and aligned heterojunction arrays with PLD technique.

The growth of epitaxial SnO<sub>2</sub> on *c*-sapphire using pulsed laser deposition is examined. X-ray diffraction analysis shows that the films are highly *a*-axis oriented SnO<sub>2</sub> with the rutile structure. The effects of Ga doping on SnO<sub>2</sub> films were studied. The Hall data showed *p*-type behavior occurs only at specific growth condition, but converted back to *n*-type and degraded as time proceeds.

## CHAPTER 1 INTRODUCTION

"There's plenty of room at the bottom", a famous quote from Richard P. Feynman in 1959, addressed the great interest and significance of nanotechnology. Nanotechnology is the ability to manipulate individual atoms and molecules to produce nanostructured materials that have applications in real world. Nanotechnology involves the production, design, and application of physical, chemical and biological systems at scales ranging from individual atoms or molecules to about 100 nanometers. It also involves the integration of the resulting nanostructures into larger systems. There are basically two main approaches to create very small structures or devices. The first approach is known as the "bottom up". The atomic or molecular building blocks are put together to create bigger objects. With this approach, individual atoms or molecules can be precisely placed by scanning probe microscopy or self-assembling. Materials and devices are built from molecular components which assemble themselves chemically by principles of molecular recognition or other techniques. The second approach is known as "top down" approach. The macro-scale systems are converted into nano-scale ones by a series of sequential reduction operations. The smallest features that can be created by the "top down" approach depend on the tools used and the system operator's experience and skills. Therefore, there are limitations in creating features smaller than 100 nanometers. In the "top-down" approach, materials are constructed from larger entities without atomic-level control. Obviously, the "top down" approach requires more work and produce considerable waste. In contrast, the "bottom up" approach is time and waste efficient. However, precision and scalability are still big challenges for the "bottom up" approach.

Nanostructures of metals, oxides and semiconductors have been studied intensely in the last several years by different chemical and physical methods.<sup>1-7</sup> Interests in one-dimensional

nanotubes and nanowires had drawn much interest with the discovery of carbon nanotubes in 1991.<sup>8-11</sup> Nanowires are one-dimensional, anisotropic structures, small in diameter, and large in surface-to-volume ratio. Unlike other low-dimensional systems, nanowires have two quantum-confined directions but one unconfined direction available for electrical conduction. This allows nanowires to be used in applications where electrical conduction, rather than tunneling transport, is required.<sup>12-14</sup> The unusual electronic, optical, magnetic and chemical properties of nanowires depend on their size has motivated intense research in this area. The great interest have resulted in better understanding of the phenomena of quantum confinement,<sup>15,16</sup> logical synthetic schemes and fabrication of novel nano-electronic devices.<sup>2,12,13</sup>

Among all materials, oxide materials appear to show the most diverse range of functionality. Metal oxides play a very important role in many research areas such as: chemistry, physics, and materials science.<sup>17</sup> The metal elements can form a large family of oxide compounds. These elements can adopt many structure geometries with an electronic structure that can exhibit metallic, semiconductor or insulator character. In technological applications, oxides are used in the fabrication of microelectronic circuits, sensors, fuel cells, piezo-electric devices, coatings for the passivation of the surfaces and as catalysts.<sup>17</sup>

In this dissertation, we concentrate on the synthesis, characterization and applications of one-dimensional metal oxide materials. The applications will be focused on their gas sensing properties. Chapter 2 presents background and a brief literature review of current research on metal oxide nanowires. In Chapter 3, experimental details such as synthesis, characterization and processing techniques will be explained. The nucleation control and selective growth of ZnO nanowires will be addressed in Chapter 4. Chapter 5 examines the applications of ZnO nanowires in gas sensing. A comparison of thin films and nanowires based hydrogen sensor will

also be described. A catalyst-free growth method to prepare varieties of metal oxide nanowires will be described in Chapter 6. Growth and characterization of undoped and Ga-doped SnO<sub>2</sub> thin films will be evaluated in Chapter 7 followed by conclusions in Chapter 8.

## CHAPTER 2 LITERATURE REVIEW

### 2.1 Introduction

This Chapter provides an overview of general properties and recent research on metal oxide nanowires. As a group of functional materials, metal oxides has a wide range of applications, including transparent electronics,<sup>18,19</sup> chemical sensors,<sup>20-22</sup> piezo-electronics,<sup>7,19,23,24</sup> light-emitting diodes,<sup>25,26</sup> etc. A basic understanding of the fundamental properties of the metal oxide system is necessary for research and development towards practical applications. Nanowires are one-dimensional, anisotropic structures, small in diameter and large in surface-to-volume ratio. The physical properties are totally different than bulk, because of their unique density of electronic states. The small diameters of nanowires are expected to exhibit significantly different electrical, optical and magnetic properties. The electron-hole interaction will have orders of magnitude enhancement in a nanostructure, due to the dramatically increased electronic density of states. Figure 2-1 shows a few of the electronic, chemical and optical processes occurring on metal oxides that can benefit from reduction in size to the nanometer range. Efforts have been made on both developing synthetic methodologies for the fabrication of nanowires, and devices based on their superior properties. The one-dimensional oxide nanostructures are expected to possess novel characteristics and promising applications for the following reasons:<sup>27</sup>

- A large surface-to-volume ratio means that a significant fraction of the atoms (or molecules) can participate in surface reactions. The surface depletion region can be changed dramatically by surface adsorbates. This is particularly useful to gas sensing applications.
- The Debye length ( $\lambda_D$ ) for most semiconducting oxide nanowires is comparable to their radius over a wide temperature and doping range. This causes their electronic properties to be strongly influenced by processes at their surface. The nanowire's conductivity could vary from a fully nonconductive state to a highly conductive state based on the surface. By well controlled dimension, this could result in better sensitivity and selectivity.

- One-dimensional nanostructure oxides are usually stoichiometrically better defined and have a greater level of crystallinity (usually single crystal) than the thin-film oxides. Normally they are either with very small amount of defects or defect free structure.
- As the diameter of the nanowires is reduced to certain value, we can expect to see the quantum effects.
- Low cost and low power consumption. One can expect the low power consumption devices based on one-dimensional materials.

The Chapter is divided into three main sections. After a brief introduction to the materials properties in the first section, the second section explores one-dimensional synthesis methods and growth mechanism. The applications of one-dimensional nanowires in chemical sensing will be addressed in the last section.

## 2.2 Material Properties

As a group of functional materials, metal oxides has a wide range of applications, including transparent electronics, chemical sensors, piezo-electronics, light-emitting diodes, etc. A basic understanding of the fundamental properties of the metal oxide system is necessary for research and development towards practical applications. The general properties of metal oxide materials studied in the dissertation including zinc oxide, zinc magnesium oxide, tin oxide and vanadium oxide will be reviewed in this section. Their bulk properties provide a basic understanding of materials and its possible applications.

### 2.2.1 Properties of ZnO

ZnO is a key technology material with numerous applications ranging from optoelectronics to chemical sensors because of unique optical, electronic, and chemical properties. Table 2-1 shows a summary of basic physical parameters of ZnO.<sup>28</sup> The lack of a center of symmetry in wurtzite results in consequently piezoelectric and pyroelectric properties. The lattice parameters of ZnO are  $a=0.32495$  nm and  $c=0.52069$  nm at 300K, with a  $c/a$  ratio of 1.602, which is close to the 1.633 ratio of an ideal hexagonal close-packed structure as shown in Figure 2-2. The Zn

atoms are tetrahedrally coordinated to four O atoms, where the Zn *d* electrons hybridize with the O *p* electrons. The oppositely charged ions produce positively charged (0001)-Zn and negatively charged (000 $\bar{1}$ )-O polar surfaces, resulting in a normal dipole moment and spontaneous polarization along the *c*-axis.<sup>1</sup> In addition, ZnO is a wide band-gap (3.37 eV) II-VI compound semiconductor that is suitable for short wavelength optoelectronic applications. The high exciton binding energy (60 meV) in ZnO crystal can ensure efficient excitonic emission at room temperature and room temperature ultraviolet (UV) luminescence.<sup>19</sup> Moreover, ZnO is transparent to visible light and can be made highly conductive by doping. Electron doping in nominally undoped ZnO has been attributed to Zn interstitials, oxygen vacancies, or hydrogen. ZnO is intrinsically an *n*-type semiconductor, owing primarily to the presence of oxygen vacancies and/or zinc interstitials. The intrinsic defect levels that lead to *n*-type doping lay approximately 0.01–0.05 eV below the conduction band.<sup>29</sup> On the other hand, considerable effort has been investigated to achieve *p*-type ZnO by incorporating group V elements.<sup>30-33</sup> The reliable and reproducible *p*-type conductivity has not yet been achieved due to many issues. The compensation of dopants by energetically favorable native defects such as zinc interstitials or oxygen vacancies is one of obstacles.<sup>19</sup> The low dopant solubility is another issue.<sup>29</sup>

Optical properties of ZnO have been extensively studied because of their promising applications in optoelectronics.<sup>29</sup> ZnO has an effective electron mass of  $\sim 0.24 m_e$ , and a large exciton binding energy of 60 meV. Furthermore, the lasing conditions can be further improved with low-dimensional ZnO structures, which enhance the exciton oscillator strength and quantum efficiency.<sup>4</sup> Therefore bulk ZnO has a small exciton Bohr radius ( $\sim 2.34$  nm). The quantum confinement effect in ZnO nanowires could be observable at the scale of an exciton

Bohr radius. It has been reported by Gu *et al.* that the excitation binding energy is significantly enhanced due to size confinement in ZnO nanorods with diameter of  $\sim 2$  nm.<sup>16</sup>

### 2.2.2 Properties of ZnMgO

The realization of band-gap engineering to create barrier layer and quantum wells in the device heterostructures is very important in optoelectronic applications. ZnMgO alloy is an important material to construct the heterostructure or superlattice to obtain high performance laser diode (LD) and light emitting diode (LED) devices.<sup>19,34</sup> The ionic radius of  $\text{Mg}^{2+}$  (0.57 Å) and  $\text{Zn}^{2+}$  (0.60 Å) are comparable,<sup>35</sup> alloying the ZnO phase with MgO has been investigated for increasing the band gap ZnO. Theoretically, the band gap of ZnO ( $E_g = 3.4$  eV) can be modulated from 3.4 to 4.0 eV by doping with different amount of MgO ( $E_g = 7.8$  eV). The energy gap  $E_g(x)$  of the ternary semiconductor  $\text{Zn}_{1-x}\text{Mg}_x\text{O}$  is determined by the following equation:<sup>29</sup>

$$E_g(x) = (1-x) E_g(\text{ZnO}) + x E_g(\text{MgO}) - bx(1-x)$$

where  $b$  is the bowing parameter and  $E_g(\text{ZnO})$  and  $E_g(\text{MgO})$  are the band-gap of ZnO and MgO, respectively. The bowing parameter  $b$  depends on the difference in electronegativities of the ZnO and MgO. In addition, MgO has a cubic structure ( $a=4.216$  Å) and it has been reported that MgO segregates in the wurtzite ZnMgO lattice above 33% of Mg, limiting the maximum band-gap to 3.9 eV.<sup>29</sup>

### 2.2.3 Properties of SnO<sub>2</sub>

Tin oxide ( $\text{SnO}_2$ ) is a wide band gap ( $E_g=3.6$  eV at 300 K) semiconductor material suitable for multiple applications that include gas sensors, transparent conducting electrodes, and solar cells.<sup>21,36,37</sup> The thermodynamically stable crystal structure of  $\text{SnO}_2$  is rutile (tetragonal) with lattice parameters  $a=4.737$  Å and  $c=3.186$  Å as shown in Figure 2-3. The crystal structure of  $\text{SnO}_2$  belongs to the point group symmetry 4/mmm and space group  $P_{42/mmm}$  with tin and oxygen

atoms in 2a and 4f positions. With a unit cell consisting of two tin atoms and four oxygen atoms, with metal and oxygen atoms having an octahedral coordination.

SnO<sub>2</sub> is suitable for multiple applications that include gas sensors, transparent conducting electrodes, and solar cells. In sensor applications, SnO<sub>2</sub> has been reported to display high gas sensitivity and selectivity.<sup>38,39</sup> The reduced size of nanostructured SnO<sub>2</sub> provides a material with a large surface-to-volume ratio. Gas sensors based on one-dimensional nanostructured SnO<sub>2</sub> have been reported to exhibit good selectivity, low detection limits, and short response and recovery time.<sup>40-42</sup> Several methods have been employed to prepare SnO<sub>2</sub> nanorods including thermal evaporation, thermal decomposition, solution-phase growth, and hydrothermal methods.<sup>43-49</sup>

#### 2.2.4 Properties of VO<sub>2</sub>

Among the metal oxides, vanadium oxides with various phases are of great interest and have been extensively investigated for their distinctive properties.<sup>50-55</sup> Vanadium oxide (VO<sub>2</sub>) has attracted great attention because of the metal to insulator transitions and reversible dramatic changes in electrical and optical properties accompanied by a structural phase transition. VO<sub>2</sub> can exhibit a sharp (by a factor of 10<sup>4</sup>–10<sup>5</sup>) and fast (sub-picosecond) metal-insulator transition close to room temperature (340 K).<sup>55</sup> The metal-insulator transition is due to a small structural distortion of the lattice from a low-temperature monoclinic (M1, semiconducting phase) to a high-temperature tetragonal rutile (R, metallic phase) structure, accompanied by large changes in conductivity and optical properties from infrared (IR) transmission to reflecting.<sup>54</sup> The structure of the low-temperature monoclinic phase has the following unit cell dimensions:  $a=5.75 \text{ \AA}$ ,  $b=4.53 \text{ \AA}$ ,  $c=5.38 \text{ \AA}$  and  $\beta=122.6^\circ$ . For the high-temperature, rutile structure the lattice constants are  $a=4.55 \text{ \AA}$  and  $c=2.86 \text{ \AA}$ . The monoclinic structure with the presence of V-V pairs along its  $a$  axis, where  $a_{\text{monoclinic}} = 2c_{\text{rutile}}$ . During the transformation, the regular V-V separation of  $2.86 \text{ \AA}$  in the tetragonal rutile structure transforms to an alternative V-V separation of  $2.65$  and  $3.12 \text{ \AA}$

leading to a doubling up of the unit cell.<sup>56</sup> It also makes it a promising material for the use in device applications to achieve reliable electrical and optical switching operations. Moreover, B phase VO<sub>2</sub> was found to have good electrochemical performance, especially for use as an electrode material for lithium batteries.<sup>57,58</sup> It exhibits a maximum reversible capacity of about 320 mA h g<sup>-1</sup> in the range 4 to 1 V in lithium cells.<sup>59,60</sup> It has been reported that the operating properties of batteries depend not only on the structure but also on the morphology of the electrode components.<sup>61</sup> Therefore, the great surface area of nanowire materials may play an important role for electrochemical applications.

### **2.3 Synthesis of One-Dimensional Nanostructures**

In this section we discuss the most common synthetic approaches that have successfully developed obtaining high quality nanowires of a large variety of materials. In order to control the diameter, aspect ratio and crystallinity, diverse techniques have been applied including laser ablation, thermal evaporation, and solution-based growth, etc.<sup>62</sup> According to the synthesis environment, they can be divided into two categories: vapor phase growth and liquid phase growth. A brief discussion of one-dimensional growth mechanism followed by various synthetic approaches will be covered in this section.

Understanding the growth mechanism of one-dimensional growth is critical in controlling nanostructures. Mechanisms for one-dimensional growth include Vapor-Liquid-Solid (VLS), screw dislocation growth, catalyst-free self-nucleation growth, and vapor-solid (VS) mechanisms.<sup>63</sup> The VLS and VS mechanism are mostly accepted to interpret the growth process; however, the detailed mechanisms are not yet understood in detail in many cases.

#### **2.3.1 Vapor-liquid-solid mechanism**

Among the various mechanisms, the VLS mechanism is well established and most widely accepted. Control over the nanowire diameter and its morphology has been demonstrated by

VLS growth.<sup>64-69</sup> The VLS mechanism was proposed by Wagner and Ellis in 1964 to explain the growth of Si whiskers using Au as metal catalysts.<sup>70</sup> As illustrated in Figure 2-4, the VLS process consist basically 3 steps: (1) Formation of the liquid alloy droplet by heating up, (2) crystal nucleation upon gas adsorption and supersaturation, and (3) axial growth from the crystalline seeds to form nanowires. According to the VLS mechanism, a liquid phase is formed initially, due to formation of a eutectic phase or the presence of a low-melting-point phase in an alloy system. The liquid phase adsorbs the reactant gaseous species more efficiently than the solid surface. On supersaturation of the liquid alloy, a nucleation center forms, and serves as a preferred site for axial growth of a nanowire. The adsorbed gas reactants are then diffused through the liquid phase to the solid/liquid interface, and the growth of the solid phase proceeds. Because of the larger sticking coefficient of the reactants in the liquid, growth is much faster at the solid/liquid interface compared to the solid/vapor interface.

The diameter of a nanowire via VLS growth is primarily determined by the liquid alloy droplet, and the thermodynamic-limited minimum radius is given by:<sup>71</sup>

$$R_{\min} = 2\sigma_{LV}V_L/RT \ln s$$

Where  $\sigma_{LV}$  is the liquid/vapor surface free energy,  $V_L$  is the molar volume of liquid, and  $s$  is the vapor phase supersaturation.

Selection of metal catalyst species depends on the formation of a eutectic phase at the temperature according to the phase diagram, as well as vapor/liquid/solid interfacial energies and chemical stability in the reaction products. A wide variety of elemental semiconductor (Si and Ge), binary compound semiconductor (GaN, GaAs, GaP, InAs) and oxide (ZnO, MgO, SnO<sub>2</sub>, CdO, TiO<sub>2</sub>, In<sub>2</sub>O<sub>3</sub> and Ga<sub>2</sub>O<sub>3</sub>) nanowires has been synthesized via the VLS method.<sup>62</sup> Relatively good control over the nanowire diameter and distribution has been achieved and reported.

### **2.3.2 Vapor-solid mechanism**

There have been numerous reports on one-dimensional nanostructure growth from vapor phase without metal catalyst, the growth mechanism usually refer to vapor-solid mechanism.<sup>72</sup> Under high temperature condition, source materials are vaporized and then directly condensed on the substrate placed in the low temperature region. Once the condensation process happens, the initially condensed molecules form seed crystals serving as the nucleation sites. As a result, they assist directional growth to minimize the surface energy. The process is illustrated in Figure 2-5.

With thermodynamic and kinetic considerations, the formation of nanowires could be possibly through different models, including an anisotropic growth, Frank's screw dislocation model and defect-induced model. In an anisotropic growth model, one-dimensional growth can be also explained by the preferential reactivity and binding of gas phase reactants along specific crystal facets, and also the desire for a system to minimize surface energies. In the dislocation and defect-induced growth models, specific defects are known to have larger sticking coefficients for gas phase species, thus resulting anisotropic growth at those sites. Although the exact mechanisms for vapor-solid growth are not well understood, a variety of nanostructures have been synthesized via this approach.<sup>66,73</sup>

### **2.3.3 Laser ablation**

Laser-assisted catalytic VLS growth is a method used to generate nanowires under non-equilibrium conditions.<sup>5,74,75</sup> A target containing the catalyst and the source materials, plasma plume containing both catalyst and source material is generated during the ablation. The nucleation occurs on the substrate where nanowires grow.

### **2.3.4 Thermal evaporation**

In thermal evaporation, a vapor reacts on the substrate to produce the desired product. In the case of nanowires, the vapor-liquid-solid (VLS) method described previously usually applies,

where the substrate usually deposit with metal catalysts serve as seed layer. The seed layer reacts with the source vapor material until it is saturated and the desired material starts to solidify and grow outward from the catalyst. The growth parameters such as: partial oxygen pressure, chamber pressure, substrate and growth temperature are crucial to the resulting structure of product. By control the oxygen pressure and growth temperature, different nanostructures such as nanorods, nanowires, nanorings, nanobelts and comb-like structures can be synthesized.<sup>76</sup>

The solid-vapor process is a relative simple setup used to synthesis a variety of metal oxide nanostructures. The process are carried out in a horizontal tube furnace, which is composed of a horizontal tube furnace, an alumina tube, a rotary pump system and a gas supply and control system. The source materials (normally powders) are loaded on an alumina boat and positioned at the center of the alumina tube, where the temperature is the highest. Substrates were placed downstream for collecting growth products. A variety of metal oxide nanowires (ZnO, SnO<sub>2</sub>, In<sub>2</sub>O<sub>3</sub>, CdO) with different nanostructures were successfully synthesized by thermal evaporation process.<sup>43,71,77-80</sup>

### **2.3.5 Solution-based chemistry**

One of the major disadvantages of high temperature approaches to one-dimensional nanowire synthesis including the high cost of fabrication, high processing temperature and the inability to produce metallic nanowires. As a result, a solution-based synthesis of nanowires with controllable diameters without the use of templates, catalysts or surfactants has been demonstrated.<sup>81-87</sup> The relative low cost setup to synthesize one-dimensional nanostructure can be realized via selective capping mechanism at low temperature. The kinetic control of the nano-crystal growth by preferentially adsorbing molecular capping agents to specific crystal faces, thus inhibiting growth of that surface, results in anisotropic growth. Because of the low

temperature process, the nanowires can be grown on inexpensive substrates, such as glass and plastic substrate.<sup>88</sup> It provides an important feature for device applications.

## **2.4 Applications of Nanowires**

### **2.4.1 Electrical applications**

The semiconductor industry continues to face technological (especially in lithography) challenges as the device feature size is decreased, especially below 100 nanometers. The self-assembly of nanowires might open a way to construct devices that do not rely on improvements in photolithography. Devices made from nanowires have several advantages over those made by photolithography. For example, a variety of approaches have been devised to organize nanowires via bottom up approaches, thus the expensive lithography techniques are not required. In addition, unlike traditional silicon processing, different semiconductors for example, metal oxides, can be used simultaneously in nanowire devices to produce diverse functionalities.

Transistors made from nanowires could also hold advantages due to their unique morphology. For example, in bulk field effect transistors (FETs), the depletion layer formed below the source and drain region results in a source–drain capacitance which limits the operation speed.<sup>89</sup> However, in nanowires, the conductor is surrounded by an oxide and thus the depletion layer cannot be formed. Thus, depending on the device design, the source–drain capacitance in nanowires could be greatly minimized and possibly eliminated.<sup>90</sup>

Nanowires have also been proposed for applications associated with electron field emission, such as flat panel displays, because of their small diameter and large curvature at the nanowire tip, which may reduce the threshold voltage for electron emission.<sup>91-95</sup> In this application, the demonstration of very high field emission currents from the sharp tip of nanowires has stimulated interest in this potential area of application for nanowires.

## 2.4.2 Optical applications

Nanowires also show promise for optical applications. One-dimensional systems exhibit novel properties in their joint density of states, allowing quantum effects in nanowires to be optically observable, sometimes even at room temperature. Since the density of states of a nanowire in the quantum limit (small wire diameter) is highly localized in energy, the available states quickly fill up with electrons as the intensity of the incident light is increased.<sup>34,68,96,97</sup> This filling up of the sub-bands, as well as other effects that is unique to low-dimensional materials, lead to strong optical nonlinearities in quantum wires. Quantum wires may thus yield optical switches with a lower switching energy and increased switching speed compared to currently available optical switches.<sup>97</sup>

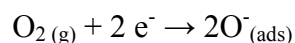
Light emission from nanowires can be achieved by photoluminescence (PL) or electroluminescence (EL), distinguished by whether the electronic excitation is achieved by optical illumination or by electrical stimulation across a p-n junction, respectively. PL is often used for optical property characterization, but from an applications point of view, EL is a more convenient excitation method. Light-emitting diodes (LEDs) have been achieved in junctions between a *p*-type and an *n*-type nanowire and in superlattice nanowires with *p*-type and *n*-type segments.<sup>3,12</sup> The light emission was localized to the junction area, and was polarized in the superlattice nanowire.

Nanowire photodetectors were also interesting applications. ZnO nanowires were found to display a strong photocurrent response to UV light irradiation. The conductivity of the nanowire increased by several orders of magnitude compared to the dark state. The response of the nanowire was reversible, and selective to photon energies above the band-gap, suggesting that ZnO nanowires could be a good candidate for optoelectronic switches.<sup>28,98,99</sup>

### 2.4.3 Chemical and biochemical sensing

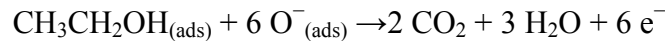
Chemical and biological sensors have a great influence in the areas of personal safety, public security, semiconductor processing, and the automotive and aerospace industries. Thin film based semiconducting metal oxides as chemical sensing materials have been extensively studied for a long time due to their advantageous feature, such as good sensitivity to the ambient conditions and ease in fabrication.<sup>21,22,37,100-103</sup> However, there are some critical limitations difficult to overcome for thin-film-based sensing devices. The thin-film based devices have a limited maximum sensitivity due to the limited surface-to-volume ratios. In the case of polycrystalline thin film devices, only a small fraction of the species adsorbed near the grain boundaries is active in modifying the electrical transport properties (Figure 2-6). Furthermore, most thin-film devices are operated at high temperatures (200–600°C) in order to achieve enhanced chemical reactivity between sensor materials and surrounding gases. These drawbacks bring inconvenience for practical applications. In contrast to thin-film-based devices, devices based on one-dimensional nanostructures have great potential to overcome these fundamental limitations.

Sensors for chemical and biochemical substances with nanowires as the sensing probe are a very attractive application area. Nanowire sensors will potentially be smaller, more sensitive, demand less power, and react faster than their macroscopic counterparts. For ZnO nanowires, the most widely accepted model is based on the modulation of the depletion layer within ZnO due to the chemisorption as illustrated schematically in Figure 2-7. When nanowires are exposure in oxidizing gas environment, oxygen adsorbs on the exposed surface of ZnO, extracting an electron from the conduction band, ionizes to  $O^-$  or  $O^{2-}$ . The  $O^-$  is believed to be dominant among all:



Consequently, depletion layers are formed in the surface as well as in the grain-boundary regions of ZnO, causing the carrier concentration and electron mobility to decrease. These chemisorbed  $O_2^-$  deplete the surface electron states and consequently reduce the channel conductivity. The resistivity increases as well.

When exposed to reducing gases such as ethanol, the ethanol will react with the adsorbed  $O^-$ :



By releasing the trapped electron back to the conduction band and, then, both the carrier concentration and the carrier mobility of ZnO increase. From the above-mentioned surface reactions, one can expect that the factors, which can affect the interaction process between the surface-reactive chemical species (adsorbed  $O^-$ ) and the target-gas molecules (ethanol for example), would be of importance for the gas-sensing performances of ZnO devices.

Moreover, the more the effective surface area, the more the oxygen-adsorption quantities and the higher the sensitivity of metal oxide sensors. Since the ZnO nanowires have a larger surface area exposed to the air and a consequent higher quantity of the surface states related to oxygen vacancies than that of the ZnO thin films, a higher gas sensitivity and a faster response time of the ZnO nanowire sensors than those of the ZnO thin film devices are reasonable. This eventually increased the conductivity of the ZnO nanowires. Because of the small diameter of nanowires, it's expected that the bulk electronic transport properties will change. Based on these properties, ZnO nanowires could be used as chemical and biochemical sensing materials.

Table 2-1. Properties of ZnO

Property	Value
Lattice parameters at 300 K	
$a_0$	0.32495 nm
$c_0$	0.52069 nm
$a_0/c_0$	1.602
$u$	0.345
Density	5.606 g cm <sup>-3</sup>
Stable phase	Wurtzite
Melting point	1975 °C
Thermal conductivity	0.6
Linear expansion coefficient	$a_0: 6.5 \times 10^{-6}$ $c_0: 3.0 \times 10^{-6}$
Static dielectric constant	8.656
Reflective index	2.008
Energy gap	3.4 eV, direct
Intrinsic carrier concentration	$<10^6$ cm <sup>-3</sup>
Exciton binding energy	60 meV
Electron effective mass	0.24
Electron Hall mobility	200 cm <sup>2</sup> V <sup>-1</sup> S <sup>-1</sup>

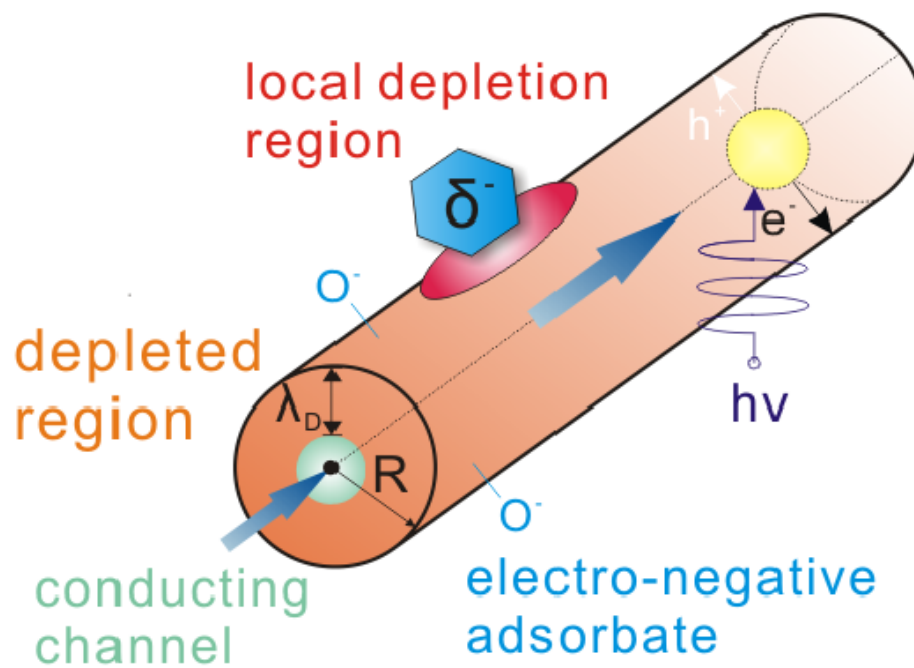


Figure 2-1. Electronic, chemical and optical processes occurring on metal oxides that can benefit from reduction in size to the nanometer range.

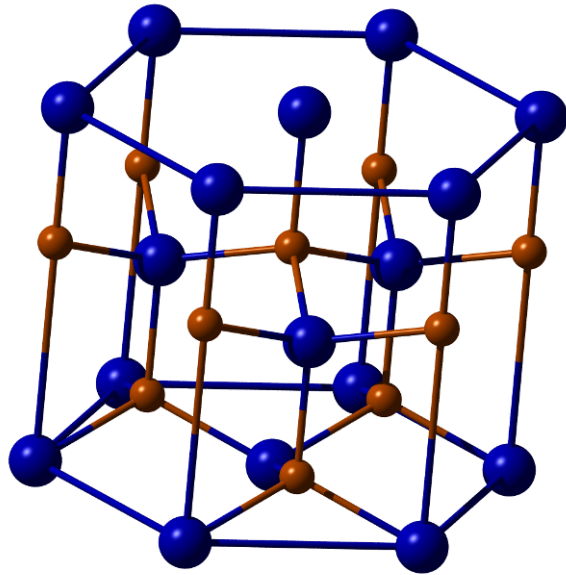


Figure 2-2. Crystal structure of wurtzite ZnO. The Zn atoms (orange) are tetrahedrally coordinated to four O atoms (blue).

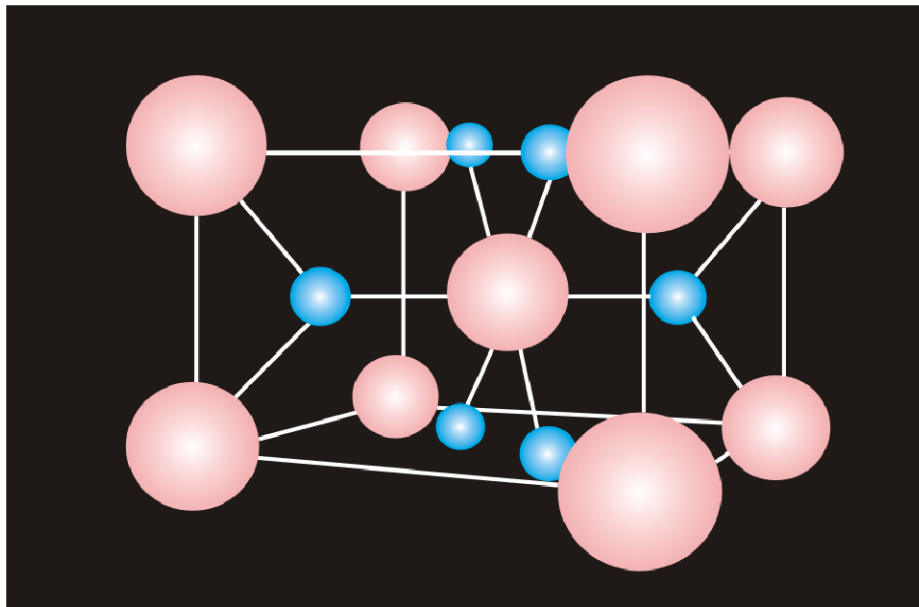


Figure 2-3. Unit cell of rutile SnO<sub>2</sub>, consisting of two tin atoms (Red) and four oxygen atoms (blue), with metal and oxygen atoms having an octahedral coordination.

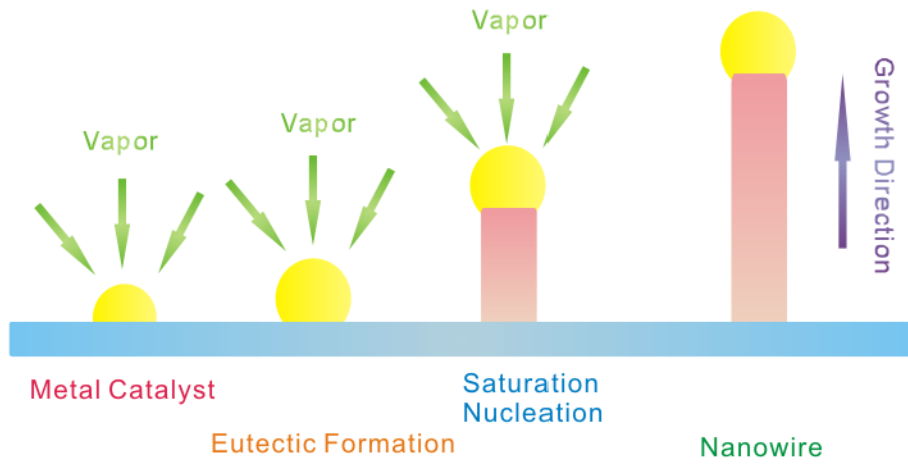


Figure 2-4. Vapor-Solid-Liquid (VLS) process.

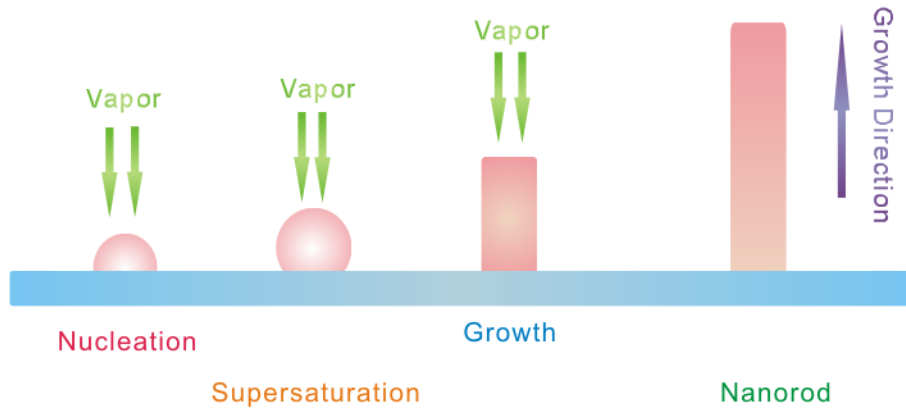


Figure 2-5. Vapor-Solid (VS) process.

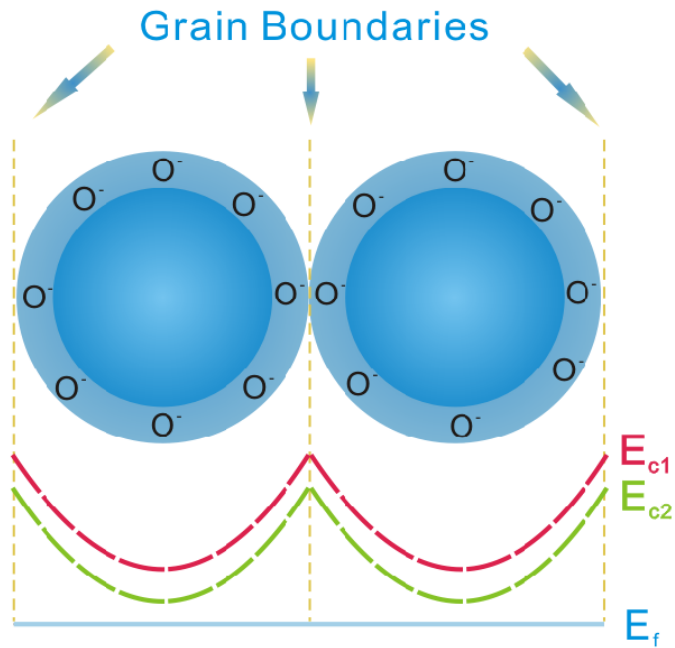


Figure 2-6. The energy band diagram of oxide thin film materials. Showing the Schottky barrier height at the grain boundary either with or without a chemically reducing ambient.

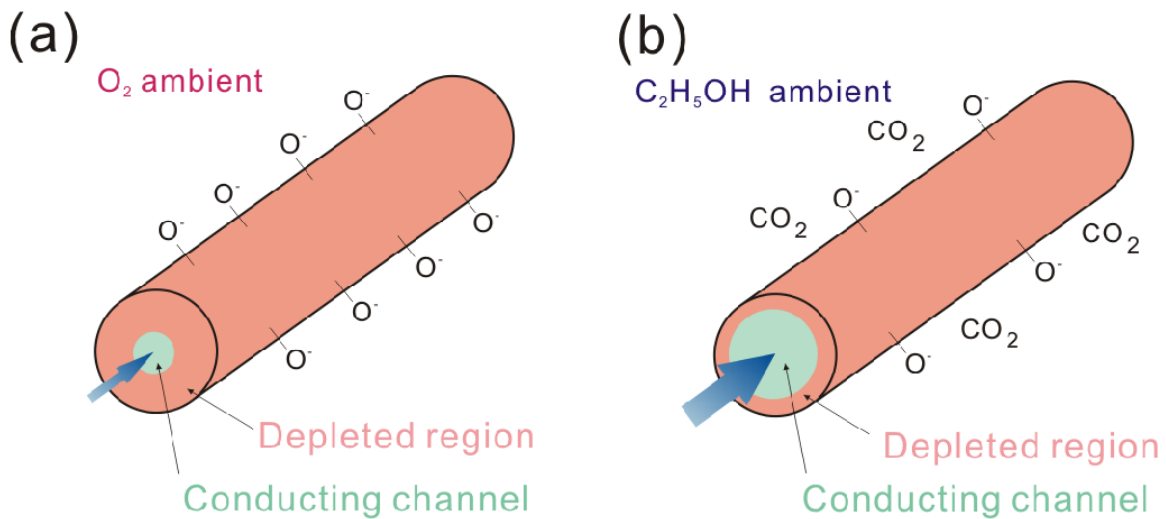


Figure 2-7. Gas sensing mechanism of ZnO nanowire. (a) The large surface depletion region caused by oxidizing ambient (b) the small surface depletion region caused by reducing ambient.

## CHAPTER 3 EXPERIMENTAL DETAILS AND CHARACTERIZATION

### 3.1 Materials Synthesis Techniques

Any performance or property of a material mainly depends on the efficiency and precise nature of the synthesis and the fabrication methods. The desirable properties of materials can be realized by the control of dimension, size, morphology, microstructure and chemical composition of materials. The ability to control these properties strongly depends on different synthesis methods. In this dissertation, various metal oxide nanowires and thin films were synthesized via two different approaches. Molecular beam epitaxy was used to synthesize ZnO nanowires by a catalyst-assisted approach, while pulsed laser deposition was employed to grow epitaxial oxide thin films and metal oxide nanowires without catalyst. The detail of materials synthesis techniques are described in following sections.

#### 3.1.1 Molecular beam epitaxy

Molecular beam epitaxy (MBE) is a material deposition technique capable of predictably and reproducibly yielding material with very low impurity levels and precise thickness control. Normally MBE requires ultra high vacuum and proceed at low growth temperature to prevent possible contamination. MBE involves the generation of fluxes of constituent matrix and doping species, the reaction take places at the heated substrate and form an ordered overlayer. Elemental or compound constituents are heated or introduced into the chamber to generate mass transfer to the substrate via the vapor phase. To maintain the high purity of flux, the ultra high vacuum is needed. The fluxes of elements can be temporally modulated either by altering the evaporation conditions or physically interrupting the beam using mechanical shutters.

The precision with composition and doping of a structure can be tailored by MBE. To achieve this level of control, deposition rates are normally around less than one monolayer per

second. The low growth rates and growth temperatures have made MBE a superb technique for growing complex hetero-epitaxial structures on atomic scale. The high vacuum provides a clean environment and allows high quality films to be grown. The growth rate is dependent on the flux of the cells and the growth temperature. Lower growth temperature and higher fluxes result in amorphous or polycrystalline films, while higher growth temperature and lower fluxes can be used to synthesize single crystal films.

The ZnO nanowires were synthesized using the catalyst-driven molecular beam epitaxy method. The growth was carried out in a conventional MBE system (Figure 3-1). The base pressure was pumped down to approximately  $5 \times 10^{-8}$  mbar using a cryopump. An ozone/oxygen mixture generated by ozone generator was used as the oxidizing source. The nitrogen-free plasma discharge ozone generator yielded an  $O_3/O_2$  ratio on the order of 1–3%. The cation flux was provided by Kundsens effusion cells using high purity Zn metal (99.9999%) as the source materials. The Zn and  $O_3/O_2$  pressures were determined by a nude ionization gauge that was placed at the substrate position prior to growth. The  $O_3/O_2$  pressure was fixed at  $5 \times 10^{-6}$  mbar by a leaking valve during growth. The Zn pressure was varied between  $5 \times 10^{-7}$  and  $4 \times 10^{-6}$  mbar controlled by temperature.

### **3.1.2 Pulsed laser deposition**

The technique of pulsed laser deposition (PLD) has been used to deposit high quality films of materials for more than a decade.<sup>104</sup> The technique uses high power laser pulses (typically  $\sim 10^8$  Wcm<sup>-2</sup>) to melt, evaporate and ionize material from the surface of a target. This process produces a transient, highly luminous plasma plume that expands rapidly away from the target surface. The ablated material is collected on a heated substrate on which it condenses and the thin film grows.

It was found to have significant benefits over other film deposition methods. The capability for stoichiometric transfer of material from target to substrate can be reproduced in the deposited film. The high deposition rates can be achieved at moderate laser fluences. Since a laser is used as an external energy source, the deposition can occur in both inert and reactive background gases. However, the plasma plume created during ablation process is highly forward directed, therefore the thickness of resulting film is highly non-uniform and the composition can vary across the film. The deposition area is also relatively small.

The oxide nanowires and thin films were synthesized using the pulsed laser deposition method. The growth was carried out in a commercial PLD system build by Neocera (Figure 3-2). The ablation target was fabricated using high purity oxide powders. The target was pressed and sintered at high temperature. A Lambda-Physik Compex 205 KrF excimer laser was used as the ablation source. The laser produces a coherent beam with a 248 nm wavelength. A desired repetition rate can be used to achieve different deposition rates, with target to substrate distance of 2.5 cm and a laser pulse energy density of 1–3 J/cm<sup>2</sup>. The growth chamber exhibits a base pressure of 10<sup>-6</sup> Torr. Prior to growth, the target was cleaned in situ by pre-ablating with approximately 2000 shots. The growth experiments were performed over a temperature range of 400–800°C in a desired oxygen pressure.

### **3.2 Characterization Techniques**

Different techniques were used to analyze the materials, including surface morphology, structural, optical, chemical and electrical analysis. The surface analysis is preformed to know the morphology and roughness of the surface. Structural analysis provides the crystal structure, phases and defects information of materials. It also provides information about alignments between materials and substrates. Optical analysis is useful to understand the optical properties in transparent materials. Chemical analysis is useful in providing both qualitative and

quantitative information, which are very valuable to know doping amounts and contaminations. Electrical analysis is important because the electrical properties directly determine the performance of materials in device applications. With all these characterization techniques not only provide a better understanding of materials but also are helpful to optimize the growth conditions, producing better materials and devices.

### **3.2.1 Scanning electron microscope**

The scanning electron microscope (SEM) is often the first analytical instrument used to quickly look at a material. The SEM is used to observe surface and cross-section images of nanowires samples. The topographical information such as diameters, length and growth direction of nanowires can be collected quickly. The electron beam is focused by condense lens into fine probe and scanned over a small area of the sample. The interaction between beam and sample surface causes elastic and inelastic interactions resulting in emission of secondary electrons. Due to their low energy, these electrons originate within a few nanometers from the surface. By collecting secondary electrons, surface topography can be observed. The measurements were performed in a JEOL 6335F system that uses a cold cathode field emission electron source. The FE-SEM was operated at 15 keV in high magnifications. In addition, the samples were not coated to prevent contamination and artificial features

### **3.2.2 Atomic force microscopy**

Atomic force microscopy (AFM) provides information on the topography and morphology of the surface. Inter-atomic forces between the atoms on the surface and those on the tip cause the deflection of a micro-fabricated cantilever. Because the magnitude of the cantilever deflection depends strongly upon the separation between the surface and tip atoms, they can be used to map out surface topography with atomic resolution in three dimensions.

AFM Dimension 3100 (Digital Instrument, Inc.) was performed in tapping mode to obtain surface topographic and roughness of metal oxide thin films.

### 3.2.3 X-ray diffraction

X-ray diffraction (XRD) is used to obtain structural information and determine the phases of the sample. X-ray diffraction is commonly used to identify unknown substances, by comparing diffraction data against a database maintained by the International Centre for Diffraction Data. It may also be used to characterize heterogeneous solid mixtures to determine relative abundance of crystalline compounds and, when coupled with lattice refinement techniques, can provide structural information on unknown materials. Powder diffraction is also a common method for determining strains in crystalline materials. The XRD measurements were performed in a Philips APD 3720 system that uses a copper x-ray source. The source emits Cu  $K_{\alpha 1}$  X-rays with a  $1.54056 \text{ \AA}$  for diffraction. The radiation impinged on the sample and undergoes constructive or destructive interference after reflecting from the sample. Constructive interference will cause a peak at a particular  $2\theta$  angle according to Bragg's law:

$$2d\sin\theta=n\lambda$$

where  $d$  is the spacing between planes,  $\lambda$  is the wavelength of the incident x-ray,  $n$  is the number of whole wavelengths. For a single crystal, there are only specific orientations that satisfy the Bragg's law. On the other hand, for a polycrystalline film with differently oriented grains, diffraction peaks appear when those grains meet the diffraction conditions. Normally the full width at half maximum (FWHM) of a diffraction peak can be used to determine the crystal quality of the materials. For nanowires, the peak positions in the X-ray diffraction pattern can be used to determine the chemical composition and the crystal phase structure of the nanowires.

High resolution XRD was performed on epitaxial thin film samples via a Philips X'pert High Resolution X-ray Diffraction system in order to determine the thickness, distribution of crystalline orientations, grain size and mosaic spread in crystalline materials.

#### **3.2.4 Transmission electron microscope**

Transmission electron microscope and high-resolution transmission electron microscopy are powerful imaging tools for studying nanowires at the atomic scale. They usually provide more detailed structural information than are seen in the SEM images. Transmission electron microscope (TEM) is performed to obtain the detail structural information. TEM is an imaging technique whereby a beam of electrons is transmitted through a specimen, then an image is formed, magnified and directed to appear either on a fluorescent screen to be detected by a CCD camera. Because the wavelength of high-energy electrons is a fraction of a nanometer, and the spacings between atoms in a solid is only slightly larger, the atoms act as a diffraction grating to the electrons, which are diffracted. Therefore, some fraction of electrons will be scattered to particular angles, determined by the crystal structure of the sample, while others continue to pass through the sample without deflection. In the diffraction mode, the selected area diffraction (SAD) is useful to identify crystal structures and examine crystal defects. It is similar to x-ray diffraction, but unique in areas as small as several hundred nanometers in size can be examined, whereas x-ray diffraction typically samples areas several centimeters in size. This is a very useful technique to determine the crystal structure of nanowire materials. An analytical TEM is one equipped with detectors that can determine the elemental composition of the specimen by analyzing its X-ray spectrum or the energy-loss spectrum of the transmitted electrons.

High resolution transmission electron microscopy (HR-TEM) is an imaging mode of the TEM that allows the imaging of the crystallographic structure of a sample at an atomic scale. Because of its high resolution, it is an invaluable tool to study nano-scale properties of crystalline

material such as semiconductors and metals. At these small scales, individual atoms and crystalline defects can be imaged. The high resolution also permits the surface structures of the nanowires to be studied. It also serves as a powerful tool to observe core-sheath nanowire structures by mass contrast imaging.

There are a number of drawbacks to the TEM technique. Many materials require extensive sample preparation to produce a sample thin enough to be electron transparent, which makes TEM analysis a relatively time consuming process with a low throughput of samples. The structure of the sample may also be changed during the preparation process. Also the field of view is relatively small, raising the possibility that the region analyzed may not be characteristic of the whole sample. There is potential that the sample may be damaged by the electron beam, particularly in the case of biological or radiation sensitive materials.

By coupling the powerful imaging capabilities of TEM with energy dispersive X-ray spectrometer within the microscope, additional properties of the nanowires can be probed with high spatial resolution. The elemental composition within the probed area can be determined. This technique is particularly useful for the compositional characterization of superlattice nanowires and core-shell nanowires. In this dissertation, HR-TEM images and selected area diffraction (SAD) patterns of metal oxide nanowires were acquired by a JEOL 2100F transmission electron microscope at 200 keV.

### **3.2.5 Photoluminescence**

Optical methods provide an easy and sensitive tool for measuring the electronic structures of a material, since optical measurements require minimal sample preparation.

Photoluminescence (PL), a powerful and nondestructive analysis technology, can reveal the band structure and the carrier transport behaviors in materials. Photoluminescence refers to emission of light resulting from optical stimulation. When an electron increases energy by absorbing light,

there is a transition from the ground state to an excited state. This excited state is not stable and has to return to the ground state. In luminescence materials the released energy is in the form of light, which is called as radiative transition. This emitted light is detected as photoluminescence. PL is typically used to determine band gap of a semiconductor and identify impurities. A He-Cd (325 nm) laser was used as the excitation source and photoluminescence was detected by a GaAs PMT detector. All the measurements were performed in a wavelength of 340–800 nm at room temperature.

### **3.2.6 Energy-Dispersive X-ray spectroscopy**

Energy-dispersive X-ray spectroscopy (EDX) is an analytical tool predominantly used for chemical characterization. EDX measures the emitted x-ray spectrum when sample is bombarded by a high-energy radiation. The emitted spectrum consists of a series of peaks representative of the type and relative amount of each element in the sample. The relative amount of each element can be calculated by comparing the peak heights with standards and applying ZAF corrections, where  $Z$  is the atomic number,  $A$  is absorption and  $F$  is the x-ray fluorescence. The EDX analysis was performed inside JEOL 6335F fitted with liquid nitrogen cooled EDX detector.

### **3.2.7 Hall measurement**

The Hall measurement is used to determine the electrical transport properties of a material. The carrier type, mobility, density and electrical resistivity can be measured from it. The Hall Effect provides a relatively simple, fast and low cost method to extract these electrical properties.<sup>105</sup>

The Lorentz force is defined as a force exerted on a charged particle in an electromagnetic field. For example, an  $n$ -type, bar shaped semiconductor shown in Figure 3-3. It is assumed that a constant current  $I$  flows along the  $x$ -axis from left to right in the presence of a  $z$ -directed magnetic field. Under Lorentz force electrons drift toward the negative  $y$ -axis and accumulate on

the side of the sample to produce an electrical surface charge. A potential drop across the sample called Hall voltage is formed. The induced electric field increases until it counteracts to the opposite Lorentz force:

$$E_y = v_x B_z = \frac{B_z j_x}{nq}$$

where  $eE_y$  is the induced electric field force,  $qv_x B$  is the Lorentz force,  $j_x = nqv_x$  is the total current density. The Hall coefficient  $R_H$  is defined as:

$$R_H = \frac{1}{nq}$$

For electrons the charge is  $q = -e$ , the hall coefficient is negative for  $n$ -type semiconductor while positive indicates  $p$ -type semiconductor.

The mobility is defined as the coefficient of proportionality between velocity and electric field:

$$\mu = \frac{v_x}{E_x} = \frac{j_x}{nqE_x} = R_H \sigma$$

where  $\sigma$  is conductivity, which is proportional to mobility.

The resistivity, carrier type, and carrier concentration of samples were determined at room temperature using a Lakeshore 7507 system with a 10 Tesla magnet. The samples were cut into a 10 mm<sup>2</sup> pieces. And indium dots are soldered onto corners to perform Van der Pauw measurement.

### 3.3 Processing and Device Fabrication

#### 3.3.1 Electron beam lithography

The electron beam lithography was used for single nanowire device fabrication. Instead of photolithography, e-beam lithography provides accessibility to exposure desired patterns in

small area without a mask. The electron gun generates a beam of electrons with a suitable current density. A single-crystal lanthanum hexaboride ( $\text{LaB}_6$ ) is used to for the electron gun. Condenser lenses are used to focus the electron beam to a spot size 10–25 nm in diameter. Beam blanking plates that turn the electron beams on and off, and beam deflection coils are computer controlled and operated at MHz or higher rates to direct the focused electron beam to any location in the scan field on the substrate. Since the scan field is much smaller than the substrate diameter, a precision mechanical stage is used to position the substrate to be patterned.

The advantages of electron-beam lithography include the generation of sub-micrometer resist geometries, highly automated and precisely controlled operation, depth of focus greater than that available from optical lithography, and direct patterning on a semiconductor wafer without using a mask. The disadvantage is that electron-beam lithographic machines have low throughput. A RAITH 150 operated at 10 keV has been used to generate patterns for single nanowire device fabrication; the details of device fabrication will be described later.

### **3.3.2 Sputter deposition**

Sputtering is basically a simple PVD process to deposit thin films. The atoms are removed from the surface of a solid by high-energy ion impacts. The plasma consisting of argon ions and electrons is ignited between the source and substrate. The target material is placed on the electrode with the voltage set to maximize the flux at the target. As the positively charged argon ions bombard the target surface, the target material is removed from the surface. The atoms impinge on the substrate and form a thin film. Sputter deposition has multiple advantages over other techniques, including low cost, large area deposition, high throughput and good uniformity. Sputtering is used extensively in the semiconductor industry to deposit thin films of various materials in integrated circuit processing. A Kurt Lesker CMS-18 multi target sputter

deposition system was used to deposit metal contacts and metal catalysts on nanowires in this dissertation.

### **3.3.3 Fabrication of multiple nanowire devices**

By the nature of nanowires is highly cross-linked on dielectric substrates, the sensing properties can simply measure the transport by put down electrodes on the substrate. Multiple nanowire devices were fabricated by sputtered Al/Ti/Au electrodes on as-grown samples by a shadow mask. The separation of electrodes was approximately 400  $\mu\text{m}$ . The samples were placed on a holder and Au wires were bounded to the contact pads for current-voltage (I-V) measurements. Figure 3-4 shows a typical gas sensor device mounted on the holder.

### **3.3.4 Fabrication of single nanowire devices**

The fabrication process of single ZnO nanowire devices is illustrated in Figure 3-6. The nanowires were released from the as-grown substrate by sonication in ethanol and then transferred to Si substrates with 100 nm thermal oxide. The silicon substrates were deposited with gold markers before nanowire dispersion. With the sputtered markers on the substrate, the location of dispersed single nanowires can be addressed. The E-beam lithography followed by metallization was used to pattern electrodes contacting both ends of a single nanowire. The separation of electrodes was approximately 3 $\mu\text{m}$ . Au wires were bounded to the contact pads for current-voltage (I-V) measurements.

### **3.3.5 Gas sensing measurement**

Transport DC-IV measurements were used to examine gas sensing properties on thin films, single and multiple nanowires devices. The measurement has been performed in a tube furnace system (Figure 3-5) connected with Hewlett Packard Model 4156 semiconductor analyzer. The system equipped with a variety of different gas ( $\text{O}_2$ ,  $\text{O}_3$ ,  $\text{N}_2$  and  $\text{H}_2$ ) and gas flow is controlled by a mass flow controller. Before measurements, the chamber was pumping down to  $10^{-5}$  Torr by a

turbo molecular pump. Current-voltage (I-V) measurement was used to examine the gas sensing properties and a fix bias (0.5 V) was applied during the measurements. The furnace can be heated up to 400°C to perform gas sensing measurements at high temperatures. The response ( $s$ ) was defined as the ratio of the electrical resistance in air ( $R_a$ ) to that in a sample gas ( $R_g$ ):

$$s = \frac{R_a}{R_g}$$

The sensitivity ( $\beta$ ) was defined as the change in resistivity ( $R_g - R_a$ ) divided by resistance in dry air ( $R_g$ ):

$$\beta = \left\| \frac{R_g - R_a}{R_a} \right\|$$

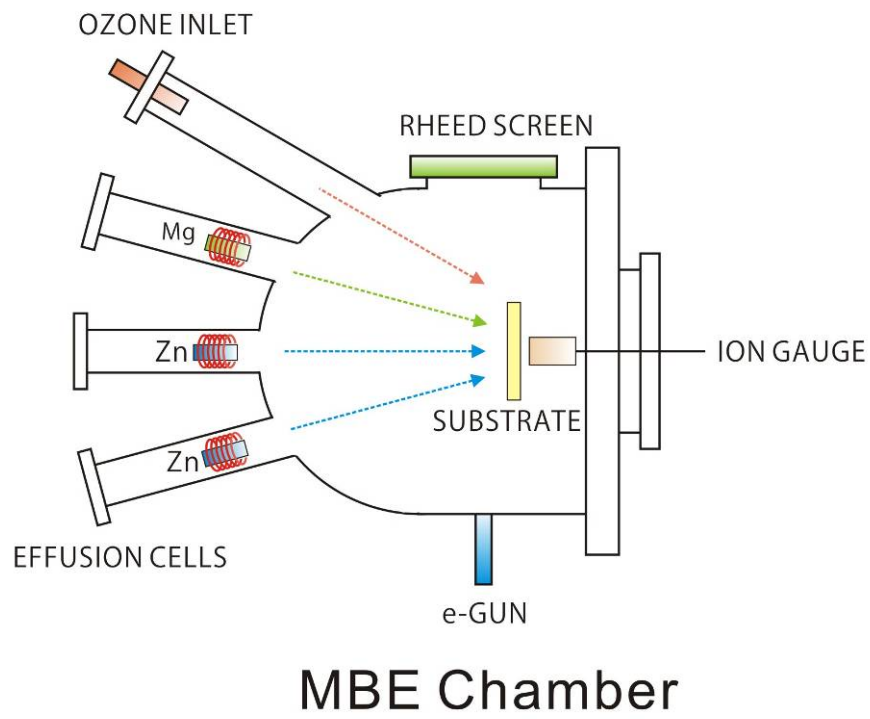


Figure 3-1. Molecule beam epitaxy chamber.

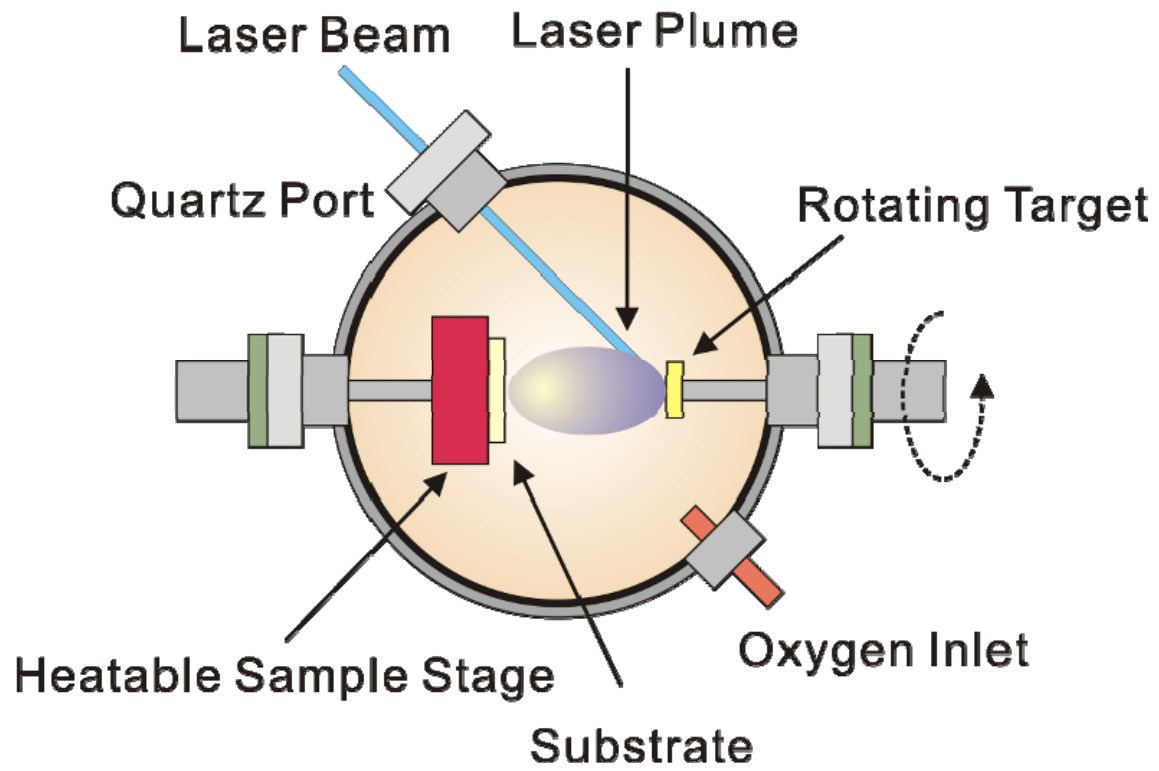


Figure 3-2. Pulsed laser deposition chamber.

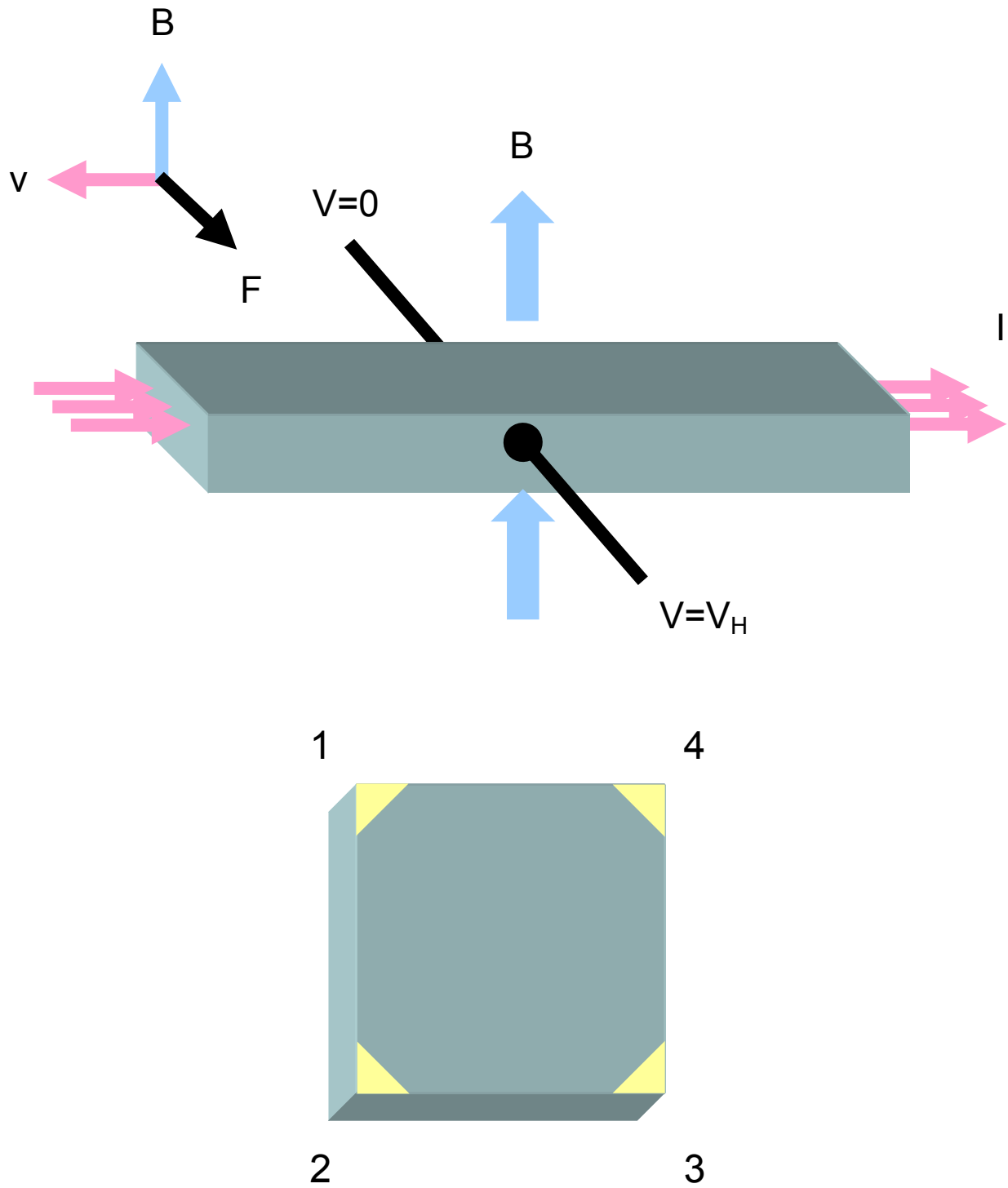


Figure 3-3. Typical Hall measurement setup and Van der Paul sample geometry.



Figure 3-4. Photograph of gas sensor device

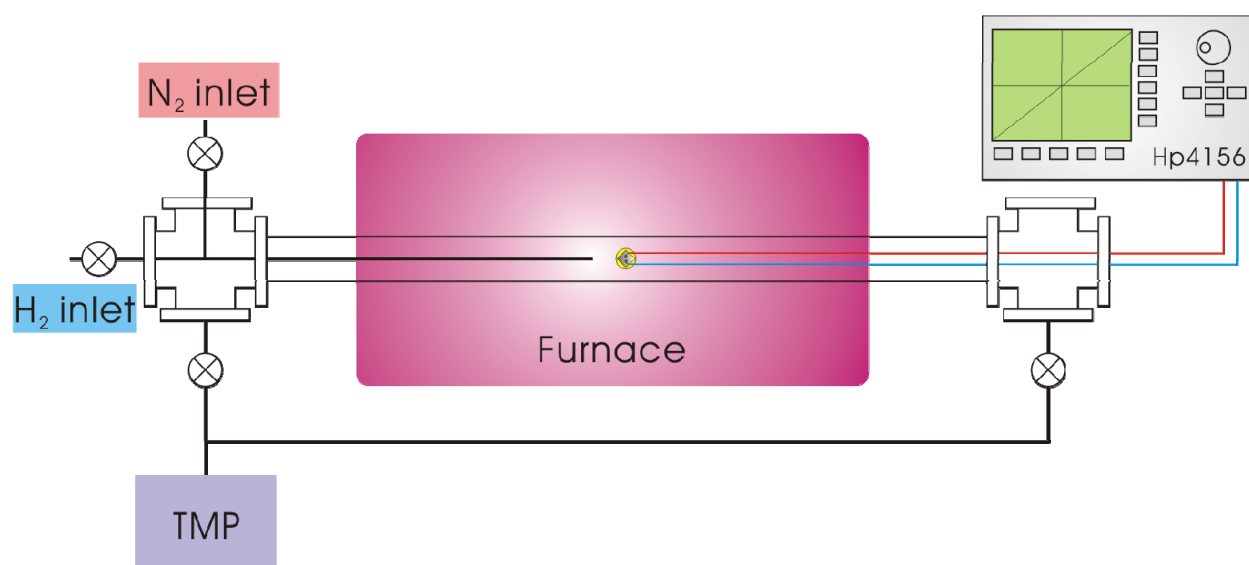


Figure 3-5. Gas sensing measurement system.

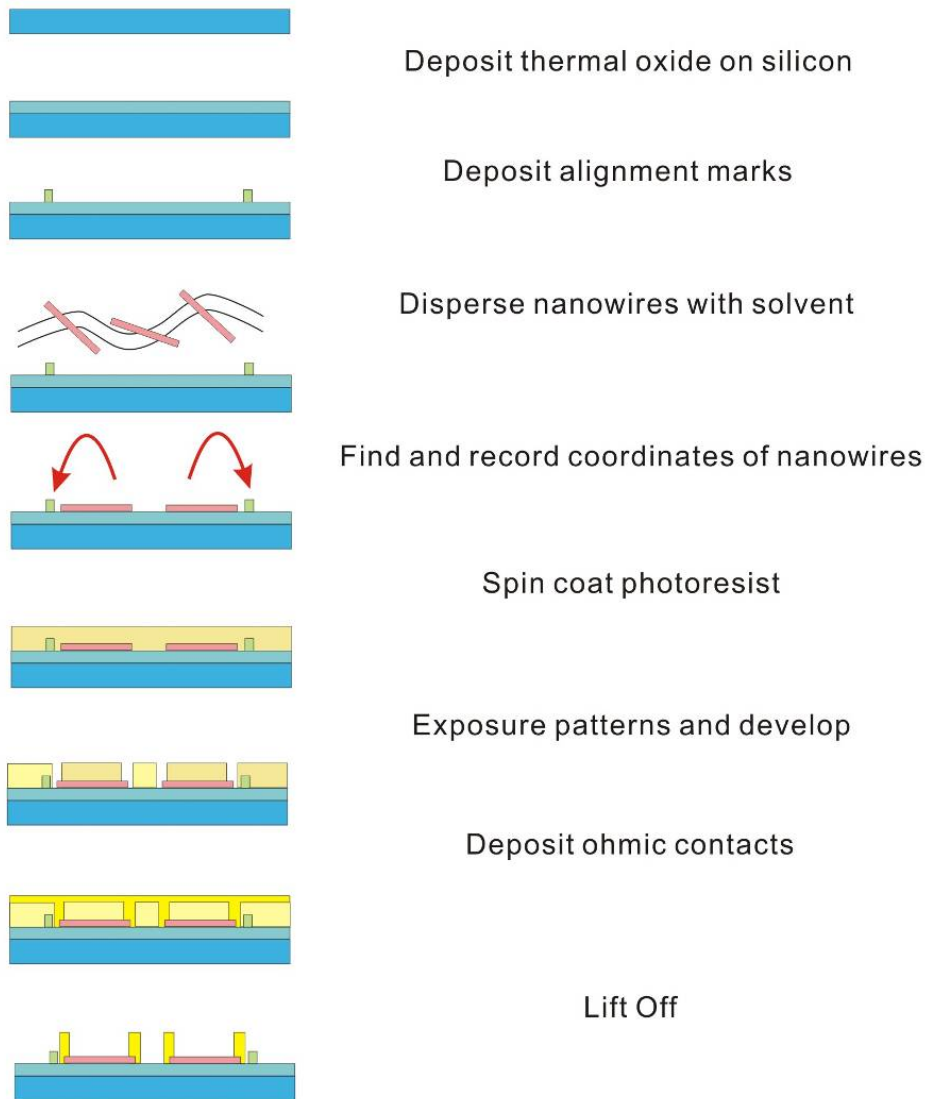


Figure 3-6. Process sketch for the fabrication of single ZnO nanowire devices.

## CHAPTER 4 NUCLEATION CONTROL AND SELECTIVE GROWTH OF ZNO NANOWIRES

### 4.1 Introduction

One-dimensional nanostructures are potential candidates for a range of device applications in nanoelectronics, optoelectronics and biosensors.<sup>3,4,7,12,14,106-111</sup> Due to its wide band gap and high excitation binding energy (60 meV), ZnO has potential for a wide range of applications. It also can form a wide range of nanostructures, including nanowires, nanorods, nanobelts, nanocombs and nanorings.<sup>19</sup> There is a strong interest in the development of ZnO nanowire device structures for potential applications in high density arrays of low power field-effect transistors (FETs), gas sensors, solar cells and UV detectors.<sup>2,28,112</sup> It is clear that nanowires and nanotubes are excellent candidates for this type of sensing, given their large surface-to-volume ratios and low weight.<sup>27,40</sup> The ability to detect hydrogen selectively at room temperature is important because it avoids the use of on-chip heaters that add to the power consumption and weight. The ability to control the nucleation site density for catalyst-driven growth of nanorods makes them candidates for micro-lasers or memory arrays. A key requirement for exploiting the potential of ZnO nanowires in these types of device applications is the control of both the density and size of the metal catalyst dots used for nucleation of the ZnO growth and demonstration of selective area growth of the nanowires.

The ZnO nanorods were synthesized by a catalyst-driven molecular beam epitaxy method. The nanorods were found only nucleate on catalyst surface followed by the VLS mechanism. In this Chapter, the density control of single crystal ZnO nanorods by varying both the annealing time and temperature is studied. It is straightforward to control the Ag cluster size in the range of 8–65 nm diameter and the cluster density from 30 to 2500 mm<sup>2</sup> using an initial Ag film

thicknesses of 25 Å and either SiO<sub>2</sub> or SiN<sub>x</sub> dielectrics on the initial Si wafer, followed by annealing at 600–800°C for 1–30 min.

In an effort to grow ZnO nanowires with longer lengths for device applications, *c*-sapphire substrates coated with gold were used. Similar procedures were performed to produce Au cluster size in the range of 50–650 nm in diameter. High density cross-linked ZnO nanowires were synthesized when Au catalysts were in the range of 50–150 nm in diameter. By selecting proper metal catalyst size and lattice matched substrate, high density ZnO nanowires were synthesized by catalyst-driven molecular beam epitaxy. A morphology evolution from nanorods to nanowires is observed when using Au on *c*-sapphire substrate. It provides alternative synthesis approach to fabricate high aspect-ratio ZnO nanowires for device applications.

## 4.2 Experimental Methods

Two different metal catalysts (silver and gold) and substrates (silicon and sapphire) were used in the study. The *p*-Si(100) substrates were coated with 100 nm of either SiO<sub>2</sub> or SiN<sub>x</sub> deposited by plasma-enhanced chemical vapor deposition and then coated with Ag films of 25 Å thickness using RF sputtering. The *c*-plane sapphire substrates were coated with Au films of 30 Å by RF sputtering. Annealing of the samples was carried out in the range of 600–800°C for 1–30 min under flowing N<sub>2</sub> gas. The annealing process causes clusters to form small islands, whose size and density were measured using scanning electron microscopy (SEM). These clusters act as nucleation sites for growth of the ZnO nanorods. The site-selective growth of ZnO nanorods was achieved by nucleating them on a patterned substrate coated with Ag. For nominal Ag thicknesses of 25 Å, discontinuous Ag clusters are realized after annealing. ZnO nanorods were synthesized by molecular beam epitaxy (MBE) with a base pressure of  $5 \times 10^{-8}$  mbar. An ozone/oxygen mixture generated by ozone generator was used as the oxidizing source. The cation flux was provided by Knudsen effusion cells using high purity Zn metal (Alfa Aesar,

99.9999%) as the source materials. The Zn pressure was varied between  $4 \times 10^{-6}$  and  $2 \times 10^{-7}$  mbar, while the pressure of the  $O_3/O_2$  mixture was  $5 \times 10^{-4}$  mbar. The growth temperature varies from 400 to 600°C and typical growth time was 2 h. After growth, the samples were characterized by X-ray diffraction (XRD), scanning electron microscopy (SEM), transmission electron microscopy (TEM) and photoluminescence (PL).

### 4.3 Results and Discussion

#### 4.3.1 Structural and optical properties of ZnO nanorods grown on Si

Figure 4-1 shows a typical top-view (a)–(c) and side-view (d) FE-SEM image of the as-grown nanostructures on silver coated silicon at 400°C. Different shapes of nanostructures including whisker, needles and rods were observed in high density. The diameter and length of the ZnO nanorods are approximately 20–60 nm and 1 μm. At higher temperatures (500°C), nanorods are observed slightly longer in length (2 μm) with lower density. Few nanorods were observed at growth temperature over 600°C. The growth temperature is found to have significant effect on the dimension and density of resulting nanostructures.

The XRD pattern of the ZnO nanorods grown at 400°C is shown in Figure 4-2. The peaks are indexed according to the hexagonal wurtzite structure of ZnO with lattice constants of  $a=3.249 \text{ \AA}$  and  $c=5.2038 \text{ \AA}$ . No impurity or secondary phase peaks were observed. Although the diffraction patterns show a randomly oriented polycrystalline material, a preferred (002) orientation is observed. A further structural characterization is performed by TEM. The low magnification TEM image of single ZnO nanorod is shown in Figure 4-3(a), which shows the diameter is approximately 20 nm. Metal tip at the top of nanorod confirms the VLS growth mechanism. Local energy-dispersive X-ray spectroscopy measurements indicate that the terminating particle is Ag. This is similar to what is observed for other nanorod synthesis that is driven by a catalytic reaction, where catalyst particles become suspended on the nanorod tip.

Evidence for termination of the ZnO nanorods tips with catalyst particles is also observed in field-emission SEM images. The high resolution TEM image of a single ZnO nanorod shows lattice fringes with [001] growth direction. The selected area electron diffraction (SAD) patterns taken from a single ZnO nanorod indicates that the as-grown nanorods are single crystal with a wurtzite structure.

The optical properties of the nanorods were examined using photoluminescence. A He–Cd (325 nm) laser was used as the excitation source. At 300 K there was strong near-band-edge emission at 375 nm as shown in Figure 4-3(d). This is consistent with luminescence reported for near-band-edge emission in epitaxial films and larger diameter ZnO nanorods.<sup>113,114</sup> A broad weak, green emission at ~520 nm was also present. This is typically associated with trap-state emission attributed to singly ionized oxygen vacancies in ZnO.<sup>115</sup>

#### **4.3.2 Growth mechanism**

By the evidence of metal segregation at tips, the growth of nanostructures can be explained by the vapor–liquid–solid (VLS) model as illustrated previously in Figure 2-4. The vapor–liquid–solid (VLS) model, as an effective route to synthesis semiconductor nanowires was proposed by Wagner and Ellis in 1964, has been widely used for the one-dimensional nanostructure synthesis.<sup>70</sup> The main features of VLS growth are that semiconductor nanowires have metal or alloy droplets on their tips and these droplets define diameters and direct the growth direction. The VLS growth can be divided into 4 steps: (1) mass transport of nanowire growth species in vapor phase, (2) chemical reaction on the liquid catalyst droplet surface, (3) diffusion in the liquid phase, and (4) crystallization at the liquid-solid interface. In this case, nanorod only nucleates on metal catalyst and site-selective growth can be realized. The size of metal catalyst determines the dimension of resulting structures.

ZnO nanoparticle formation via the internal oxidation of Zn in Ag/Zn alloys has previously been reported.<sup>116</sup> In these studies, oxygen is diffused into an Ag/Zn alloy, with nanoscale ZnO precipitates forming in the bulk of the sample. For the present case of nanorod formation, the reaction between ozone/oxygen flux and the Ag islands appears to result in surface and subsurface oxygen diffusion in the metal island, perhaps involving the intermediate formation of Ag<sub>2</sub>O. Zn atoms impinging on the Ag island surface then diffuse either on the surface or in the bulk of the island, where they react with the Ag<sub>2</sub>O to form ZnO. The solid solubility of Zn in Ag is on the order of 25 wt.% for the temperatures considered in these experiments. Zn addition to Ag significantly suppresses the melting point to 710°C at 25 wt.% Zn. The melting point of Zn is 420°C. Based on these arguments, one might anticipate rather high diffusion rates for Zn in Ag for the temperatures considered. It should also be noted that the addition of Ag during the growth of complex oxide thin film has been reported to be effective in enhancing the oxidation process for various oxide thin-film compounds.<sup>117</sup>

#### **4.3.3 Nucleation control and site-selective growth**

Figure 4-4 shows SEM micrographs of 25 Å Ag films on SiO<sub>2</sub>/Si after different annealing temperature and time: (a) 700°C for 5 min; (b) 700°C for 30 min; (c) 600°C for 5 min; and (d) 800°C for 5 min. The effect of the annealing is the creation of Ag clusters. The cluster size increases with anneal temperature from 8 nm at 600°C to 30 nm at 800°C while the cluster density decreases rapidly (by about a factor of 25) in this range. Similar data is shown in Figure 4-5 for the Ag films on SiN<sub>x</sub>/Si substrates. The same general trends are seen as with the SiO<sub>2</sub>/Si. The variation of both cluster diameter and density are shown in Figure 4-6 and 4-7 for the SiO<sub>2</sub>/Si and SiN<sub>x</sub>/Si templates, respectively. Note that we can control the cluster density in the range of 100–2500 mm<sup>2</sup> for SiO<sub>2</sub>/Si and 30–1900 mm<sup>2</sup> for SiN<sub>x</sub>/Si using an initial Ag film thicknesses of 25 Å and annealing temperatures of 600–800°C. The corresponding range of

cluster diameters is 8–30 nm on SiO<sub>2</sub> and 10–65 nm on SiN<sub>x</sub>. At 700°C, the annealing time has a much stronger effect on cluster density than size in both cases, while the growth of the clusters and associated decrease in density is much more significant at the higher temperatures, as expected. Preliminary atomic force microscopy results show that the height of the clusters also increases as the diameter increases.

To examine the selective area growth of ZnO nanorods on regions, we patterned parallel lines by lift-off of e-beam deposited 25 Å thick films with width 20 nm and separation of 450 nm were patterned. The samples were annealed at 800°C for 1 min to create the Ag clusters and then ZnO nanorods were grown, as described previously. FE-SEM micrographs taken at different magnifications of the selectively grown wires are shown in Figure 4-8. The ability to control both the wire density and location is useful in applications where, for example, the wires need to be grown on an electrode for sensing or UV photodetection.

#### **4.3.4 Structural and optical properties of ZnO nanowires grown on sapphire**

From the previous experimental results, it's clear that nanowires grown on silicon substrate tend to be short and tapered. Generally, 1-D nanomaterials with high aspect ratios are highly desired for device applications. The low aspect ratio structures limited their applications in device application. Therefore, efforts have been made on synthesis longer and relatively untapered nanowires. Long nanowires provide higher surface-to-volume ratios and are beneficial to device applications.

The choice of the substrate material is another concern in synthesis of 1-D materials. Silicon has a lot of advantages such as low cost and easy process integrations; however the large lattice mismatch makes it difficult to control the growth. Epitaxial ZnO films have been realized on various substrate orientations of sapphire (Al<sub>2</sub>O<sub>3</sub>) substrates, the small lattice mismatch makes them suitable substrates for II-VI semiconductor growth.<sup>29</sup> For a wide range of growth conditions,

*c*-axis oriented epitaxial ZnO films have been realized on *c*-plane sapphire. In the concern of lattice mismatch, the *c*-sapphire substrates coated with gold were used for nanowire growth substrates. Similar procedures were performed to produce Au cluster size in the range of 50–650 nm in diameter. As shown in Figure 4-9, no 1-D growth observed when the Au clusters are larger than 200 nm. The size of gold clusters slightly increased and surface became rough after growth, which suggests some surface reaction occurred. When the sizes of Au catalysts are smaller than 150 nm, high density ZnO nanowires were synthesized as shown in Figure 4-10. Therefore, the dimensions of Au catalysts have significant effect on nanowire growth. By selecting proper metal catalyst size and lattice matched substrates, high density ZnO nanowires were synthesized by catalyst-driven molecular beam epitaxy. A morphology evolution from nanorods to nanowires is observed when using Au catalyst on *c*-sapphire substrate. It provides alternative synthesis approach to produce high aspect-ratio ZnO nanowires for device applications.

Figure 4-11 shows top-view and side-view FE-SEM image of the ZnO nanowires grew on *c*-plane sapphire at 500 and 600°C. In contrast of pervious case (silicon), the nanowires grown on sapphire have higher aspect ratios and uniform diameters. The nanowires nucleate on Au particles on the surface and highly cross-linked together with *c*-axis orientation. The diameters of the ZnO nanowire are approximately 20–60 nm and length up to 8μm. At higher temperatures (600°C), nanorods are observed with slightly longer length (10μm) with smaller diameters. As a result, high growth temperature provides sufficient activation energy of crystallization results in longer nanowires growth.

The XRD pattern of the nanowires grown on sapphire at 500°C is shown in Figure 4-12. Only a strong (002) and weak (101) peaks are observed, which suggest a more uniform growth direction and high density of nanowires. Figure 4-13 shows the room temperature

photoluminescence spectra of ZnO nanowires grown at 500°C on sapphire. Compared with nanorods grown on Ag/Si, a much stronger near band edge emission at ~380 nm with relative small deep level emission, which suggest they are highly crystalline with relative low defects. ZnO nanowires grew on Au/sapphire appears to have better quality and optical property than those on Ag/Si. These high quality ZnO nanowires appear to be candidates for nano-electronics, nano-sensor applications.

#### 4.4 Summary and Conclusions

In summary, the synthesis and nucleation control of ZnO nanowires via VLS growth mechanism is studied. The control of initial Ag film thickness and subsequent annealing conditions is shown to provide an effective method for controlling the size and density of nucleation sites for catalyst-driven growth of ZnO nanorods. By using Ag film thickness of 25 Å on SiO<sub>2</sub> or SiN<sub>x</sub> layers on Si substrates, we have shown that annealing between 600 and 800°C creates Ag cluster size in the range of 8–30 nm diameter for SiO<sub>2</sub> and 10–65 nm for SiN<sub>x</sub> with a cluster density from 100 to 2500 mm<sup>2</sup> for SiO<sub>2</sub> and 30 to 1900 mm<sup>2</sup> for SiN<sub>x</sub>. Conventional optical lithography to create parallel Ag stripes shows that completely selective growth is possible on either dielectric. High density cross-linked ZnO nanowires were synthesized when Au catalysts were in the range of 50–150 nm in diameter. By selecting proper metal catalyst size and lattice matched substrate, high density ZnO nanowires were synthesized by catalyst-driven molecular beam epitaxy. A morphology evolution from nanorods to nanowires is observed when using Au on *c*-sapphire substrate. It provides alternative synthesis approach to produce high aspect-ratio ZnO nanowires for nano-device applications. Those nanowires will be applied for gas sensing applications and described in the next Chapter.

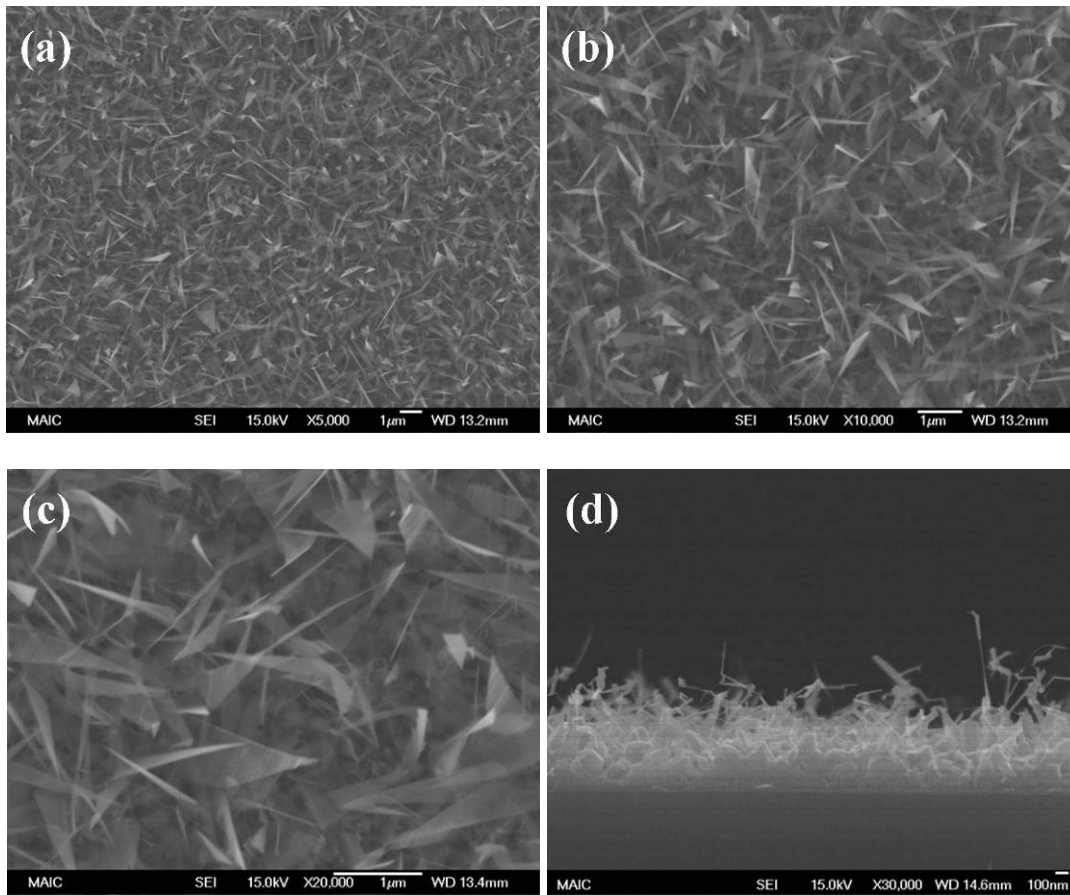


Figure 4-1. (a)–(b) Top view (d) side view FE-SEM images of ZnO nanorods on a Ag coated silicon grew at 400°C.

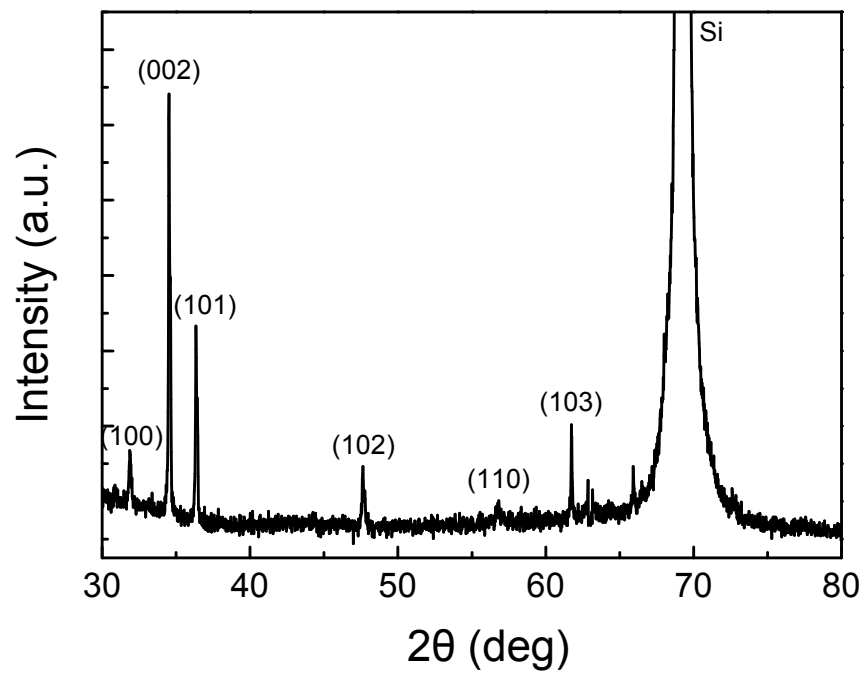


Figure 4-2. X-ray diffraction pattern of ZnO nanorods grown on a 20Å Ag coated SiO<sub>2</sub>/Si substrate at 400°C.

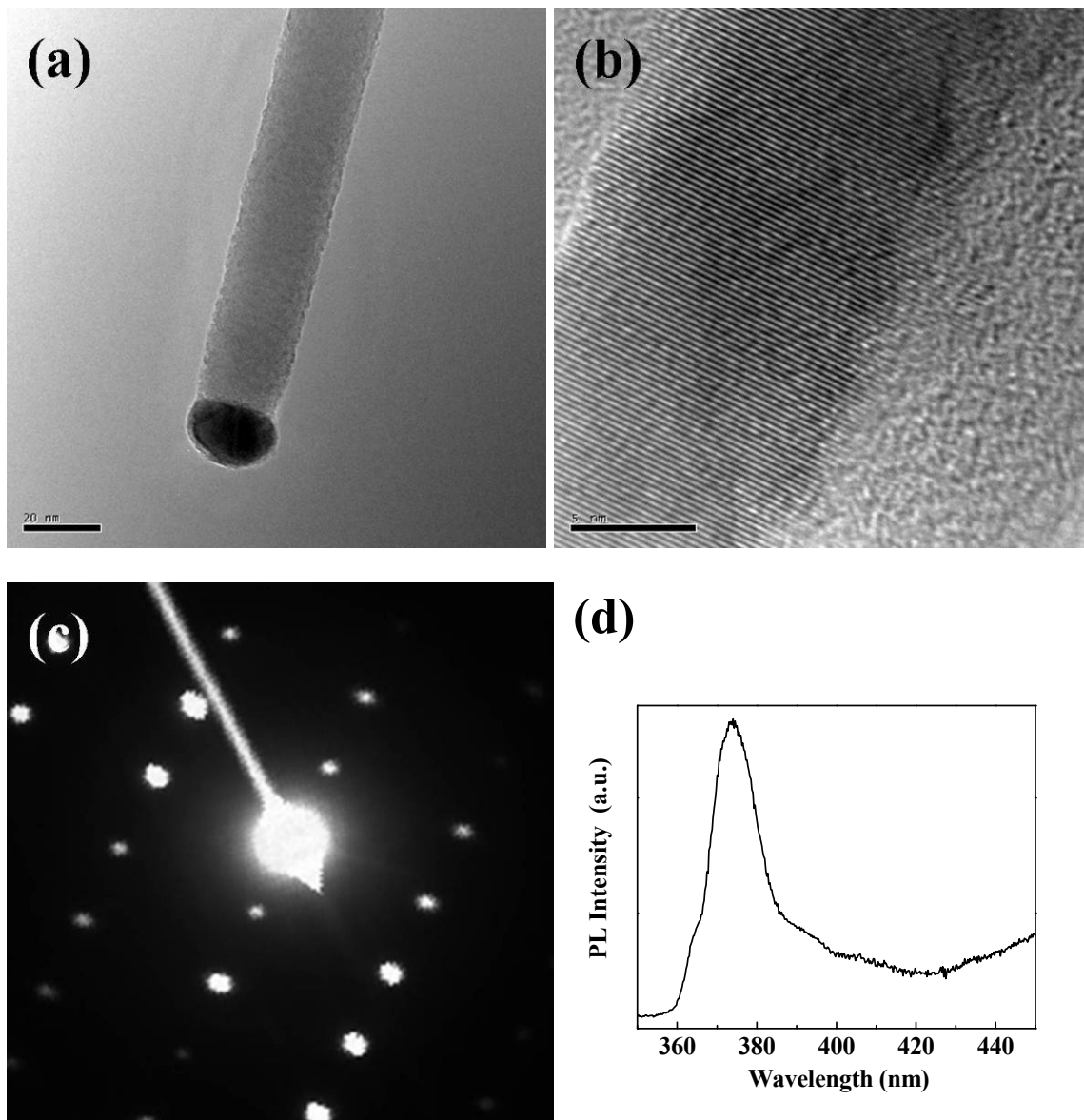


Figure 4-3. (a) Low magnification TEM image of single ZnO nanorod. (b) High resolution TEM image of a single ZnO nanorod with lattice fringes. (c) Select area diffraction patterns taken from a single ZnO nanorod showing the single crystal wurtzite structure. (d) Room temperature PL spectra of as-grown ZnO nanorods.

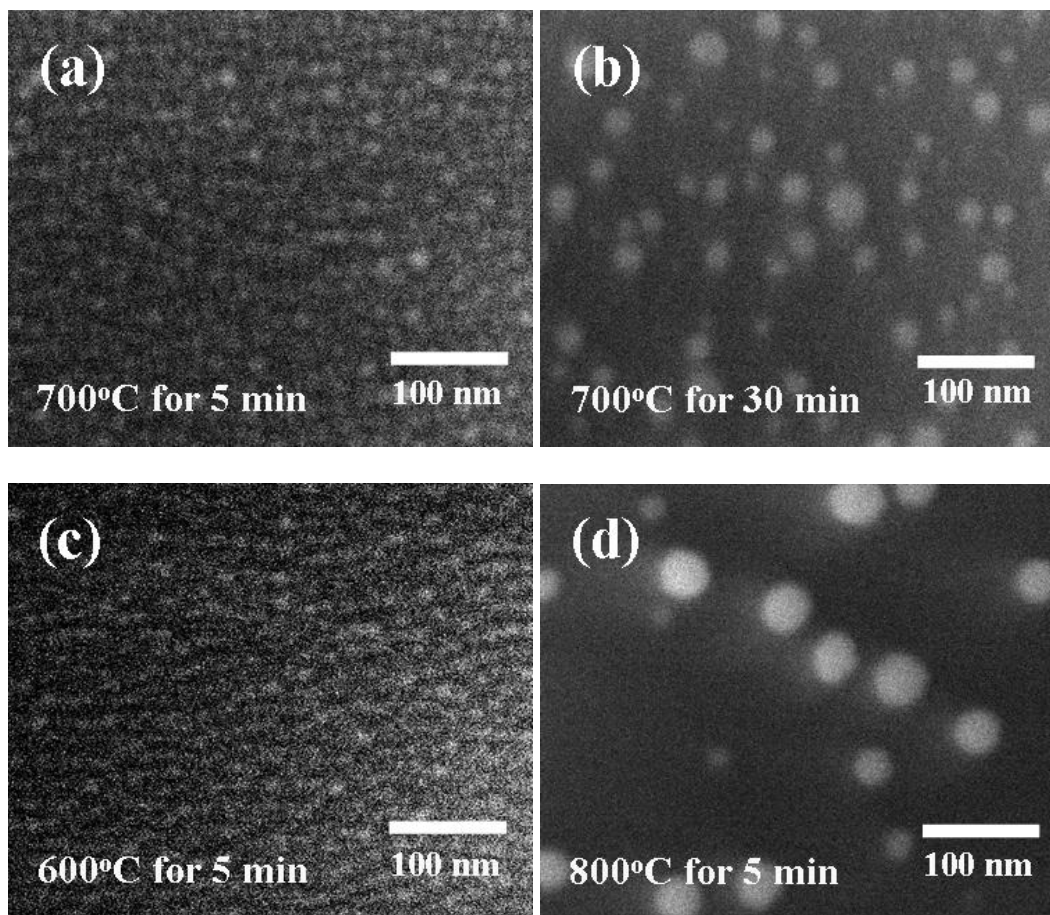


Figure 4-4. 25Å Ag on SiO<sub>2</sub>/Si with different annealing temperature and time: (a) 700°C for 5 minutes (b) 700°C for 30 minutes (c) 600°C for 5 minutes and (d) 800°C for 5 minutes.

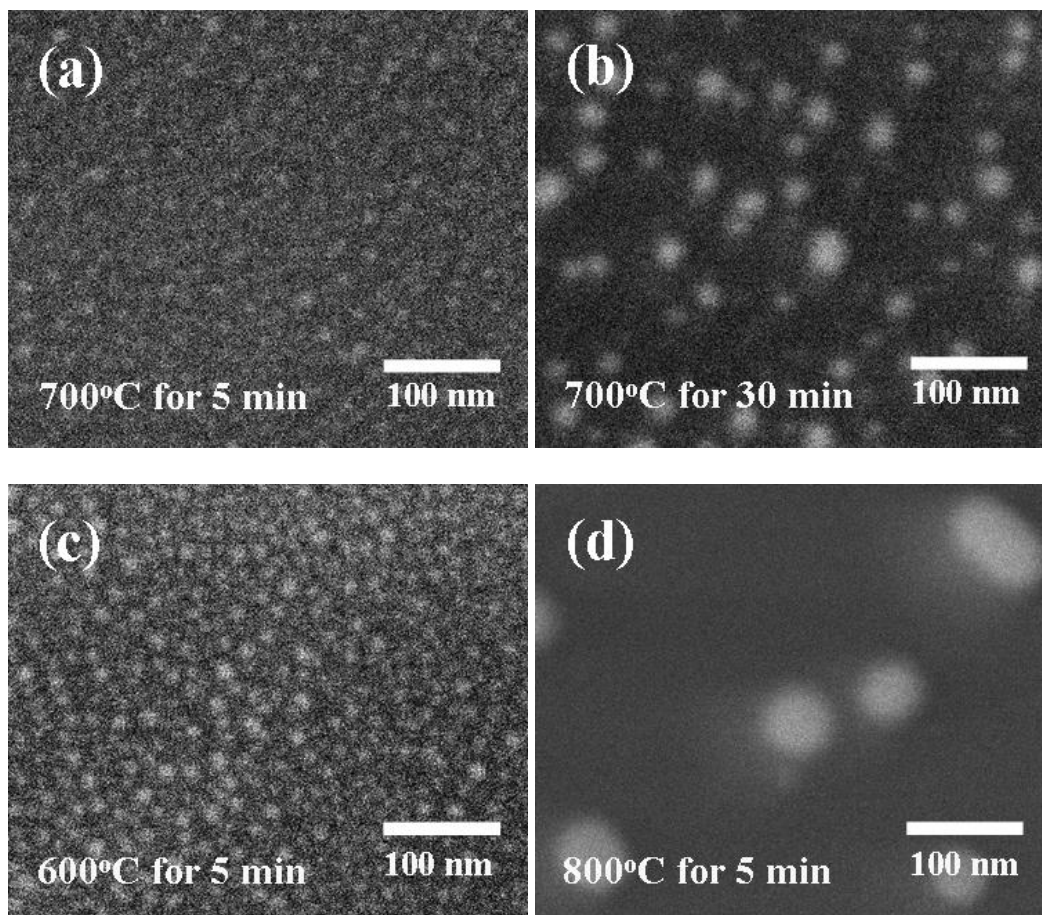


Figure 4-5. 25Å Ag on Si<sub>3</sub>N<sub>4</sub>/Si with different annealing temperature and time: (a) 700°C for 5 minutes (b) 700°C for 30 minutes (c) 600°C for 5 minutes and (d) 800°C for 5 minutes.

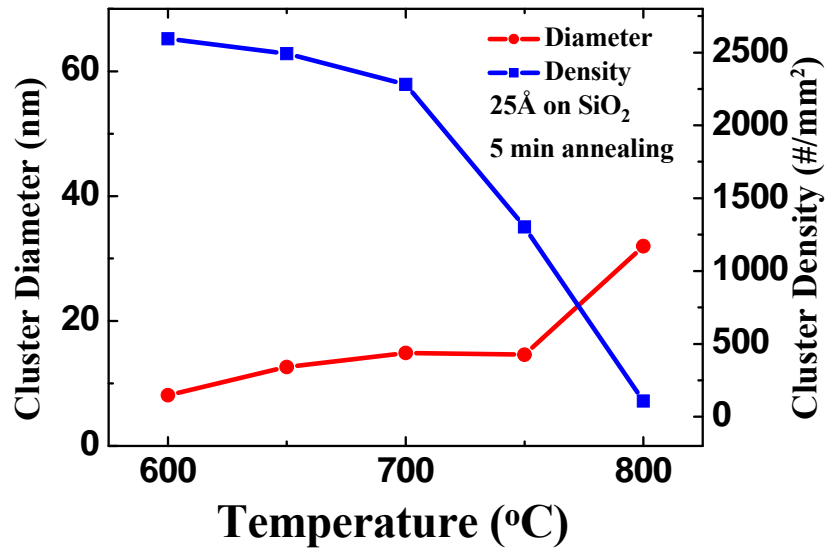
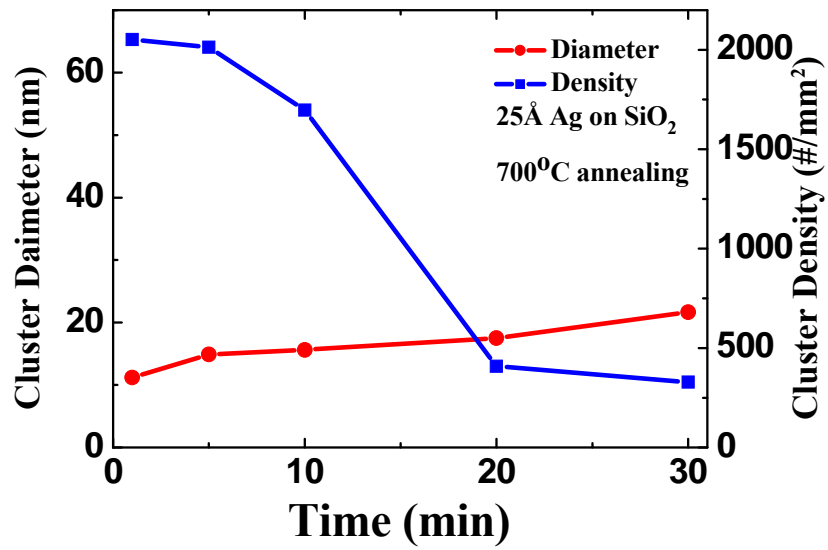


Figure 4-6. The top plot shows the density and average size of the resulting Ag clusters on SiO<sub>2</sub> as a function of anneal time at 700°C. The bottom plot shows density and average size of the resulting Ag clusters on SiO<sub>2</sub> as a function of anneal temperature for 5 min anneals.

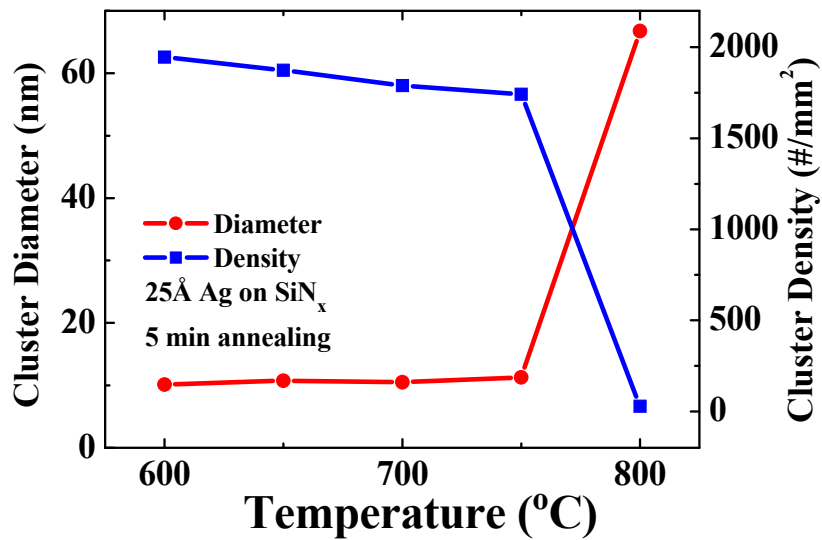
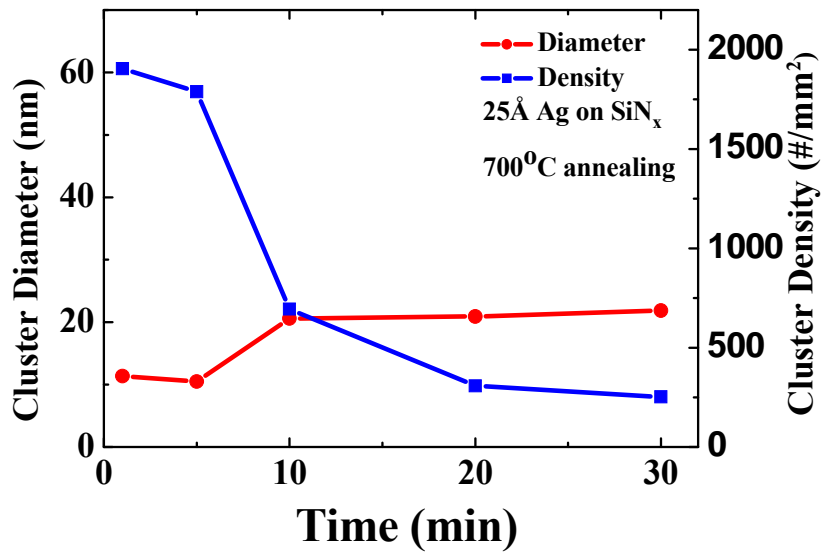


Figure 4-7. The top plot shows the density and average size of the resulting Ag clusters on Si<sub>3</sub>N<sub>4</sub> as a function of anneal time at 700°C. The bottom plot shows density and average size of the resulting Ag clusters on Si<sub>3</sub>N<sub>4</sub> as a function of anneal temperature for 5 min anneals.

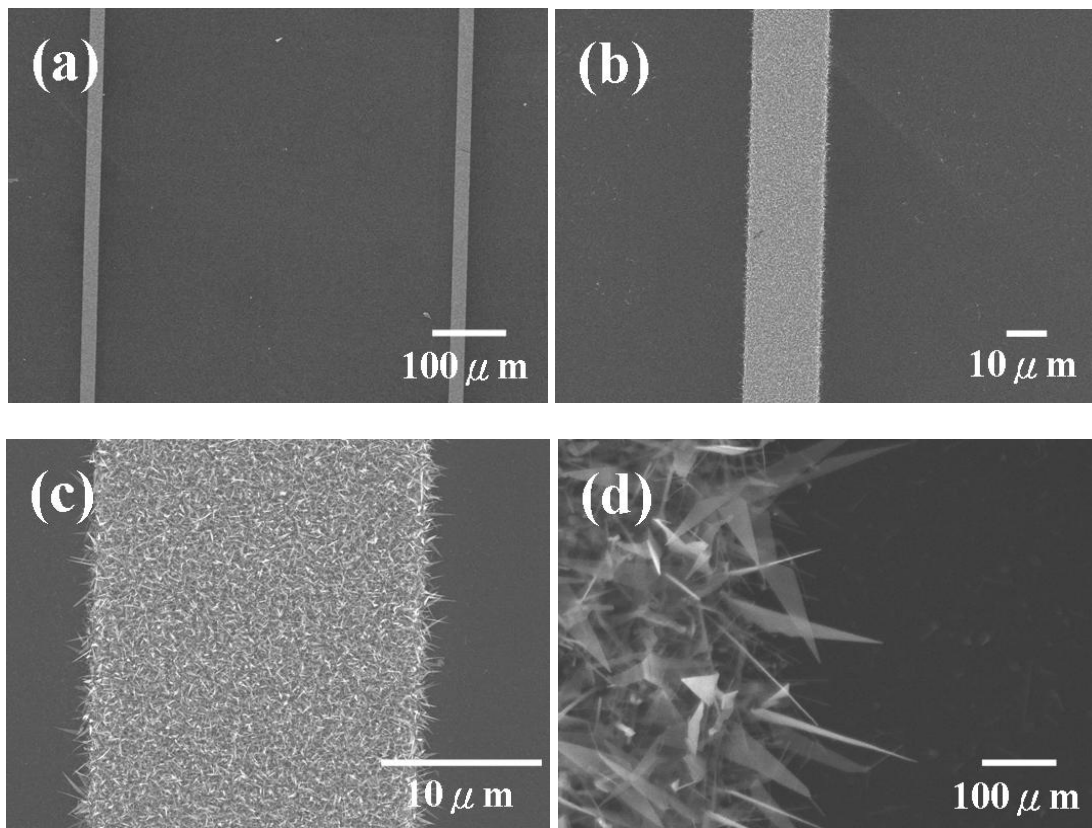


Figure 4-8. Scanning electron microscope images of selectively grown ZnO nanorods on 25 Å Ag/SiO<sub>2</sub>.

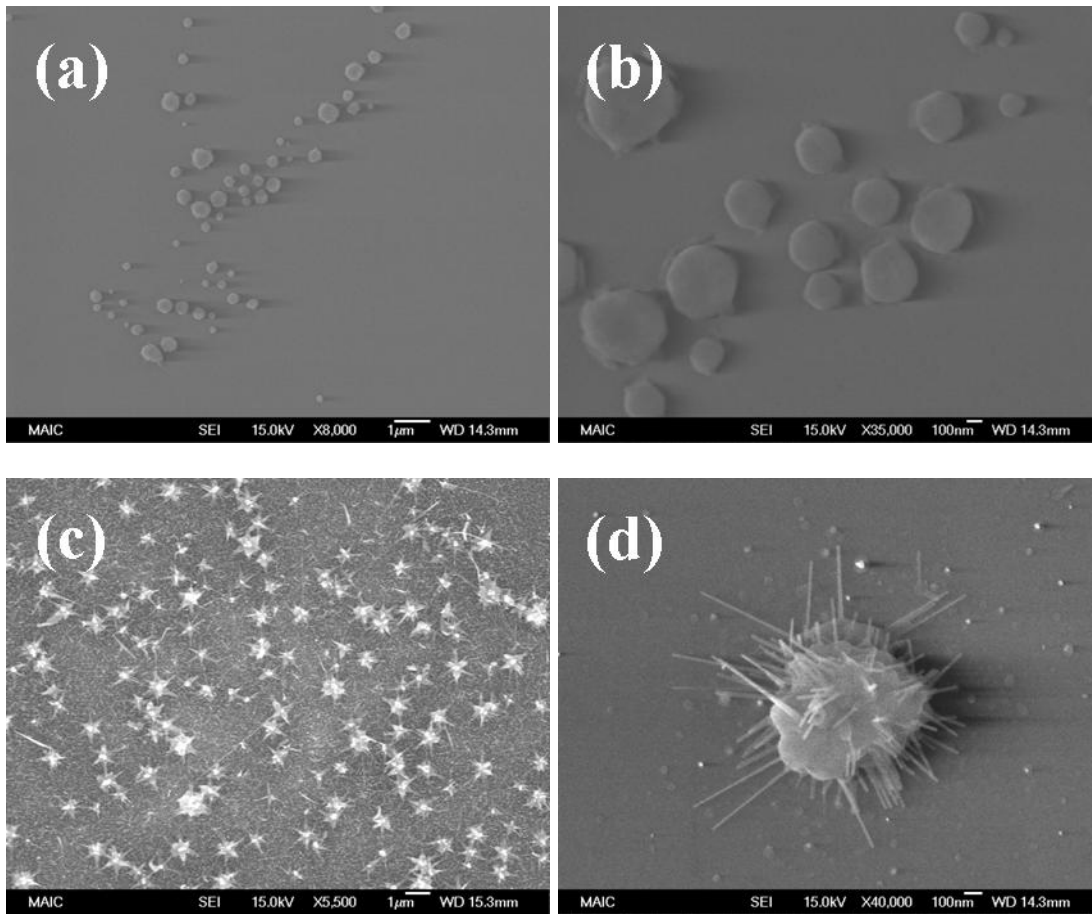


Figure 4-9. (a), (b) Scanning electron microscope images of 200–650 nm of Au clusters on sapphire. (c), (d) resulting ZnO nanowires.

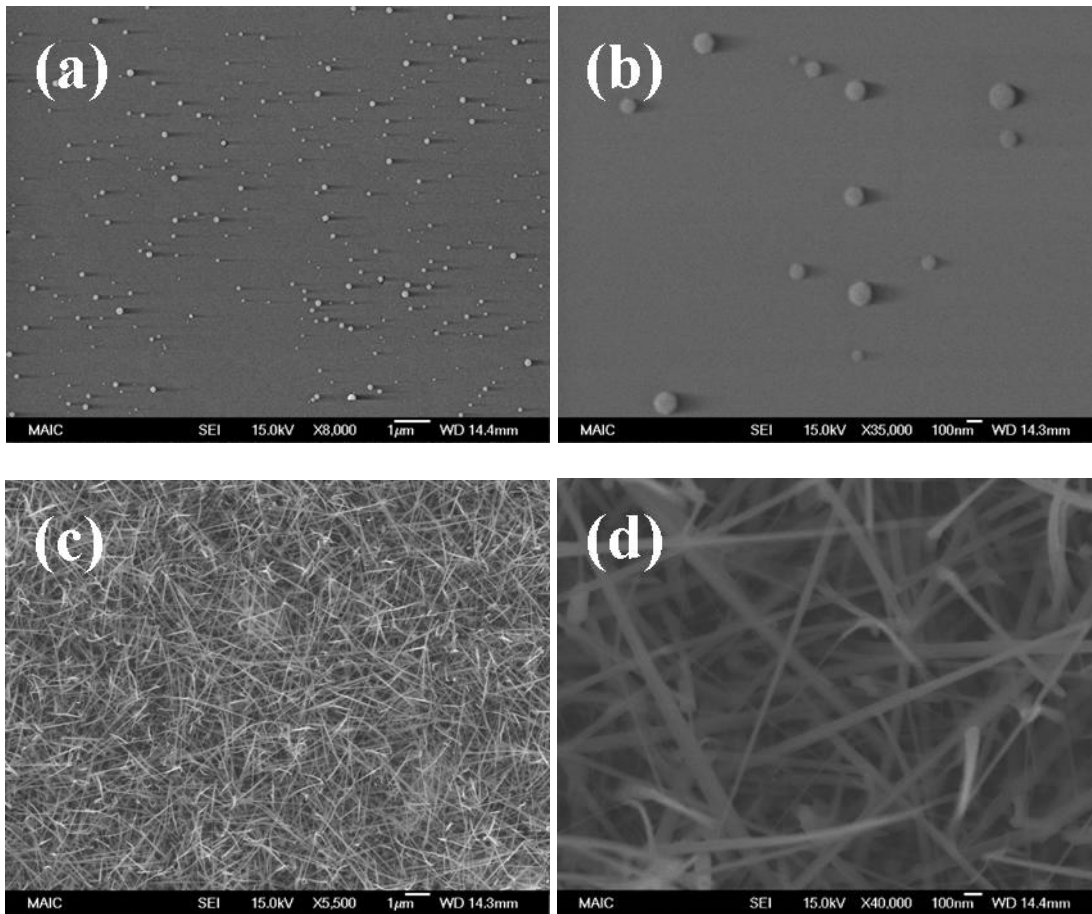


Figure 4-10. (a), (b) Scanning electron microscope images of 50–150 nm of Au clusters on sapphire. (c), (d) resulting ZnO nanowires.

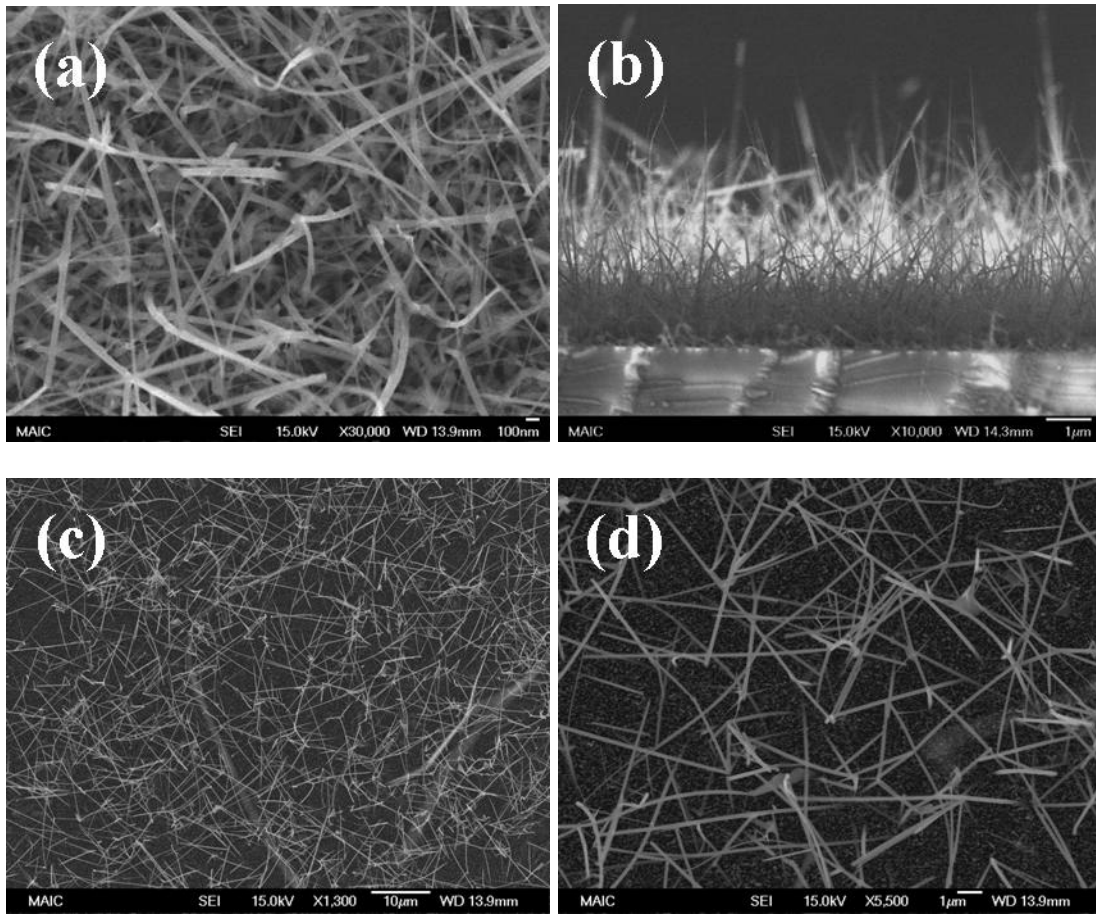


Figure 4-11. (a), (b) Top view and side view scanning electron microscope images of ZnO nanowires on an Au coated *c*-sapphire grew at 500°C (c), (d) SEM images of ZnO nanowires on an Au coated *c*-sapphire grew at at 600°C.

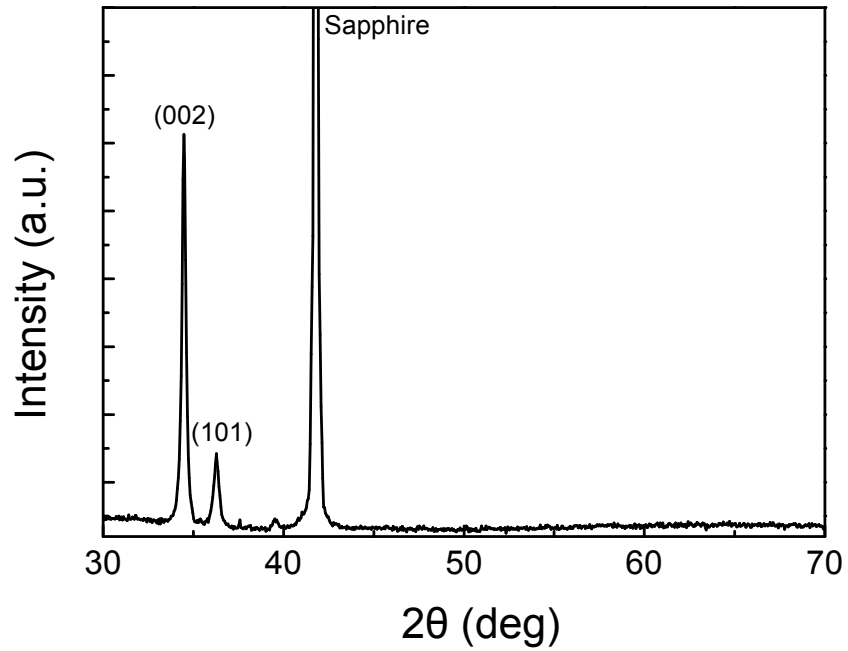


Figure 4-12. X-ray diffraction pattern of ZnO nanowires grown on a sapphire substrate at 600°C.

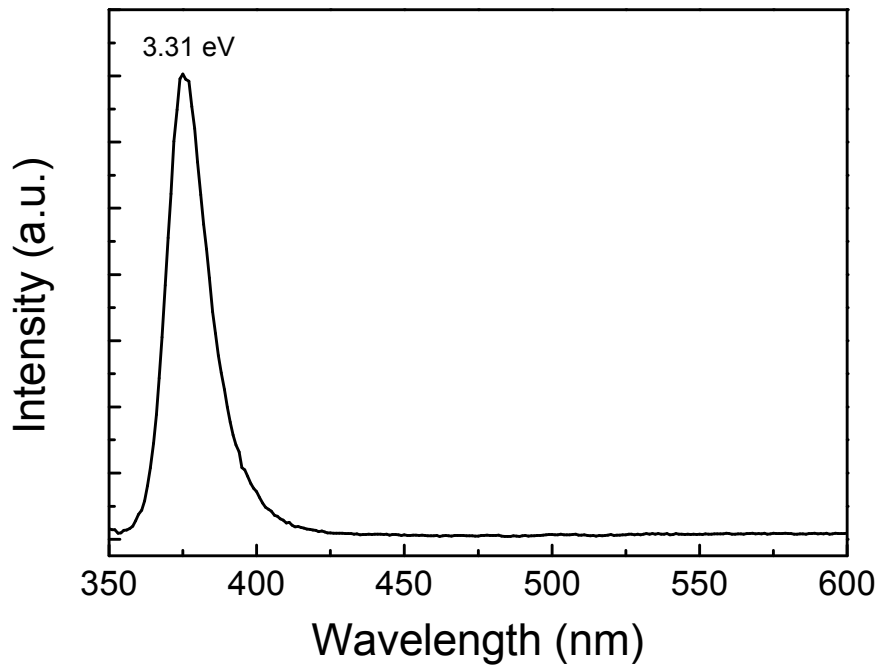


Figure 4-13. Room temperature photoluminescence spectra of ZnO nanowires grown on sapphire at 600°C.

## CHAPTER 5 ZNO NANOWIRES FOR HYDROGEN SENSING APPLICATIONS

### 5.1 Introduction

Solid-state gas sensors play an important role in environmental monitoring, chemical process controlling and personal safety. Semiconductor metal oxide sensors have been widely used due to their low cost and high compatibility with microelectronic processing.<sup>21,100</sup> In the case of the polycrystalline thin film devices, only a small fraction of the species adsorbed near grain boundaries is active in modifying transport properties.<sup>103,118</sup> The low surface-to-volume ratios also result the limitations in their applications, some drawbacks such as low sensitivity and slow response.

Recently, there is strong interest in developing hydrogen sensors for use with proton-exchange membrane and solid oxide fuel cells for space craft and other long-term applications. A key requirement for these sensors is the ability to selectively detect hydrogen at room temperature with minimal power use and weight. It is clear that nanowires and nanotubes are excellent candidates for this type of sensing, given their large surface-to-volume ratios and low weight. The ability to detect hydrogen selectively at room temperature is important because it avoids the use of on-chip heaters that add to the power consumption and weight. In the case of hydrogen sensing with carbon nanotubes (CNTs), several groups have reported that use of Pd doping or films or loading with Pd nanoparticles can functionalize the surface of nanotubes for catalytic dissociation of H<sub>2</sub> to atomic hydrogen.<sup>119-125</sup> Of course, thin-film sensors of Si, GaAs, InP, SiC, and GaN with Pd contacts have been used previously as hydrogen sensors.<sup>124</sup>

ZnO nanowires are attractive for a wide variety of sensing applications because of the ease of synthesis, ability to readily transfer them to cheap substrates and their bio-safe characteristics. ZnO nanowires and nanowires have shown potential for use in gas, humidity, and chemical

sensing. The ability to make arrays of nanowires with large total surface area has been demonstrated with a number of different growth methods and a large variety of ZnO one-dimensional structures has been demonstrated. To date, most of the work on ZnO nanostructures has focused on the synthesis methods. The large surface area of the nanowires and biosafe characteristics of ZnO makes them attractive for both chemical sensing and biomedical applications. There are still many aspects of this approach that require work, including quantifying the sensitivity, detection limits at room temperature, power consumption of the sensors, and time response upon switching away from the H<sub>2</sub>-containing ambient.

Tin oxide (SnO<sub>2</sub>) *n*-type semiconductor sensors are widely used for detection of reducing gases and carbon monoxide.<sup>37,39,126</sup> In general, these sensors have suffered from relatively low selectivity for different gases and long-term instabilities in their response. New directions towards solving these problems include use of nanocrystalline thin films or use of catalysts to increase dissociation of gases at lower temperatures. The sensitivity of SnO<sub>2</sub> sensors can be enhanced by reducing the nanocrystallite size below 10 nm.<sup>127</sup> SnO<sub>2</sub> operates at lower temperatures (300°C) and is sensitive to a wider range of gases in comparison with many other thin film sensor candidates.<sup>128,129</sup> This makes it possible to change its sensitivity to a specific compound or group of compounds by the addition of the appropriate substances. For example, previous work has shown that the sensitivity and selectivity of SnO<sub>2</sub> to ethanol can be improved by adding La<sub>2</sub>O<sub>3</sub>, Y, Pd or Pt<sup>128-130</sup> and to CO can be improved by adding MoO<sub>3</sub>.<sup>131</sup> SnO<sub>2</sub> or multilayers of SnO<sub>2</sub>, ZnO, TiO<sub>2</sub> and WO<sub>3</sub> with the addition of Pd coatings have been reported for the detection of the mixtures of methanol and acetone.<sup>132-136</sup> There has also been recent interest in the use of ZnO nanowires for sensing. ZnO has been effectively used as a gas sensor material

based on the near-surface modification of charge distribution with certain surface-absorbed species.<sup>137</sup>

In this Chapter, applications of ZnO nanowires as material for hydrogen sensors will be addressed. The addition of sputter-deposited metal clusters to the surface of ZnO nanowires produces a significant increase in detection sensitivity for hydrogen at room temperature. The sensors are shown to detect ppm hydrogen at room temperature using <0.4 mW of power when using multiple nanowires. When using a single ZnO nanowire sensor, the power consumption can further pushing down to  $\mu$ W range. Furthermore, a comparison study of the hydrogen-sensing characteristics of ZnO thin films with different thickness and ZnO nanowires will be described. Both types of sensors are shown to be capable of the detection of ppm hydrogen at room temperature with nW power levels, but the nanowires show different recovery characteristics, consistent with the expected higher surface coverage of adsorbed hydrogen. The use of single-crystal ZnO nanowires provide a convenient template for coating with SnO<sub>2</sub> and the resulting structure can be used to detect hydrogen at 400°C.

## **5.2 Experimental Methods**

### **5.2.1 Synthesis and fabrication of ZnO nanowires sensors**

The site-selective growth of ZnO nanowires was achieved by nucleating the nanowires on a substrate coated with Au islands as has been described in Chapter 3. In general, ZnO nanowires were synthesized by molecular beam epitaxy with a base pressure of  $5 \times 10^{-8}$  mbar using high purity Zn metal (Alfa Aesar, 99.9999%) and an O<sub>3</sub>/O<sub>2</sub> plasma discharge as the source chemicals. The Zn pressure was varied between  $4 \times 10^{-6}$  and  $2 \times 10^{-7}$  mbar, while the beam pressure of the O<sub>3</sub>/O<sub>2</sub> mixture was varied between  $5 \times 10^{-6}$  and  $5 \times 10^{-4}$  mbar. The growth time was  $\sim 2$  h at 500°C. The typical length of the as-grown nanowire was 2–10  $\mu$ m, with typical diameters in the range of 30–150 nm.

A shadow mask was used to pattern sputtered Al/Ti/Au electrodes on the ZnO nanowire/Al<sub>2</sub>O<sub>3</sub> substrates. The separation of the electrodes was 30 μm. In some cases, the nanowires were coated with metal catalyst thin films (~100 Å thick) deposited by sputtering. This forms clusters of metal with ~70% coverage of the nanowire surface and rms roughness of ~80 Å. Figure 5-1 illustrates the metal catalysts decorated ZnO nanowire. Au wires were bonded to the contact pad for current-voltage (I-V) measurements performed at 25°C in a range of different ambients (N<sub>2</sub>, O<sub>2</sub> or 10–500 ppm H<sub>2</sub> in N<sub>2</sub>). Note that no currents were measured through the discontinuous Au islands and no thin film of ZnO was observed with the growth condition for the nanowires. The I-V characteristics from the multiple nanowires were linear with typical currents of 0.8 mA at an applied bias of 0.5 V.

### 5.2.2 Synthesis and fabrication of ZnO thin films sensors

The ZnO thin films were grown by Pulsed Laser Deposition on *c*-plane sapphire substrates at 450°C, as described previously. The thickness of thin film was varied from 20–350 nm. A 3% O<sub>3</sub>/O<sub>2</sub> mixture was used as background gas resulting lower carrier density (~10<sup>17</sup> cm<sup>-3</sup>). The films were nominally undoped with low *n*-type 10<sup>17</sup> cm<sup>-3</sup> carrier concentration. The Ohmic contacts of sputtered Al/Ti/Au were patterned by a shadow mask. In some cases, the sensors were coated with Pt thin films 10 Å thick deposited by sputtering. Au wires were bonded to the contact pad for current-voltage I-V measurements performed at 25°C in air, N<sub>2</sub> or 500 ppm H<sub>2</sub> in N<sub>2</sub>. No currents were measured through the discontinuous Au islands.

### 5.2.3 Synthesis and fabrication of single ZnO nanowire sensors

The nanowires were removed from the original substrate by sonication and transferred to a Si substrate. The e-beam lithography was used to pattern sputtered Al/Ti/Au electrodes contacting both ends of single nanowires on the Si substrates. The separation of the electrodes was 10 μm. In some cases, the nanowires were coated with discontinuous Pt cluster (10–20 Å

thick) deposited by sputtering as shown in Figure 5-1. Au wires were bonded to the contact pad for current-voltage (I-V) measurements performed at 25°C in a range of different ambient (vacuum, N<sub>2</sub>, O<sub>2</sub> or 100–500 ppm H<sub>2</sub> in N<sub>2</sub>). The I-V characteristics from the uncoated single nanowires were linear with typical currents in the nA at an applied bias of 0.5 V.

#### **5.2.4 Synthesis and fabrication of SnO<sub>2</sub>-ZnO nanowire sensors**

The SnO<sub>2</sub> layers were deposited on as-grown ZnO nanowires by PLD at 600°C, a partial pressure of O<sub>2</sub> of 50 mTorr and 130 mJ of laser power with 1 Hz repetition rate, with two different deposition times of 5 or 10 min. The pattern sputtered Al/Ti/Au electrodes contacting both ends of multiple nanowires on the Al<sub>2</sub>O<sub>3</sub> substrates using a shadow mask. The separation of the electrodes was 3 μm. Au wires were bonded to the contact pad for current–voltage (I-V) measurements performed over the range 25–400°C in a range of different ambients (N<sub>2</sub>, vacuum or 500 ppm H<sub>2</sub> in N<sub>2</sub>).

### **5.3 Results and Discussion**

#### **5.3.1 Catalyst functionalized ZnO nanowires**

Previous results show that ZnO nanowires are not very sensitive to hydrogen at room temperature.<sup>138</sup> In order to enhance sensitivity at room temperature and realize gas sensing applications, efforts have been working on surface fictionalizations. One method for increasing hydrogen detection sensitivity is to use a catalytic metal coating or to actually dope the sensor material with the transition metal. This leads to catalytic dissociation of H<sub>2</sub> to atomic hydrogen, which produces a sensor response through binding to surface atoms and altering the surface potential.

A comparison study of different metal coating layers on multiple ZnO nanowires for enhancing the sensitivity to detection of hydrogen at room temperature has been done. Figure 5-2 shows the time dependence of relative resistance change of either metal-coated or uncoated

multiple ZnO nanowires as the gas ambient is switched from N<sub>2</sub> to 500 ppm of H<sub>2</sub> in air and then back to N<sub>2</sub> as time proceeds. These were measured at a bias voltage of 0.5V. The first point of note is that there is a strong increase (by approximately a factor of five) in the response of the Pt-coated nanowires to hydrogen relative to the uncoated devices. The maximum response was approximately 8%. There is also a strong enhancement in response with Pd coatings, but the other metals produce little or no change. This is consistent with the known catalytic properties of these metals for hydrogen dissociation. Pd has a higher permeability than Pt but the solubility of H<sub>2</sub> is larger in the former.<sup>139,140</sup> Moreover, studies of the bonding of H to Ni, Pd and Pt surfaces have shown that the adsorption energy is lowest on Pt.<sup>141</sup> There was no response of either type of nanowire to the presence of O<sub>2</sub> in the ambient at room temperature.

Once the hydrogen is removed from the ambient, the recovery of the initial resistance is rapid (< 20 s). By sharp contrast, upon introduction of the hydrogen, the effective nanowire resistance continues to change for periods of >15 min. This suggests that the kinetics of the chemisorption of molecular hydrogen onto the metal and its dissociation to atomic hydrogen are the rate-limiting steps in the resulting change in conductance of ZnO.<sup>142</sup> An activation energy of 12 kJ/mole was calculated from a plot of the rate of change of nanowire resistance. This energy is somewhat larger than that of a typical diffusion process and suggests that the rate-limiting-step mechanism for this sensing process is more likely to be the chemisorption of hydrogen on the Pd surface. This reversible change in conductance of metal oxides upon chemisorption of reactive gases has been discussed previously.<sup>142</sup> The gas-sensing mechanisms suggested in the past include the desorption of adsorbed surface hydrogen and grain boundaries in poly-ZnO<sup>143</sup>, exchange of charges between adsorbed gas species and the ZnO surface leading to changes in depletion depth<sup>144</sup> and changes in surface or grain-boundary conduction by gas

adsorption/desorption.<sup>145</sup> We should also point out that the I-V characteristics were the same when measured in vacuum as in air, indicating that the sensors are not sensitive to humidity.

The power requirements for the sensors were very low. The I-V characteristics measured at 25 °C in both a pure N<sub>2</sub> ambient and after 15 min in a 500 ppm H<sub>2</sub> in N<sub>2</sub> ambient. Under these conditions, the resistance response is 8% and is achieved for a power requirement of only 0.4 mW. This compares well with competing nanotechnologies for hydrogen detection such as Pd-loaded carbon nanotubes. Moreover, the 8% response compares very well to the existing SiC-based sensors, which operate at temperatures > 100 °C through an on-chip heater in order to enhance the hydrogen dissociation efficiency.<sup>124</sup> Figure 5-3 and 5-4 shows the response of Pt and Pd coated nanowire sensor to 10–500 ppm H<sub>2</sub> in N<sub>2</sub>. The Pt-coated sensors can detect 100 ppm H<sub>2</sub> while Pd-coated sensors can detect down to 10 ppm H<sub>2</sub>.

In conclusion, Pt is found to be the most effective catalyst, followed by Pd. The resulting sensors are shown to be capable of detecting hydrogen in the range of ppm at room temperature using very small current and voltage requirements and recover quickly after the source of hydrogen is removed.

### **5.3.2 Room temperature hydrogen selective sensing with ZnO nanowires**

A more detail study of hydrogen sensing with catalyst functionalized ZnO nanowires will be discussed in this section. Figure 5-5 shows the time dependence of resistance of either Pd-coated or uncoated multiple ZnO nanowires as the gas ambient is switched from N<sub>2</sub> to various concentrations of H<sub>2</sub> in air (10–500 ppm) as time proceeds. There are several aspects of the data. First, there is a strong increase (approximately a factor of 5) in the response of the Pd-coated nanowires to hydrogen relative to the uncoated devices. The addition of the Pd appears to be effective in catalytic dissociation of the H<sub>2</sub> to atomic hydrogen. Second, there was no response of either type of nanowire to the presence of O<sub>2</sub> in the ambient at room temperature. Third, the

effective conductivity of the Pd-coated nanowires is higher due to the presence of the metal. Fourth, the recovery of the initial resistance is rapid (20 s) upon removal of the hydrogen from the ambient, while the nanowire resistance is still changing at least 15 min after the introduction of the hydrogen. The reversible chemisorption of reactive gases at the surface of metal oxides such as ZnO can produce a large and reversible variation in the conductance of the material.<sup>143</sup> Fifth, the relative response of Pt-coated nanowires is a function of H<sub>2</sub> concentration in N<sub>2</sub>.

The Pd-coated nanowires detected hydrogen down to 10 ppm with relative responses of 2.6% at 10 ppm and 4.2% at 500 ppm H<sub>2</sub> in N<sub>2</sub> after a 10 min exposure, as shown in Figure 5-6. By comparison, the uncoated devices showed relative resistance changes of 0.25% for 500 ppm H<sub>2</sub> in N<sub>2</sub> after a 10 min exposure, and the results were not consistent for lower concentrations. The gas-sensing mechanisms suggested in the past include the desorption of adsorbed surface hydrogen and grain boundaries in poly-ZnO<sup>144</sup>, exchange of charges between adsorbed gas species and the ZnO surface leading to changes in depletion depth<sup>146</sup> and changes in surface or grain boundary conduction by gas adsorption/desorption.<sup>145</sup> The detection mechanism is still not firmly established in these devices and needs further study. It should be remembered that hydrogen introduces a shallow donor state in ZnO and this change in near-surface conductivity may also play a role.

Figure 5-7 shows the time dependence of resistance change of Pt-coated multiple ZnO nanowires as the gas ambient is switched from vacuum to N<sub>2</sub>, oxygen or various concentrations of H<sub>2</sub> in air (10–500 ppm) and then back to air. These data confirm the absence of sensitivity to O<sub>2</sub>. The resistance change during the exposure to hydrogen was slower in the beginning and the rate resistance change reached maximum at 1.5 min of the exposure time. This could be due to some of the Pd becoming covered with native oxide, which is removed by exposure to hydrogen.

Since the available surface Pd for catalytic chemical absorption of hydrogen increased after the removal of oxide, the rate of resistance change increased. However, the Pd surface gradually saturated with the hydrogen and the rate of resistance change decreased. When the gas ambient switched from hydrogen to air, the oxygen reacted with hydrogen right away, with the resistance of the nanowires changed back to the original value instantly. Moreover, the data were recorded at a power level of 0.4 mW which is low even in comparison with CNTs.<sup>123,125</sup> This is attractive for long-term hydrogen sensing applications.

The rate of resistance change for the nanowires exposed to the 500 ppm H<sub>2</sub> in N<sub>2</sub> was measured at different temperatures as shown in Figure 5-8. Figure 5-9 shows the Arrhenius plot of nanowire resistance change rate. An activation energy of 12 kJ/mole was calculated from the slope of the Arrhenius plot. This value is larger than that of a typical diffusion process. Therefore, the dominant mechanism for this sensing process is more likely to be the chemisorption of hydrogen on the Pd surface.

In conclusion, Pd-coated ZnO nanowires appear well suited to detection of ppm concentrations of hydrogen at room temperature. The recovery characteristics are fast upon removal of hydrogen from the ambient. The ZnO nanowires can be placed on cheap transparent substrates such as glass, making them attractive for low-cost sensing applications and operate at very low power conditions.

### **5.3.3 Single ZnO nanowire sensors**

In this section, we describe how the addition of sputter-deposited Pt clusters to the surface of single ZnO nanowires produces a significant increase in detection sensitivity for hydrogen at room temperature. The sensors are shown to detect ppm hydrogen at room temperature using  $\mu$ W of power. Figure 5-10 shows that the addition of the Pt-coatings increased the effective conductivity of the nanowires by over an order of magnitude. Because the Pt films

are discontinuous as evidenced by both field-emission scanning electron microscopy and atomic force microscopy, this suggests that the sputtering process itself changes the resistance of the nanowires, most likely through the introduction of oxygen vacancies which are donor states in ZnO.<sup>147,148</sup> There was a strong increase approximately a factor of 5 in the response of the Pt-coated nanowires to hydrogen relative to the uncoated devices. Figure 5-11 shows the I-V characteristics of Pt-coated nanowires as a function of both the measurement ambient and the time after exposure to 500 ppm H<sub>2</sub> in N<sub>2</sub>. There are several aspects of the data. There was no response of either coated or uncoated nanowires to the presence of O<sub>2</sub> in the ambient at room temperature and indeed the I-V characteristics were independent of the measurement ambient for vacuum, air, or pure N<sub>2</sub>. By sharp contrast, the nanowires were sensitive to the presence of H<sub>2</sub> in the ambient, with the response being time-dependent. The nanowire resistance was still changing at least 15 min after the introduction of the hydrogen. An Arrhenius plot of the rate of resistance change for the nanowires exposed to the 500 ppm H<sub>2</sub> in N<sub>2</sub> for 10 min produced an activation energy of 15 kJ/mol. This is larger than that expected for typical diffusion processes and suggests that the rate-limiting step may be chemisorption of hydrogen on the Pt surface. The reversible chemisorption of reactive gases at the surface of ZnO can produce a large reversible variation in the resistance.<sup>142</sup> In addition, atomic hydrogen introduces a shallow donor state into ZnO and this may play a role in the increased conductance of the nanowires.<sup>147,149</sup> The diffusion coefficient of the hydrogen is also much faster in ZnO than in any other wide band-gap semiconductor. Note the very low power consumption of the nanowire sensors, which is in the range 15-30 μW. This is approximately a factor of 25 lower than multiple ZnO nanowires operated under the same conditions and more than a factor of 50 lower than carbon nanotubes doped with Pd that were

used for hydrogen detection.<sup>123,125</sup> The low power consumption is clearly of advantage in many types of remote sensing or long-term sensing applications.

Figure 5-12 shows the time dependence of current (top) or relative resistance change (bottom) in both the uncoated and Pt-coated nanowires exposed to 500 ppm H<sub>2</sub> in N<sub>2</sub>. The relative resistance responses were 20 and 50%, respectively, after 10 or 20 min exposure. By comparison, the uncoated devices showed relative resistance changes of 2 and 3%, respectively, after 10 or 20 min exposure. The resistance change during the exposure to hydrogen was slower in the first few minutes, as is clear in Figure 5-13. This may be due to removal by the atomic hydrogen of native oxide on the Pt. As the effective surface area of the Pt would increase as the oxide was removed, the rate of change of resistance due to hydrogen adsorption should also increase. At fixed voltage, the relative resistance change was linear as a function of hydrogen content in the measurement ambient up to a few percent and then increased more slowly at higher concentrations. This may indicate a saturation of bonding sites for hydrogen at high concentrations. We have not yet investigated the long-term reliability and reproducibility of the nanowire sensors, but this aspect will be a key for practical applications. We have measured the time recovery characteristics of the single nanowires when hydrogen is removed from the ambient and find the recovery is limited by the time needed to flush the hydrogen out of the test fixture a few seconds and not by the nanowire response.

In summary, Pt-coated ZnO single nanowires are shown to selectively detect hydrogen at room temperature with very low power consumption. The disadvantage of this approach relative to using a network of multiple nanowires is the additional processing that is needed to contact a single nanowire, but the power consumption is significantly (a factor of ~25) lower.

### 5.3.4 A comparison of ZnO thin film and nanowire sensors

Previous work, ZnO nanowires have been demonstrated to have good sensitivity as sensing material due to their larger surface area and high aspect ratio. However, to this point, there has been no clear demonstration of improved detection sensitivity with nanowires compared to thin films. In this section, we report on a comparison of the hydrogen-sensing characteristics of ZnO thin films of different thicknesses and ZnO nanowires, both with Pt coatings. Both types of sensors are shown to be capable of the detection of ppm hydrogen at room temperature with nW power levels, but the nanowires show different recovery characteristics, consistent with the expected higher surface coverage of adsorbed hydrogen.

Two types of ZnO were employed in these experiments: nanowires and thin films. The thin films were grown by Pulsed Laser Deposition on sapphire substrates at 450 °C, as described in detail previously. The ZnO thickness was varied from 20–350 nm. Figure 5-13 shows the I-V characteristics measured between the Ohmic contacts on the thin film ZnO samples of either 20 or 350 nm thickness, both before and after the Pt deposition on the surface. The current increase as a result of the Pt deposition is approximately a factor of 2 for the thinnest sample and remains in the nA range at 0.5 V bias, i.e., the power consumption is 4 nW at this operating voltage. The effective conductivity of the Pt-coated films is higher due to the presence of the metal. At longer Pt sputtering times, we would typically see a transition to much higher currents, as the Pt film became continuous and the conductivity of the structure was no longer determined by the ZnO layer itself.

Figure 5-14 (top) shows the time dependence of current change at 0.5 V bias on the Pt-coated ZnO films of different thickness as the gas ambient is switched from N<sub>2</sub> to 500 ppm H<sub>2</sub> in N<sub>2</sub> and back to air as time proceeds. This data shows that the sensors are insensitive to N<sub>2</sub> and that there is a strong ZnO thickness dependence to the response to hydrogen. The bottom of

Figure 5-14 shows the change in current at 0.5 V bias when switching from N<sub>2</sub> to the hydrogen-containing ambient for the ZnO films of different thickness. At small thicknesses, the current change is small, which is probably related to poorer crystal quality and also at large film thickness where the bulk conductivity dominates the total resistance.

Figure 5-15 shows the time dependence of current in both the Pt-coated multiple ZnO nanowires and the thin films, as the gas ambient is switched from N<sub>2</sub> to 500 ppm H<sub>2</sub> in N<sub>2</sub> and then back to air as time proceeds. It is clear that the nanowires have a much larger response roughly a factor of 3, even for the optimal response for the thin films to the introduction of hydrogen into the ambient compared to their thin film counterparts. This is consistent with the expectation of a higher relative response based on their larger surface-to-volume ratio. Although not shown here, there was no response of either type of sensor to the presence of O<sub>2</sub> in the ambient at room temperature. The recovery of the initial resistance is rapid 90%, 20 s upon removal of the hydrogen from the ambient by either O<sub>2</sub> or air, while the nanowire resistance is still changing at least 15 min after the introduction of the hydrogen. The response is faster at higher temperatures.

The nanowires show a slower recovery than the thin films, most likely due to the relatively higher degree of hydrogen adsorption. The expected sensing mechanism suggested previously is that reversible chemisorption of the hydrogen on the ZnO produces a reversible variation in the conductance, with the exchange of charges between the hydrogen and the ZnO surface leading to changes in the depletion depth.<sup>142,143,146</sup> The conductivity of both the ZnO thin film and nanowires did change when the ambient switched from N<sub>2</sub> to air. Figure 5-16 shows the maximum current change at 0.5V bias for exposure of the nanowires and thin films to the 500ppm H<sub>2</sub> in N<sub>2</sub>. As discussed earlier, a key requirement in long-term hydrogen-sensing

applications is the sensor power consumption. Both the thin film and multiple nanowire sensors can operate at 0.5 V bias and powers 4 nW. We have also demonstrated hydrogen sensing with single ZnO nanowires at power levels approximately an order of magnitude lower than this, but the devices show poorer long-term current stability than multiple nanowire sensors.

In conclusion, Pt-coated ZnO thin films and multiple nanowires both are capable of the detection of ppm concentrations of hydrogen at room temperature. The thin films show optimum responses to the presence of hydrogen at moderate thicknesses. The nanowires show larger responses to hydrogen than the thin films, consistent with their large surface-to-volume ratios and have the advantage in terms of flexibility of the choice of substrate.

### **5.3.5 Surface functionalized SnO<sub>2</sub>-ZnO nanowire sensors**

In this section we show the use of single-crystal ZnO nanowires provide a convenient template for coating with SnO<sub>2</sub> and the resulting structure can be used to detect hydrogen at 400°C. Since the metal oxides exhibit different sensing characteristics toward chemical or gas species. Therefore, the rationale for this work is that it is straightforward to grow ZnO nanowires and the method provides an approach for integrating a range of oxides with high surface-to-volume ratio.

Figure 5-17 (top and center) shows scanning electron microscopy (SEM) micrographs of the SnO<sub>2</sub>/ZnO structures while the bottom of the figure shows an energy dispersive X-ray (EDX) spectrum. The latter shows characteristic Sn X-rays and confirms the presence of the SnO<sub>2</sub> layer. Figure 5-18 shows X-ray diffraction (XRD) spectra from the SnO<sub>2</sub>-coated ZnO nanowires. The (200) peak from the SnO<sub>2</sub> is readily detected, while the (301) peak is barely visible in the samples deposited for 10 min. When take N in consideration with the electron microscopy images discussed below, the data is consistent with the SnO<sub>2</sub> being polycrystalline.

Figure 5-19 shows some high-resolution transmission electron microscopy (HR-TEM) images from the hybrid structure. It is clear that the SnO<sub>2</sub> is deposited on only one side of the ZnO nanowires, the thickness of the SnO<sub>2</sub> is around 10 nm and that these layers are polycrystalline. A lattice image of the SnO<sub>2</sub>/ZnO structures is shown in Figure 5-20, emphasizing the ZnO is single-crystal while the SnO<sub>2</sub> is polycrystalline. EDX line scans shown in figure 5-21 confirmed that the SnO<sub>2</sub> was present on only one side of the ZnO, as expected from the line-sight geometry in the PLD chamber.

To perform the gas detection measurements, the multiple nanowires were contacted and mounted on a standard header. Figure 5-22 shows the current–voltage (I-V) characteristics from SnO<sub>2</sub>-coated ZnO nanowires for two different deposition times (top) and time dependence of current at fixed bias of 0.5 V as a function of measurement ambient (bottom). The devices with the thinner SnO<sub>2</sub> has a higher current, suggesting there is less surface depletion in the ZnO nanowire under these conditions. It is not clear why the addition of another 5–10 nm of SnO<sub>2</sub> should increase the effective resistance of the underlying ZnO nanowire. There was no response at room temperature to the introduction of 500 ppm hydrogen into the measurement ambient and the structure shows more drift in current in air relative to pure N<sub>2</sub>.

Figure 5-23 shows I-V characteristics from SnO<sub>2</sub>-coated ZnO nanowires at room temperature or 400°C (top) and current at fixed bias of 0.5 V as the wires are heated as a function of time (bottom). The conductivity of the ZnO is clearly sensitive to temperature, with the current being thermally activated with activation energy  $0.42 \pm 0.11$  eV. This probably represents the ionization energy of the dominant interfacial state between the ZnO and SnO<sub>2</sub> since pure ZnO nanowires without any coating exhibit lower activation energy for their conductivity (0.11 eV).

Figure 5-24 shows the current at fixed bias of 0.5 V and temperature of 400°C in the SnO<sub>2</sub>/ZnO structures as a function of time as the ambient is switched from N<sub>2</sub> to 500 ppm H<sub>2</sub> in N<sub>2</sub> or vacuum. Upon exposing the structures to 500 ppm H<sub>2</sub>, the conductivity increases, but neither the introduction of pure N<sub>2</sub> or vacuum helps for obtaining 100% recovery of the initial current prior to the introduction of the trace amounts of hydrogen. The sensor continues to show drift in the current at fixed voltage, as generally reported for SnO<sub>2</sub>. For the initial detection of the hydrogen, the sensitivity was high 70%. However, the effective sensitivity for subsequent detection events is lowered due to the current drift. There are multiple possible detection mechanisms for hydrogen in this hybrid structure, including the doping of ZnO by hydrogen donors, desorption of adsorbed surface oxygen and grain boundaries in poly-ZnO<sup>143</sup>, exchange of charges between adsorbed gas species and the ZnO surface leading to changes in depletion depth<sup>144</sup> and changes in surface or grain boundary conduction by gas adsorption/desorption.<sup>145</sup>

In conclusion, single-crystal ZnO nanowires were coated with SnO<sub>2</sub> using pulsed laser deposition and characterized with SEM, TEM, XRD and EDX. The SnO<sub>2</sub> was polycrystalline, with typical thickness of order 10 nm. The hybrid structure shows a strong sensitivity to 500 ppm H<sub>2</sub> in N<sub>2</sub> at 400°C. This approach provides a relatively straightforward method to integrate different oxides on templates with large surface-to-volume ratio.

#### 5.4 Summary and Conclusions

The applications of ZnO nanowires as material for hydrogen sensors were addressed. A variety of different metal catalysts (Pt, Pd, Au, Ag, Ti and Ni) sputter-deposited on multiple ZnO nanowires have been compared for their enhancement for detecting hydrogen at room temperature. It is found that the sensitivity for detecting hydrogen is greatly enhanced by sputter-depositing metal catalysts (Pt and Pt) on surface. Pt-coated ZnO nanowires can detect hydrogen down to 100 ppm with relative response of 4%. Pd-coated ZnO nanowires can detect hydrogen

down to 10 ppm with a relative smaller response than Pt-coated devices. Approximately 95% of the initial conductance after exposure to hydrogen was recovered within 20 s by exposing the device to air. The sensors are shown to detect ppm hydrogen at room temperature using  $<0.4$  mW of power when using multiple nanowires. When using a single ZnO nanowire coated with Pt as sensing material, the power consumption can further pushing down to  $\mu$ W range. These sensors are not sensitive to oxygen, nitrogen, humidity and air at room temperature, suggests high selectivity for hydrogen sensing applications. Furthermore, a comparison study of the hydrogen-sensing characteristics of ZnO thin films with different thickness and ZnO nanowires was described. The Pt-coated single nanowires show a current response of approximately a factor of 3 larger at room temperature upon exposure to 500 ppm of hydrogen. Both types of sensors are shown to be capable of the detection of ppm hydrogen at room temperature with nW power levels, but the nanowires show different recovery characteristics, consistent with the expected higher surface coverage of adsorbed hydrogen. Finally, SnO<sub>2</sub> coated ZnO nanowires were used as materials for hydrogen sensors. There was no response to 500 ppm hydrogen at room temperature but showed a 70% response at 400°C. The use of single-crystal ZnO nanowires provide a convenient template for coating with SnO<sub>2</sub> and the resulting structure can be used to detect hydrogen at 400°C.

Table 5-1. Relative resistance response of metal-coated multiple nanowires as the gas ambient is switched from nitrogen to 500 ppm of hydrogen in air.

Metal Catalyst	$ \Delta R /R$ (%)
Platinum (Pt)	8.49
Palladium (Pd)	4.26
Gold (Au)	0.66
Titanium (Ti)	0.39
Nickel (Ni)	0.28
Silver (Ag)	0.16

Table 5-2. Relative resistance response of Pd and Pt coated multiple nanowires as the gas ambient is switched from nitrogen to different concentration of hydrogen in air.

Concentration (ppm)	Pd-ZnO $ \Delta R /R$ (%)	Pt-ZnO $ \Delta R /R$ (%)
10	2.41	0.25
100	3.14	4.67
250	3.79	6.44
500	4.28	8.50

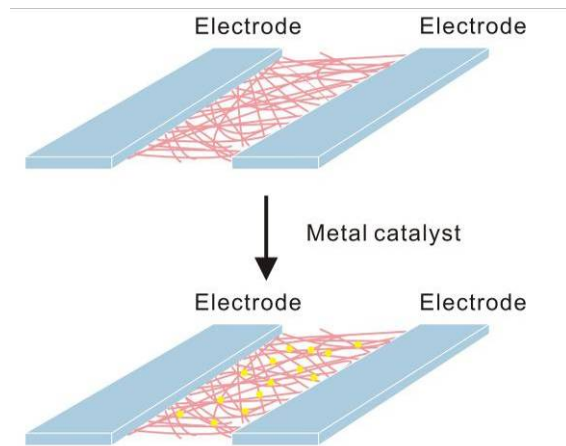


Figure 5-1. Metal catalysts decorated ZnO nanowires.

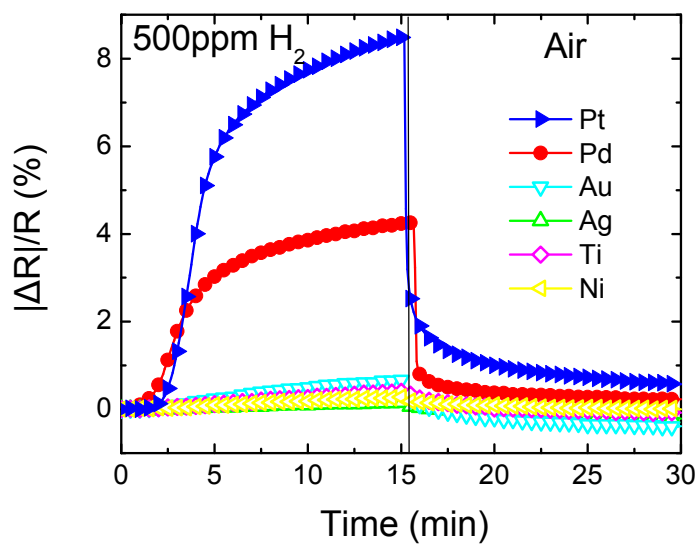


Figure 5-2. Time dependence of relative resistance response of metal-coated multiple nanowires as the gas ambient is switched from  $N_2$  to 500 ppm of  $H_2$  in air as time proceeds.

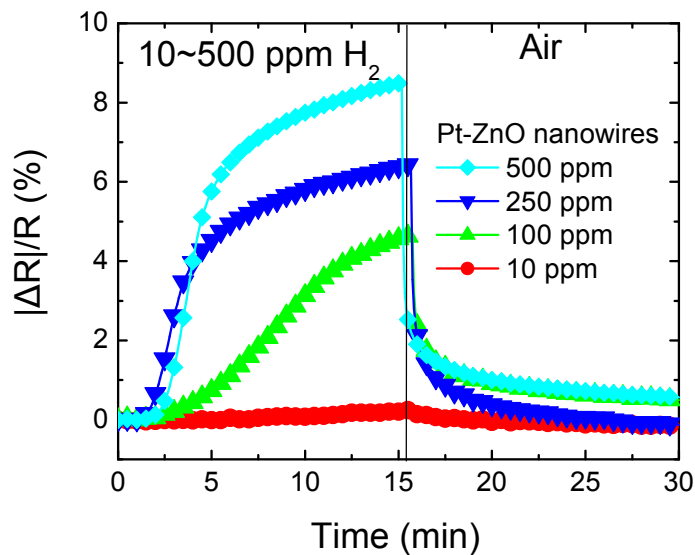


Figure 5-3. Time dependence of resistance change of Pt-coated multiple ZnO nanowires as the gas ambient is switched from  $N_2$  to various concentrations of  $H_2$  in air (10–500 ppm) and then back to  $N_2$ .

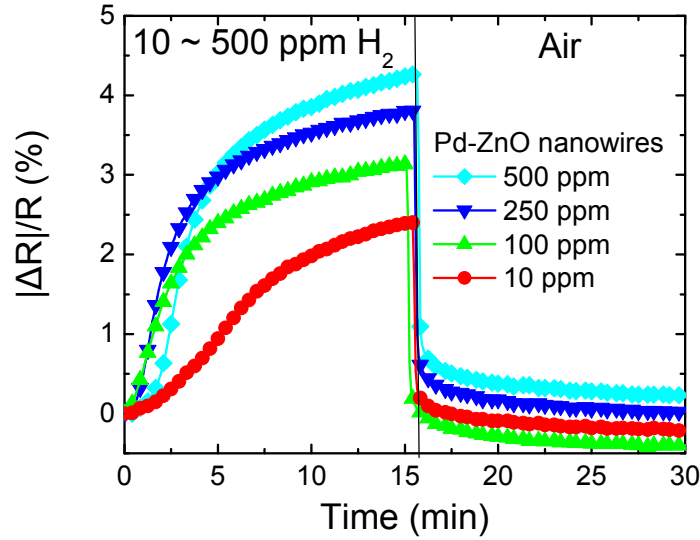


Figure 5-4. Time dependence of resistance change of Pd-coated multiple ZnO nanowires as the gas ambient is switched from N<sub>2</sub> to various concentrations of H<sub>2</sub> in air (10–500 ppm) and then back to N<sub>2</sub>.

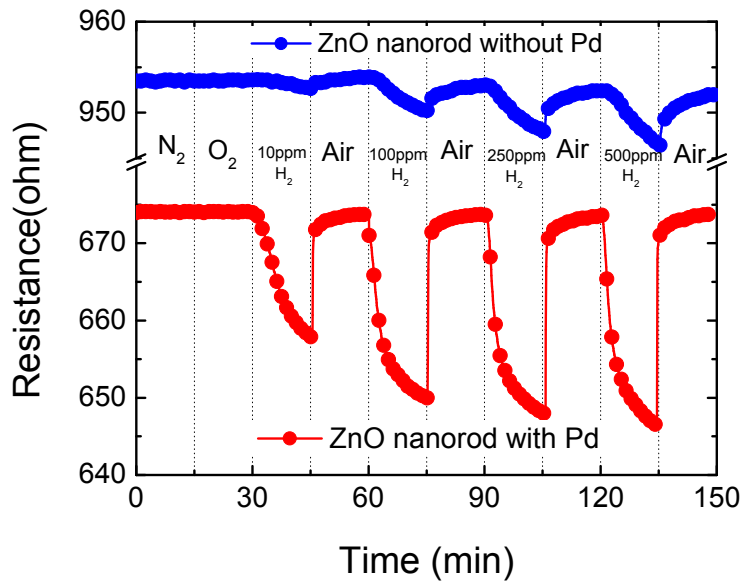


Figure 5-5. Time dependence of resistance of either Pd-coated or uncoated multiple ZnO nanowires as the gas ambient is switched from N<sub>2</sub> to various concentrations of H<sub>2</sub> in air (10–500 ppm) as time proceeds. There was no response to O<sub>2</sub>.

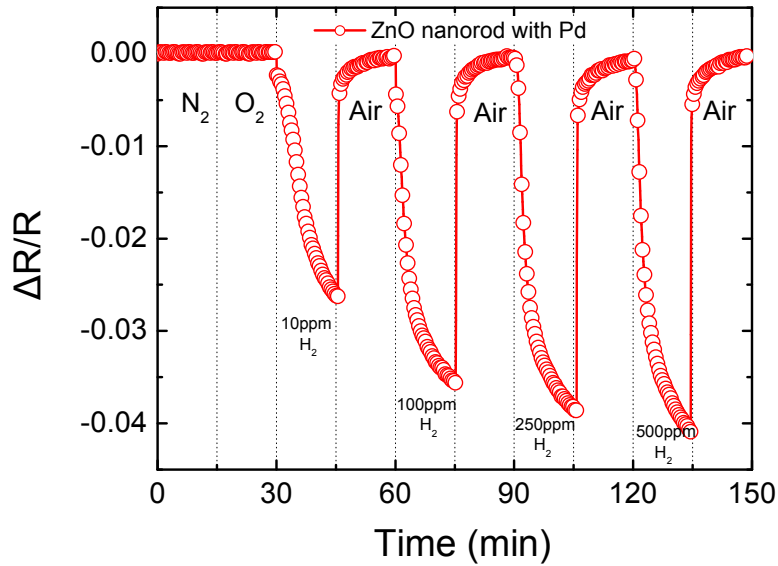


Figure 5-6. Relative response of Pd-coated nanowires as a function of H<sub>2</sub> concentration in N<sub>2</sub>.

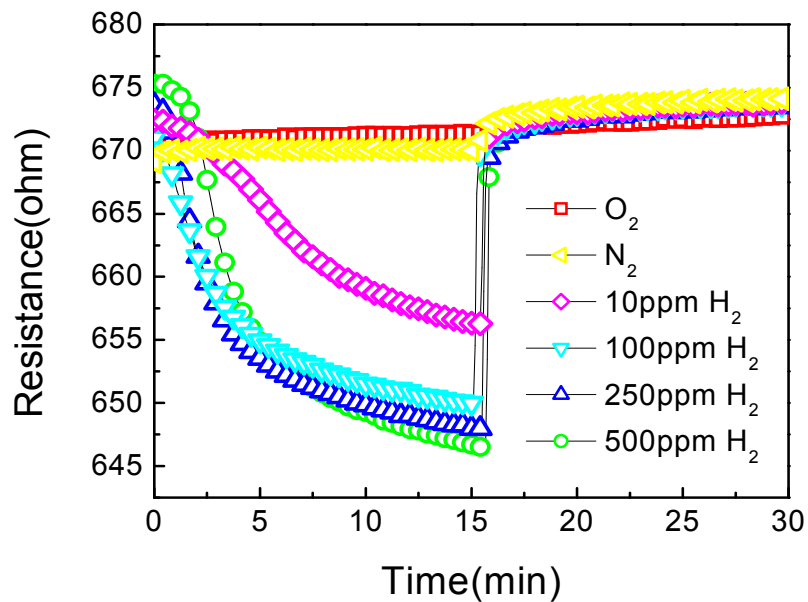


Figure 5-7. Time dependence of resistance change of Pd-coated multiple ZnO nanowires as the gas ambient is switched from N<sub>2</sub> to oxygen or various concentrations of H<sub>2</sub> in air (10–500 ppm) and then back to N<sub>2</sub>.

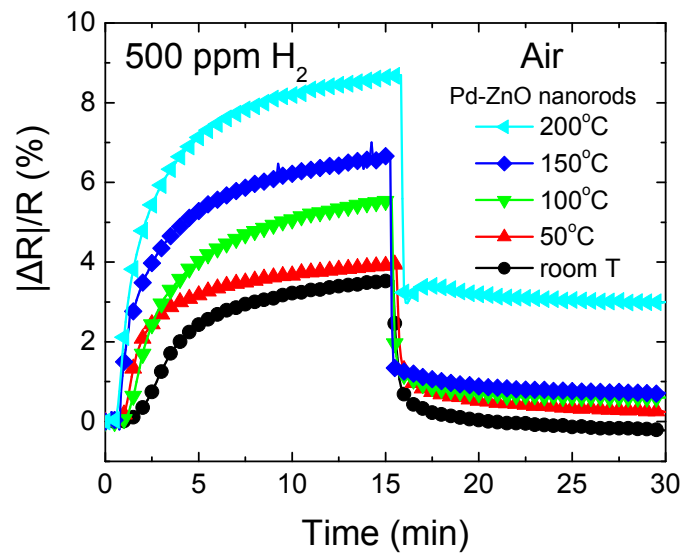


Figure 5-8. Rate of resistance change after exposure to 500 ppm H<sub>2</sub> in N<sub>2</sub> was measured at different temperatures.

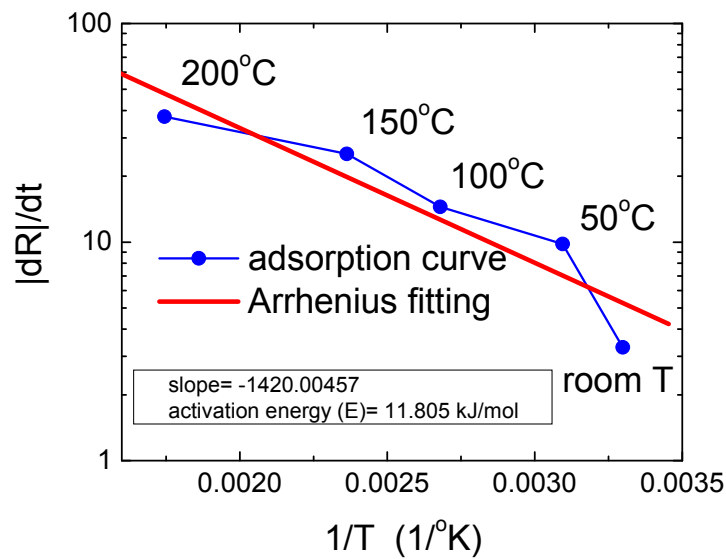


Figure 5-9. Arrhenius plot of rate of resistance change after exposure to 500 ppm H<sub>2</sub> in N<sub>2</sub>.

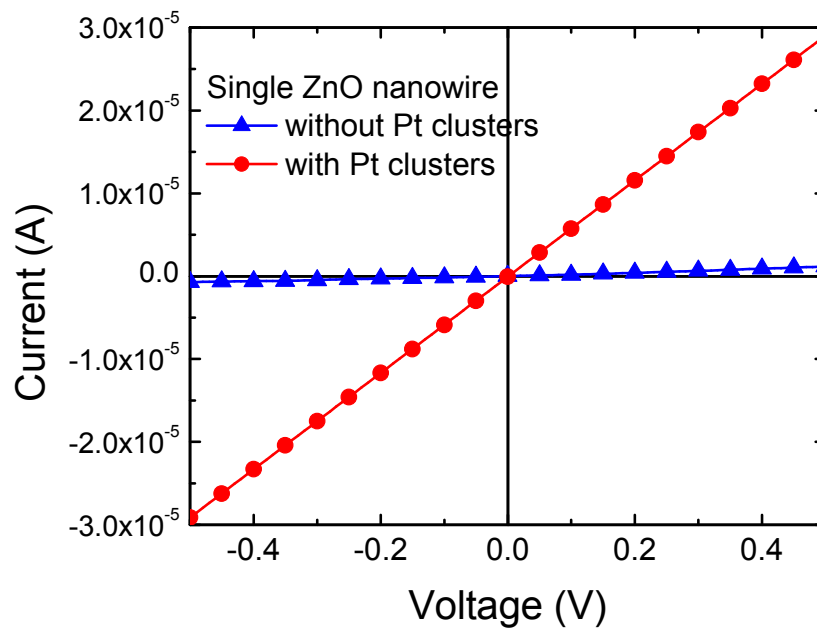


Figure 5-10. Current-voltage (I-V) plot of uncoated or Pt-coated single ZnO nanowires measured at room temperature in pure  $N_2$ .

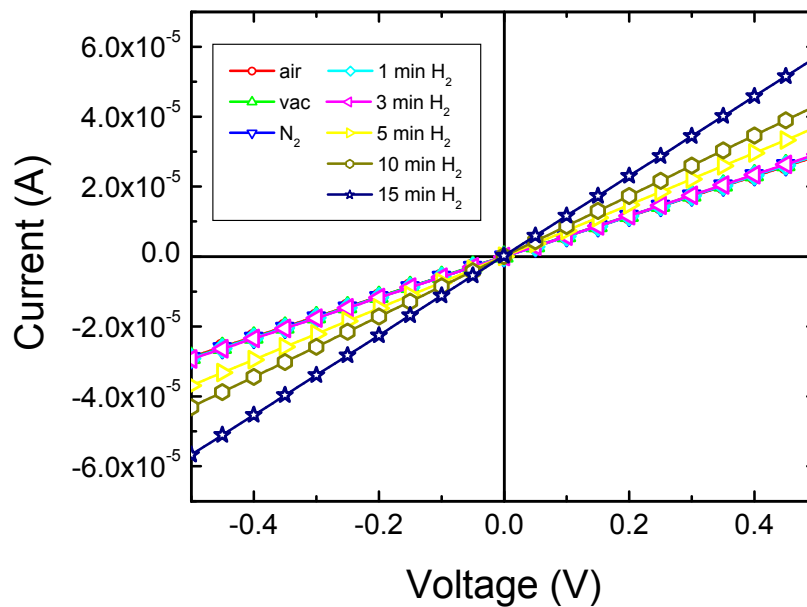


Figure 5-11. Current-voltage (I-V) characteristics of Pt-coated ZnO single nanowires measured in vacuum, air,  $N_2$  or 500ppm  $H_2$  in  $N_2$  ambients. The latter responses were time-dependent.

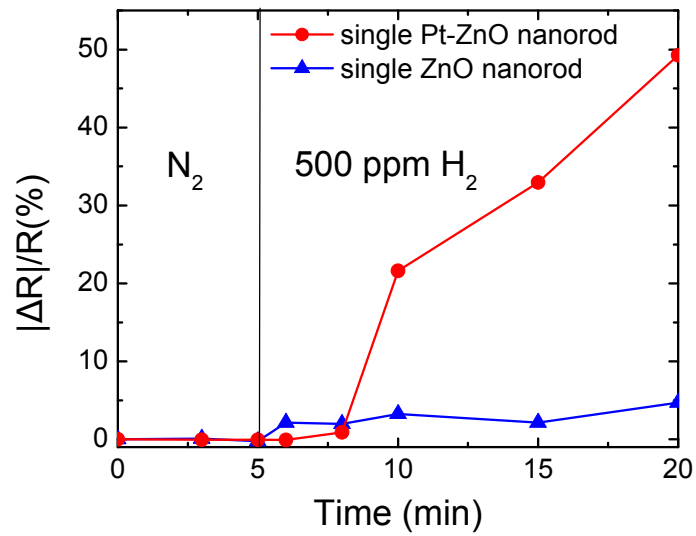
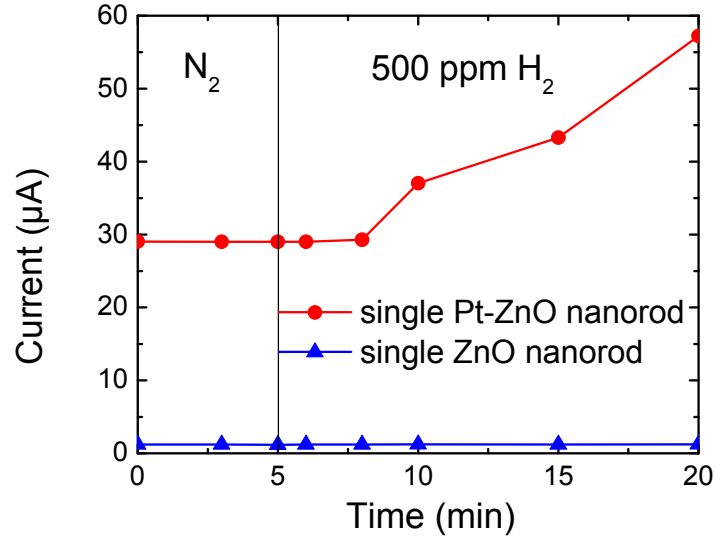


Figure 5-12. Current versus time plot for single ZnO nanowires either with or without Pt coatings (top) and corresponding  $|\Delta R|/R(\%)$ -time plots (bottom).

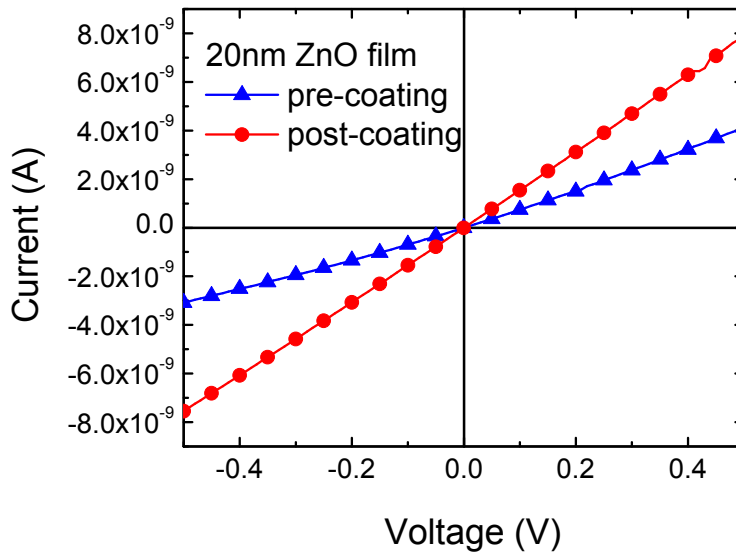
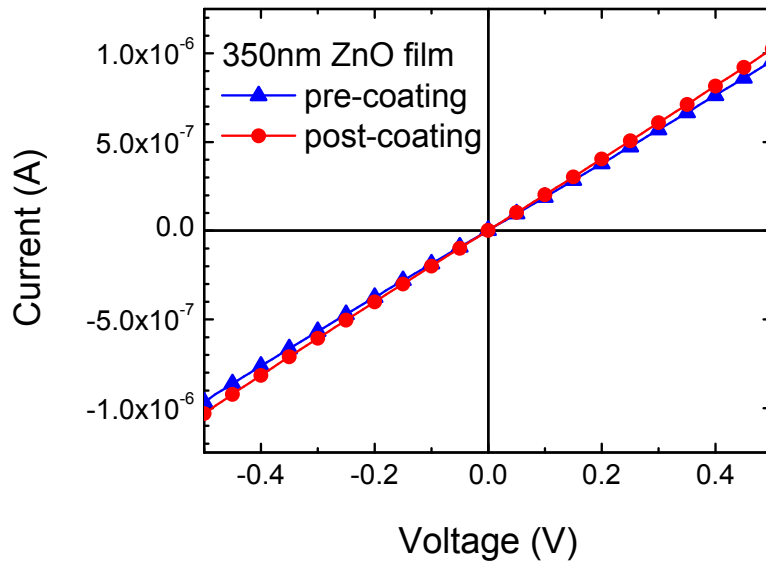


Figure 5-13. Room temperature I-V characteristics from ZnO thin films of thickness 20 or 350 nm measured in air before and after coating with Pt.

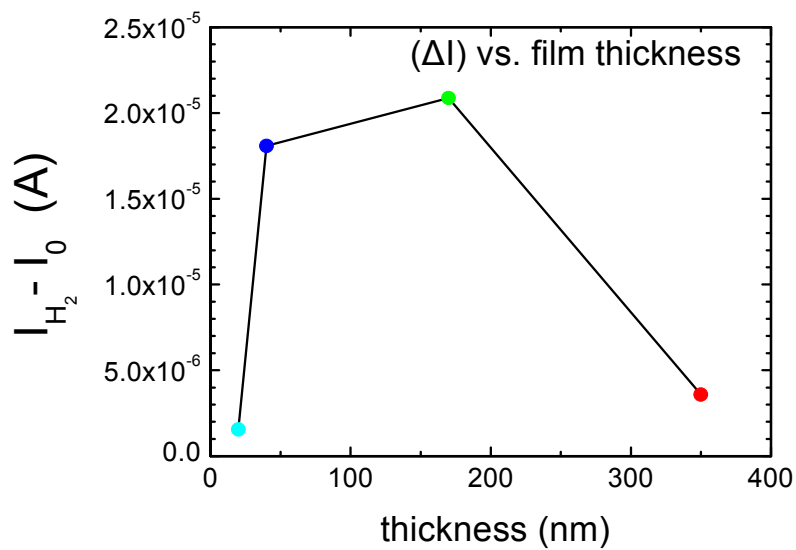
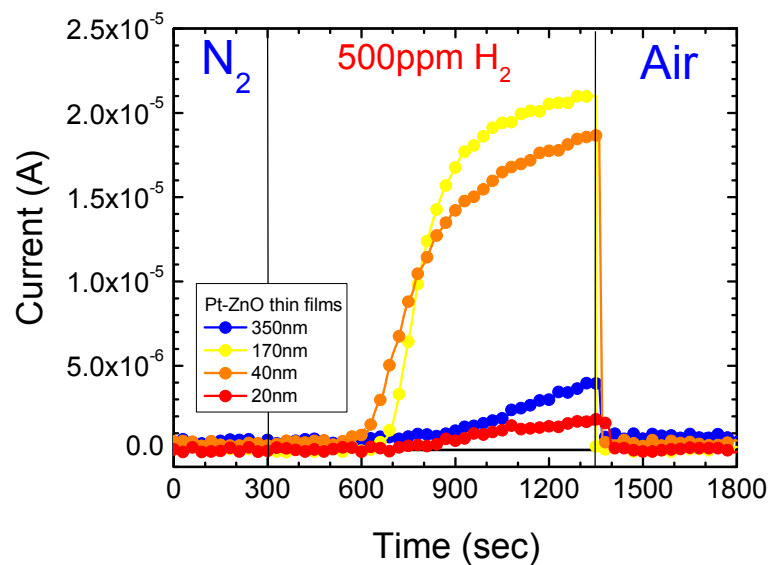


Figure 5-14. Current as a function of time for Pt-coated ZnO thin films of different thickness cycled from N<sub>2</sub> to 500 ppm H<sub>2</sub> in N<sub>2</sub> to air ambient (top) and change in current at fixed bias (0.5V) when switching to the H<sub>2</sub>-containing ambient (bottom).

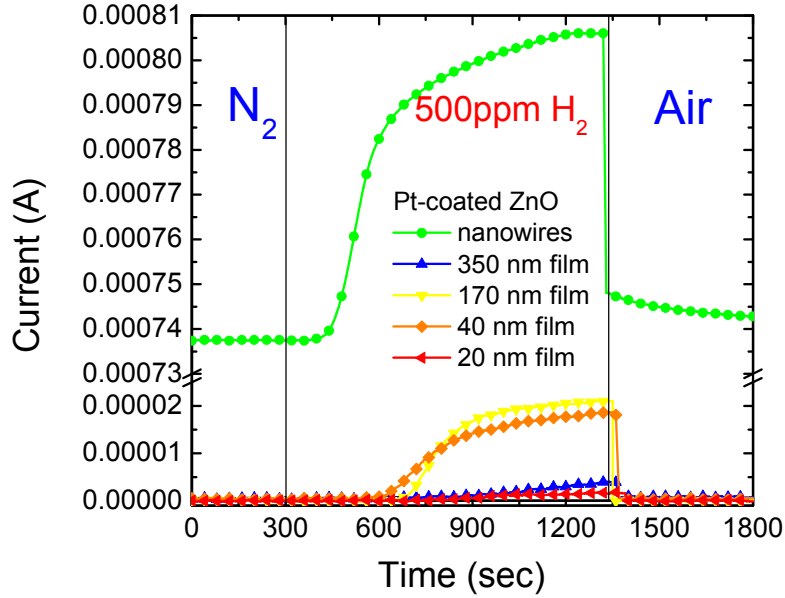


Figure 5-15. Time dependence of current from Pt-coated ZnO nanowires and thin films as the gas ambient is switched from N<sub>2</sub> to 500 ppm H<sub>2</sub> in N<sub>2</sub>, then to air for recovery.

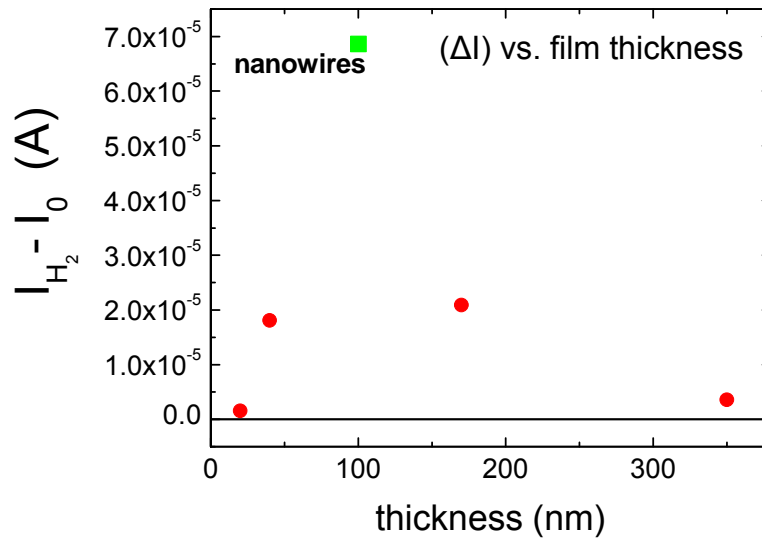


Figure 5-16. Change in current at fixed bias (0.5V) when switching to the H<sub>2</sub>-containing ambient of either Pt-coated ZnO nanowires or thin films as the gas ambient is switched from N<sub>2</sub> to 500 ppm H<sub>2</sub> in N<sub>2</sub>, then to air for recovery.

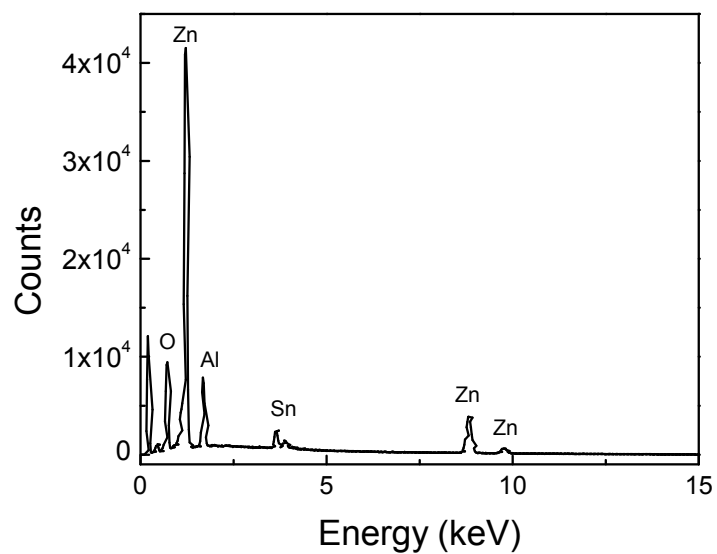
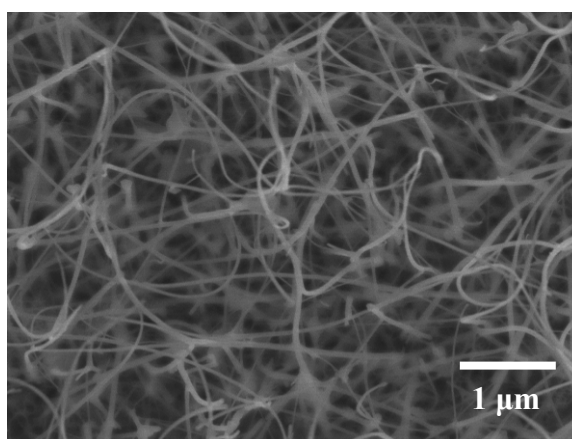
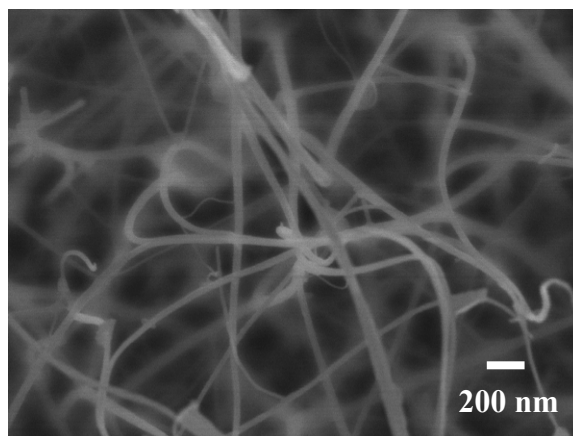


Figure 5-17. Scanning electron microscopy micrographs (top and center) of SnO<sub>2</sub>-coated ZnO nanowires and EDX spectrum (bottom).

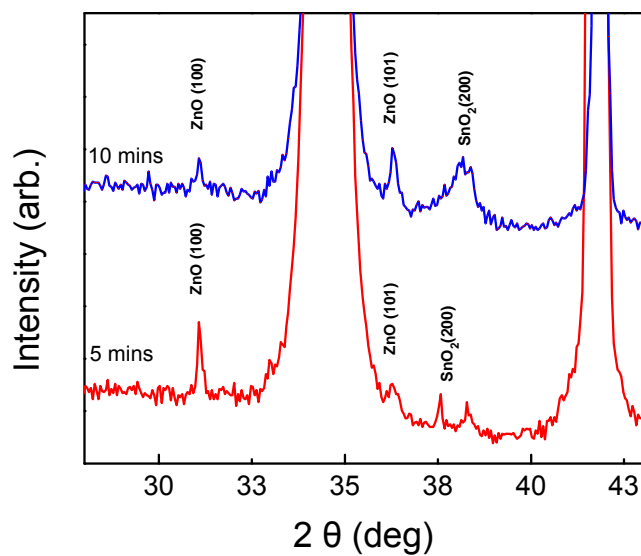
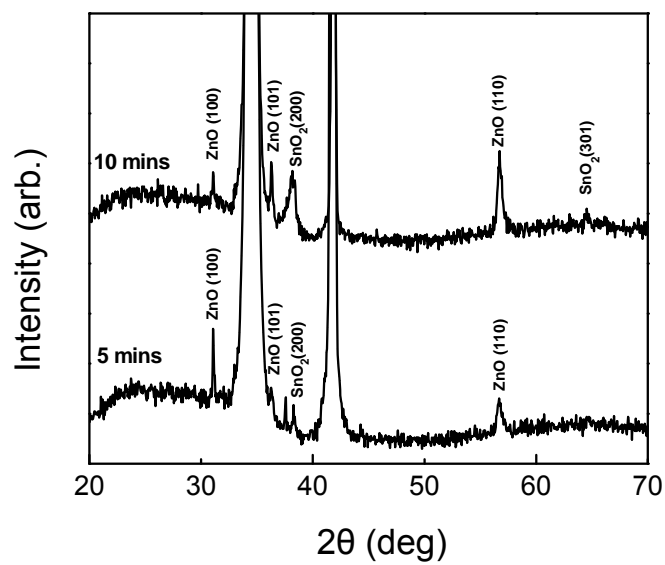


Figure 5-18. X-ray diffraction pattern from SnO<sub>2</sub>-coated ZnO nanowires. The data is consistent with the SnO<sub>2</sub> being polycrystalline.

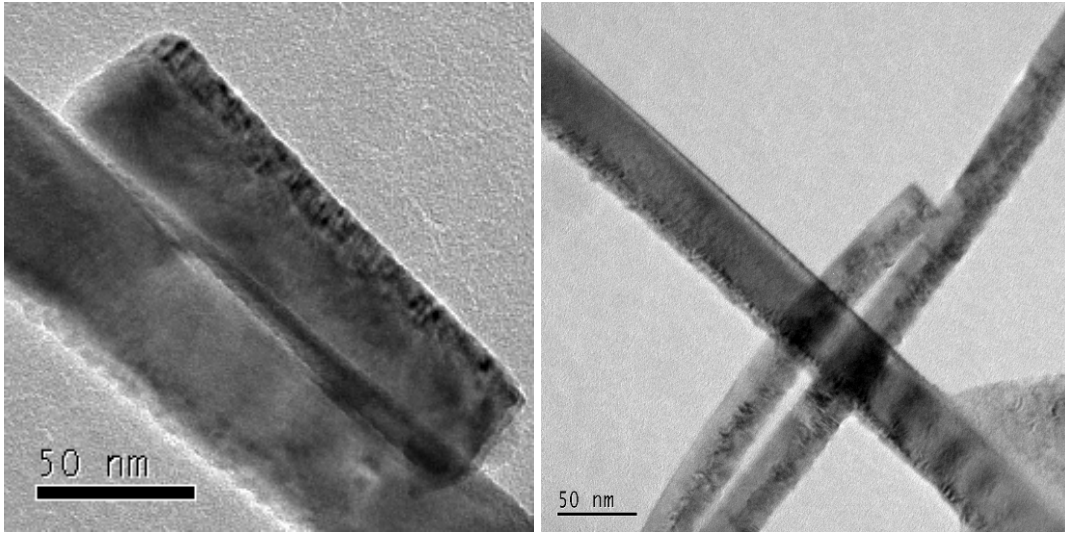


Figure 5-19. High resolution transmission electron microscope images of SnO<sub>2</sub>/ZnO nanowires showing deposition of SnO<sub>2</sub> on one side of the nanowires.

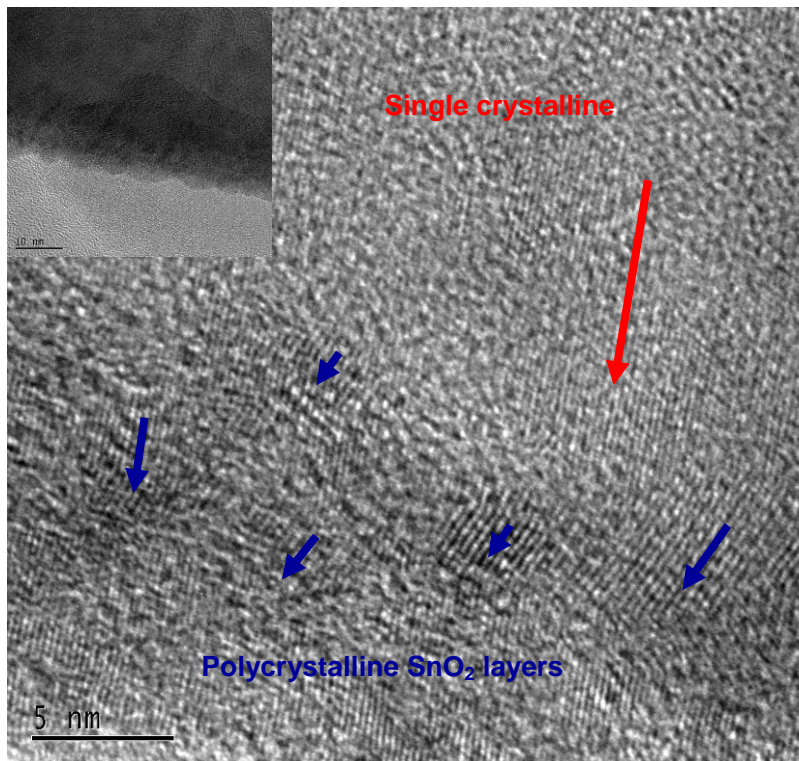


Figure 5-20. High resolution transmission electron microscope image of SnO<sub>2</sub>-coated ZnO nanowire.

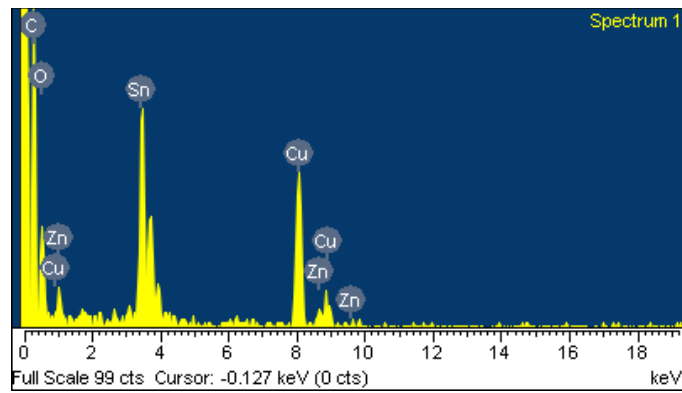
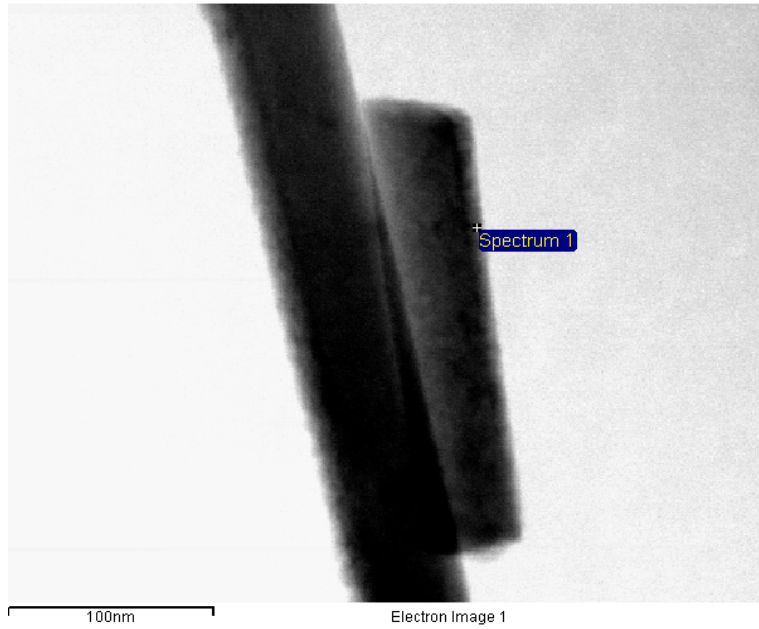


Figure 5-21. Energy-Dispersive X-ray Spectroscopy analysis of SnO<sub>2</sub>/ZnO nanowires.

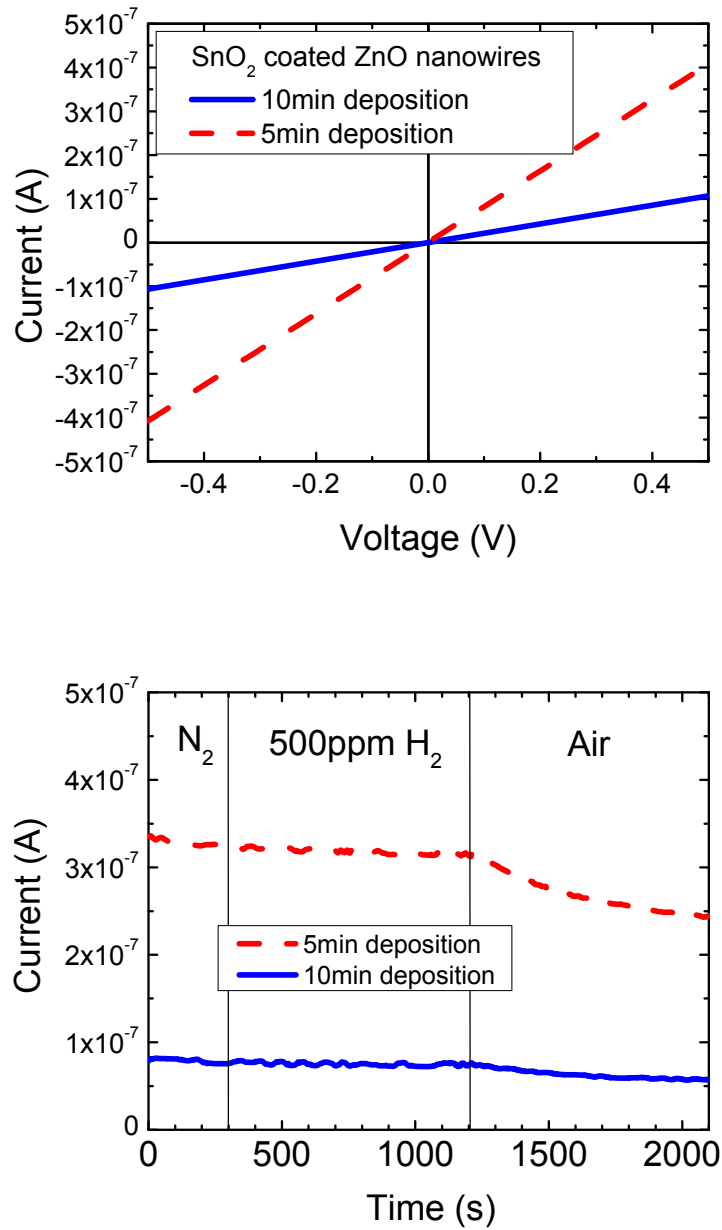


Figure 5-22. Current-voltage (I-V) characteristics from SnO<sub>2</sub>-coated ZnO nanowires for two different deposition times (top) and time dependence of current at fixed bias of -0.5V as a function of measurement ambient (bottom).

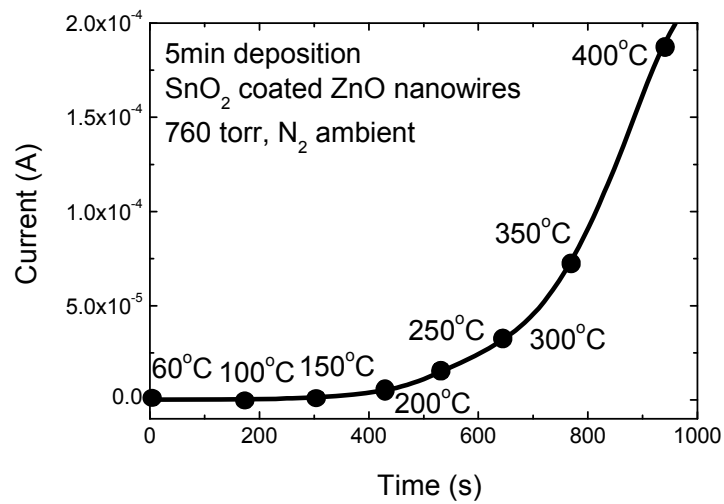
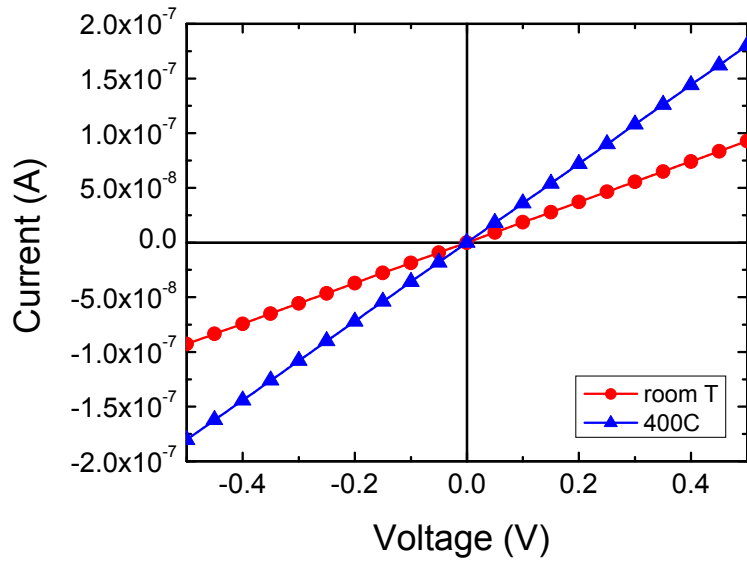


Figure 5-23. Current-voltage (I-V) characteristics from SnO<sub>2</sub>-coated ZnO nanowires at room temperature or 400°C (top) and current at fixed bias of -0.4 V as the nanowires are heated as a function of time (bottom).

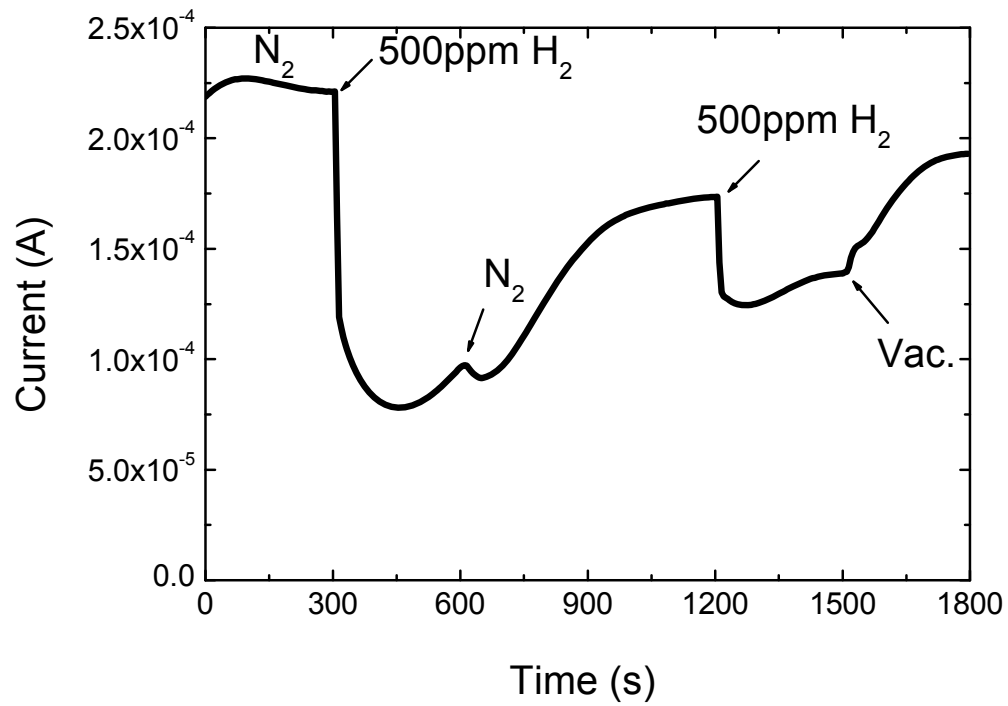


Figure 5-24. Current at fixed bias of -0.5 V and temperature of 400°C as a function of time as the ambient is switched from N<sub>2</sub> to 500ppm H<sub>2</sub> in N<sub>2</sub> or vacuum.

## CHAPTER 6 CATALYST-FREE GROWTH OF METAL OXIDE NANOWIRES

### 6.1 Introduction

The synthesis of one-dimensional (1-D) semiconductor nanostructures has attracted great interest due to the unique physical and chemical properties of these materials. There is significant interest in one-dimensional semiconducting nanostructures due to their unique optical, electronic and chemical properties. Electronic nanomaterials are being pursued as possible building blocks in fabricating nanoscale electronics, optoelectronic, magnetic storage devices, and chemical sensors.

Zinc oxide (ZnO) is a wide-band-gap *n*-type semiconductor with direct band gap of 3.37 eV that has been extensively studied due to its applicability in transparent electronics,<sup>33,150,151</sup> chemical and gas sensors,<sup>108,119,138,152-155</sup> spin functional devices<sup>28,66,156-159</sup>, Schottky diodes,<sup>160,161</sup> nanoelectronics,<sup>112</sup> and blue light-emitting diodes.<sup>25,26,162,163</sup> The synthesis of ZnO nanowires has been reported using a variety of methods, including thermal evaporation<sup>71</sup>, molecular beam epitaxy,<sup>164</sup> solution-phase growth<sup>165</sup> and hydrothermal methods.<sup>166</sup> Vertically aligned ZnO nanowires are potentially useful for vertical device fabrication, with proposed device implementations that include light-emitting-diodes,<sup>163,167</sup> dye-sensitized solar cells<sup>165,168</sup> and nanopiezoelectrics.<sup>7</sup> Considerable effort has been made to fabricate aligned ZnO nanowires on various substrates using either physical vapor deposition (PVD)<sup>169</sup>, chemical vapor deposition (CVD)<sup>170,171</sup> or metal-organic chemical vapor deposition (MOCVD).<sup>98,172</sup> It remains challenging to controllably grow well-aligned ZnO nanowires. In many cases, the growth of semiconductor nanowires proceeds via a vapor-liquid-solid (VLS) growth mechanism that requires a metal catalyst.<sup>70</sup> However, metal catalysts can also serve as impurities in the nanowires, thus limiting material properties.

Recent progress in semiconductor nanowire heterostructure synthesis provides possibilities in developing high-performance electronic, optoelectric, and sensing devices.<sup>15,173-181</sup> The composition modulated nanowire heterostructures have great potential as building blocks for the fabrication of high performance optoelectronics.<sup>15,182-184</sup> Composition modulation in the radial direction can efficiently confine both the carriers and emitted photons. For example, if a shell layer in a coaxial nanowire heterostructure has wider band gap energy and a lower reflective index than a core layer, confinement of both carrier and photons in the core nanowire can be significantly enhanced.<sup>15,176</sup> Alloying the ZnO phase with MgO has been investigated for increasing the band gap of ZnO-based nanowires.<sup>29</sup> Theoretically, the band gap of ZnO can be modulated from 3.3 to 4.0 eV by doping with different amount of MgO.<sup>19,185</sup> ZnMgO alloy is an important material to construct the heterostructure or superlattice to obtain high performance laser diode (LD) and light emitting diode (LED) devices.<sup>15,186</sup> Previously, we have observed the formation of various core/shell nanowires when adding Mg to the Zn and O flux during growth of Au-catalyst nucleated ZnO nanowires by molecular beam epitaxy.<sup>183,187</sup> However, a clean and abrupt interface has not been produced because of spontaneous phase separation inducing self-ordered formation of coaxial heterostructures.

Tin oxide ( $\text{SnO}_2$ ) is a wide band gap ( $E_g=3.6$  eV at 300K) semiconductor material suitable for multiple applications that include gas sensors<sup>38,188</sup>, transparent conducting electrodes<sup>189</sup>, and solar cells.<sup>190,191</sup> In sensor applications,  $\text{SnO}_2$  has been reported to display high gas sensitivity and selectivity.<sup>38,127</sup> The reduced size of nanostructured  $\text{SnO}_2$  provides a material with a large surface-to-volume ratio.<sup>155</sup> Gas sensors based on one-dimensional nanostructured  $\text{SnO}_2$  have been reported to exhibit good selectivity, low detection limits, and short response and recovery time.<sup>37,42,192-194</sup> Several methods have been employed to prepare  $\text{SnO}_2$  nanorods including

thermal evaporation,<sup>6,195</sup> thermal decomposition,<sup>45,196</sup> solution-phase growth,<sup>47,197</sup> and hydrothermal methods.<sup>198</sup> Among these, the thermal evaporation approach has been used to synthesize a wide variety of one-dimensional materials.<sup>5</sup> This often has involved the use of a catalyst in which nanowire growth proceeds by a vapor-liquid-solid (VLS) mechanism.<sup>70</sup> However, metal catalysts can serve as impurities in the nanowires, possibly forming defect states that limit their application in devices.

Vanadium oxide (VO<sub>2</sub>) nanowires have attracted great attention because of their metal to insulator transitions and reversible dramatic changes in electrical and optical properties accompanied by a structural phase transition.<sup>50,54,58,59</sup> It also makes it a promising material for the use in device applications to achieve reliable electrical and optical switching operations. VO<sub>2</sub> can exhibit a sharp (by a factor of 10<sup>4</sup>–10<sup>5</sup>) and fast (sub-picosecond) metal-insulator transition close to room temperature (340 K).<sup>55</sup> The metal-insulator transition is due to a small structural distortion of the lattice from a low-temperature monoclinic (semiconducting phase) to a high-temperature tetragonal rutile (metallic phase) structure, accompanied by large changes in conductivity and optical properties from infrared (IR) transmission to reflecting.<sup>54</sup> Moreover, B phase VO<sub>2</sub> was found to have good electrochemical performance, especially for use as an electrode material for lithium batteries.<sup>57,58</sup> It exhibits a maximum reversible capacity of about 320 mA h g<sup>-1</sup> in the range 4 to 1 V in lithium cells.<sup>59,60</sup> It has been reported that the operating properties of batteries depend not only on the structure but also on the morphology of the electrode components.<sup>61</sup> Therefore, the great surface area of nanowire materials may play an important role for electrochemical applications.<sup>155</sup>

In this chapter, we report the synthesis of metal oxide nanowires by high-pressure assisted pulsed laser deposition. A variety of metal oxide nanowires (ZnO, SnO<sub>2</sub>, and VO<sub>2</sub>) can be

synthesized without metal catalyst. The doping effects of Mg in ZnO nanowires were also examined. In the first section, the growth of well-aligned ZnO nanowires by high-pressure assisted pulsed laser deposition (PLD) is reported. The nanowire growth requires a ZnO template for nucleation, but proceeds without the use of any metal catalyst. The structure and properties of the nanowires are characterized, revealing high quality single crystal ZnO nanowires. The effects of growth temperature and background pressure on nanowire growth and properties are discussed. The addition of Mg into ZnO has been examined as well. The resulting structures show the segregation of Mg because of big lattice mismatch and limited solubility. By switching MgO and ZnO targets during growth, a core-sheath structure is observed. The synthesis of aligned SnO<sub>2</sub> nanorods is described in the second section. The nanorod morphology is observed for PLD growth conditions that include a relatively high background pressure, high substrate temperature, and a non-epitaxial relationship between the SnO<sub>2</sub> and substrate. SnO<sub>2</sub> nanorod growth is achieved without the use of any metal catalyst. In the last section, high aspect ratio monoclinic VO<sub>2</sub> nanowires grew laterally on the silicon and *c*-sapphire substrates at 600°C in 500 mTorr argon. The nanowires randomly nucleate on the surface with the diameter of 90–200 nm, length up to 50 μm. Since pulsed laser deposition is a convenient means for achieving stoichiometric transfer in growing multi-element materials<sup>199</sup>, these results suggest the possibility of growing oxide nanowires with complex crystal structures and/or multi-cation stoichiometry.

## **6.2 Experimental Methods**

### **6.2.1 ZnO nanowires growth**

Pulsed laser deposition was used for the ZnO nanowire growth. The ablation target was fabricated using high purity ZnO (Alfa Aesar, 99.9995%). The target was pressed and sintered at 1000°C for 12 h in air. A KrF excimer laser was used as the ablation source. A repetition rate of 5 Hz was used, with target to substrate distance of 2.5 cm and a laser pulse energy density of 1–3

J/cm<sup>2</sup>. The growth chamber exhibits a base pressure of 10<sup>-6</sup> Torr. In order to achieve well-ordered ZnO nanowires, a thin (75–200 nm) ZnO template layer was grown on the *c*-plane sapphire substrate prior to nanowire nucleation. The ZnO template film was *c*-axis oriented. Prior to deposition, the substrates were ultrasonically cleaned with trichloroethylene, acetone and methanol, followed by compressed N<sub>2</sub> drying. The substrates were attached to the heater using Ag paint. Prior to growth, the target was cleaned *in situ* by pre-ablating with approximately 2000 shots. The growth experiments were performed over a temperature range of 500–800°C in a background pressure of 150–500 mTorr. Three different gas ambient (O<sub>2</sub>, Ar and O<sub>2</sub>/Ar mixture) were used to investigate the effects of oxidation and gas-phase collisions in the formation of nanowires. The typical growth time was 2 h. After growth, the samples were cooled under the same gas ambient as was used during growth. The as-grown samples were characterized using X-ray diffraction (XRD) (Philips 3720, Cu-K<sub>α</sub>), field emission scanning electron microscopy (FE-SEM) (JEOL 6335F) and high resolution transmission electron microscopy (HR-TEM) (JEOL 2010F). The optical properties of the nanowires were examined using photoluminescence at room temperature. A He-Cd (325 nm) laser was used as the excitation source.

### 6.2.2 ZnMgO nanowires growth

The synthesis of ZnMgO nanowires was carried out by pulsed laser deposition. The ablation target was fabricated using powder mixture of high purity ZnO (Alfa Aesar, 99.9995%) and MgO (Alfa Aesar, 99.95%) with Mg:Zn atomic ratios of 1:4. The target was pressed and sintered at 1000°C for 12 h in air. A KrF excimer laser was used as the ablation source. A repetition rate of 5 Hz was used, with target to substrate distance of 2.5 cm and a laser pulse energy density of 1–3 J/cm<sup>2</sup>. The growth chamber exhibits a base pressure of 10<sup>-6</sup> Torr. The *c*-plane sapphire was used as the substrate materials in this study. Prior to deposition, the substrates were ultrasonically cleaned with trichloroethylene, acetone and methanol, followed by

compressed N<sub>2</sub> drying. The substrates were attached to the heater using Ag paint. Prior to growth, the target was cleaned *in situ* by pre-ablating with approximately 2000 shots. The growth temperature was 800°C in a background pressure of 500 mTorr of oxygen. The typical growth time was 2 h. After growth, the samples were cooled under the same gas ambient as was used during growth. The as-grown samples were characterized using X-ray diffraction (XRD) (Philips 3720, Cu-K<sub>α</sub>), field emission scanning electron microscopy (FE-SEM) (JEOL 6335F) and high resolution transmission electron microscopy (HR-TEM) (JEOL 2010F). The optical properties of the nanowires were examined using photoluminescence at room temperature. A He-Cd (325 nm) laser was used as the excitation source.

### 6.2.3 SnO<sub>2</sub> nanorods growth

Pulsed laser deposition (PLD) was used for the SnO<sub>2</sub> nanorod growth. The ablation target was fabricated using high purity SnO<sub>2</sub> (Alfa Aesar, 99.996%). The target was pressed and sintered at 1300°C for 16 h in air. A KrF excimer laser was used as the ablation source. A repetition rate of 5 Hz was used, with a target to substrate distance of 2.5 cm and a laser pulse energy density of 1–3 J/cm<sup>2</sup>. The growth chamber exhibits a base pressure of 10<sup>-6</sup> Torr. Single crystal *p*-silicon (100) and *c*-plane sapphire were used as the substrate materials in this study. Previous work has shown that SnO<sub>2</sub> can grow epitaxially on sapphire. Prior to deposition, the substrates were ultrasonically cleaned with trichloroethylene, acetone and methanol, followed by compressed N<sub>2</sub> drying. The substrates were attached to the heater using Ag paint. Prior to growth, the target was cleaned *in situ* by pre-ablating with approximately 2000 shots. The growth experiments were performed over a temperature range of 700–800°C in a background pressure of 500 mTorr. The typical growth time was 30 minutes. The as-grown samples were characterized using X-ray diffraction (XRD) using a Philips 3720, field emission scanning electron microscopy

(FE-SEM) using a JEOL 6335F and high resolution transmission electron microscopy (HR-TEM) using a JEOL 2010F.

#### **6.2.4 VO<sub>2</sub> nanowires growth**

Pulsed laser deposition (PLD) was used for the VO<sub>2</sub> nanowire growth. The ablation target was fabricated using high purity V<sub>2</sub>O<sub>5</sub> (Alfa Aesar, 99.99%). The target was pressed and sintered at 700°C for 12 h in air. A KrF excimer laser was used as the ablation source. A repetition rate of 5 Hz was used, with a target to substrate distance of 2.5 cm and a laser pulse energy density of 1–3 J/cm<sup>2</sup>. The growth chamber exhibits a base pressure of 10<sup>-6</sup> Torr. Single crystal *p*-silicon (100) and *c*-plane sapphire were used as the substrate materials in this study. Previous work has shown that VO<sub>2</sub> can grow epitaxially on sapphire. Prior to deposition, the substrates were ultrasonically cleaned with trichloroethylene, acetone and methanol, followed by compressed N<sub>2</sub> drying. The substrates were attached to the heater using Ag paint. Prior to growth, the target was cleaned *in situ* by pre-ablating with approximately 2000 shots. The growth experiments were performed over a temperature range of 500–700°C in a background pressure of 500 mTorr. The typical growth time was 2 h. The as-grown samples were characterized using X-ray diffraction (XRD) using a Philips 3720, field emission scanning electron microscopy (FE-SEM) using a JEOL 6335F and high resolution transmission electron microscopy (HR-TEM) using a JEOL 2010F. The optical properties of the nanowires were examined using photoluminescence at room temperature. A He-Cd (325 nm) laser was used as the excitation source.

### **6.3 Results and Discussion**

#### **6.3.1 Synthesis and characterization of vertical-aligned ZnO nanowires**

In general, nanowire growth was achieved via PLD growth at relatively high temperature and high background pressure. Figure 6-1 shows cross-section and plan view FE-SEM images of ZnO nanowire arrays grown at 800°C in 500 mTorr oxygen, 500 mTorr argon, or a 325 mTorr Ar

/ 175 mTorr O<sub>2</sub> mixture. In the case of pure argon, the only oxygen supplied during growth was from the ZnO in the ablation plume. Vertically well-aligned nanowires were observed by cross-sectional FE-SEM, showing that the growth is highly *c*-axis oriented along the normal direction of the substrate. At low magnification, a relatively uniform distribution of diameter is observed for the nanowires. The diameters are around 50–90 nm. Moreover, the nanowires grow as a high density array and are uniformly distributed over the entire substrate. For the samples in Figure 6-1, the length of the nanowires was approximately 6 μm. At high magnification, nanowires with smooth hexagonal facets can be observed. As expected, no catalyst particles are observed on the tips of the nanowires, which indicates that the nanowire growth does not proceed by a vapor-liquid-solid mechanism. The composition of the nanowires was investigated by Energy-dispersive X-ray (EDX) analysis. The results indicate that the nanowires are composed of zinc and oxygen with no significant impurities found in the EDX data.

The orientation and crystalline properties of the ZnO nanowires was characterized with XRD and transmission electron microscopy (TEM). Figure 6-2 shows the x-ray diffraction patterns of ZnO nanowires grown in pure argon. Two sharp ZnO (002) and (004) peaks with high intensity dominate the diffraction patterns, consistent with ZnO nanowires that are highly oriented along the *c*-axis. A relatively weak ZnO (110) peak is also observed. The patterns can be indexed to the ZnO hexagonal wurtzite structure with lattice constants of  $a=0.325$  nm and  $c=0.512$  nm. Additional structure characterization was carried out using HR-TEM. Figure 6-3(a) shows low magnification images for parallel nanowires that were mechanically removed from the substrate. The nanowires have a relatively uniform diameter (50–90 nm) and are a few micrometers in length. Note that no metal particles are observed at the top or bottom of the nanowires. These results are consistent with the FE-SEM observations as shown in Figure 6-1.

The image in Figure 6-3(b) shows that the nanowires are tapered and faceted at the ends. In order to further investigate the structure, selected-area electron diffraction was performed on a single nanowire. The pattern is consistent with a single crystal wurtzite structure. Figure 6-3(d) shows the high-resolution transmission electron microscopy images, showing that the nanowire is structurally uniform and contains few defects. In the high resolution images, lattice fringes show lattice spacing of 0.26 nm, which corresponds to 1/2 the *c*-axis lattice constant, confirming that the ZnO nanowires are oriented in the *c*-axis direction. Since the (001) planes of ZnO are the closest packed plane, stacking along the *c*-axis is the most energetically favorable. This growth direction is commonly observed in ZnO nanowires.<sup>71</sup>

The morphology and microstructure of the nanowires were examined as a function of growth conditions, in particular total background pressure, oxygen pressure, and substrate temperature. Figure 6-4 shows the FE-SEM images of samples deposited in pure oxygen at O<sub>2</sub> pressures ranging from 150 to 500 mTorr. The growth temperature was 800°C. All samples were grown on a thin template layer of ZnO on the sapphire substrate. At a growth pressure of 150 mTorr O<sub>2</sub>, the deposited ZnO consists of a continuous, smooth thin film as seen in Figure 6-4(a) and (b). Increasing the oxygen pressure to 300 mTorr resulted in the nucleation and growth of oriented microcrystals with hexagonal facets as seen in Figure 6-4(c). The size of microcrystals varies from 1 to 5 μm, growing normal to the substrate. When the pressure was further increased to 500 mTorr, the growth mode undergoes a transition from continuous thin film to highly aligned nanowire growth. A highly dense array of nanowires with hexagonal facets is observed. The nanowires are oriented with their *c*-axis perpendicular to the surface with relatively uniform diameter and density. Note that very few nanowires were obtained when the pressure was further increased to 1 Torr.

In addition to pressure, the effect of substrate temperature in the formation of nanowires was also examined. Figure 6-5 shows the cross-sectional and plan-view FE-SEM images of ZnO nanorods grown at an oxygen pressure of 500 mTorr at temperatures ranging from 550–800°C. At 550°C (Figure 6-5(a) and (b)), the diameters of the nanowires are on the order of 500 nm. At 750°C, the diameter is reduced to approximately 150 nm. At 800°C, the diameter of the nanowires is less than 100 nm. One explanation for this temperature dependency of nanowire diameter relates to surface diffusion. A higher surface mobility is realized for higher growth temperatures. High temperatures provide sufficient energy for deposited species from the ablation target to migrate to low energy sites for growth. If substrate temperature is low (<650°C), surface species will remain at higher energy sites, thus yielding large diameter nanowires or simply rough, granular films. In order to achieve one dimensional growth, it is important to provide sufficient surface mobility for species to reach low energy nucleation sites.

The variation in optical properties for the ZnO nanowires grown in different background ambients was investigated using room temperature photoluminescence measurements. Figure 6-6(a) shows the typical room temperature PL spectra of the ZnO nanowires grown at 800°C and 500 mTorr oxygen. A weak near-band-edge-emission in the UV region at 380 nm and a strong broad band deep-level-emission at 520 nm is observed. The green band around 520 nm is commonly attributed to deep-level or trap-state emission due to vacancies and/or interstitials of zinc and oxygen in the crystal.<sup>115</sup> In order to further investigate the origin of deep-level emissions, PL measurements were carried out for nanowires grown using the three different ambients (500 mTorr O<sub>2</sub>, 500 mTorr Ar and 175 mTorr O<sub>2</sub>/ 325 mTorr Ar mixture) at 800°C. The near-band-edge emission was higher for nanowires grown using pure argon. However, the deep-level emission was enhanced as well, suggesting a high density of defects due to the

oxygen deficient ambient. In order to investigate this further, nanowire grown using the argon/oxygen mixture were examined. The near-band-edge emission intensity increased 20 times relative to nanowires grown using pure oxygen. However, the broad green emission remained unchanged in the spectra for all cases. A plot of PL spectra for nanowires grown in the different background gases is shown in Figure 6-6(b). The results show that the deep-level emission persists in all ambients considered. The large deep-level emission was also observed on high temperature grown nanowires. Liu et al. attributed modification in ZnO nanowire PL properties to size effects and oxygen stoichiometry.<sup>200</sup> Future work will examine the transport properties of individual PLD-grown nanowires and compare their properties to those grown by other techniques.<sup>201</sup>

### 6.3.2 Synthesis and characterization of ZnMgO nanowires

Figure 6-7 depicts the FE-SEM images of the formation of high density well-aligned ZnMgO nanowires. The diameters of the nanowires are on the order of 90–120 nm. A cross-sectional FE-SEM image of the ZnMgO nanowire on the sapphire substrate as shown in Figure 6-7(d) demonstrates that most of the nanowires were grown perpendicularly to the sapphire substrate. The chemical composition of the nanowires was determined using energy dispersive spectroscopy (EDX). Figure 6-8 shows a typical EDX spectra for pulsed laser deposited ZnMgO. The elements detected are zinc, magnesium and oxygen. Structural characterization was performed by XRD. Figure 6-9 shows the diffraction pattern of ZnMgO nanowires. In addition to ZnO diffraction peaks, MgO (200) and (220) peaks were also detected. Additional peaks from ZnO were also detected. The *c*-axis lattice constants calculated from the (002) peaks for the ZnMgO nanowires (5.1656Å) is slightly smaller than ZnO nanowires (5.199Å), which may result from the stress derived from secondary phase and MgO segregation.

Further structural characterizations of the ZnMgO nanowires were performed using the HR-TEM analysis. Figure 6-10(a) illustrates TEM image of single ZnMgO nanowire. The lattice fringes images indicate the segregation of secondary phase in ZnO matrix, resulting in a polycrystalline structure with multiple growth orientations as illustrates in figure 6-10(b) and (c). Furthermore, stacking faults were also observed in the lattice images in figure 6-10(d), suggesting the inhomogeneous growth. Generally speaking, the solubility of Mg in ZnO depends on the growth methods as well as conditions. In this case, the solubility limit of Mg in ZnO has been exceeding, resulting defects and secondary phase growth.

In the efforts to increase the solubility of Mg and decrease defects of the nanowires, a different growth recipe has been used. In this approach, a 30 minutes growth period of ZnO was initially performed to provide seeding sites on the substrate, followed by switching between ZnO and  $Zn_{0.8}Mg_{0.2}O$  target over during the growth (10 minutes each). Finally end up with a 30 minute growth period of ZnO. Figure 6.11(a)-(c) show the FE-SEM images of as-grown samples. Note that small circles with diameter approximately 20–90 nm were found on the facets of naowires. The ZnMgO nanowires have uniform diameter and well-aligned along *c*-axis as shown in Figure 6-11(d). In contrast with previous case, XRD shows only *c*-oriented ZnO peaks in Figure 6-12. No MgO or secondary phase peaks were found suggests a higher solubility and incorporation of Mg into Zn sites. Furthermore, the *c*-axis lattice constants calculated from the (002) peaks for the cored ZnMgO nanowires (5.1932 Å) is very close to ZnO nanowires (5.199 Å), which suggests a smaller stress inside the sample.

In order to further investigate the structural properties, HR-TEM was used to characterize the sample. The HR-TEM images in Figure 6-13 clearly reveal the core-sheath structure of the nanowires. In the Figure, the nanowire displays a difference in brightness intensity between the

core and sheath regions. The contrast across the diameter of the nanowire is predominantly mass contrast, reflecting a difference in average atomic number ( $Z$ ) of the core and sheath region. The darker core region contains more Zn, while the lighter sheath region more Mg. The core and sheath is approximately 80 nm and 40 nm in diameter respectively. The selected-area diffraction pattern shows that the nanowire is with single crystal wurtzite structure, which is consistent with XRD results. The HR-TEM lattice fringes image in Figure 6-13(d) confirmed the single crystal structure. No segregated cluster of impurity phase appears via HR-TEM observation. The absence of the diffraction peaks of MgO in the XRD and SAD patterns suggest that the Mg incorporated within the ZnO nanowires by means of substituting Zn. There has been no investigation of the transport properties of the heterostructured nanowires. They represent opportunities to examine transport in electron-confining structures due to the larger band-gap ZnMgO sheath.

### 6.3.3 Synthesis and characterization of SnO<sub>2</sub> nanorods

The initial characterization focused on the phase formation and microstructure of SnO<sub>2</sub> materials deposited at high temperatures and pressures. The XRD pattern shown in Figure 6-14(a) is for SnO<sub>2</sub> deposited on silicon at a temperature of 800°C and oxygen pressure of 500 mTorr. All of the peaks could be indexed to the tetragonal rutile structure of SnO<sub>2</sub> with lattice constants of  $a=4.3738 \text{ \AA}$  and  $c=3.188 \text{ \AA}$  from JCPDS file (41-1445). No impurity or secondary phase peaks were observed. The nanorods show no preferred crystalline texture when deposited on silicon. Figure 6-14(b) shows the XRD results for SnO<sub>2</sub> deposited on sapphire using similar deposition conditions. In this case, the deposited material is strongly  $a$ -axis textured. This is consistent with an epitaxial relationship between SnO<sub>2</sub> and  $c$ -plane sapphire. The chemical composition of the deposited material was determined using energy dispersive spectroscopy

(EDX). Figure 6-15 shows a typical EDX spectra for pulsed laser deposited SnO<sub>2</sub>. The only elements detected are tin and oxygen.

The morphology and microstructure of the deposited SnO<sub>2</sub> were characterized by FE-SEM and HR-TEM. Figure 6-16(a) shows a typical top-view FE-SEM image of the as-grown film deposited at high temperature and background pressure on a silicon substrate. Nanorod growth is observed. The materials grow by a columnar growth mode that is maintained for the duration of the deposition. As shown in Figures 6-16(b)–(d), an aligned SnO<sub>2</sub> nanorod array is evident in cross-sectional FE-SEM. The diameters of the SnO<sub>2</sub> nanorods are on the order of 50–90 nm. The nanowire length is 1.5 μm for the sample considered. Figure 6-17 shows FE-SEM micrographs for SnO<sub>2</sub> films deposited on *c*-plane sapphire. For materials nucleated directed on the sapphire at high pressure (~ 500 mTorr), a SnO<sub>2</sub> nanorod microstructure was observed as seen in Figure 6-17(a) and (b). Interestingly, if a thin nucleation layer is initially deposited at low pressure (50 mTorr) with high pressure deposition following, the microstructure does not yield distinct nanorods. Instead, a dense, small grain polycrystalline film is observed as seen in Figure 6-17(c) and (d). The lower pressure results in a higher density of densely spaced nucleation sites.

The HR-TEM image of laterally aggregated SnO<sub>2</sub> nanorods grown on silicon is shown in Figure 6-18(a). The selected area electron diffraction (SAD) pattern from an individual nanorod with a  $[10\bar{2}]$  zone axis is shown in Figure 6-18(b). The SAD data indicates that the individual as-grown SnO<sub>2</sub> nanorods are single crystals with the rutile structure. The HR-TEM image in Figure 6-18(c) shows lattice fringes near the edge of the nanorods indicating an interplanar spacing is 2.3 Å, corresponding to the (100) plane of a rutile SnO<sub>2</sub> lattice. The lattice fringes in Figure 6-18(d) show the two distinct spacing of 3.4 Å and 3.2 Å corresponding to (110) and (001) planes respectively.

Since no catalyst was used in the synthesis, the growth of SnO<sub>2</sub> nanorods cannot be explained by a VLS mechanism. Instead, the nanorods grow via a simple columnar growth mechanism. Note that the high background pressure (500 mTorr) was necessary in order to achieve small grain columnar growth that persists over the duration of the deposition. In pulsed laser deposition at such high pressures, the interaction between plume and gas molecules reduces the plume-induced kinetic energy of the ablated species to negligible values. While the initial nucleation of SnO<sub>2</sub> on the silicon substrate follows a three-dimensional island growth mechanism, subsequent growth proceeds by adhesion to existing sites, yielding one-dimensional vapor-solid growth of SnO<sub>2</sub> nanorods. The formation of distinct nanorods was also favored for deposition on silicon where epitaxy does not occur.

#### **6.3.4 Synthesis and characterization of VO<sub>2</sub> nanowires**

The XRD pattern shown in Figure 6-19(a) is for VO<sub>2</sub> nanowires deposited on silicon at a temperature of 600°C and argon pressure of 500 mTorr. All of the peaks could be indexed to the monoclinic B phase of VO<sub>2</sub> with lattice constants of  $a=12.03 \text{ \AA}$ ,  $b=3.693 \text{ \AA}$ ,  $c=6.42 \text{ \AA}$  and  $\beta=106.6^\circ$  from JCPDS file (31-1438). No impurity or secondary phase peaks were observed. The nanowires show no preferred crystalline texture when deposited on silicon. The chemical composition of the deposited material was determined using energy dispersive spectroscopy (EDX). Figure 6-20 shows a typical EDX spectra for pulsed laser deposited VO<sub>2</sub>. The only elements detected are vanadium and oxygen, which confirmed the catalyst-free growth.

The morphology and microstructure of the deposited VO<sub>2</sub> were characterized by FE-SEM and HR-TEM. Figure 6-21 show typical top-view FE-SEM images of the as-grown nanowires deposited at 600°C and relative high background pressure (500 mTorr argon) on a silicon substrate. As shown in figure 6-21(a), a typical low-magnification FE-SEM image indicates that the as-synthesized products consists a large quantity of nanowires with uniform diameter and

very high aspect ratio. The materials randomly nucleate on the surface and maintained for the duration of the deposition. As shown in Figures 6-21(b)-(d), high density VO<sub>2</sub> nanowires are evident in top view FE-SEM. The diameters of the VO<sub>2</sub> nanowires are on the order of 90–200 nm. The nanowire length is up to 50 μm for the sample considered. Figure 6-21(f) shows side-view FE-SEM micrographs for VO<sub>2</sub> nanowires grew on silicon, which confirmed the randomly nucleation growth. For materials nucleated directed on the sapphire at same condition, similar microstructure was observed but with slightly larger diameters. This suggests the growth may not be related to lattice mismatch between substrates. Although the exact growth mechanism is still unclear, we suggest the growth follows a diffusion-based vapor-solid mechanism. Interestingly, no nanostructures were observed when using a lower background pressure. The high background pressure may still play an important role in the formation of VO<sub>2</sub> nanowires in this case. Further investigations are required to clarify the interplay between the surface energetics and surface effects.

The HR-TEM image of as-grown VO<sub>2</sub> nanowires grown on silicon is shown in Figure 6-22. The selected area electron diffraction (SAD) pattern from an individual nanowire is shown in Figure 6-22(b). The SAD data indicates that the individual as-grown VO<sub>2</sub> nanowires are single crystals with the monoclinic structure. The HR-TEM image in Figure 6-22(c) shows lattice fringes near the edge of the nanowires indicating an interplanar spacing is 3.05 Å, corresponding to the (002) plane of a monoclinic VO<sub>2</sub> lattice. The lattice fringes in Figure 6-22(d) show the two distinct spacing of 3.62 Å and 3.05 Å corresponding to (110) and (002) planes respectively.

The optical properties of as-grown VO<sub>2</sub> nanowires were investigated by room temperature photoluminescence. Figure 6-23 shows that the VO<sub>2</sub> nanowires, in comparison with VO<sub>2</sub> thin films grew at low oxygen background pressure (30 mTorr) and same temperature (600°C),

exhibit a broad PL peak centered at 2.44 eV. The broad PL peak might be related to the crystalline defects induced during the growth. The defects might be caused by the high background pressure, resulting oxygen vacancies. On the other hand, no emission was observed from VO<sub>2</sub> thin film sample grown at low oxygen pressure. This suggests the emission is related to growth pressure and dimension of VO<sub>2</sub> material. Low temperature PL is required to investigate the origin of the peak.

To further investigate the transport properties of VO<sub>2</sub> nanowires, a single nanowire device has been fabricated on a 1000 Å thick thermally grown SiO<sub>2</sub>/Si substrate. The fabrication process is similar as described in Chapter 5. The electrodes (Ti/Al/Pt/Au 200/800/400/800 Å) were deposited by e-beam evaporation at room temperature without further annealing. Figure 6-24(a) shows the FE-SEM image of single nanowire device. The distance between the two electrodes was 13 μm. The measurement was performed in air ambient. At room temperature, the device exhibited linear, symmetric current-voltage (I-V) characteristics as shown in figure 6-24(c). The linear dependence can be observed in relatively wide current range from approximately 2.25 to -2.25 μA, indicating good Ohmic contacts between the nanowire and electrodes. The diameter size (160 nm) and the length (13 μm) of the VO<sub>2</sub> nanowire can be measured through FE-SEM image as shown in figure 6-24(a) and (b), and the resistivity of the VO<sub>2</sub> nanowire is calculated to be  $1.471 \times 10^3 \Omega \text{ m}$  at room temperature.

#### 6.4 Summary and Conclusions

A high-pressure assisted pulsed laser deposition has been applied to fabricate a variety of metal oxide nanowires (ZnO, ZnMgO, SnO<sub>2</sub> and VO<sub>2</sub>) without catalysts. Vertically well-aligned ZnO and Zn<sub>x</sub>Mg<sub>1-x</sub>O arrays were grown on *c*-sapphire substrates at 600–800°C. The nanowires growth proceeds without employing catalysts for nucleation, although an epitaxial ZnO thin film template is necessary in order to achieve uniform alignment. The ZnO nanowire diameters are as

small as 50–90 nm, with diameters largely determined by growth pressure and temperature. The SnO<sub>2</sub> nanowires with single crystal rutile structure were grown on silicon substrates at 700°C. The growth of SnO<sub>2</sub> nanorods on silicon begins as small grain columnar with a subsequent vapor-solid growth mechanism at high pressure yielding one-dimensional SnO<sub>2</sub> nanorods. The diameter and length of the SnO<sub>2</sub> nanorods are approximately 50–90 nm and 1.5 μm, respectively. High aspect ratio monoclinic VO<sub>2</sub> nanowires grew laterally on the silicon and *c*-sapphire substrates at 600°C. The nanowires randomly nucleate on the surface with the diameter of 90–200 nm, length up to 50 μm. A broad emission peak was observed at 510 nm by room temperature photoluminescence measurement. A single nanowire device has been fabricated to measure transport properties of single VO<sub>2</sub> nanowire. The device exhibits linear, symmetric I-V characteristics and the resistivity of the nanowire is approximately  $1.471 \times 10^3 \Omega \text{ m}$ . Further investigations such as temperature dependant transport, optoelectronic response and gas sensing measurements are needed for further device applications.

The metal oxide nanowires are attractive for numerous applications. This study provides a relative convenient approach to synthesize a wide range of metal oxide nanowires. By choosing proper growth parameters such as substrate materials, growth temperature and gas pressure, it has been demonstrated that the present approach can be extended to obtain a large family of semiconducting metal oxide nanowires. The results also suggest the possibility of growing complex metal oxide nanostructures, including tailored heterostructures, with PLD.

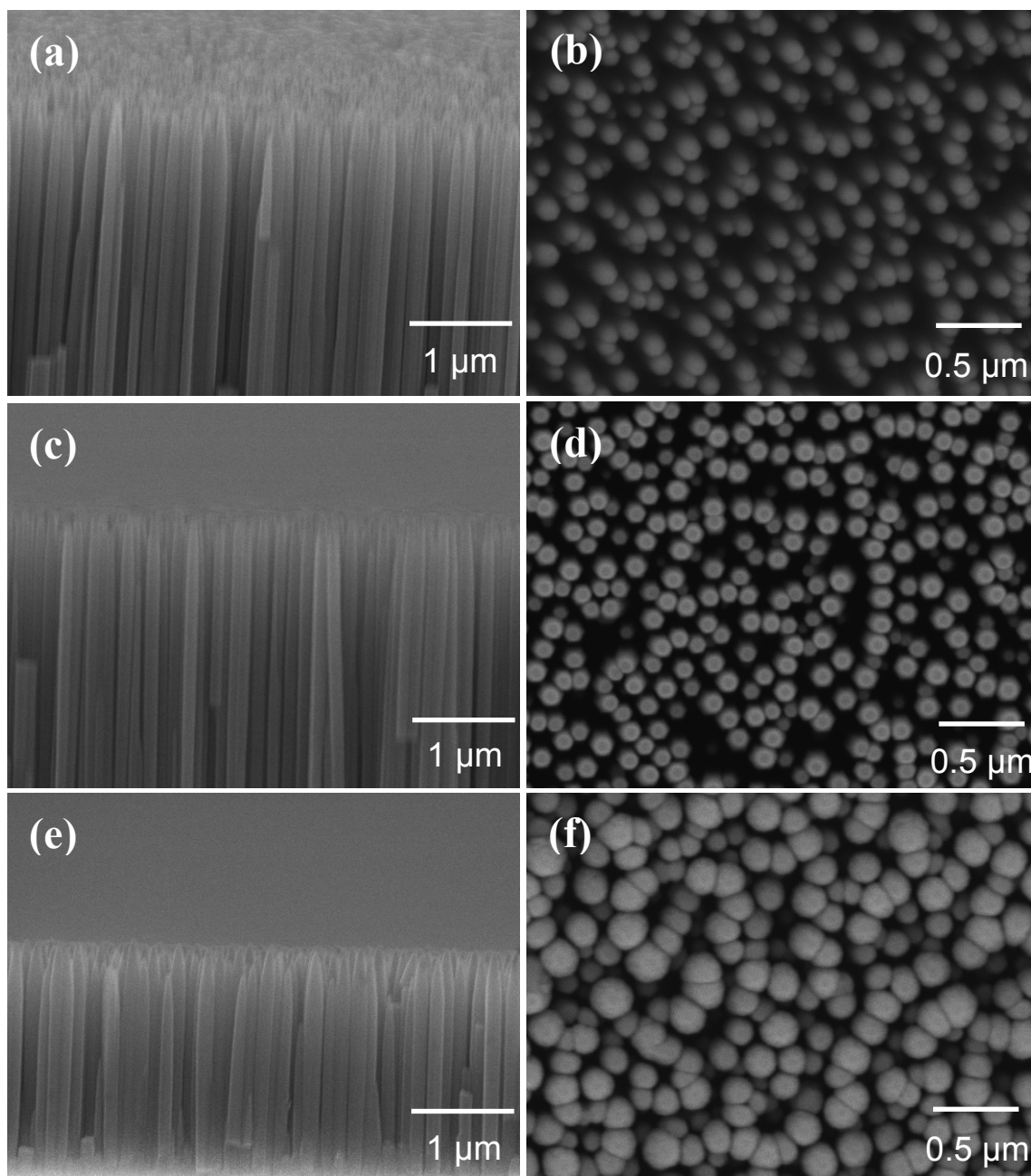


Figure 6-1. Scanning electron microscope images of well-aligned ZnO nanowires grown on a ZnO thin film template in (a), (b) 500 mTorr pure oxygen, (c), (d) 500 mTorr pure argon, and (e), (f) a 325 mTorr / 175 mTorr argon/oxygen mixture.

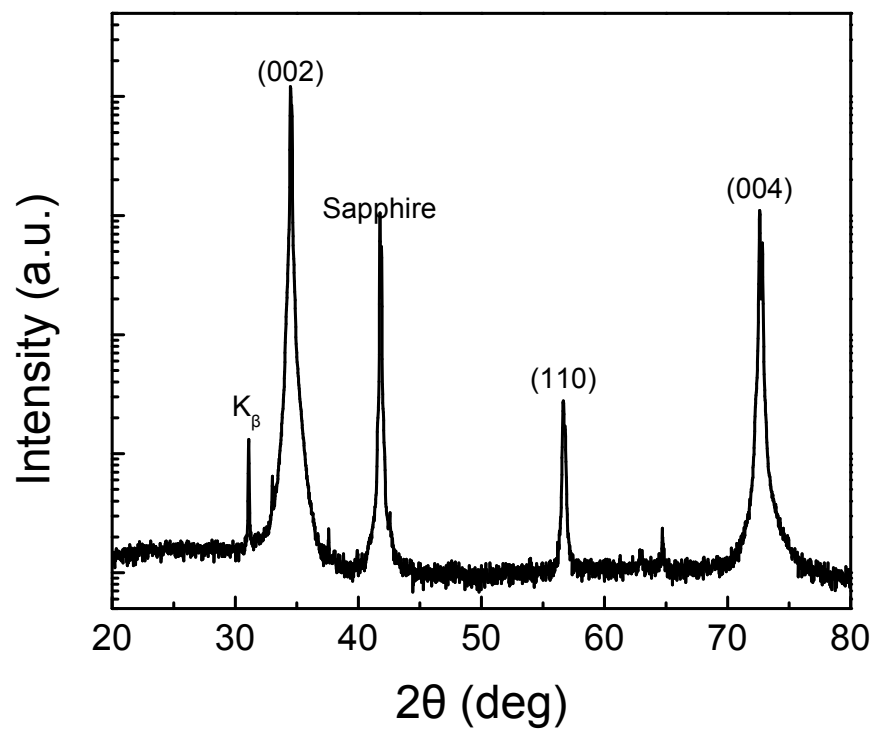


Figure 6-2. X-ray diffraction  $\theta$ - $2\theta$  scan of ZnO nanowires grown at 800°C in 500 mTorr Ar.

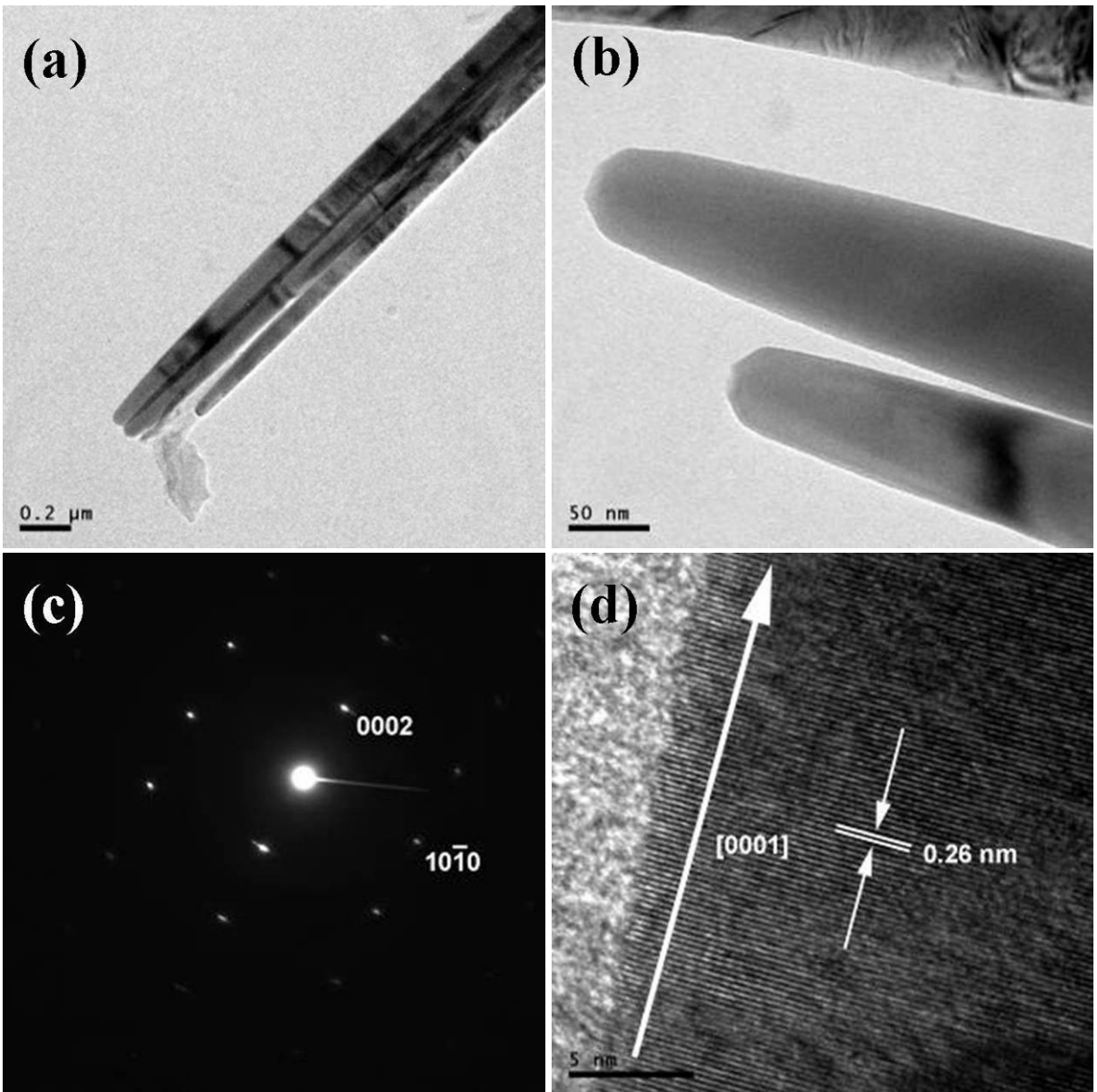


Figure 6-3. Low magnification (a), (b) TEM images of ZnO nanowires grown on a ZnO thin film at 800°C in 500 mTorr Ar. Also shown is (c) a selected area electron diffraction pattern taken from a single ZnO nanowire, showing the single crystal wurtzite structure, as well as (d) an HR-TEM image of a single ZnO nanowire showing lattice fringes.

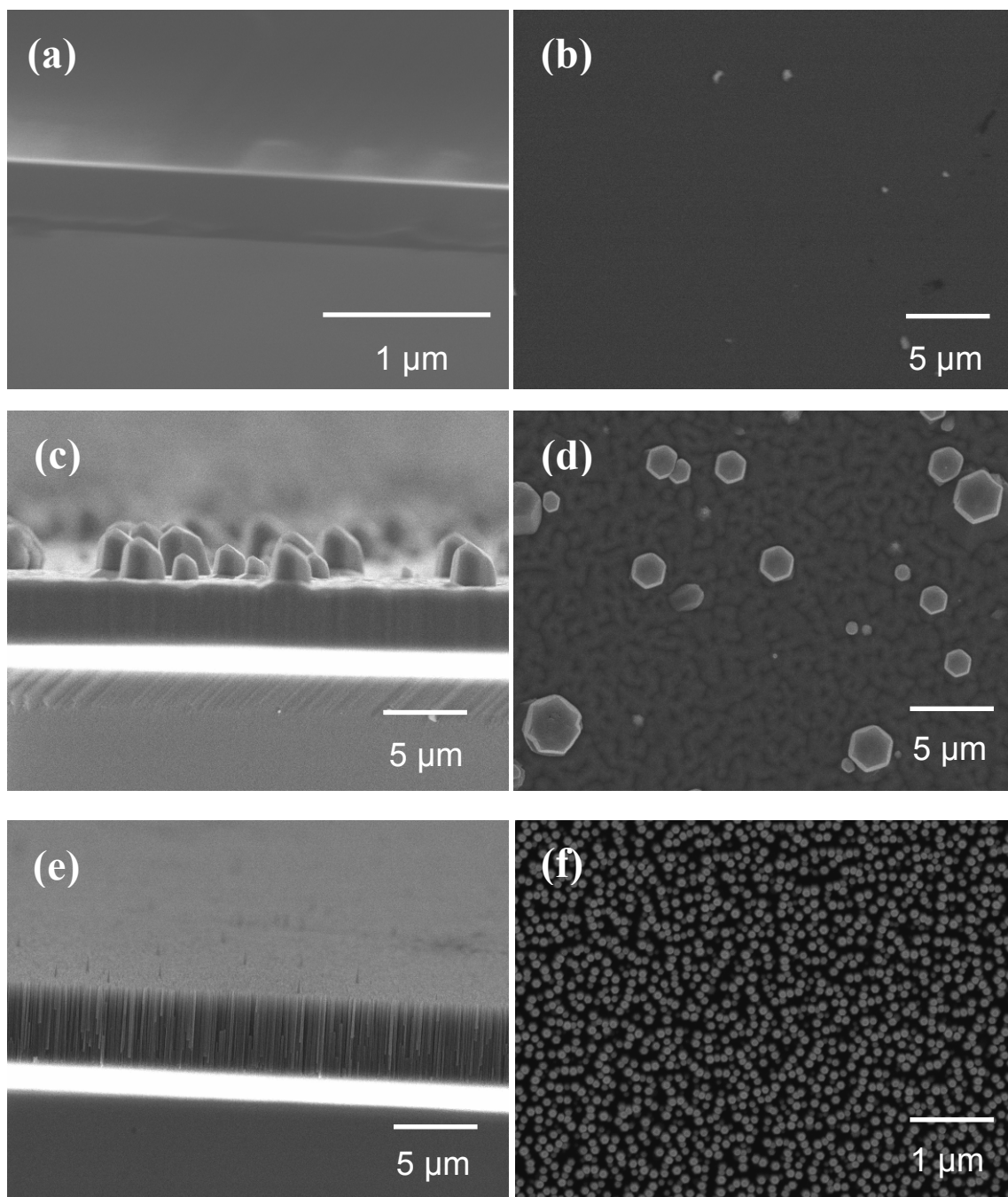


Figure 6-4. Cross-sectional and top view scanning electron microscope images of the ZnO nanowires grown at 800°C in pure oxygen with oxygen background pressures of (a), (b) 150 mTorr, (c), (d) 300 mTorr, and (e) (f) 500 mTorr.

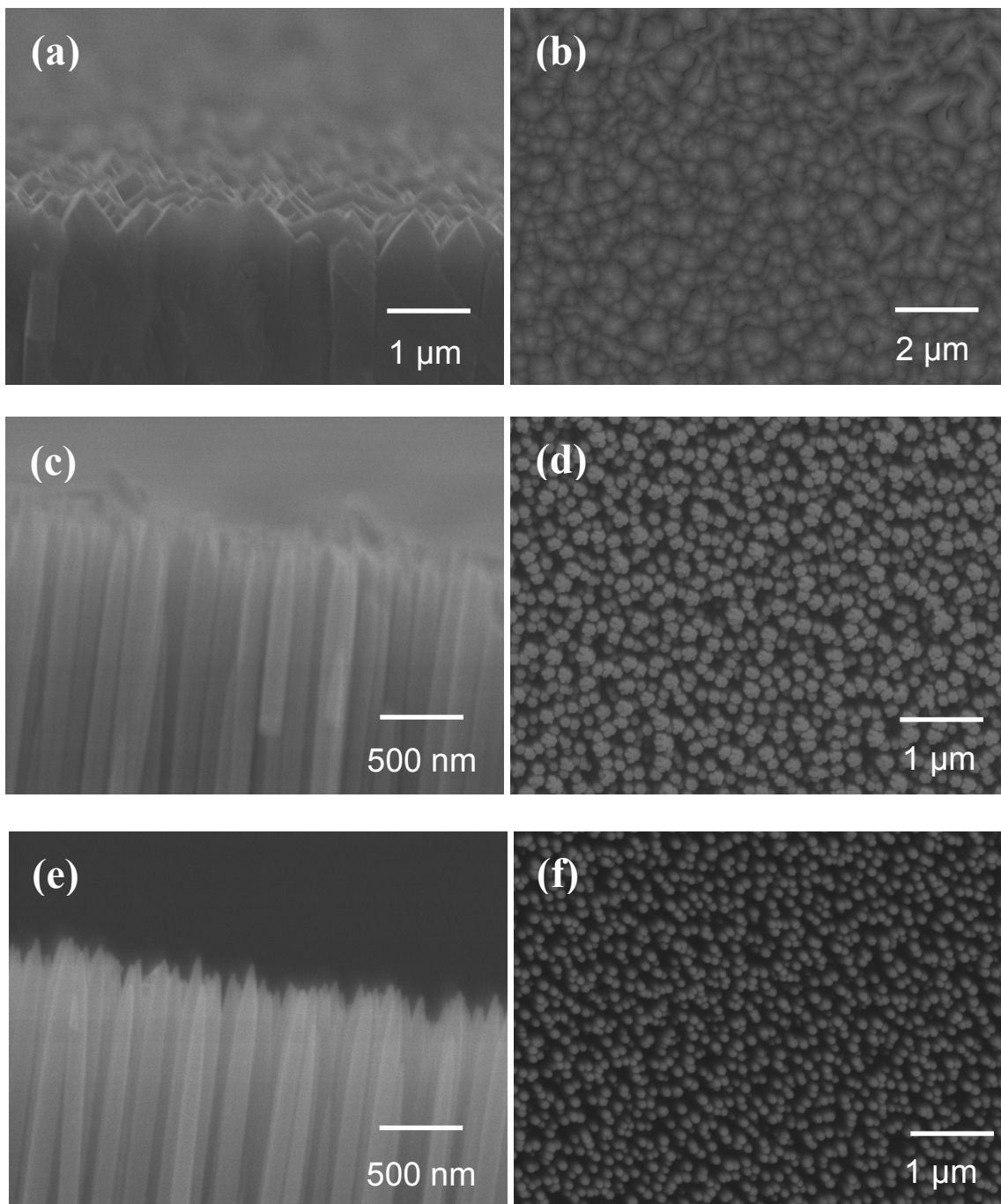


Figure 6-5. Cross-sectional and top view scanning electron microscope images of the ZnO nanorods grown under 500 mTorr of oxygen at different temperatures. (a), (b) 550°C, (c), (d) 750°C, (e), (f) 800°C, respectively

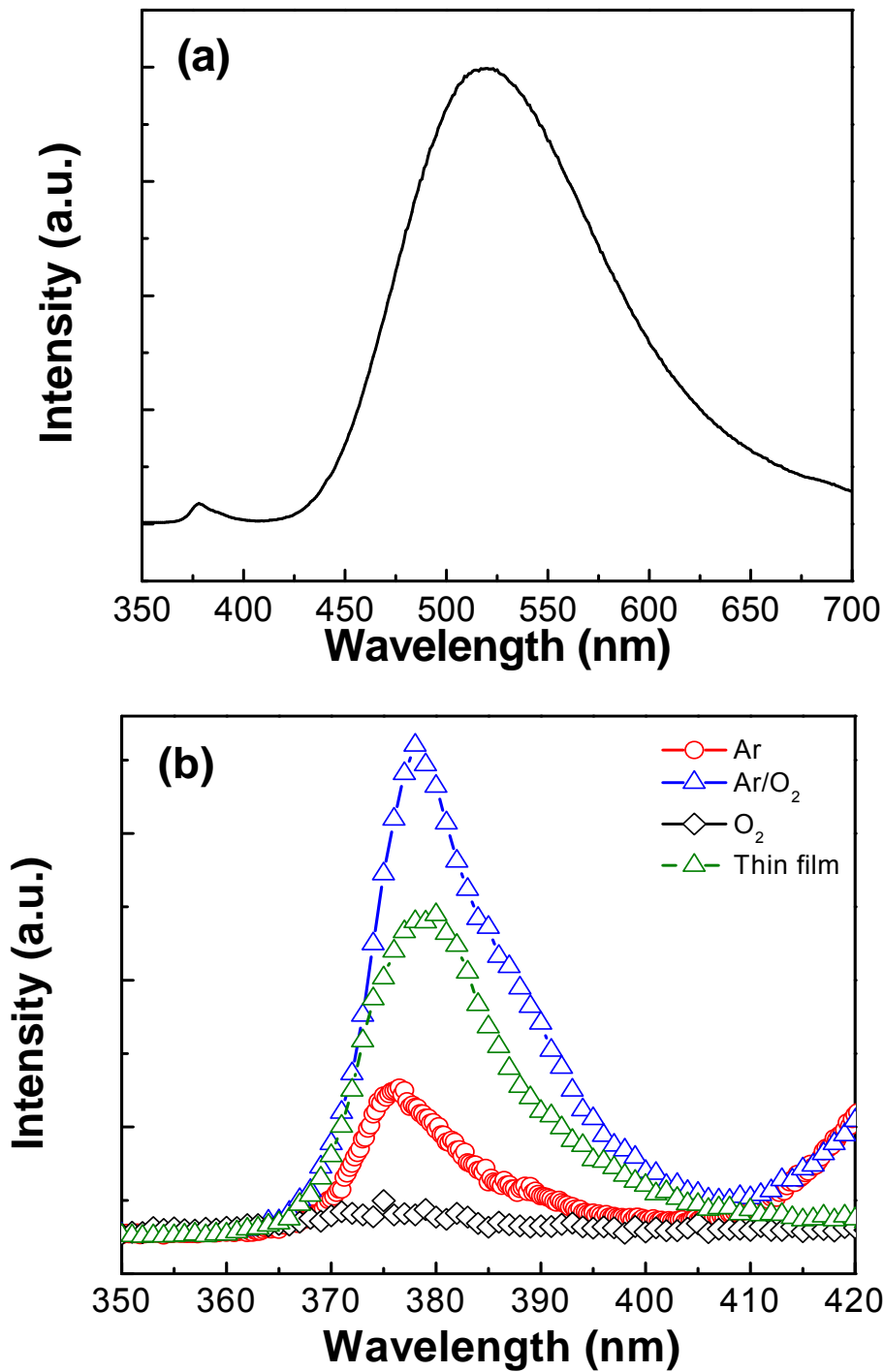


Figure 6-6. Room temperature PL spectra of ZnO nanowires and near-band-edge-emission of ZnO thin film and ZnO nanowires grown under different background ambient (a) Room temperature PL spectra of ZnO nanowires grown at 800°C in 500 mTorr oxygen (b) near-band-edge-emission of ZnO thin film and ZnO nanowires grown under different background ambient at 800°C.

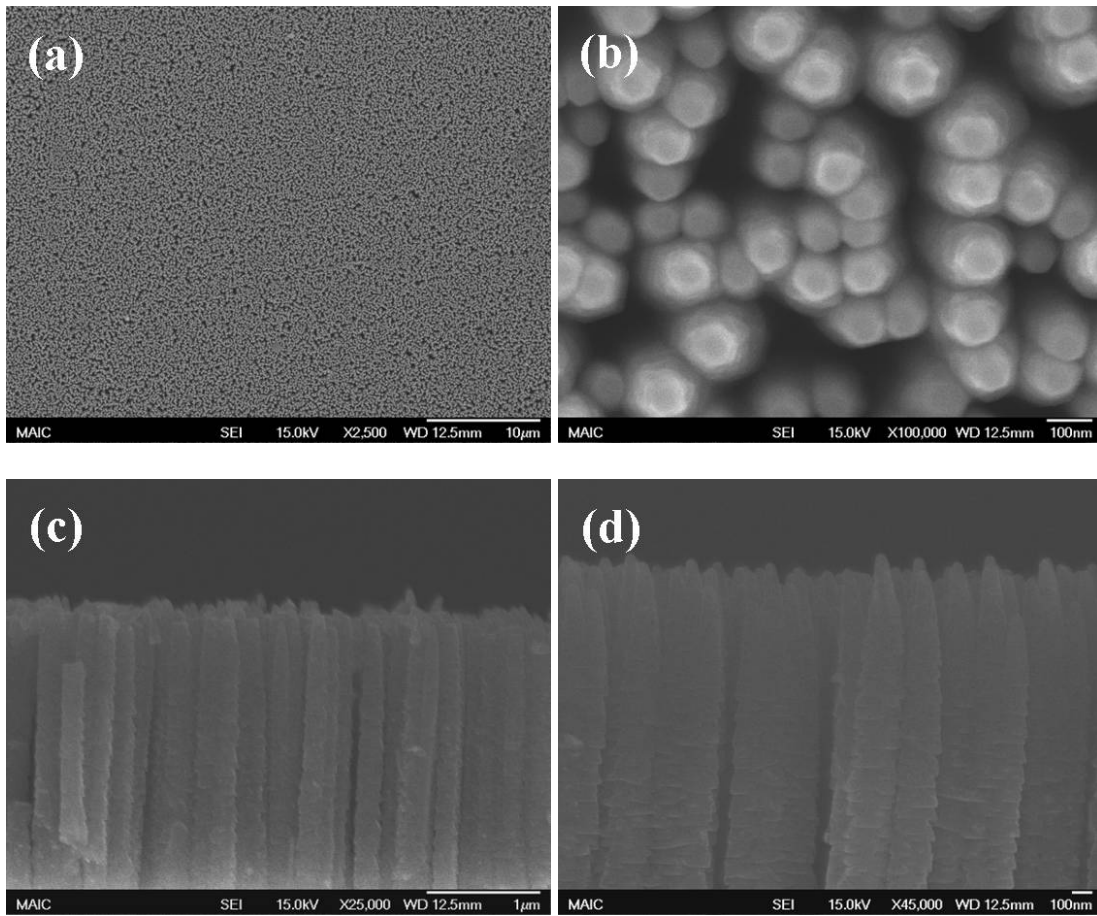


Figure 6-7. (a), (b) Top and (c), (d) cross-sectional view scanning electron microscope images of the ZnMgO nanowires grown at 800°C in 500 mTorr Ar.

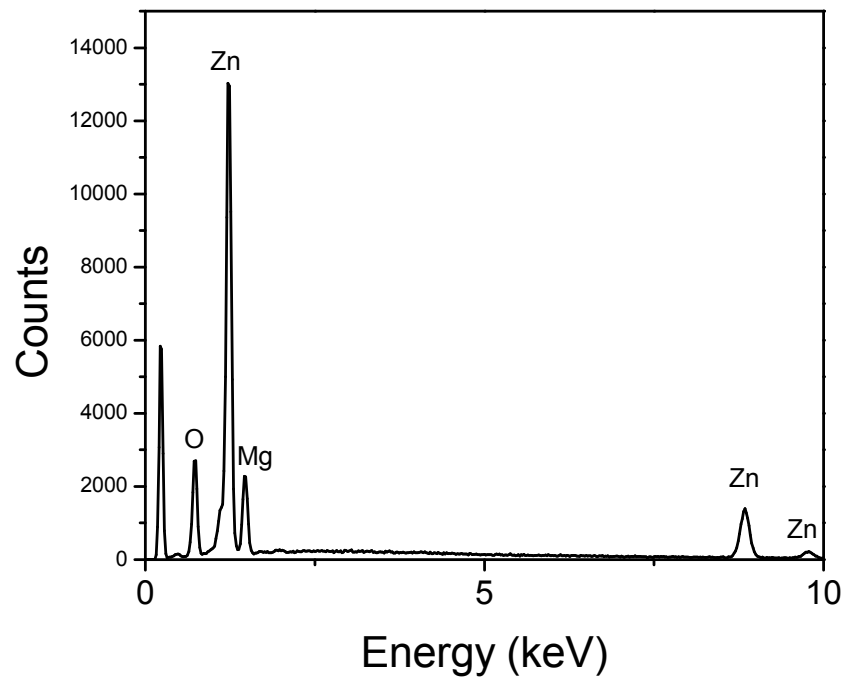


Figure 6-8. Energy-dispersive spectroscopy spectra for ZnMgO nanowires grown on sapphire at 800°C in 500 mTorr Ar.

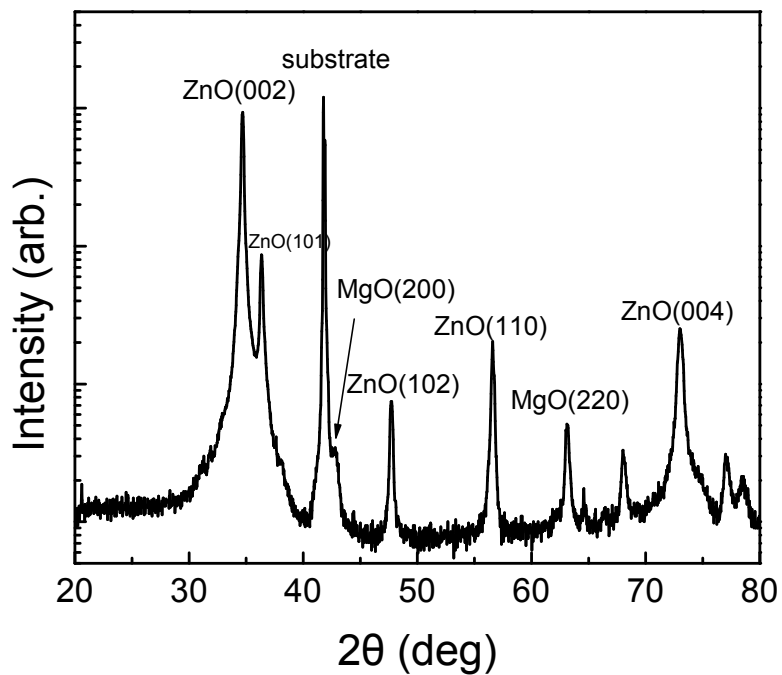


Figure 6-9. X-ray diffraction  $\theta$ - $2\theta$  scan of ZnMgO nanowires grown on sapphire at 800°C in 500 mTorr Ar.

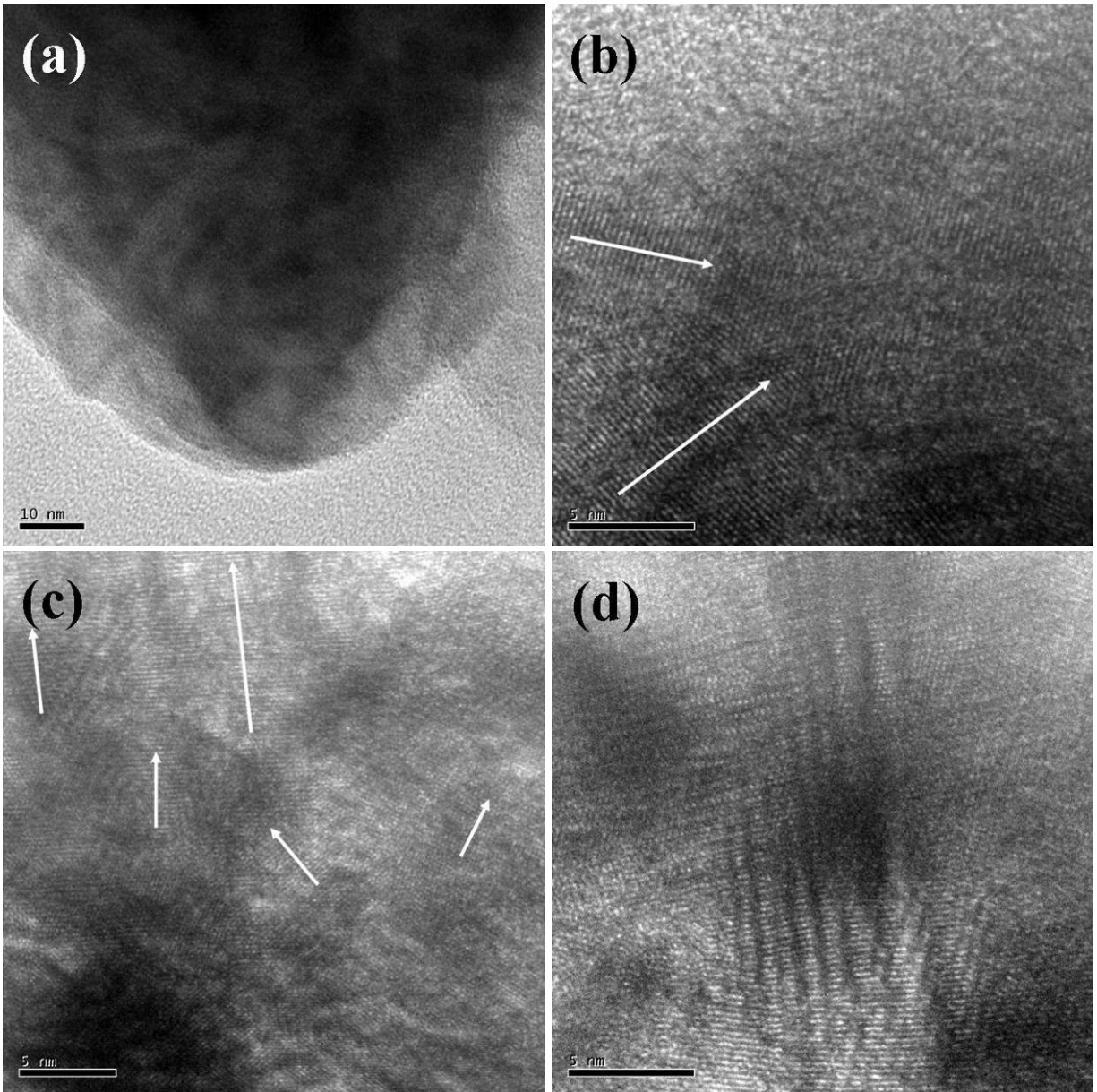


Figure 6-10. (a) High resolution transmission electron microscope image of single ZnMgO nanowire (b)-(d) HR-TEM lattice fringes images indicate the segregation of secondary phase in ZnO matrix. Defects such as stacking faults were also observed in the lattice images as well.

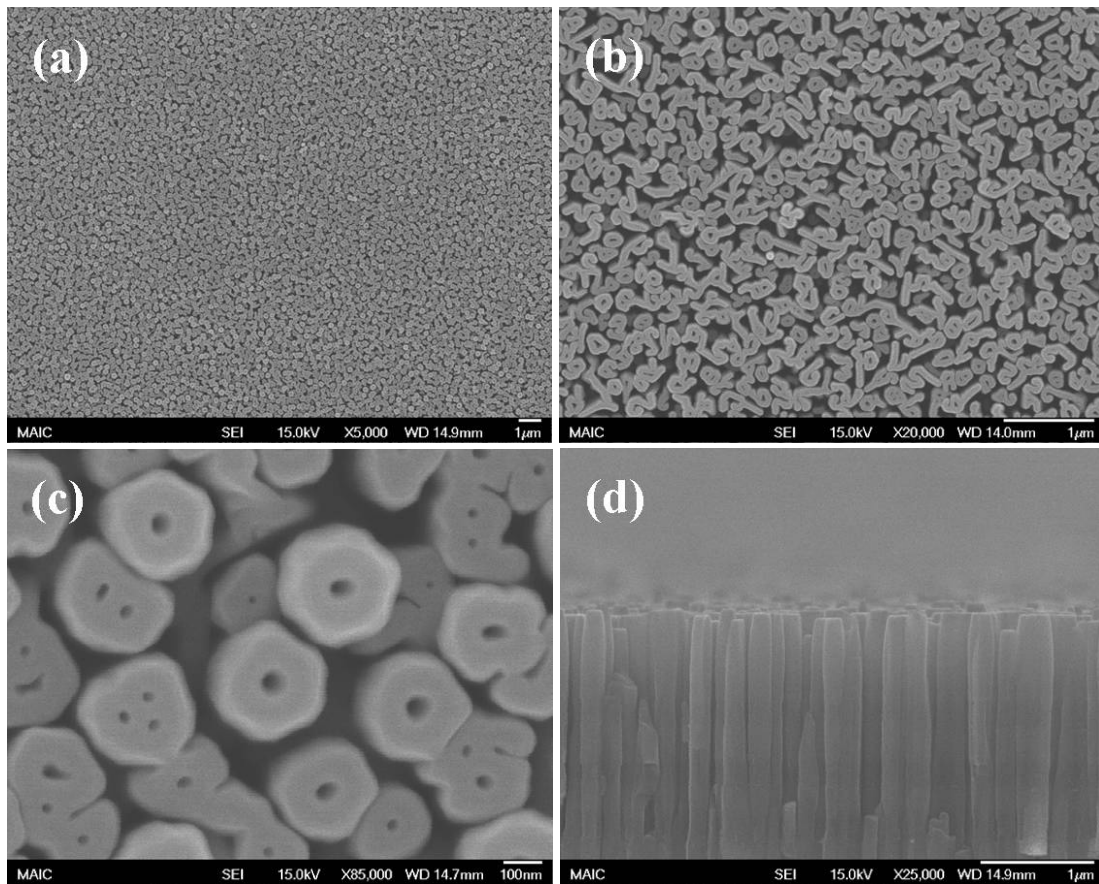


Figure 6-11. (a)–(c) Top and (d) cross-sectional view scanning electron microscope images of the cored ZnMgO nanowires grown on sapphire at 800°C in 500 mTorr Ar.

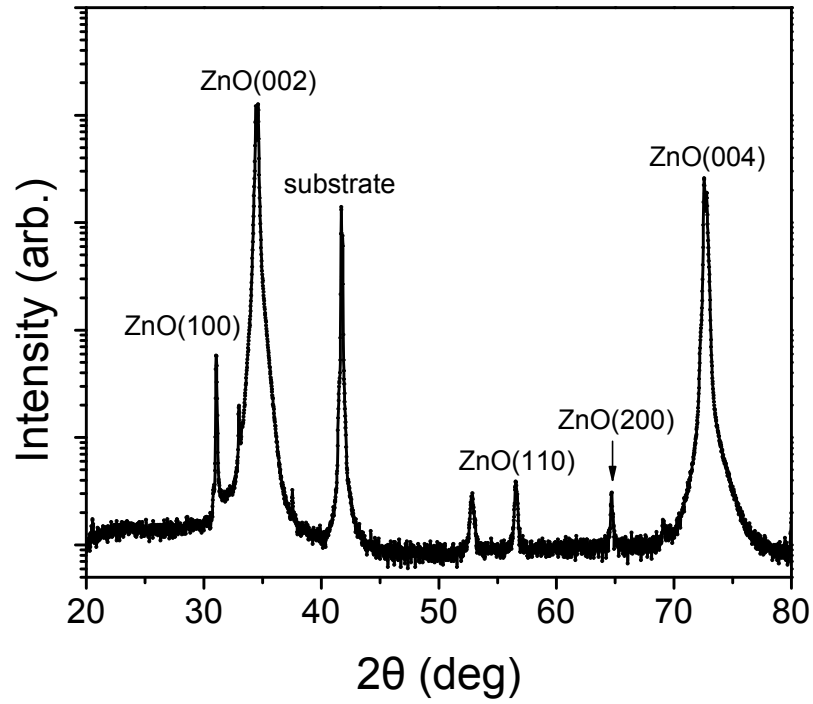


Figure 6-12. X-ray diffraction  $\theta$ - $2\theta$  scan of cored ZnMgO nanowires grown on sapphire on sapphire at 800°C in 500 mTorr Ar.

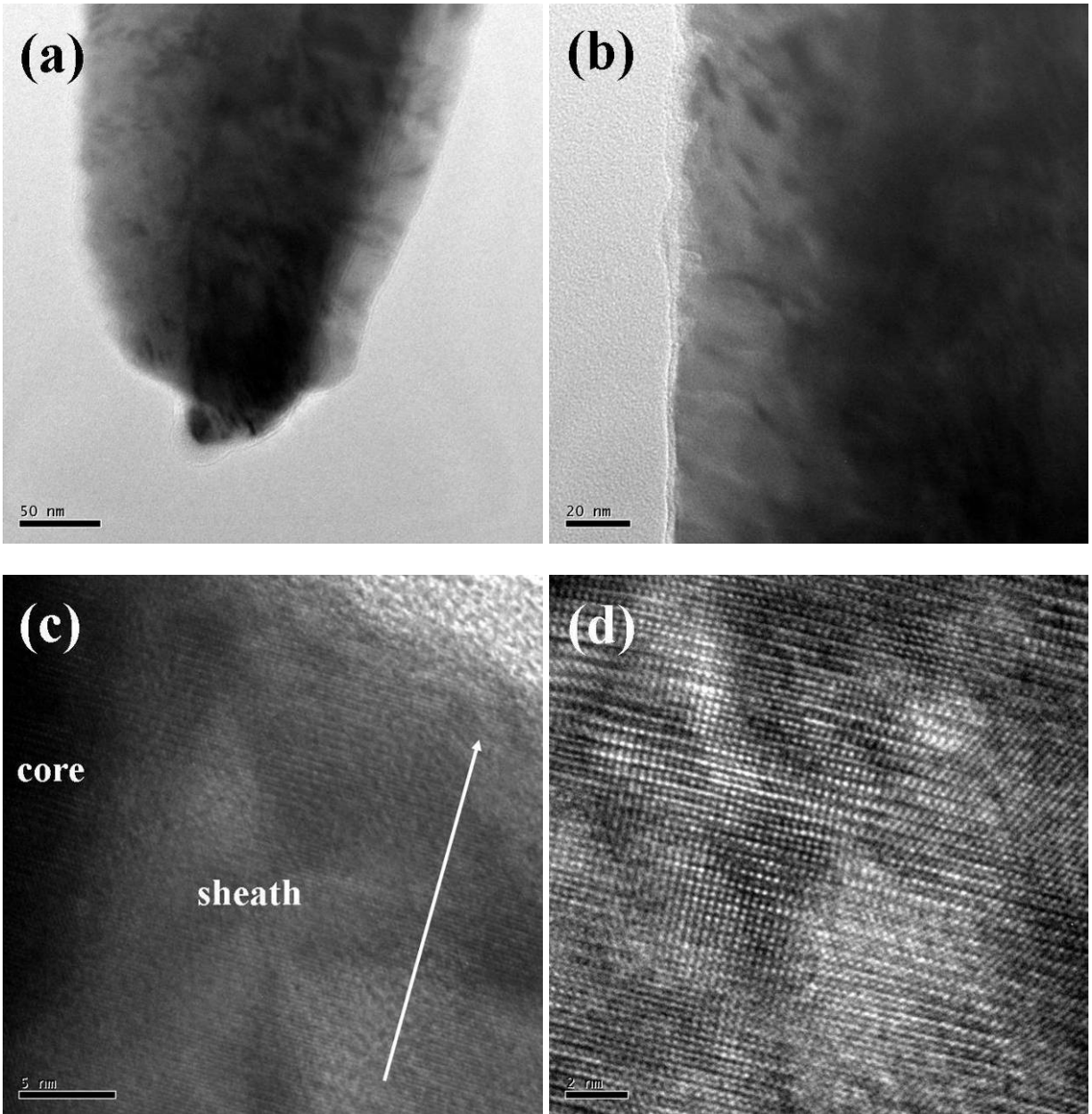


Figure 6-13. (a), (b) Low magnification TEM image of single cored ZnO/ZnMgO nanowire (c), (d) HR-TEM lattice fringes images indicate the mass contrast of core-sheath structure.

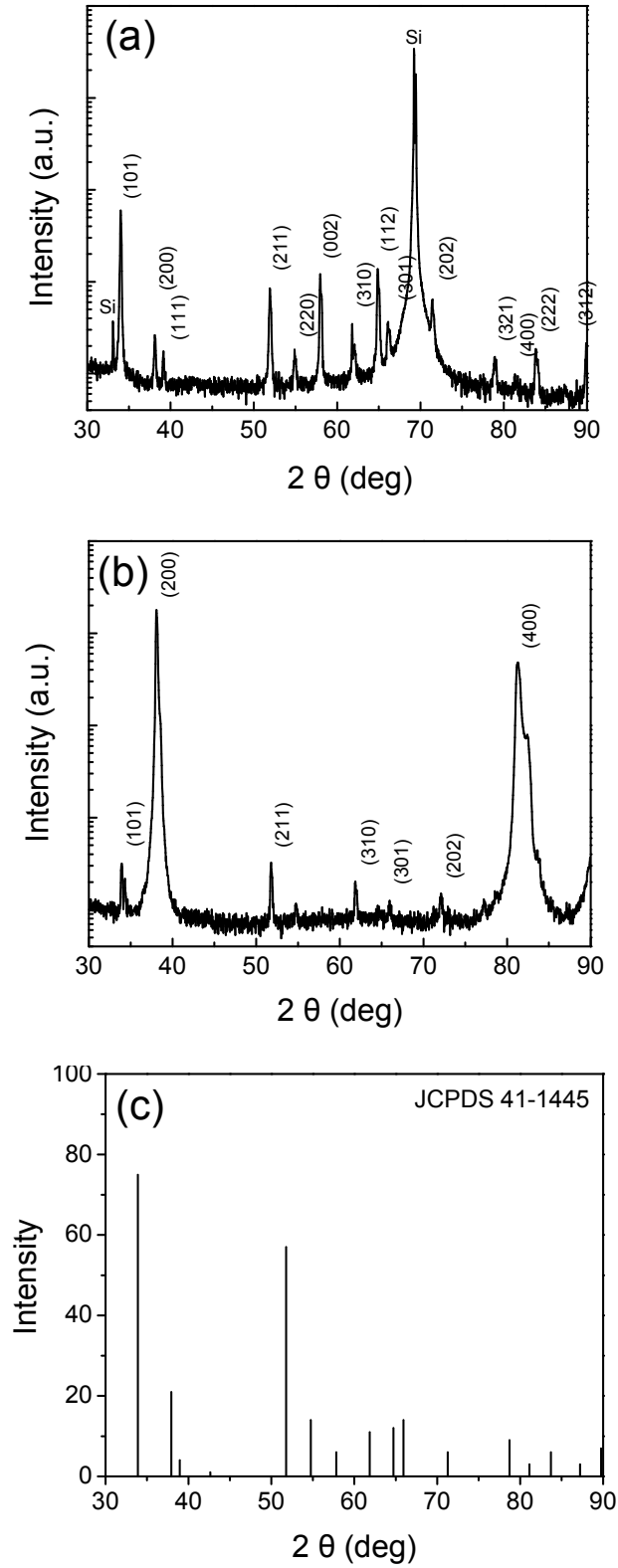


Figure 6-14. X-ray diffraction patterns of SnO<sub>2</sub> nanorods grown at 800°C in 500 mTorr oxygen on (a) silicon and (b) sapphire. (c) diffraction intensities of rutile SnO<sub>2</sub> from JCPDS file.

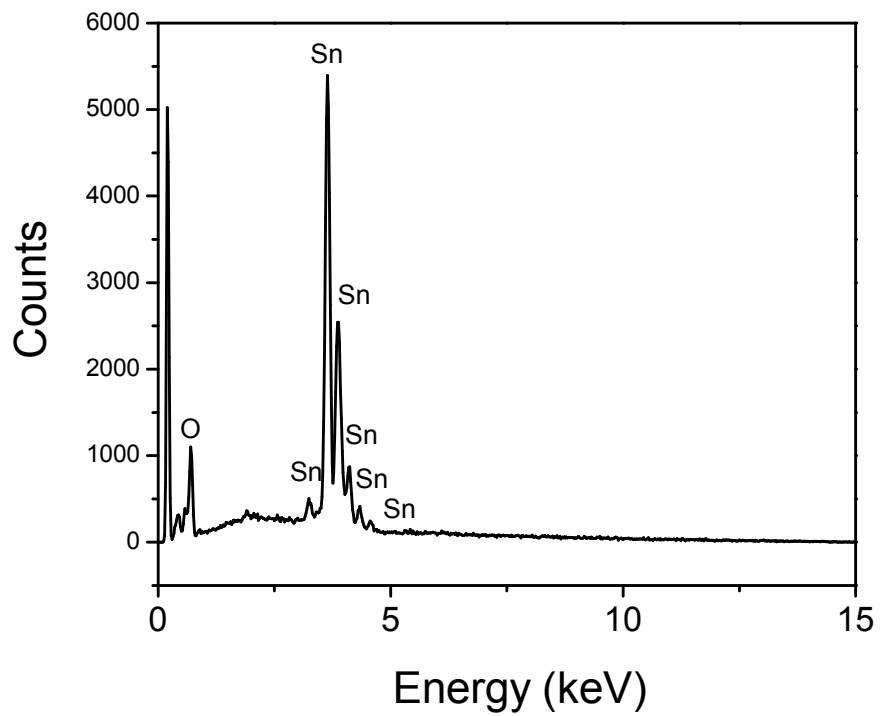


Figure 6-15. Energy-dispersive spectroscopy spectra of SnO<sub>2</sub> nanorods grown on sapphire at 800°C.

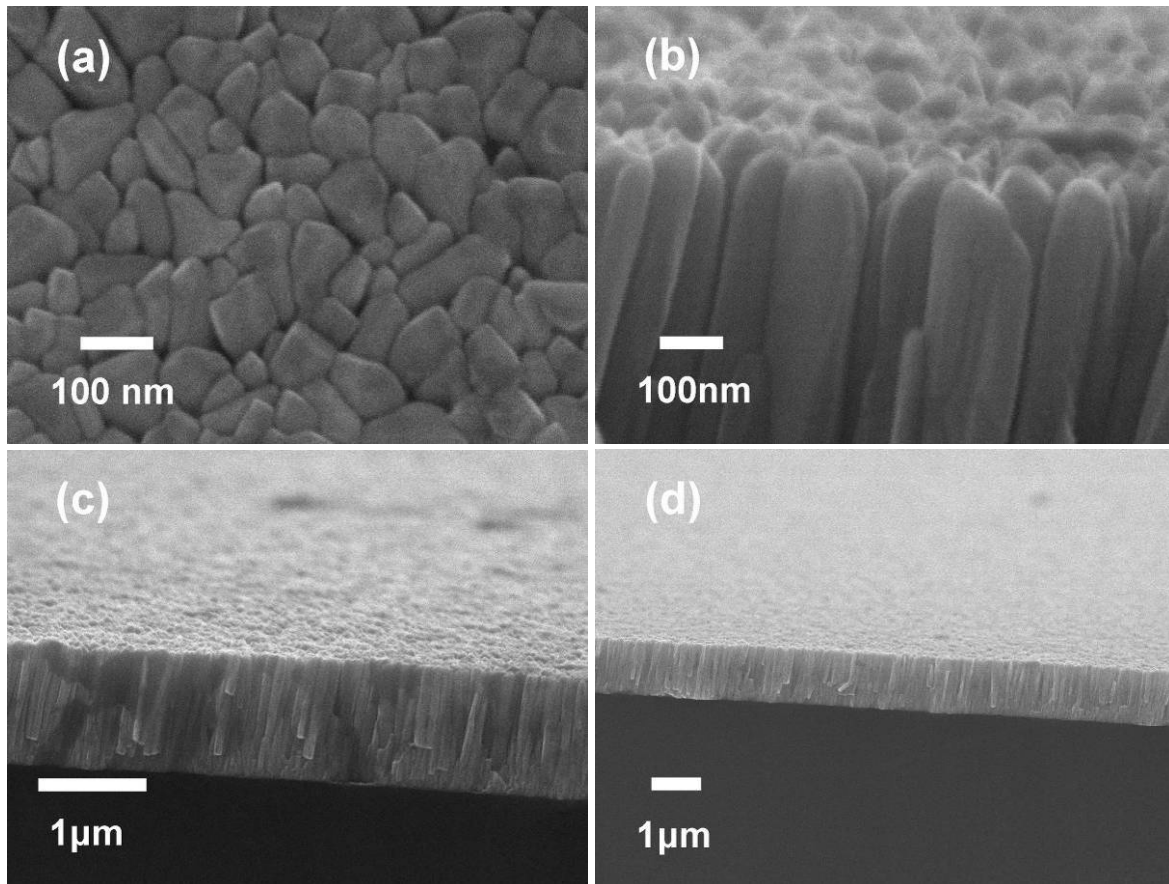


Figure 6-16. Scanning electron microscope morphologies of SnO<sub>2</sub> nanorods grown on silicon. (a) Top-view of as-grown nanorods. (b) - (d) Cross-sectional views of as-grown SnO<sub>2</sub> nanorods.

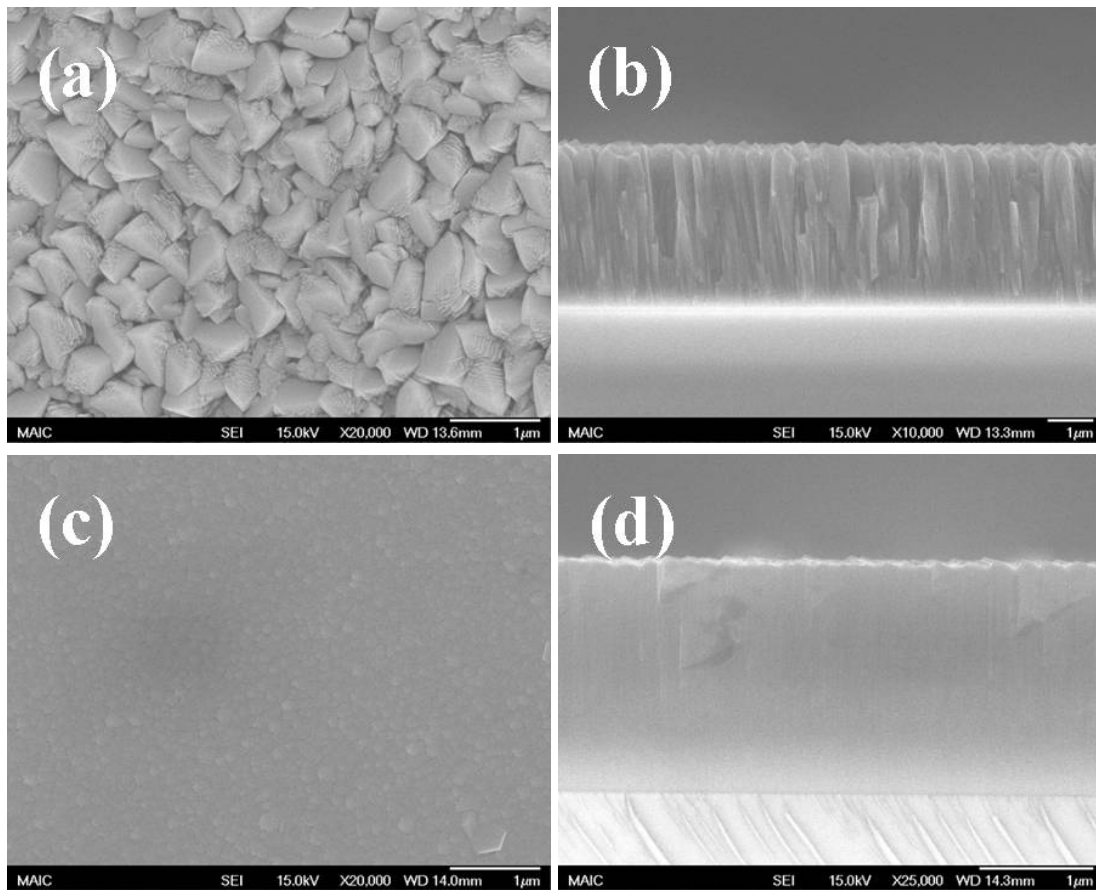


Figure 6-17. Scanning electron microscope images showing (a) the surface morphology and (b) cross-section of SnO<sub>2</sub> nanorods deposited by pulsed laser deposition at 800°C directly on sapphire. Also shown are (c) the surface morphology and (d) cross-section of SnO<sub>2</sub> deposited on sapphire under similar conditions but with a thin epitaxial SnO<sub>2</sub> nucleation layer first grown at 50 mTorr.

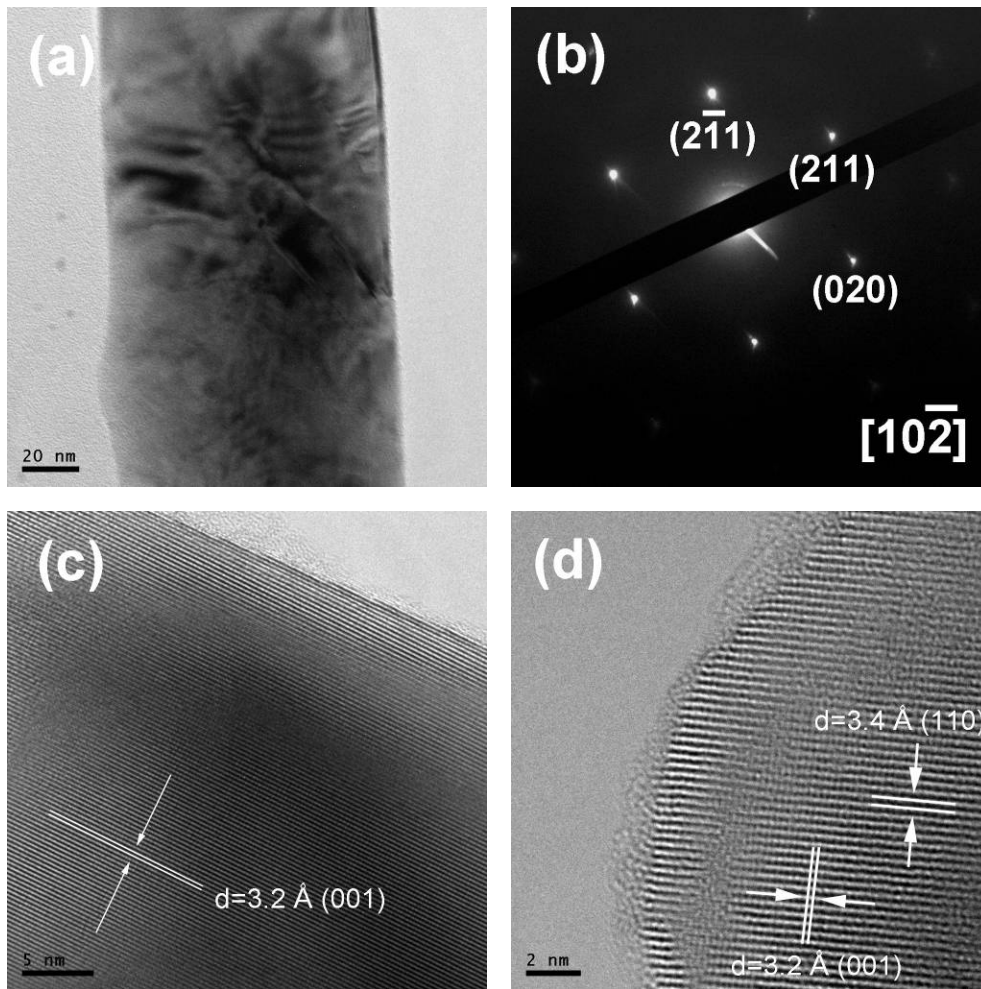


Figure 6-18. (a) High resolution transmission electron microscope image of SnO<sub>2</sub> nanorods (b) SAD patterns recorded from an individual nanorod with an electron beam along the  $[10\bar{2}]$  direction. (c), (d) HR-TEM lattice fringes images indicate their single crystal rutile structure.

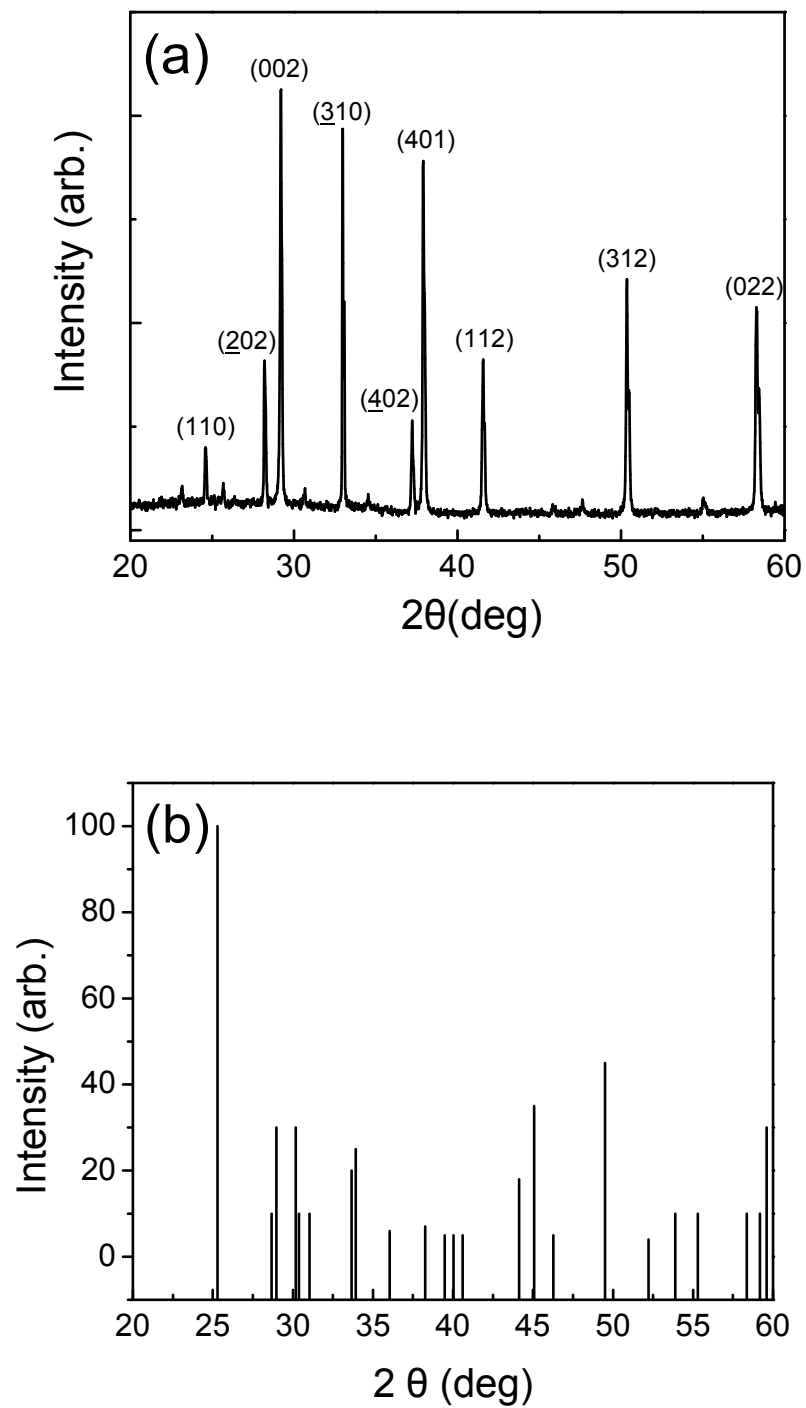


Figure 6-19. X-ray diffraction patterns of VO<sub>2</sub> nanowires grown at 600°C in 500 mTorr oxygen on (a) silicon. (b) Diffraction intensities of monoclinic VO<sub>2</sub> (B) from JCPDS file.

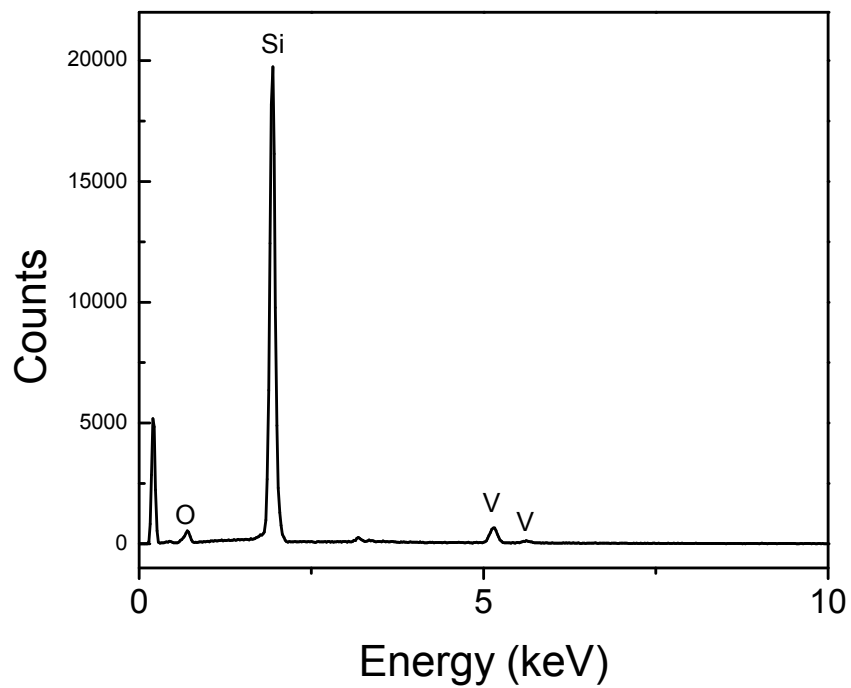


Figure 6-20. Energy-dispersive spectroscopy spectra for VO<sub>2</sub> nanowires grown on silicon at 600°C.

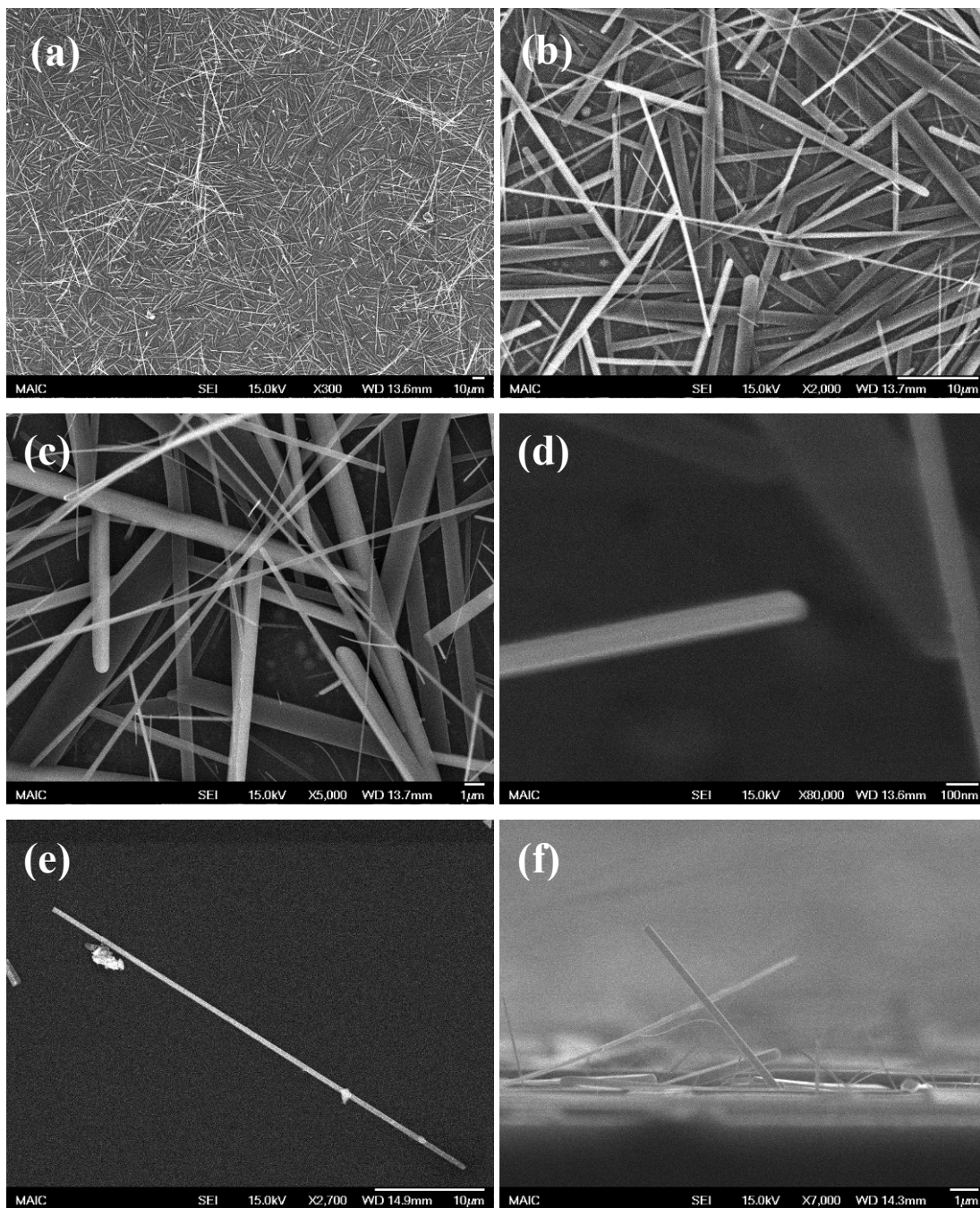


Figure 6-21. (a)–(d) Top view scanning electron microscope images of VO<sub>2</sub> nanowires on silicon grew at 600°C (e) individual VO<sub>2</sub> nanowire dispersed on the silicon substrate (f) side view scanning electron microscope images of VO<sub>2</sub> nanowires on silicon grew at 600°C.

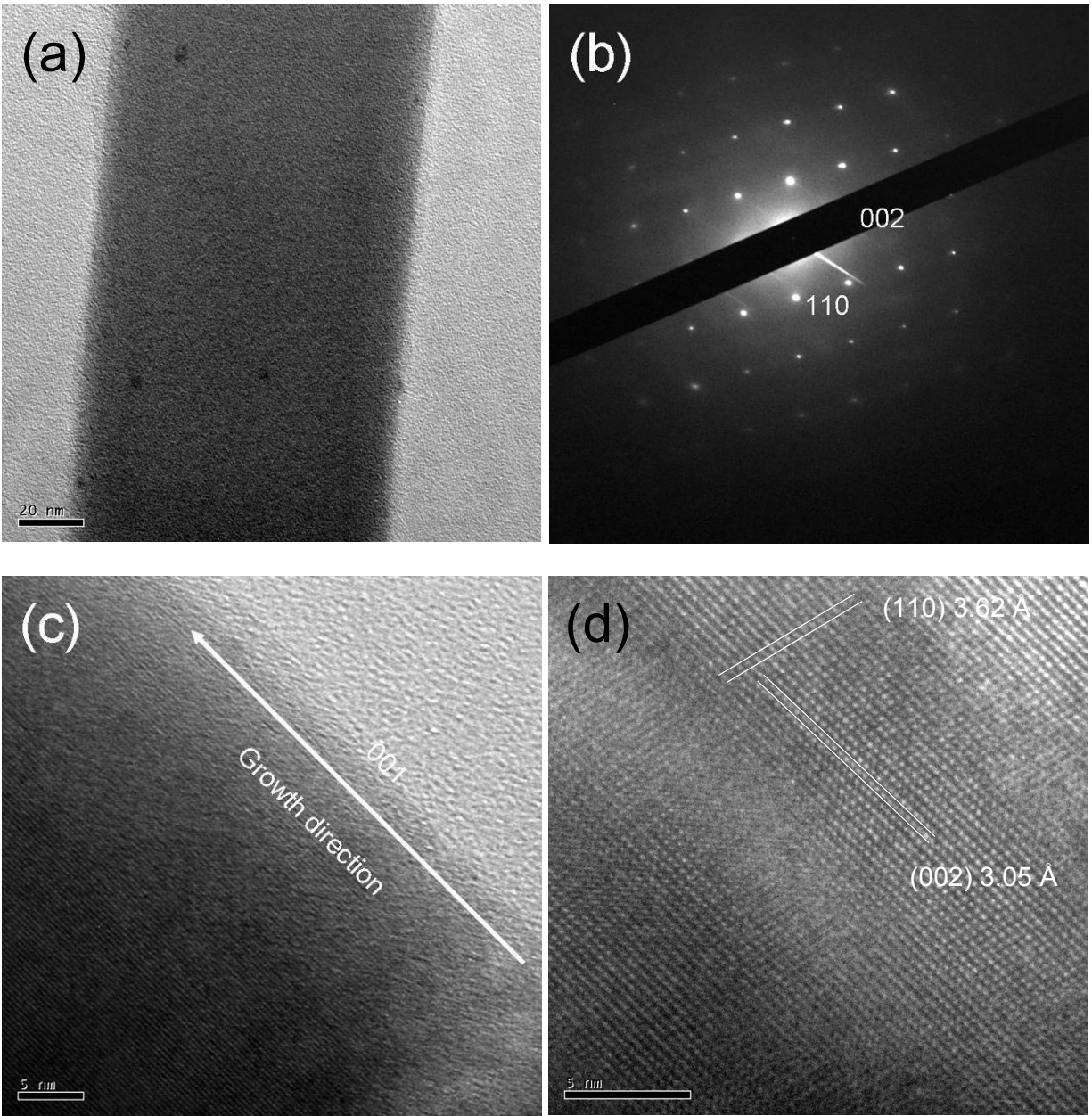


Figure 6-22. (a) High resolution transmission electron microscope image of  $\text{VO}_2$  nanowires (b) SAD patterns recorded from an individual nanowire (c), (d) HR-TEM lattice fringes images indicate their single crystal monoclinic structure.

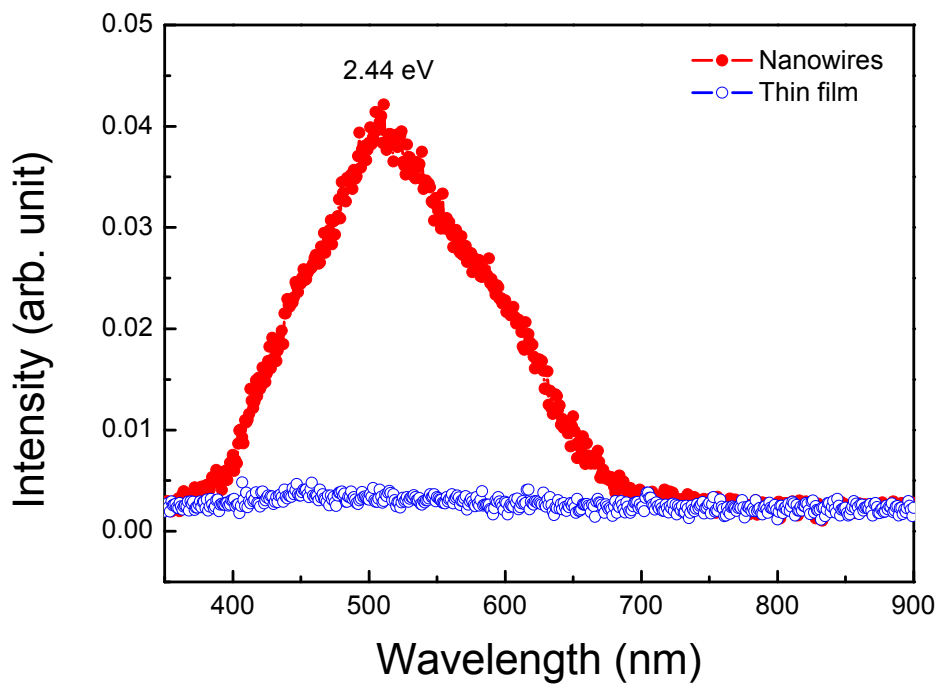


Figure 6-23. The photoluminescence spectra of VO<sub>2</sub> thin film and nanowires grown at different oxygen pressure.

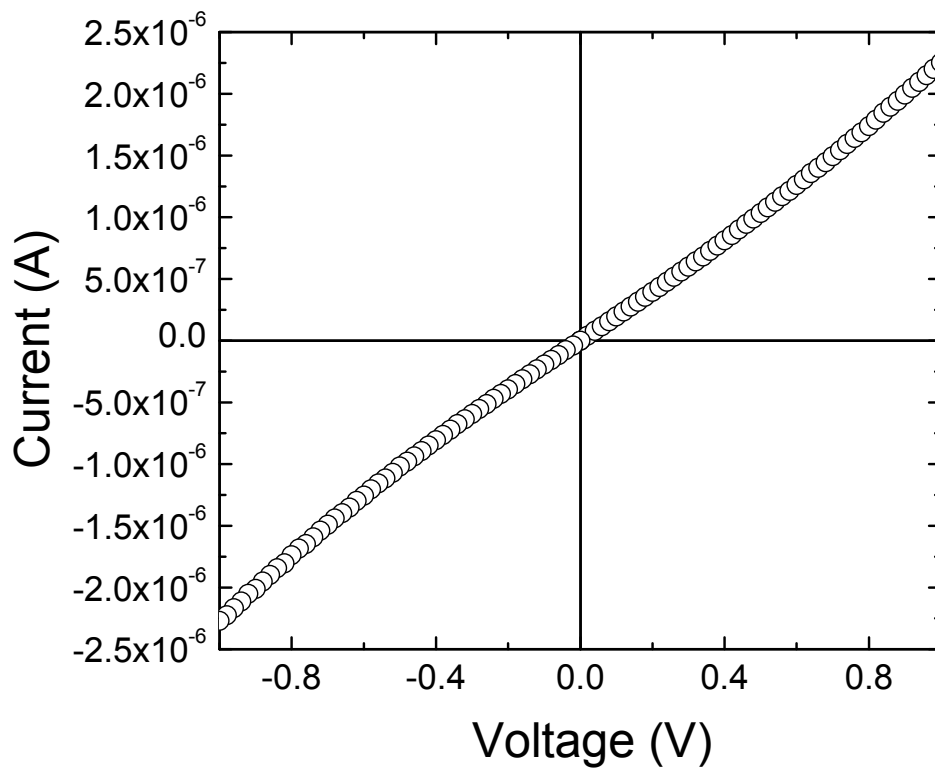
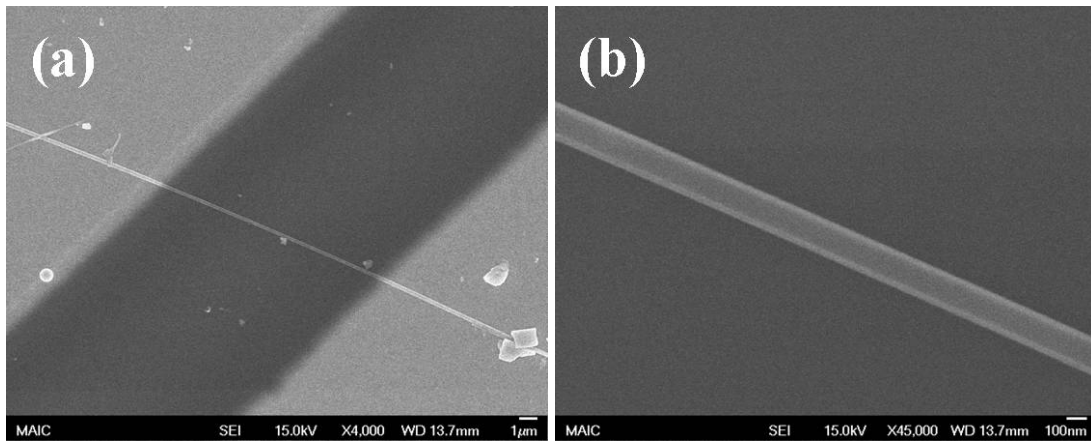


Figure 6-24. (a), (b) Scanning electron microscope images of fabricated single nanowire device. (c) I-V characteristics of the individual VO<sub>2</sub> nanowire measured in air ambient at room temperature.

## CHAPTER 7 EPITAXIAL GROWTH OF TRANSPARENT TIN OXIDE THIN FILMS

### 7.1 Introduction

In recent years, there has emerged significant interest in the epitaxial growth and properties of functional oxide thin films.<sup>17,202</sup> Functional oxide of interest include superconductors,<sup>203-205</sup> ferroelectrics,<sup>206</sup> dielectrics,<sup>207</sup> phosphors,<sup>208,209</sup> and semiconductors.<sup>210,211</sup> The latter class of oxides, namely semiconductors, has emerged as particularly interesting for sensors, thin-film electronics, and photonics. Tin oxide ( $\text{SnO}_2$ ) is a wide band gap (3.6 eV) metal oxide semiconductor with excellent optical transparency in the visible range.<sup>212</sup> It possesses the rutile (tetragonal) crystal structure with  $a=4.738 \text{ \AA}$  and  $c=3.188 \text{ \AA}$ . With a relatively high conductivity, visible wavelength transparency, chemical stability and thermal stability in oxidizing environments,<sup>213</sup> tin oxide films are being explored for a number of applications. As a wide band-gap semiconductor,  $\text{SnO}_2$  is attractive for use in photonic applications, such as solar cells, where transparent electrodes are required.<sup>18,214</sup>  $\text{SnO}_2$  thin films are used for gas sensor devices based on changes in conductivity when exposed to selected chemical species.<sup>21,37,188</sup> In addition, there is also interest in the possibility of inducing ferromagnetism in  $\text{SnO}_2$  through transition metal doping,<sup>215,216</sup> an approach that is also being pursued for other wide band-gap semiconductors.<sup>217,218</sup>

$\text{SnO}_2$  thin films have been fabricated by a variety of techniques including sol-gel method,<sup>219</sup> electron beam evaporation,<sup>220</sup> reactive sputtering,<sup>221</sup> chemical vapor deposition<sup>222,223</sup> and sputtering.<sup>36,224</sup> One of the major challenges in synthesizing  $\text{SnO}_2$  thin films is the control over oxygen stoichiometry. When deposition is carried out in vacuum conditions at high temperatures,  $\text{SnO}_2$  films tend to be nonstoichiometric, frequently including metastable phases

such as SnO and Sn<sub>3</sub>O<sub>4</sub>.<sup>225</sup> The existence of these metastable phases and relaxed crystal defects will strongly affect the properties of the films.

While previous applications of SnO<sub>2</sub> for sensors or transparent conductors have primarily relied on polycrystalline material, many of the emerging applications for functional wide band-gap semiconductors require highly crystalline epitaxial films. As such, understanding the effects of growth parameters and substrate selection on the epitaxial growth of SnO<sub>2</sub> is important. Epitaxial growth kinetics can yield specific defect structures that significantly affect the oxide thin film properties.<sup>226,227</sup> This becomes increasingly important as targeted thin film structures involve heterointerfaces, multilayers, or superlattices.<sup>226-229</sup>

Similar to most metal oxide materials, undoped SnO<sub>2</sub> is an *n*-type semiconductor because of intrinsic defects (oxygen deficient or metal excess). The fabrication of high quality *p*-type transparent conducting oxides (TCOs) is one the major challenges in the fabrication of p-n junction based devices.<sup>230</sup> As is well known that doping in semiconductor with selective elements offers an effective approach to adjust the electrical, optical, and magnetic properties, which is crucial for practical applications. A perusal of the periodic table suggests that possible acceptor candidates for SnO<sub>2</sub> include Group III elements such as B, Al, Ga, and In substituting for Sn. Theoretically if effective substitution of Sn with group III elements, the *p*-type SnO<sub>2</sub> can be realized. However, only a few groups reported the *p*-type conductivity in SnO<sub>2</sub> thin films up to date.<sup>230-234</sup> The difficulties can come from a variety of causes. Difficulty of obtaining *p*-type SnO<sub>2</sub> may due to its low dopant solubility and self-compensating process on doping. Furthermore, dopants may be compensated by low-energy native defects, such as Sn<sub>i</sub> and V<sub>O</sub> or background impurities. Low solubility of the dopant in the host material is also another issue.

Deep impurity level can also be a source of doping problem causing significant resistance to the formation of shallow acceptor level.

Bagheri-Mohagheghi *et al.* reported the *p*-type conductivity on Li-doped SnO<sub>2</sub> thin film by spray pyrolysis.<sup>231</sup> The heavily Li-doped SnO<sub>2</sub> films (~2 wt.%; 37 at.%) show a carrier conversion from electrons to holes. Because of similar ionic radius of Sn<sup>4+</sup> (0.71 Å) and Li<sup>+</sup> (0.68 Å), three holes are produced when the substitution occurs. Ji *et al.* reported *p*-type In-doped SnO<sub>2</sub> with In/Sn ratio of 0.2 by spray pyrolysis.<sup>232,234</sup> Similar result has also been reported by Huang *et al.* with Ga-doped SnO<sub>2</sub> films (0.2%) by DC magnetron sputtering.<sup>233</sup> However, the electric properties of these films were not good because of the limitations of sol-gel method, such as poor crystalline quality and poor process control.

Pulsed laser deposition (PLD) has been widely used in synthesis complex oxide thin films, such as high T<sub>c</sub> superconductors and perovskite oxides. PLD has the advantage of operating in a reactive atmosphere over a wide range of oxygen pressure.<sup>104</sup> In this Chapter, we study the epitaxial growth of SnO<sub>2</sub> thin films on (0001) sapphire by PLD, including the specific crystalline orientation of this rutile structure on a hexagonal template. The effects of growth parameters on the electrical transport property and surface morphology will be discussed as well. The effects of gallium doping will be examined in the second section.

## 7.2 Experimental Methods

Pulsed laser deposition was used for thin film growth. The ablation target was fabricated using high purity SnO<sub>2</sub> (Alfa Aesar, 99.996%). For gallium doped thin films, the ablation target was fabricated using powder mixture of high purity ZnO (Alfa Aesar, 99.9995%) and Ga<sub>2</sub>O<sub>3</sub> (Alfa Aesar, 99.999%) with Ga:Zn atomic ratios of 1:99. The targets were pressed and sintered at 1300°C for 16 h in air. A KrF excimer laser was used as the ablation source. A repetition rate of 1 Hz was used, with target to substrate distance of 4 cm and a laser pulse energy density of 1–3

J/cm<sup>2</sup>. The growth chamber exhibits a base pressure of 10<sup>-6</sup> Torr. Single crystal (0001) Al<sub>2</sub>O<sub>3</sub> (sapphire) was used as the substrate material in this study. Prior to deposition, the Al<sub>2</sub>O<sub>3</sub> substrates were ultrasonically cleaned with trichloroethylene, acetone and methanol, followed by compressed N<sub>2</sub> drying. The substrates were attached to the heater using Ag paint. Prior to growth, the target was cleaned in situ by pre-ablating with approximately 2000 shots. Film growth experiments were performed over a temperature range of 300–800°C in an oxygen pressure range of 20–150 mTorr. Film thickness ranged from 200–300 nm and typical growth time was 2 h. The deposited films were characterized using X-ray diffraction, atomic force microscopy and field emission microscopy. Four-point van der Pauw Hall measurements were performed to determine transport properties. A Perkin-Elmer Lambda 800 UV/Vis double-beam spectrometer was used for optical absorption measurements.

### 7.3 Results and Discussion

#### 7.3.1 Properties of undoped SnO<sub>2</sub> thin films

Epitaxial SnO<sub>2</sub> films on (0001) Al<sub>2</sub>O<sub>3</sub> were realized for deposition at temperature as low as 400 °C in an oxygen pressure of 50 mTorr. Figure 7-1 shows the X-ray diffraction (XRD)  $\theta$ -2 $\theta$  patterns for SnO<sub>2</sub> thin film prepared by PLD at different temperatures. The (200) and (400) SnO<sub>2</sub> are the dominant peaks in all scans, which indicates that the films are highly *a*-axis oriented; i.e. the principal out-of plane orientation is SnO<sub>2</sub> (100) // Al<sub>2</sub>O<sub>3</sub> (0001). The weak peaks for SnO<sub>2</sub> (101) grains are also observed at higher temperatures. The results clearly show that epitaxial growth of *a*-axis oriented SnO<sub>2</sub> grains on the (0001) Al<sub>2</sub>O<sub>3</sub> substrate is favored, placing the film *c*-axis in the plane of the surface. As seen in Figure 7-2, the *a*-axis lattice parameter shows an increase with increasing growth temperature. However, the *a*-axis spacing is consistently less than that seen in bulk SnO<sub>2</sub>.

The epitaxial crystallinity of the films was confirmed by looking at both out-of-plane rocking curves and in-plane  $\phi$ -scans. The rocking curve through the (200) plane for SnO<sub>2</sub> film grown at 700°C is shown in Figure 7-3, yields a full width half maximum (FWHM) of 0.0156°, which confirms that the film is highly oriented with the *a*-axis perpendicular to the surface. With increasing growth temperature, the crystallinity significantly improved as reflected in corresponding smaller FWHM values. Overall, the films exhibit good out-of-plane alignment of the (100) planes.

The in-plane alignment of the SnO<sub>2</sub> film is seen from the  $\phi$ -scan in Figure 7-4. The film in-plane mosaic ( $\Delta\theta \sim 10^\circ$ ) is much larger than the out-of-plane mosaic. The in-plane alignment can be described as SnO<sub>2</sub> [010] // Al<sub>2</sub>O<sub>3</sub>  $\langle 1\bar{1}\bar{2}0 \rangle$  or equivalently SnO<sub>2</sub> [001] // Al<sub>2</sub>O<sub>3</sub>  $\langle 01\bar{1}0 \rangle$  and 60° rotations. The SnO<sub>2</sub> films grow epitaxially on the (0001) Al<sub>2</sub>O<sub>3</sub> substrate with three orientations rotated 60° in plane with respect to each other due to the six-fold symmetry of the *c*-plane surface of Al<sub>2</sub>O<sub>3</sub>. This epitaxial structure is consistent with the matching of the oxygen octahedral arrangements existing on the SnO<sub>2</sub> (100) surface and on the Al<sub>2</sub>O<sub>3</sub> (0001) surface as illustrated in Figure 7-5, resulting in the epitaxial growth of (100) oriented SnO<sub>2</sub>. This in-plane variant structure with three different symmetry-equivalent orientations has also been observed on films synthesized by metal-organic chemical vapor deposition (MOCVD)<sup>223</sup> and sputtering approaches.<sup>235</sup> A likely explanation as to why the in-plane mosaic is much larger than the out-of-plane is that the rotational mosaic is due to lattice matching between the film (tetragonal symmetry) and the substrate (rhombohedral symmetry). On average the film (010) and (001) planes are aligned with low-index sapphire directions. But then other low-index film planes are not aligned. For example, the film (011) planes are 56.3° from (010) planes and 33.7° from (001) planes. Thus, if these planes tend to align with low-index Al<sub>2</sub>O<sub>3</sub> planes, they would be frustrated

by  $\sim 4^\circ$  on average. All crystal directions can not be aligned when a tetragonal film grows on a rhombohedral (pseudo-hexagonal) *c*-axis substrate. Figure 7-6 shows the growth rate of SnO<sub>2</sub> thin films at different temperatures. The growth rate is measured to be approximately 0.3–0.4 Å/s. For all growth temperatures, the growth rate shows a weakly linear relation to growth temperature, suggesting that an increase in growth temperature enhances the SnO<sub>2</sub> phase formation.

The surface morphology of the SnO<sub>2</sub> film was measured using atomic force microscopy (AFM) measurements. AFM measurements were performed in air using a Veeco Nanoscope III. All samples were scanned over a 5  $\mu\text{m}$   $\times$  5  $\mu\text{m}$  area. In Figure 7-7, the AFM images for SnO<sub>2</sub> grown on sapphire at 700°C are shown. The surfaces showed a dense columnar structure with an rms roughness of 16.76 Å. With increasing temperature, the surface roughness increases, reflected in the formation of large columns.

The resistivity and carrier concentration of the films were determined at room temperature using Hall measurements (Lakeshore 7507). The Hall data is shown in Table 7-2. Hall measurements showed that the epitaxial SnO<sub>2</sub> films were *n*-type semiconductors with carrier concentration varying from  $4 \times 10^{17} \text{ cm}^{-3}$  to  $4.2 \times 10^{19} \text{ cm}^{-3}$ . Figure 7-8 shows the resistivity and carrier concentration of SnO<sub>2</sub> grown on sapphire as a function of deposition temperature. It has been postulated that the conductivity is related to the existence of shallow donor levels near the conduction band, formed by a large concentration of oxygen vacancies. The electrical conduction in undoped SnO<sub>2</sub> is associated with nonstoichiometry and with oxygen-related intrinsic defects.<sup>189</sup> The resistivity increase with growth temperature suggests that fewer oxygen vacancies formed during high temperature deposition, resulting in lower carrier concentrations as well.

Optical absorption measurement was used to determine the band-gap of films. Figure 7-9(a) shows transmission data for SnO<sub>2</sub> film grown at 400°C in 50 mTorr of oxygen, showing a maximum transmission of 70%. The band-gap of the film was calculated by  $(\alpha h\nu)^2 - h\nu$  plot in Figure 7-9(b). The band-gap was approximately 3.89 eV, which is in the range of the SnO<sub>2</sub> thin film reported elsewhere.

### 7.3.1 Properties of gallium-doped SnO<sub>2</sub> thin films

In order to optimize the growth conditions and examine the effects of Ga doping on the films, different growth temperature and oxygen pressure were used. The EDX (Figure 7-10) was used to examine the Ga dopant in the film, the detected elements are Al, Sn, O and Ga. No other impurity or contamination was detected. The X-ray diffraction was used to examine the crystallinity of the films grown at temperature from 400 to 700°C in 50 mTorr of oxygen. All the SnO<sub>2</sub> films showed (200) and (400) SnO<sub>2</sub> peaks, which indicates that the films are highly *a*-axis oriented, same as described in undoped SnO<sub>2</sub> films previously. The results show that dopants do not affect the epitaxial growth of SnO<sub>2</sub> on the (0001) Al<sub>2</sub>O<sub>3</sub> substrate. A comparison of *a*-axis lattice parameter between undoped and Ga-doped SnO<sub>2</sub> films shows an increase with increasing growth temperature in both cases. However, the *a*-axis spacing is consistently less than that seen in bulk SnO<sub>2</sub>. Note that the Ga-doped SnO<sub>2</sub> films have slightly smaller *a*-axis constant in all growth temperature. This might indicate that the Ga<sup>3+</sup> does not substitute the Sn<sup>4+</sup> sites, which leads to the decrease of the lattice constants due to the larger size of Ga<sup>3+</sup> (0.76 Å) compared to Sn<sup>4+</sup> (0.71 Å). The effects of oxygen pressure on the films were further examined. Figure 7-12 shows the X-ray diffraction patterns of SnO<sub>2</sub> films deposited at different oxygen pressure at 400°C. The results show that the *a*-axis parameter (Figure 7-13) decreased with increasing oxygen pressure, while the crystallinity increased with oxygen pressure. The *a*-axis parameter

was close to bulk at 10 mTorr of oxygen, suggests a loose structure which is consistent with a larger full width half maximum (FWHM) value of (200) peak.

Optical absorption measurement was used to determine the band-gap of films. Figure 7-14(a) shows transmission data for Ga-doped SnO<sub>2</sub> film grew at 400°C in 50 mTorr of oxygen, showing a maximum transmission of 80%. The band-gap of the film was calculated by  $(\alpha h\nu)^2 - h\nu$  plot in Figure 7-14(b). The band-gap was approximately 3.94 eV, which is close to value of undoped SnO<sub>2</sub> reported previously. The results show that no remarkable changes were found for the band-gap of Ga-doped films.

The resistivity and carrier concentration of the Ga-doped films were determined at room temperature using Hall measurements (Lakeshore 7507). The Hall data is shown in Table 7-3 and 7-4. Hall measurements showed that the Ga-doped SnO<sub>2</sub> films in most case were *n*-type semiconductors with carrier concentration varying from  $4.8 \times 10^{15} \text{ cm}^{-3}$  to  $4.2 \times 10^{19} \text{ cm}^{-3}$ . In general, the Hall data can be explained by considering the donor (intrinsic defects) and acceptors (substitution of Sn by Ga) in the films. At low temperature, the gallium atoms were not activated as acceptors and the films were *n*-type because of large numbers of intrinsic defects. At high temperature, the number of intrinsic defects decreased and results in high resistivity and low carrier concentration. However, the gallium atoms may compensate with donor due to high temperature and do not behave as acceptors. Interestingly, the *p*-type SnO<sub>2</sub> film can be realized at specific growth parameter (400°C and 50 mTorr O<sub>2</sub>) and was reproduced again in same condition. The optimum temperature and oxygen pressure was realized and Ga atoms were activated and the film showed *p*-type characteristic with carrier concentration approximately  $10^{19} \text{ cm}^{-3}$ .

In order to further confirm the p-type behavior, a  $B \cdot R_H - B$  plot was used to determine the Hall coefficient. In Hall measurement, the measured Hall voltage ( $V_{\text{measured}}$ ) is given by:

$$V_{\text{measured}} = V_H + V_{\text{offset}} + V_{\text{noise}}$$

For Hall system, the recorded Hall voltage ( $V_{\text{measured}}$ ) that calculates Hall coefficient ( $R_H$ ) for single magnetic field polarity, includes noise ( $V_{\text{noise}}$ ) and offset voltages ( $V_{\text{offset}}$ ). However, the noise and offset voltages are both magnetic field independent. If we plot the Hall coefficient times magnetic field ( $B \cdot R_H$ ) versus magnetic field ( $B$ ), we can extract the actual Hall coefficient ( $V_H$ ) by the slope of the linear fit line. The carrier concentration is given by the equation:

$$R_H = \frac{1}{nq}$$

Figure 7-15(a) shows the  $B \cdot R_H - B$  plot for Ga-doped  $\text{SnO}_2$  film (312 nm) grew at  $400^\circ\text{C}$  in 50 mTorr of oxygen, clearly showing a positive slope with Hall coefficient of  $0.2291 \text{ cm}^3 \cdot \text{C}^{-1}$ . The carrier concentration of film is  $2.7 \times 10^{19} \text{ cm}^{-3}$ , which is close to the results given by Hall system. A similar approach has been used on another sample (184 nm) to confirm *p*-type characteristics as shown in Figure 7-16(a). Although the data points were more scattered in this case, the slope was also positive with carrier concentration of  $3 \times 10^{18} \text{ cm}^{-3}$ . The results show that the Ga-doped  $\text{SnO}_2$  films were *p*-type at specific growth condition. However, the *p*-type behavior was not stable and degraded as time proceeds. The Hall measurements were preformed again on the same samples after one month. The carrier type was found convert from *p*-type to *n*-type after one month (Figure 7-15(b) and 7-16(b)). Similar behavior was also observed on thermal annealed Ga-doped  $\text{SnO}_2$  film shown in Figure 7-17(a), showing *p*-type with carrier concentration of  $7 \times 10^{17} \text{ cm}^{-3}$  after annealing at  $800^\circ\text{C}$  in oxygen for 1 h. The carrier type converted back to *n*-type after 2 weeks (Figure 7-17(b)). The results suggest the instability of Ga dopants in the  $\text{SnO}_2$  films, similar results were found in other oxide materials.

#### 7.4 Summary and Conclusions

In conclusion, epitaxial SnO<sub>2</sub> thin films were realized on (0001) Al<sub>2</sub>O<sub>3</sub> substrates using pulsed laser deposition. X-ray diffraction shows that the films have a phase-pure rutile structure and grow along the (100) plane. The epitaxial relationship can be described as SnO<sub>2</sub> [010] // Al<sub>2</sub>O<sub>3</sub> <11 $\bar{2}$ 0> or equivalently SnO<sub>2</sub> [001] // Al<sub>2</sub>O<sub>3</sub> <01 $\bar{1}$ 0> and 60° rotations. The undoped SnO<sub>2</sub> films were *n*-type semiconductor with carrier concentration varied from 4×10<sup>17</sup> cm<sup>-3</sup> to 4.2×10<sup>19</sup> cm<sup>-3</sup>. The electrical transport properties are strongly dependent on the growth temperature. The effects of Ga doping on SnO<sub>2</sub> films were studied. The Ga-doped SnO<sub>2</sub> films were epitaxially grown on (0001) Al<sub>2</sub>O<sub>3</sub> substrate with slightly smaller *a*-axis parameters. No remarkable changes were found for the band-gap of Ga-doped films. The Hall data showed *p*-type behavior occurs only at specific growth condition, but converted back to *n*-type and degraded as time proceeds. More work is needed to study the *p*-type instability on Ga-doped SnO<sub>2</sub> films.

Table 7-1. Candidate dopant atoms for SnO<sub>2</sub>

Atom	Valence	Radius (Å)
Sn	+4	0.71
O	-2	1.38
Li	+1	0.68
In	+3	0.94
Ga	+3	0.76

Table 7-2. Hall data of SnO<sub>2</sub> thin films grown at different temperature.

Temp (°C)	Thickness (nm)	Resistivity (ohm cm)	Hall Coefficient (cm <sup>3</sup> /C)	Carrier Density (1/cm <sup>3</sup> )	Hall Mobility (cm <sup>2</sup> /VS)
300	205	0.047	-0.149	4.2×10 <sup>19</sup>	3.1
400	239	0.296	-0.728	8.6×10 <sup>18</sup>	2.4
500	223	0.244	-0.703	8.9×10 <sup>18</sup>	2.9
600	237	15.193	-10.3	6.1×10 <sup>17</sup>	0.67
700	279	28.534	-16.417	4.0×10 <sup>17</sup>	0.58

Table 7-3. Hall data of Ga-doped SnO<sub>2</sub> films grown at different temperature.

Temp (°C)	Thickness (nm)	Resistivity (ohm cm)	Type	Carrier Density (1/cm <sup>3</sup> )	Hall Mobility (cm <sup>2</sup> /VS)
350	400	0.762	n	6.9×10 <sup>18</sup>	1.19
400	312	0.039	p	2.9×10 <sup>19</sup>	6.75
500	328	0.316	n	7.1×10 <sup>18</sup>	2.8
600	227	0.437	n	7.5×10 <sup>18</sup>	1.92
750	806	5130	n	4.8×10 <sup>15</sup>	0.265

Table 7-4. Hall data of Ga-doped SnO<sub>2</sub> films grown at different oxygen pressure.

Pressure (°C)	Thickness (nm)	Resistivity (ohm cm)	Type	Carrier Density (1/cm <sup>3</sup> )	Hall Mobility (cm <sup>2</sup> /VS)
20	260	0.011	n	4.2×10 <sup>19</sup>	6.09
50	184	0.337	p	2.7×10 <sup>18</sup>	8.36
100	163	6.175	n	8.9×10 <sup>18</sup>	1.04
150	113	36.568	n	6.1×10 <sup>17</sup>	2.32

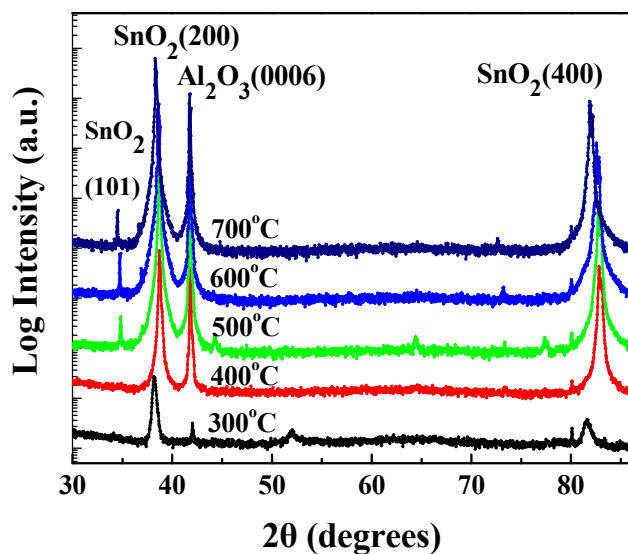


Figure 7-1. X-ray diffraction patterns of SnO<sub>2</sub> films deposited on (0001) Al<sub>2</sub>O<sub>3</sub> at different temperature.

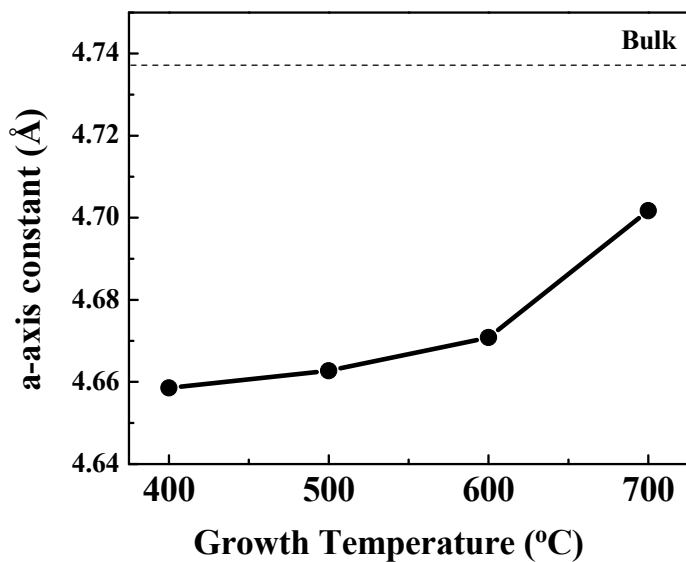


Figure 7-2. *a*-axis constant as a function of growth temperature.

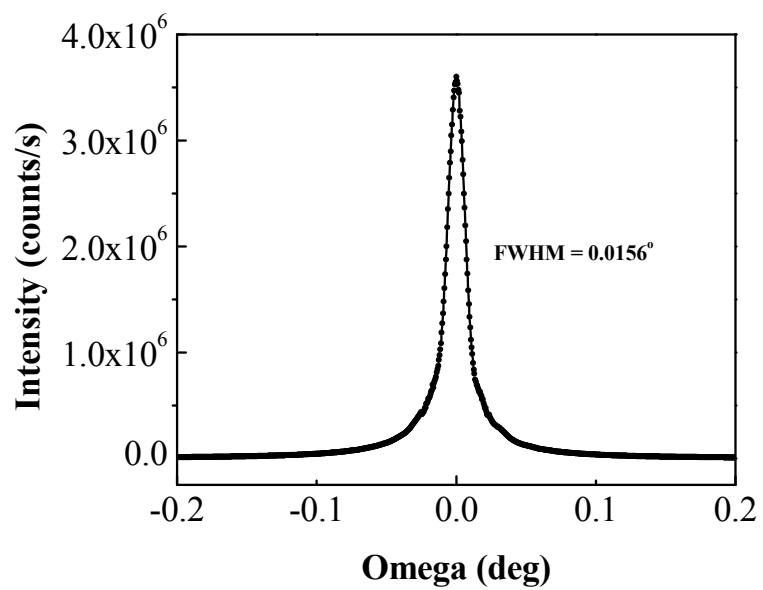


Figure 7-3. Rocking curve of (200) reflection of SnO<sub>2</sub> films grown at 700°C.

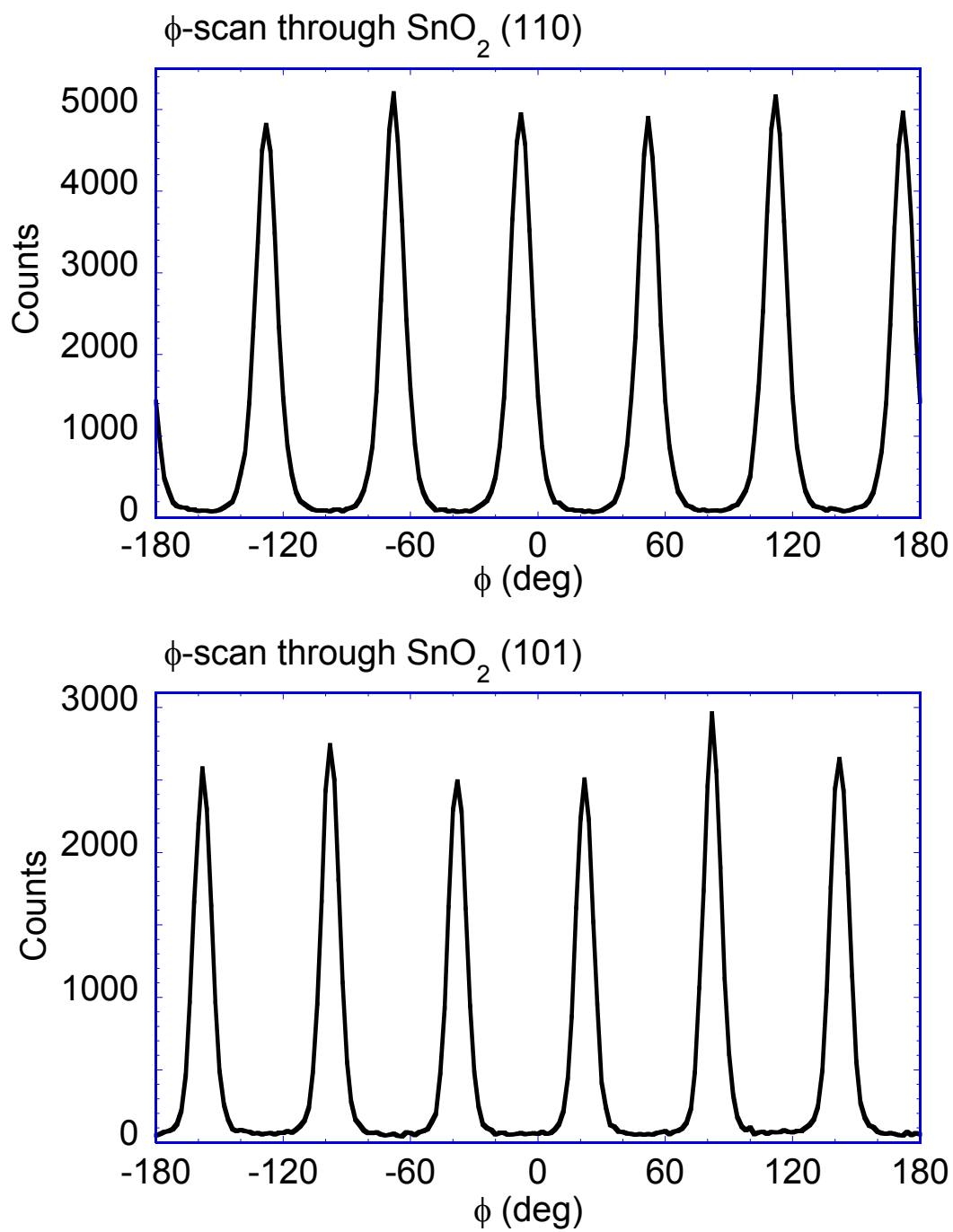


Figure 7-4.  $\phi$ -scans (a) through the  $\text{SnO}_2(110)$  and (b) through the  $\text{SnO}_2(101)$  reflections.

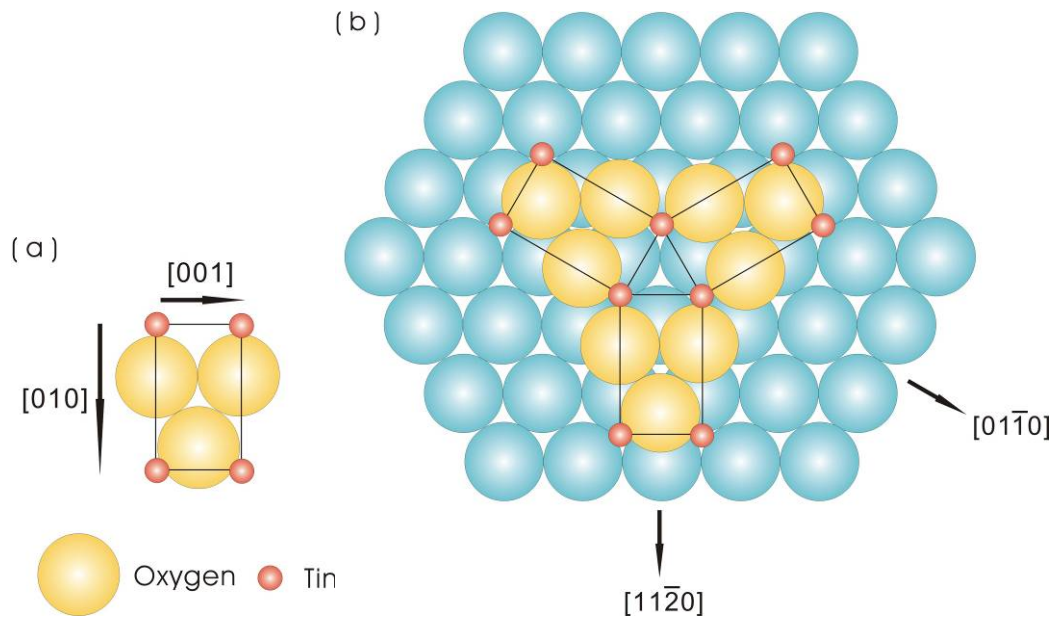


Figure 7-5. The (a) SnO<sub>2</sub> crystal structure projection on the (100) plane, and (b) in-plane epitaxial growth orientations by SnO<sub>2</sub> (100) on sapphire (0001) plane.

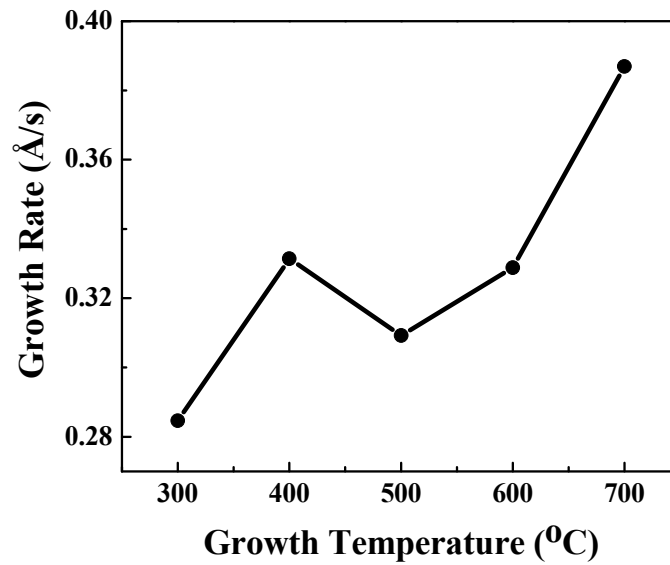


Figure 7-6. Growth rate of SnO<sub>2</sub> films on (0001) Al<sub>2</sub>O<sub>3</sub> as a function of temperature.

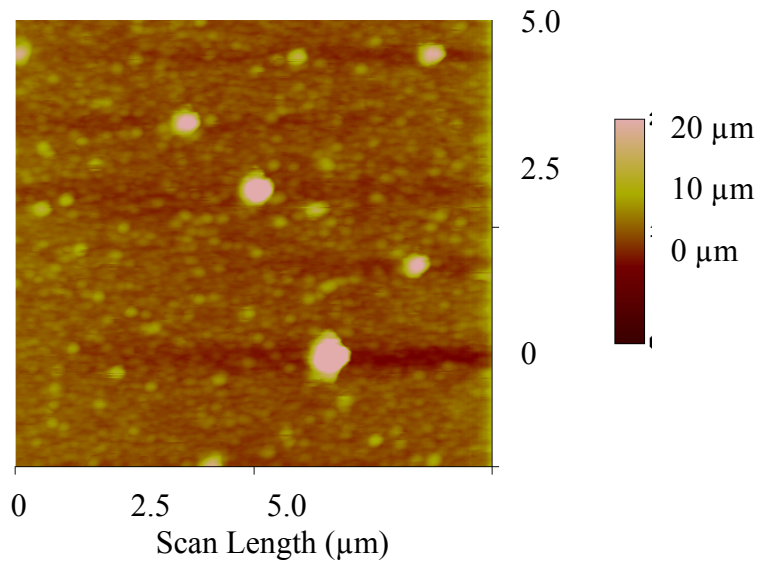


Figure 7-7. Atomic force microscope images of SnO<sub>2</sub> thin film grown at 700°C.

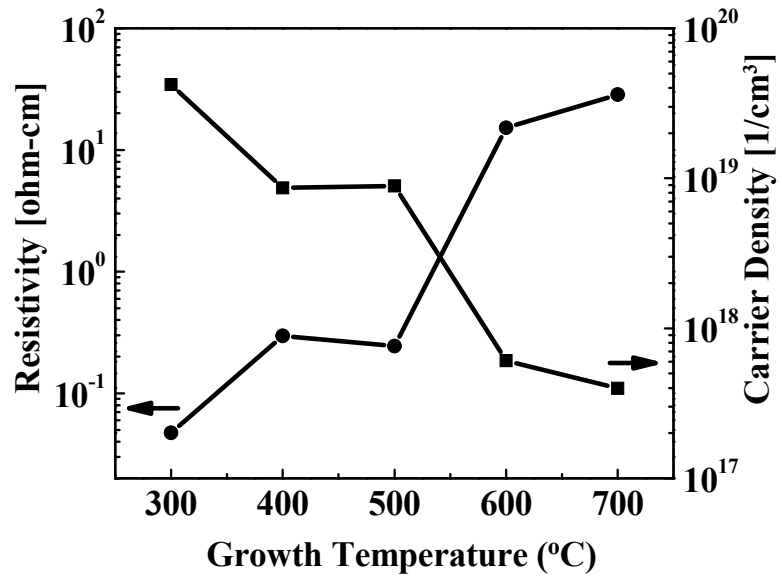


Figure 7-8. Resistivity and carrier density of SnO<sub>2</sub> films grown at different temperatures.

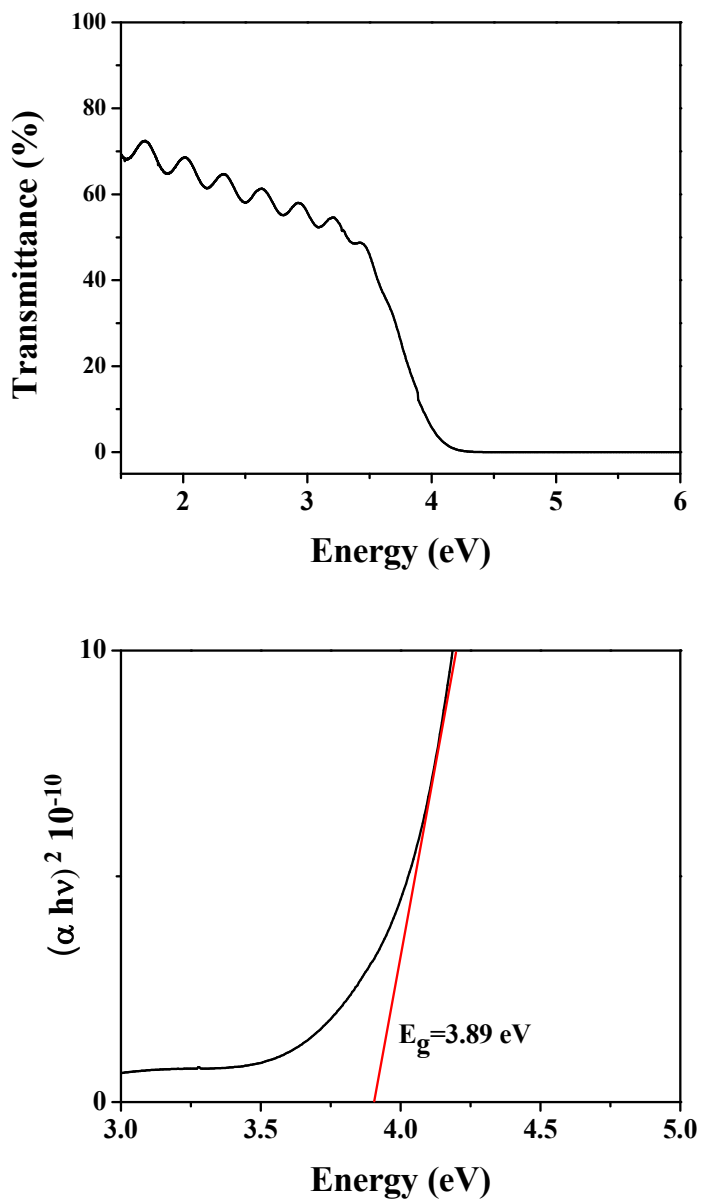


Figure 7-9. (a) Transmission spectra of the SnO<sub>2</sub> film grew at 400°C in 50 mTorr oxygen. (b)  $(\alpha h\nu)^2 - h\nu$  plot shows the band-gap was approximately 3.89 eV.

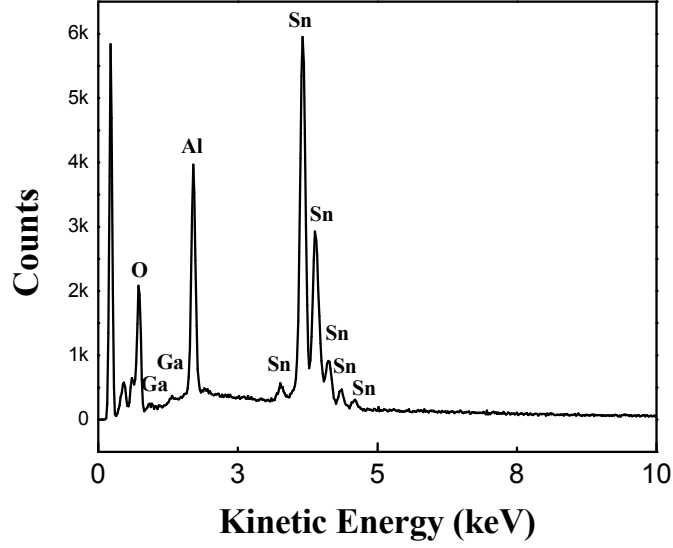


Figure 7-10. Energy-Dispersive X-ray Spectroscopy analysis of Ga-doped SnO<sub>2</sub> thin film grew at 400°C in 50 mTorr O<sub>2</sub>

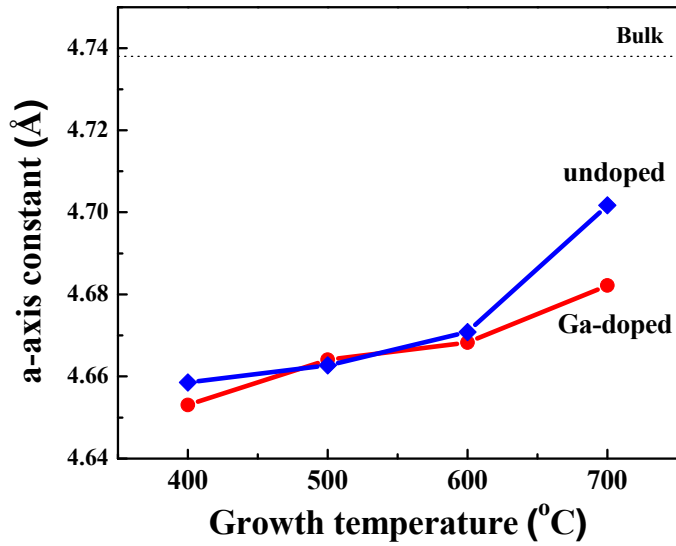


Figure 7-11. Comparison of *a*-axis constant as a function of growth temperature.

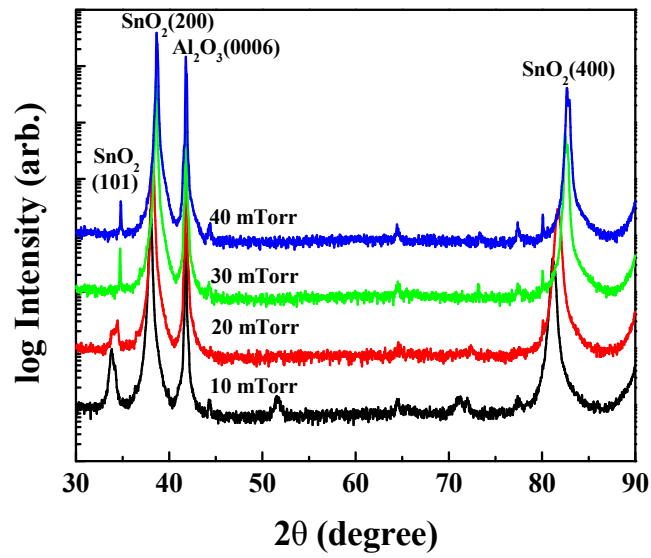


Figure 7-12. X-ray diffraction patterns of Ga-doped SnO<sub>2</sub> films deposited on (0001) Al<sub>2</sub>O<sub>3</sub> at different oxygen pressure.

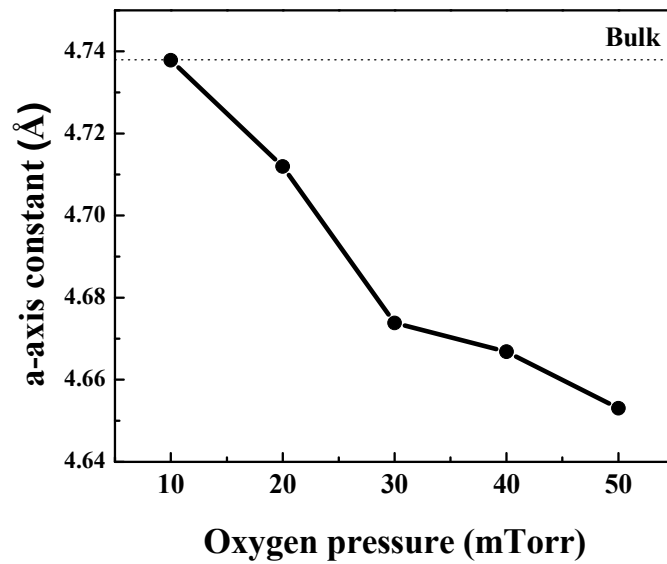


Figure 7-13. *a*-axis constant of Ga-doped SnO<sub>2</sub> films as a function of growth pressure.

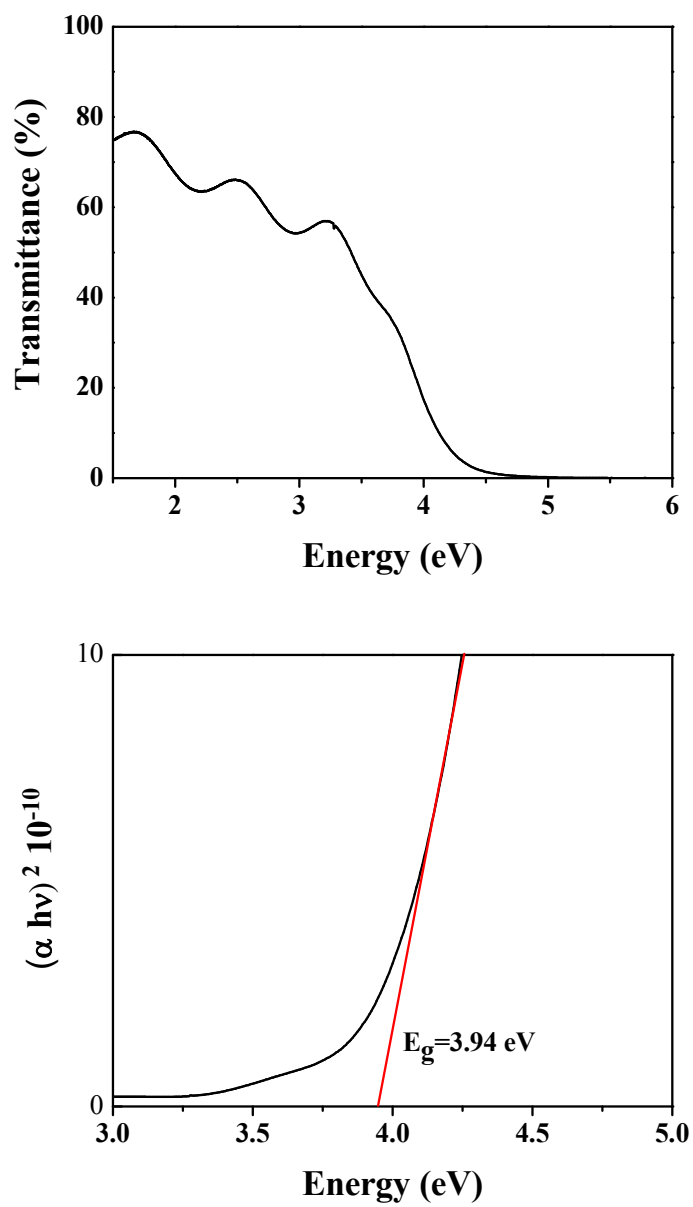


Figure 7-14. (a) Transmission spectra of the Ga-doped SnO<sub>2</sub> film grew at 400°C in 50 mTorr oxygen. (b)  $(\alpha hv)^2-hv$  plot shows the band-gap was approximately 3.94 eV.

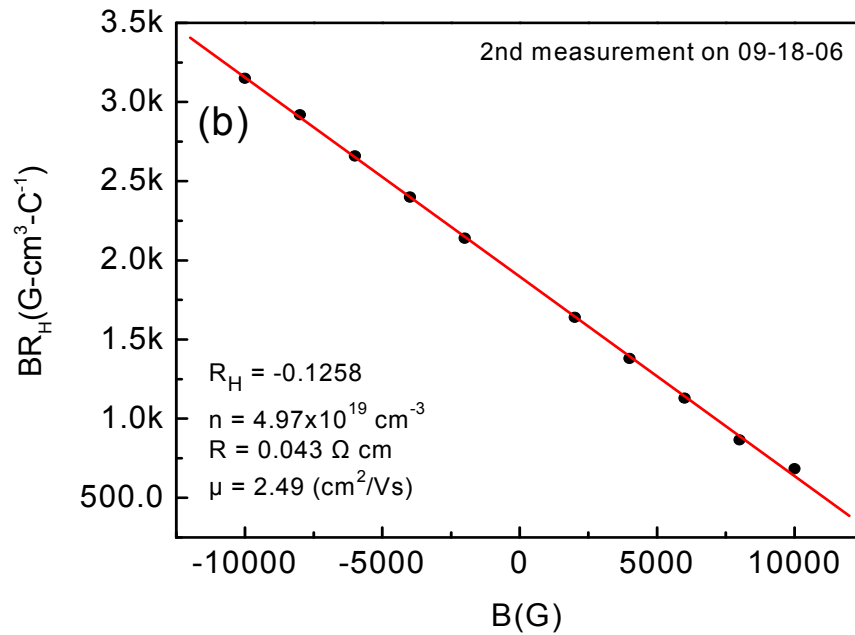
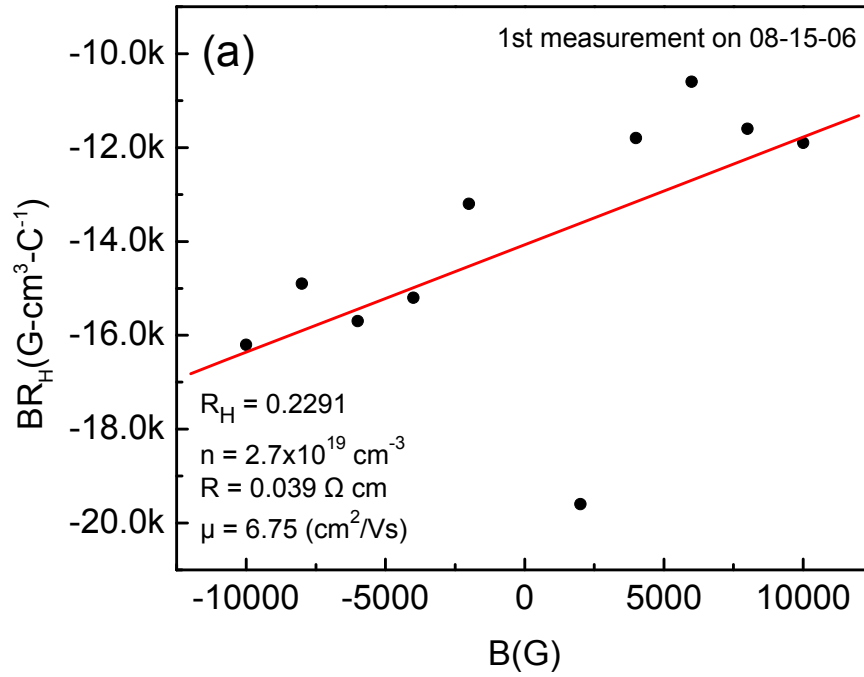


Figure 7-15. Hall plot ( $B \cdot R_H - B$ ) of Ga-doped SnO<sub>2</sub> film grew at 400°C in 50 mTorr oxygen, (a) measured immediately after grown, (b) measured after 1 month.

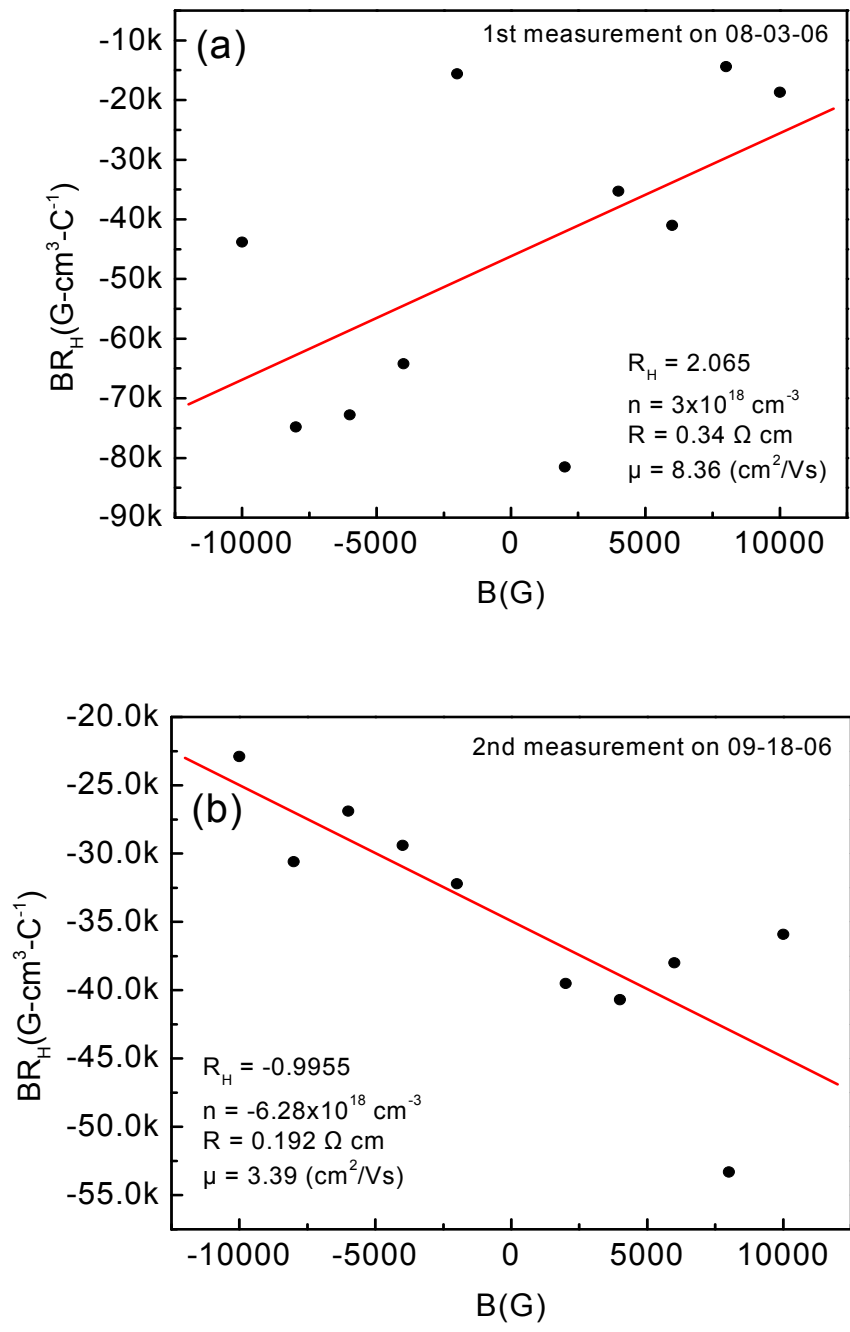


Figure 7-16. Hall plot ( $B \cdot R_H - B$ ) of Ga-doped SnO<sub>2</sub> film grew at 400°C in 50 mTorr oxygen, (a) measured immediately after grown, (b) measured after 1 month.

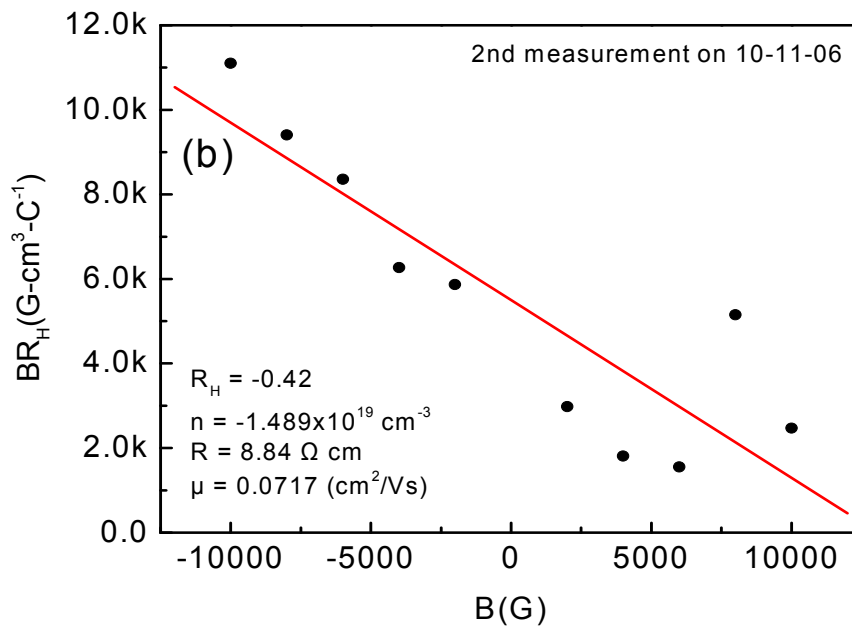
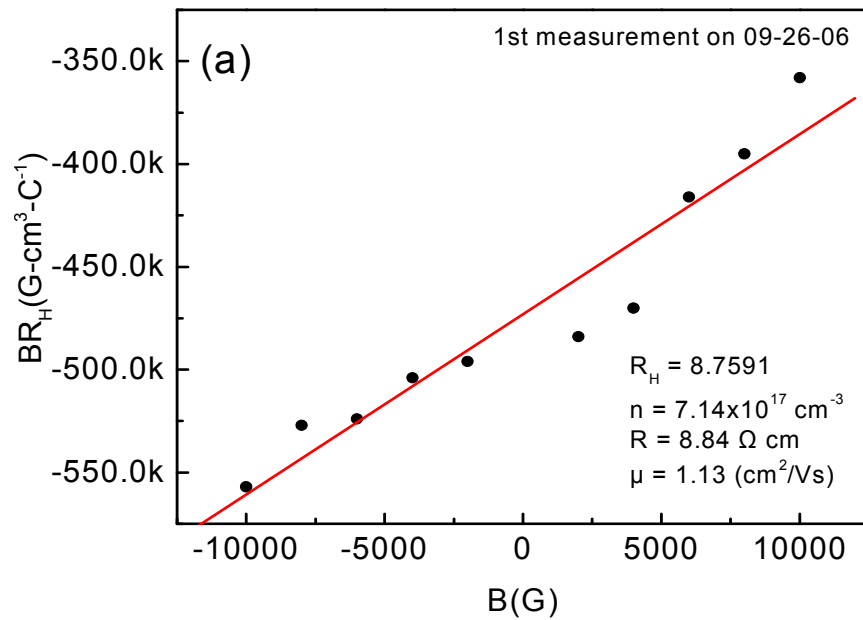


Figure 7-17. Hall plot ( $B \cdot R_H - B$ ) of Ga-doped  $\text{SnO}_2$  film grew at  $400^\circ\text{C}$  in 20 mTorr oxygen and annealed at  $800^\circ\text{C}$  in oxygen for 1h, (a) measured immediately after annealing, (b) measured after 0.5 month.

## CHAPTER 8 CONCLUSION

This work focused on the synthesis of one-dimensional metal oxide nanowires and hydrogen sensing applications. In the synthesis part, the control of initial Ag film thickness and subsequent annealing conditions is shown to provide an effective method for controlling the size and density of nucleation sites for catalyst-driven growth of ZnO nanorods. The completely selective growth is possible on dielectric and silicon substrates. High density cross-linked ZnO nanowires can be synthesized by selecting proper metal catalyst size and lattice matched substrate. A high-pressure assisted pulsed laser deposition has been applied to fabricate a variety of metal oxide nanowires (ZnO, ZnMgO, SnO<sub>2</sub> and VO<sub>2</sub>) without catalysts. Vertically well-aligned ZnO and Zn<sub>x</sub>Mg<sub>1-x</sub>O arrays were grown on *c*-sapphire substrates at 600–800°C. The nanowires growth proceeds without employing catalysts for nucleation, although an epitaxial ZnO thin film template is necessary in order to achieve uniform alignment. This study provides a relative convenient approach to synthesize a wide range of metal oxide nanowires.

For hydrogen sensing applications, it is found that the sensitivity for detecting hydrogen is greatly enhanced by sputter-depositing metal catalysts (Pt and Pt) on ZnO nanowires surface. Pt-coated ZnO nanowires can detect hydrogen down to 100 ppm with relative response of 4%. Pd-coated ZnO nanowires can detect hydrogen down to 10 ppm with a relative smaller response than Pt-coated devices. Approximately 95% of the initial conductance after exposure to hydrogen was recovered within 20 s by exposing the device to air. The sensors are shown to detect ppm hydrogen at room temperature using <0.4 mW of power when using multiple nanowires. When using a single ZnO nanowire coated with Pt as sensing material, the power consumption can further pushing down to μW range. The sensors are not sensitive to oxygen, nitrogen, humidity and air at room temperature, suggests high selectivity for hydrogen sensing

applications. A comparison study of the hydrogen-sensing characteristics of ZnO thin films with different thickness and ZnO nanowires was described. The Pt-coated single nanowires show a current response of approximately a factor of 3 larger at room temperature upon exposure to 500 ppm of hydrogen. Both types of sensors are shown to be capable of the detection of ppm hydrogen at room temperature with nW power levels, but the nanowires show different recovery characteristics, consistent with the expected higher surface coverage of adsorbed hydrogen. Finally, SnO<sub>2</sub> coated ZnO nanowires were used as materials for hydrogen sensors. There was no response to 500 ppm hydrogen at room temperature but showed a 70% response at 400°C. The use of single-crystal ZnO nanowires provide a convenient template for coating with SnO<sub>2</sub> and the resulting structure can be used to detect hydrogen at 400°C. The results show that ZnO nanowires have superior properties in gas sensing applications.

The epitaxial SnO<sub>2</sub> thin films were realized on *c*-sapphire substrates using pulsed laser deposition. X-ray diffraction shows that the films have a phase-pure rutile structure and grow along the (100) plane. The epitaxial relationship can be described as SnO<sub>2</sub> [010] // Al<sub>2</sub>O<sub>3</sub>  $\langle 1\bar{1}20 \rangle$  or equivalently SnO<sub>2</sub> [001] // Al<sub>2</sub>O<sub>3</sub>  $\langle 01\bar{1}0 \rangle$  and 60° rotations. The undoped SnO<sub>2</sub> films were *n*-type semiconductor with carrier concentration varied from  $4 \times 10^{17} \text{ cm}^{-3}$  to  $4.2 \times 10^{19} \text{ cm}^{-3}$ . The electrical transport properties are strongly dependent on the growth temperature. The effects of Ga doping on SnO<sub>2</sub> films were studied. The Ga-doped SnO<sub>2</sub> films were epitaxially grown on (0001) Al<sub>2</sub>O<sub>3</sub> substrate with slightly smaller *a*-axis parameters. No remarkable changes were found for the band-gap of Ga-doped films. The Hall data showed *p*-type behavior occurs only at specific growth condition, but converted back to *n*-type and degraded as time proceeds.

## LIST OF REFERENCES

- 1 Z. L. Wang, Annual Review of Physical Chemistry **55**, 159-196 (2004).
- 2 Y. W. Heo, D. P. Norton, L. C. Tien, Y. Kwon, B. S. Kang, F. Ren, S. J. Pearton, and J. R. LaRoche, Materials Science & Engineering R-Reports **47**, 1-47 (2004).
- 3 M. S. Gudiksen, L. J. Lauhon, J. Wang, D. C. Smith, and C. M. Lieber, Nature **415**, 617-620 (2002).
- 4 M. H. Huang, S. Mao, H. Feick, H. Q. Yan, Y. Y. Wu, H. Kind, E. Weber, R. Russo, and P. D. Yang, Science **292**, 1897-1899 (2001).
- 5 A. M. Morales and C. M. Lieber, Science **9**, 208 (1998).
- 6 Z. W. Pan, Z. R. Dai, and Z. L. Wang, Science **291**, 1947 (2001).
- 7 Z. L. Wang and J. Song, Science **312**, 243-246 (2006).
- 8 T. W. Ebbesen and P. M. Ajayan, Nature **358**, 220-222 (1992).
- 9 W. A. Deheer, A. Chatelain, and D. Ugarte, Science **270**, 1179-1180 (1995).
- 10 S. J. Tans, A. R. M. Verschueren, and C. Dekker, Nature **393**, 49-52 (1998).
- 11 R. H. Baughman, A. A. Zakhidov, and W. A. de Heer, Science **297**, 787-792 (2002).
- 12 X. Duan, Y. Huang, Y. Cui, J. Wang, and C. M. Lieber, Nature **409**, 66 (2001).
- 13 Y. Cui and C. M. Lieber, Science **291**, 851 (2001).
- 14 Y. Huang, X. Duan, Y. Cui, L. J. Lauhon, K.-H. Kim, and C. M. Lieber, Science **294** (2001).
- 15 W. I. Park, G. C. Yi, M. Kim, and S. J. Pennycook, Advanced Materials **15**, 526-529 (2003).
- 16 Y. Gu, I. L. Kuskovsky, M. Yin, S. O'Brien, and G. F. Neumark, Applied Physics Letters **85**, 3833-3835 (2004).
- 17 D. P. Norton, Materials Science & Engineering R-Reports **43**, 139-247 (2004).
- 18 M. Okuya, S. Kaneko, K. Hiroshima, I. Yagi, and K. Murakami, J. Euro. Ceramic. Society **21**, 2099 (2001).
- 19 D. P. Norton, Y. W. Heo, M. P. Ivill, K. Ip, S. J. Pearton, M. F. Chisholm, and T. Steiner, Materials Today **7**, 34-40 (2004).
- 20 G. S. T. Rao and D. T. Rao, Sensors and Actuators B-Chemical, 166 (1999).

- 21 C. K. Kim, S. M. Choi, I. H. Noh, J. H. Lee, C. Hong, H. B. Chae, G. E. Jang, and H. D. Park, *Sensors and Actuators B-Chemical* **77**, 463 (2001).
- 22 R. Martins, E. Fortunato, P. Nunes, I. Ferreira, A. Marques, M. Bender, N.Katsarakis, V. Cimalla, and G. Kiriakidis, *J. Appl. Phys* **96**, 1398 (2004).
- 23 X. D. Wang, J. Zhou, J. H. Song, J. Liu, N. S. Xu, and Z. L. Wang, *Nano Letters* **6**, 2768-2772 (2006).
- 24 P. X. Gao, J. Song, J. Liu, and Z. L. Wang, *Advanced Materials* **19**, 67-72 (2007).
- 25 S. J. Jiao, Z. Z. Zhang, Y. M. Lu, D. Z. Shen, B. Yao, J. Y. Zhang, B. H. Li, D. X. Zhao, X. W. Fan, and Z. K. Tang, *Applied Physics Letters* **88**, 031911 (2006).
- 26 J.-H. Lim, C.-K. Kong, K.-K. Kim, I.-K. Park, D.-K. Hwang, and S.-J. Park, *Advanced Materials* **18**, 2720-2724 (2006).
- 27 A. Kolmakov and M. Moskovits, *Annual Review of Materials Research* **34**, 151-180 (2004).
- 28 S. J. Pearton, D. P. Norton, Y. W. Heo, L. C. Tien, M. P. Ivill, Y. Li, B. S. Kang, F. Ren, J. Kelly, and A. F. Hebard, *Journal of Electronic Materials* **35**, 862-868 (2006).
- 29 U. Ozgur, Y. I. Alivov, C. Liu, A. Teke, M. A. Reshchikov, S. Dogan, V. Avrutin, S. J. Cho, and H. Morkoc, *Journal of Applied Physics* **98** (2005).
- 30 X.-L. Guo, H. Tabata, and T. Kawai, *J. Cryst. Growth* **223**, 135 (2001).
- 31 D. Look, D. Reynolds, C. Litton, R. Jones, D. Eason, and G. Cantwell, *Applied Physics Letters* **81**, 1830-1832 (2002).
- 32 L. G. Wang and A. Zunger, *Physical Review Letters* **90**, 256401 (2003).
- 33 Y. W. Heo, Y. W. Kwon, Y. Li, S. J. Pearton, and D. P. Norton, *Journal of Electronic Materials* **34**, 409-415 (2005).
- 34 T. Makino, Y. Segawa, M. Kawasaki, and H. Koinuma, *Semiconductor Science and Technology* **20**, S78-S91 (2005).
- 35 J. A. Kerr, *CRC Handbook of Chemistry and Physics 1999-2000 :A Ready-Reference Book of Chemical and Physical Data* (CRC Press, 2000).
- 36 R. G. Goodchild, J. B. Webb, and D. F. Williams, *J. Appl. Phys.* **57**, 2308 (1985).
- 37 A. Khanna, R. Kumar, and S. S. Bhatti, *Applied Physics Letters* **82**, 4388 (2003).
- 38 Y. Lie, E. Kpep, and M. Liu, *Chem. Mater.* **17**, 3997 (2005).

- 39 J. W. Kim, K. H. Yun, G. Y. Cha, G. H. Rue, D. D. Lee, and J. S. Huh, *Rare Metal Materials and Engineering* **35**, 385-388 (2006).
- 40 A. Kolmakov, Y. X. Zhang, G. S. Cheng, and M. Moskovits, *Advanced Materials* **15**, 997-+ (2003).
- 41 E. Comini, G. Faglia, G. Sberveglieri, D. Calestani, L. Zanotti, and M. Zha, *Sensors and Actuators B-Chemical* **111**, 2-6 (2005).
- 42 X. Y. Xue, Y. J. Chen, Y. G. Liu, S. L. Shi, Y. G. Wang, and T. H. Wang, *Applied Physics Letters* **88** (2006).
- 43 Y. K. Liu, C. L. Zheng, W. Z. Wang, C. R. Yin, and G. H. Wang, *Advanced Materials* **13**, 1883-+ (2001).
- 44 Y. K. Liu, C. L. Zheng, W. Z. Wang, Y. J. Zhan, and G. H. Wang, *Journal of Crystal Growth* **233**, 8-12 (2001).
- 45 C. K. Xu, X. L. Zhao, S. Liu, and G. H. Wang, *Solid State Communications* **125**, 301-304 (2003).
- 46 D. F. Zhang, L. D. Sun, J. L. Yin, and C. H. Yan, *Advanced Materials* **15**, 1022-+ (2003).
- 47 B. Cheng, J. M. Russell, W. S. Shi, L. Zhang, and E. T. Samulski, *Journal of the American Chemical Society* **126**, 5972-5973 (2004).
- 48 C. X. Guo, M. H. Cao, and C. W. Hu, *Inorganic Chemistry Communications* **7**, 929-931 (2004).
- 49 J. H. He, T. H. Wu, C. L. Hsin, K. M. Li, L. J. Chen, Y. L. Chueh, L. J. Chou, and Z. L. Wang, *Small* **2**, 116-120 (2006).
- 50 M. Fukuma, S. Zembutsu, and S. Miyazawa, *Applied Optics* **22**, 265-268 (1983).
- 51 E. E. Chain, *Applied Optics* **30**, 2782-2787 (1991).
- 52 H. L. M. Chang, H. You, J. Guo, and D. J. Lam, *Applied Surface Science* **48-9**, 12-18 (1991).
- 53 P. Jin and S. Tanemura, *Japanese Journal of Applied Physics Part 1-Regular Papers Short Notes & Review Papers* **33**, 1478-1483 (1994).
- 54 H. S. Choi, J. S. Ahn, J. H. Jung, T. W. Noh, and D. H. Kim, *Physical Review B* **54**, 4621-4628 (1996).
- 55 Y. Muraoka and Z. Hiroi, *Applied Physics Letters* **80**, 583-585 (2002).
- 56 M. S. Grinolds, V. A. Lobastov, J. Weissenrieder, and A. H. Zewail, *PNAS* **103**, 18427-18431 (2006).

- 57 M. S. Whittingham, *Chemical Reviews* **104**, 4271-4301 (2004).
- 58 D. W. Murphy, P. A. Christian, F. J. Disalvo, and J. N. Carides, *Journal of the Electrochemical Society* **126**, 497-499 (1979).
- 59 C. Tsang and A. Manthiram, *Journal of the Electrochemical Society* **144**, 520-524 (1997).
- 60 W. Li, J. R. Dahn, and D. S. Wainwright, *Science* **264**, 1115-1118 (1994).
- 61 C. R. Sides, N. C. Li, C. J. Patrissi, B. Scrosati, and C. R. Martin, *Mrs Bulletin* **27**, 604-607 (2002).
- 62 J. G. Lu, P. Chang, and Z. Fan, *Materials Science and Engineering: R: Reports* **52**, 49-91 (2006).
- 63 Y. N. Xia, P. D. Yang, Y. G. Sun, Y. Y. Wu, B. Mayers, B. Gates, Y. D. Yin, F. Kim, and Y. Q. Yan, *Advanced Materials* **15**, 353-389 (2003).
- 64 E. I. Givargizov, *Journal of Crystal Growth* **31**, 20-30 (1975).
- 65 J. Westwater, D. P. Gosain, S. Tomiya, S. Usui, and H. Ruda, *Journal of Vacuum Science & Technology B* **15**, 554-557 (1997).
- 66 H. Z. Zhang, Y. C. Kong, Y. Z. Wang, X. Du, Z. G. Bai, J. J. Wang, D. P. Yu, Y. Ding, Q. L. Hang, and S. Q. Feng, *Solid State Communications* **109**, 677-682 (1999).
- 67 C. C. Chen, C. C. Yeh, C. H. Chen, M. Y. Yu, H. L. Liu, J. J. Wu, K. H. Chen, L. C. Chen, J. Y. Peng, and Y. F. Chen, *Journal of the American Chemical Society* **123**, 2791-2798 (2001).
- 68 P. D. Yang, H. Q. Yan, S. Mao, R. Russo, J. Johnson, R. Saykally, N. Morris, J. Pham, R. R. He, and H. J. Choi, *Advanced Functional Materials* **12**, 323-331 (2002).
- 69 X. D. Wang, C. J. Summers, and Z. L. Wang, *Nano Letters* **4**, 423-426 (2004).
- 70 R. S. Wagner and W. C. Ellis, *Applied Physics Letters* **4**, 89 (1964).
- 71 M. H. Huang, Y. Y. Wu, H. Feick, N. Tran, E. Weber, and P. D. Yang, *Advanced Materials* **13**, 113-116 (2001).
- 72 M. Law, J. Goldberger, and P. D. Yang, *Annual Review of Materials Research* **34**, 83-122 (2004).
- 73 Y. C. Zhu, Y. Bando, and D. F. Xue, *Applied Physics Letters* **82**, 1769-1771 (2003).
- 74 J. Q. Hu, Y. Bando, Q. L. Liu, and D. Golberg, *Advanced Functional Materials* **13**, 493-496 (2003).

- 75 Z. Q. Liu, D. H. Zhang, S. Han, C. Li, T. Tang, W. Jin, X. L. Liu, B. Lei, and C. W. Zhou, *Advanced Materials* **15**, 1754-+ (2003).
- 76 Z. L. Wang, *Journal of Physics-Condensed Matter* **16**, R829-R858 (2004).
- 77 X. C. Wu, J. M. Hong, Z. J. Han, and Y. R. Tao, *Chemical Physics Letters* **373**, 28-32 (2003).
- 78 Y. W. Wang, C. H. Liang, G. Z. Wang, T. Gao, S. X. Wang, J. C. Fan, and L. D. Zhang, *Journal of Materials Science Letters* **20**, 1687-1689 (2001).
- 79 W. Z. Wang, C. K. Xu, G. H. Wang, Y. K. Liu, and C. L. Zheng, *Journal of Applied Physics* **92**, 2740-2742 (2002).
- 80 J. X. Wang, D. F. Liu, X. Q. Yan, H. J. Yuan, L. J. Ci, Z. P. Zhou, Y. Gao, L. Song, L. F. Liu, W. Y. Zhou, G. Wang, and S. S. Xie, *Solid State Communications* **130**, 89-94 (2004).
- 81 J. H. Choy, E. S. Jang, J. H. Won, J. H. Chung, D. J. Jang, and Y. W. Kim, *Advanced Materials* **15**, 1911-+ (2003).
- 82 L. Vayssieres, *Advanced Materials* **15**, 464-466 (2003).
- 83 B. Liu and H. C. Zeng, *Langmuir* **20**, 4196-4204 (2004).
- 84 C. H. Ye, X. S. Fang, Y. H. Wang, T. W. Xie, A. W. Zhao, and L. D. Zhang, *Chemistry Letters* **33**, 54-55 (2004).
- 85 M. Wang, C.-H. Ye, Y. Zhang, G.-M. Hua, H.-X. Wang, M.-G. Kong, and L.-D. Zhang, *Journal of Crystal Growth* **291**, 334-339 (2006).
- 86 X. Wang and Y. D. Li, *Pure and Applied Chemistry* **78**, 45-64 (2006).
- 87 Y. J. Xiong, Y. Xie, Z. Q. Li, X. X. Li, and S. M. Gao, *Chemistry-a European Journal* **10**, 654-660 (2004).
- 88 C.-L. Hsu, S.-J. Chang, H.-C. Hung, Y.-R. Lin, C.-J. Huang, Y.-K. Tseng, and I. C. Chen, *Journal of the Electrochemical Society* **152**, 378-381 (2005).
- 89 S. M. Sze, *Physics of Semiconductor Devices*, 2nd ed. (John Wiley & Sons, 1983).
- 90 R. Chau, S. Datta, M. Doczy, B. Dotyle, B. Jin, J. Kavalieros, A. Majumdar, M. Metz, and M. Radosavljevic, *IEEE Transactions on Nanotechnology* **4**, 153-158 (2005).
- 91 C. J. Lee, T. J. Lee, S. C. Lyu, Y. Zhang, H. Ruh, and H. J. Lee, *Applied Physics Letters* **81**, 3648-3650 (2002).
- 92 L. F. Dong, J. Jiao, D. W. Tuggle, J. M. Petty, S. A. Elliff, and M. Coulter, *Applied Physics Letters* **82**, 1096-1098 (2003).

- 93 S. H. Jo, J. Y. Lao, Z. F. Ren, R. A. Farrer, T. Baldacchini, and J. T. Fourkas, *Applied Physics Letters* **83**, 4821-4823 (2003).
- 94 C. X. Xu and X. W. Sun, *Applied Physics Letters* **83**, 3806-3808 (2003).
- 95 Y. W. Zhu, H. Z. Zhang, X. C. Sun, S. Q. Feng, J. Xu, Q. Zhao, B. Xiang, R. M. Wang, and D. P. Yu, *Applied Physics Letters* **83**, 144-146 (2003).
- 96 A. B. Djuricic and Y. H. Leung, *Small* **2**, 944-961 (2006).
- 97 H. Kind, H. Q. Yan, B. Messer, M. Law, and P. D. Yang, *Advanced Materials* **14**, 158-+ (2002).
- 98 J. Y. Park, Y. S. Yun, Y. S. Hong, H. Oh, J.-J. Kim, and S. S. Kim, *Applied Physics Letters* **87**, 123108 (2005).
- 99 S. E. Ahn, J. S. Lee, H. Kim, S. Kim, B. H. Kang, K. H. Kim, and G. T. Kim, *Applied Physics Letters* **84**, 5022-5024 (2004).
- 100 H. Nanto, T. Minami, and S. Takata, *J. Appl. Phys* **60**, 482 (1986).
- 101 M. Egashira, Y. Shimizu, Y. Takao, and S. Sako, *Sensors and Actuators B-Chemical* **35-36**, 62 (1996).
- 102 N. Koshizaki and T. Oyama, *Sensors and Actuators B-Chemical* **66**, 119 (2000).
- 103 J. Xu, Y. Shun, Q. Pan, and J. Qin, *Sensors and Actuators B-Chemical* **66**, 161 (2000).
- 104 D. B. Chrisey and G. K. Hubler, *Pulsed Laser Deposition of Thin Films* (John Wiley & Sons, Inc., 1994).
- 105 <http://www.eeel.nist.gov/812/hall.html>, *Hall Effect Measurements*.
- 106 Y. Cui, Q. Wei, H. Park, and C. M. Lieber, *Science*, 1289 (2001).
- 107 M. H. Yun, N. V. Myung, R. P. Vasquez, C. S. Lee, E. Menke, and R. M. Penner, *Nano Letters* **4**, 419-422 (2004).
- 108 Q. Wan, Q. H. Li, Y. J. Chen, T. H. Wang, X. L. He, J. P. Li, and C. L. Lin, *Applied Physics Letters* **84**, 3654-3656 (2004).
- 109 C. Li, D. H. Zhang, X. L. Liu, S. Han, T. Tang, J. Han, and C. W. Zhou, *Applied Physics Letters* **82**, 1613-1615 (2003).
- 110 A. Star, T.-R. Han, V. Joshi, J.-C. P. Gabriel, and G. Gruner, *Advanced Materials* **16**, 2049 (2004).
- 111 Z. Zhong, D. Wang, Y. Cui, M. W. Bockrath, and C. M. Lieber, *Science* **302**, 1377 (2003).

- 112 Y. W. Heo, L. C. Tien, Y. Kwon, D. P. Norton, S. J. Pearton, B. S. Kang, and F. Ren, *Applied Physics Letters* **85**, 2274-2276 (2004).
- 113 P. J. Poole, J. Lefebvre, and J. Fraser, *Applied Physics Letters* **83**, 2055 (2003).
- 114 Y. C. Kong, D. P. Yu, B. Zhang, W. Fang, and S. Q. Feng, *Applied Physics Letters* **78**, 407-409 (2001).
- 115 K. Vanheusden, W. L. Warren, C. H. Seager, D. R. Tallant, J. A. Voigt, and B. E. Gnade, *Journal of Applied Physics* **79**, 7983 (1996).
- 116 K. Sakurai, D. Iwata, and S. Fujita, *Japanese Journal of Applied Physics Part 1-Regular Papers Brief Communications & Review Papers* **38**, 2606 (1999).
- 117 M. A. L. Johnson, S. Fujita, W. H. Rowland Jr., W. C. Hughes, J. W. Cook Jr., and J. F. Schetzina, *Journal of Electronic Materials* **25**, 855 (1996).
- 118 P. R. Bueno, E. R. Leite, M. M. Oliveira, M. O. Orlandi, and E. Longo, *Applied Physics Letters* **79**, 48 (2001).
- 119 L. C. Tien, P. W. Sadik, D. P. Norton, L. F. Voss, S. J. Pearton, H. T. Wang, B. S. Kang, F. Ren, J. Jun, and J. Lin, *Applied Physics Letters* **87**, 222106 (2005).
- 120 L. C. Tien, H. T. Wang, B. S. Kang, F. Ren, P. W. Sadik, D. P. Norton, S. J. Pearton, and J. Lin, *Electrochemical and Solid-State Letters* **8**, 230-232 (2005).
- 121 H. T. Wang, B. S. Kang, F. Ren, L. C. Tien, P. W. Sadik, D. P. Norton, S. J. Pearton, and J. Lin, *Applied Physics A: Materials Science and Processing* **81**, 1117-1119 (2005).
- 122 H. T. Wang, B. S. Kang, F. Ren, L. C. Tien, P. W. Sadik, D. P. Norton, S. J. Pearton, and J. Lin, *Applied Physics Letters* **86**, 243503 (2005).
- 123 I. Sayago, E. Terrado, E. Lafuente, M. C. Horillo, W. K. W. Maser, A. M. Benito, R. Navarro, E. P. E. Urriolabeita, and M. T. G. Matrtinez, *J., Synth. Met.* **148**, 15 (2005).
- 124 G. W. Hunter, P. G. Neudeck, R. S. Okojie, G. M. Beheim, V. Thomas, L. Chen, D. Lukco, C. C. Liu, B. B. Ward, and D. Makel, *Electrochem. Soc. Proc.* **3**, 93 (2002).
- 125 Y. Lu, J. Li, H. T. Ng, C. Binder, C. Partridge, and M. Meyyapan, *Chemical Physics Letters* **391**, 344 (2004).
- 126 T. Hyodo, S. Abe, Y. Shimizu, and M. Egashira, *Sensors and Actuators B-Chemical* **93**, 590-600 (2003).
- 127 S. Shukla, P. Zhang, H. J. Cho, Z. Rahman, C. Drake, and S. Seal, *J. Appl. Phys* **98**, 104306 (2005).
- 128 N. Yamazoe, *Sensors and Actuators B-Chemical*, 7 (1991).

- 129 T. Maekawa, J. Tamaki, N. Miura, N. Yamazoe, and S. Matsushima, *Sensors and Actuators B-Chemical* **9**, 63 (1992).
- 130 R. S. Niranjana, S. R. Sainkar, K. P. Vijayamohanana, and I. S. Mulla, *Sensors and Actuators B-Chemical* **82**, 82 (2002).
- 131 Z. A. Ansari, S. G. Anasri, T. Ko, and J. H. Oh, *Sensors and Actuators B-Chemical*, 105 (2002).
- 132 Y. Wang, X. Wu, Y. Li, and Z. Zhou, *Solid-State Electronics* **48**, 627 (2004).
- 133 A. Tiburcio-Silver and A. Sanchez-Juarez, *Materials Science and Engineering B-Solid State Materials for Advanced Technology* **110**, 268 (2004).
- 134 Y. Matsushima, Y. Nemoto, T. Tamazaki, K. Meaeda, and T. Suzuki, *Sensors and Actuators B-Chemical* **96**, 133 (2003).
- 135 G. H. Rue, D. S. Lee, and D. D. Lee, *Japanese Journal of Applied Physics Part 1-Regular Papers Brief Communications & Review Papers* **43**, 3493 (2004).
- 136 E. Llobet, X. Viilanova, J. Berezmes, J. E. Sueiras, R. Alcubilla, and X. Correig, *J. Electrochem. Soc.* **145**, 1772 (1998).
- 137 W. P. Kang and C. K. Kim, *Sensors and Actuators B-Chemical* **13/14**, 682 (1993).
- 138 B. S. Kang, Y. W. Heo, L. C. Tien, D. P. Norton, F. Ren, B. P. Gila, and S. J. Pearton, *Applied Physics A: Materials Science and Processing* **80**, 1029-1032 (2005).
- 139 <http://www.rebresearch.com/H2perm2.htm>, *The permeability of hydrogen in metal*.
- 140 <http://www.rebresearch.com/H2sol2.htm>, *The solubility of hydrogen in metal*.
- 141 W. Eberhardt, F. Greunter, and E. W. Plummer, *Physical Review Letters* **46**, 1085 (1981).
- 142 A. A. Tomchenko, G. P. Harmer, B. T. Marquis, and J. W. Allen, *Sensors and Actuators B-Chemical* **93**, 126 (2003).
- 143 K. D. Mitzner, J. Sternhagen, and D. W. Galipeau, *Sensors and Actuators B-Chemical* **93**, 92 (2003).
- 144 P. Mitra, A. P. Chatterjee, and H. S. Maiti, *Materials Letters* **35**, 33 (1998).
- 145 J. F. Chang, H. H. Kuo, I. C. Leu, and M. H. Hon, *Sensors and Actuators B-Chemical* **84**, 258 (1994).
- 146 H. L. Hartnagel, A. L. Dawar, A. K. Jain, and C. Jagadish, *Semiconducting Transparent Thin Films* (IOP, Bristol, 1995).

- 147 S. J. Pearton, D. P. Norton, K. Ip, Y. W. Heo, and T. Steiner, *Prog. Mater. Sci.* **50**, 293 (2005).
- 148 D. C. Look, B. Clafin, Y. I. Alivov, and S. J. Park, *Phys. Status Solid A* **201**, 2203 (2004).
- 149 K. Ip, M. Overberg, Y. W. Heo, D. P. Norton, S. J. Pearton, C. E. Stutz, B. Luo, F. Ren, D. C. Look, and J. M. Zavada, *Applied Physics Letters* **82**, 385 (2003).
- 150 P. F. Carcia, R. S. McLean, M. H. Reilly, and G. Nunes Jr, *Applied Physics Letters* **82**, 1117-1119 (2003).
- 151 S. Masuda, K. Kitamura, Y. Okumura, S. Miyatake, H. Tabata, and T. Kawai, *Journal of Applied Physics* **93**, 1624-1630 (2003).
- 152 Z. Y. Fan, D. W. Wang, P. C. Chang, W. Y. Tseng, and J. G. Lu, *Applied Physics Letters* **85**, 5923-5925 (2004).
- 153 Q. H. Li, Y. X. Liang, Q. Wan, and T. H. Wang, *Applied Physics Letters* **85**, 6389-6391 (2004).
- 154 H. T. Wang, B. S. Kang, F. Ren, L. C. Tien, P. W. Sadik, D. P. Norton, S. J. Pearton, and J. Lin, *Applied Physics Letters* **86** (2005).
- 155 L. C. Tien, P. W. Sadik, D. P. Norton, L. F. Voss, S. J. Pearton, H. T. Wang, B. S. Kang, F. Ren, J. Jun, and J. Lin, *Applied Physics Letters* **87**, 222106 (2005).
- 156 L. Q. Liu, B. Xiang, X. Z. Zhang, Y. Zhang, and D. P. Yu, *Applied Physics Letters* **88**, 063104 (2006).
- 157 C. Ronning, P. X. Gao, Y. Ding, Z. L. Wang, and D. Schwen, *Applied Physics Letters* **84**, 783-785 (2004).
- 158 T. Fukumura, Z. Jin, M. Kawasaki, T. Shono, T. Hasegawa, S. Koshihara, and H. Koinuma, *Applied Physics Letters* **78**, 958-960 (2001).
- 159 J. Cui, Q. Zeng, and U. J. Gibson, *Journal of Applied Physics* **99**, 08-113 (2006).
- 160 Y. W. Heo, L. C. Tien, D. P. Norton, S. J. Pearton, B. S. Kang, F. Ren, and J. R. LaRoche, *Applied Physics Letters* **85**, 3107-3109 (2004).
- 161 A. Y. Polyakov, N. B. Smirnov, E. A. Kozhukhova, V. I. Vdovin, K. Ip, Y. W. Heo, and D. P. Norton, *Applied Physics Letters* **83**, 575 (2003).
- 162 Z. P. Wei, Y. M. Lu, D. Z. Shen, Z. Z. Zhang, B. Yao, B. H. Li, J. Y. Zhang, D. X. Zhao, X. W. Fan, and Z. K. Tang, *Applied Physics Letters* **90**, 042113 (2007).
- 163 M. C. Jeong, B. Y. Oh, M. H. Ham, and J. M. Myoung, *Applied Physics Letters* **88** (2006).

- 164 Y. W. Heo, V. Varadarajan, M. Kaufman, K. Kim, D. P. Norton, F. Ren, and P. H. Fleming, *Applied Physics Letters* **81**, 3046-3048 (2002).
- 165 L. E. Greene, M. Law, D. H. Tan, M. Montano, J. Goldberger, G. Somorjai, and P. Yang, *Nano Letters* **5**, 1231-1236 (2005).
- 166 M. Guo, P. Diao, and S. Cai, *Journal of Solid State Chemistry* **178**, 1864-1873 (2005).
- 167 R. Konenkamp, R. C. Word, and C. Schlegel, *Applied Physics Letters* **85**, 6004-6006 (2004).
- 168 Z. Fan, D. Dutta, C.-J. Chien, H.-Y. Chen, E. C. Brown, P.-C. Chang, and J. G. Lu, *Applied Physics Letters* **89**, 213110 (2006).
- 169 L. S. Wang, X. Z. Zhang, S. Q. Zhao, G. Y. Zhou, Y. L. Zhou, and J. J. Qi, *Applied Physics Letters* **86** (2005).
- 170 J. J. Wu, S. C. Liu, C. T. Wu, K. H. Chen, and L. C. Chen, *Applied Physics Letters* **81**, 1312-1314 (2002).
- 171 G. Zhang, A. Nakamura, T. Aoki, J. Temmyo, and Y. Matsui, *Applied Physics Letters* **89**, 113112 (2006).
- 172 G. C. Yi, W. I. Park, D. H. Kim, and S. W. Jung, *Appl. Phys. Lett.* **80**, 4232 (2002).
- 173 R. Kling, C. Kirchner, T. Gruber, F. Reuss, and A. Waag, *Nanotechnology* **15**, 1043-1046 (2004).
- 174 M. J. Zhi, L. P. Zhu, Z. Z. Ye, F. Z. Wang, and B. H. Zhao, *Journal of Physical Chemistry B* **109**, 23930-23934 (2005).
- 175 H. C. Hsu, C. Y. Wu, H. M. Cheng, and W. F. Hsieh, *Applied Physics Letters* **89** (2006).
- 176 C. Kim, W. I. Park, G. C. Yi, and M. Kim, *Applied Physics Letters* **89** (2006).
- 177 H. P. Tang, H. P. He, L. P. Zhu, Z. Z. Ye, M. J. Zhi, F. Yang, and B. H. Zhao, *Journal of Physics D-Applied Physics* **39**, 3764-3768 (2006).
- 178 L. P. Zhu, M. J. Zhi, Z. Z. Ye, and B. H. Zhao, *Applied Physics Letters* **88** (2006).
- 179 C. J. Pan, H. C. Hsu, H. M. Cheng, C. Y. Wu, and W. F. Hsieh, *Journal of Solid State Chemistry* **180**, 1188-1192 (2007).
- 180 G. Wang, Z. Z. Ye, H. P. He, H. P. Tang, and J. S. Li, *Journal of Physics D-Applied Physics* **40**, 5287-5290 (2007).
- 181 J. R. Wang, Z. Z. Ye, H. P. He, L. P. Zhu, J. Jiang, and Y. J. Zeng, *Applied Physics Letters* **91** (2007).

- 182 L. J. Lauhon, M. S. Gudiksen, D. Wang, and C. M. Lieber, *Nature* **420**, 57-61 (2002).
- 183 Y. W. Heo, C. Abernathy, K. Pruessner, W. Sigmund, D. P. Norton, M. Overberg, F. Ren, and M. F. Chisholm, *Journal of Applied Physics* **96**, 3424-3428 (2004).
- 184 Y. J. Hu, H. O. H. Churchill, D. J. Reilly, J. Xiang, C. M. Lieber, and C. M. Marcus, *Nature Nanotechnology* **2**, 622-625 (2007).
- 185 A. Ohtomo, *Superlattices* **75**, 980 (1999).
- 186 S. W. Jung, W. I. Park, G. C. Yi, and M. Kim, *Advanced Materials* **15**, 1358-+ (2003).
- 187 Y. W. Heo, M. Kaufman, K. Pruessner, K. N. Siebein, D. P. Norton, and F. Ren, *Applied Physics a-Materials Science & Processing* **80**, 263-266 (2005).
- 188 D. S. Lee, G. H. Rue, J. S. Huh, S. D. Choi, and D. D. Lee, *Sensors and Actuators B-Chemical* **77**, 90 (2001).
- 189 C. Kilic and A. Zunger, *Physical Review Letters* **88**, 095501-1 (2002).
- 190 K. J. Bachmann, H. Schreiber, W. R. S. Jr., P. H. Schmidt, F. A. Thiel, E. G. Spencer, G. Pasteur, W. L. Feldmann, and K. SreeHarsha, *J. Appl. Phys* **50**, 3441 (1979).
- 191 H. Kobayashi, T. Ishida, K. Nakamura, Y. Nakato, and H. Tsubomura, *J. Appl. Phys* **72**, 5288 (1992).
- 192 Y. J. Chen, X. Y. Xue, Y. G. Wang, and T. H. Wang, *Applied Physics Letters* **87**, 233503 (2005).
- 193 Y. J. Chen, L. Nie, X. Y. Xue, Y. G. Wang, and T. H. Wang, *Applied Physics Letters* **88** (2006).
- 194 M. Law, H. Kind, B. Messer, F. Kim, and P. Yang, *Angewandte Chemie-International Edition* **41**, 2405 (2002).
- 195 B. Wang, Y. H. Yang, C. X. Wang, and G. W. Yang, *J. Appl. Phys.* **98**, 073520 (2005).
- 196 C. K. Xu, G. D. Xu, Y. K. Liu, X. L. Zhao, and G. H. Wang, *Scripta Materialia* **46**, 789-794 (2002).
- 197 L. Vayssieres and M. Graetzel, *Angewandte Chemie-International Edition* **43**, 3666-3670 (2004).
- 198 S. K. Soumen Das, and Subhadra Chaudhuri *J. Appl. Phys* **99**, 114303 (2006).
- 199 D. H. Lowndes, D. B. Geohegan, A. A. Puretzky, D. P. Norton, and C. M. Rouleau, *Science* **273**, 898-903 (1996).
- 200 Z. W. Liu, C. K. Ong, T. Yu, and Z. X. Shen, *Applied Physics Letters* **88**, 053110 (2006).

- 201 Y. W. Heo, L. C. Tien, D. P. Norton, B. S. Kang, F. Ren, B. P. Gila, and S. J. Pearton, *Applied Physics Letters* **85**, 2002-2004 (2004).
- 202 M. S. Bhuiyan, M. Paranthaman, and K. Salama, *Superconductor Science & Technology* **19**, R1 (2006).
- 203 F. A. List, A. Goyal, M. Paranthaman, D. P. Norton, E. D. Specht, D. F. Lee, and D. M. Kroeger, *Physica C C* **302**, 87 (1998).
- 204 M. Paranthaman, C. Park, X. Cui, A. Goyal, D. F. Lee, P. M. Martin, T. G. Chirayil, D. T. Verebelyi, D. P. Norton, D. K. Christen, and D. M. Kroeger, *Journal of Materials Research* **15** (2000).
- 205 D. P. Norton, D. H. Lowndes, B. C. Sales, J. D. Budai, E. C. Jones, and B. C. Chakoumakos, *Physical Review B* **49**, 4182 (1994).
- 206 H.-M. Christen, L. A. Boatner, J. D. Budai, M. F. Chisholm, L. A. Gea, P. J. Marrero, and D. P. Norton, *Applied Physics Letters* **68**, 1488 (1996).
- 207 C. Y. Yang, S. E. Babcock, A. Goyal, M. Paranthaman, F. A. List, D. P. Norton, D. M. Kroeger, and A. Ichinose, *Physica C* **307**, 87 (1998).
- 208 Y. E. Lee, D. P. Norton, and J. D. Budai, *Applied Physics Letters* **74**, 3155 (1999).
- 209 Y. E. Lee, D. P. Norton, J. D. Budai, P. D. Rack, and M. D. Potter, *Applied Physics Letters* **77**, 678 (2000).
- 210 S. J. Pearton, D. P. Norton, K. Ip, Y. W. Heo, and T. Steiner, *Superlattices and Microstructures* **34**, 3 (2003).
- 211 Y. W. Heo, Y. W. Kwon, Y. Li, S. J. Pearton, and D. P. Norton, *Applied Physics Letters* **84**, 3474 (2004).
- 212 S. K. Song, *Physical Review B* **60**, 11137 (1999).
- 213 W. J. Kim, W. H. Koo, S. J. Jo, C. S. Kim, H. K. Baik, J. Lee, and S. Im, *Appl. Surf. Sci.* **252**, 1332 (2005).
- 214 A. E. Rakhshani, Y. Makdisi, and H. A. Ramazaniyan, *J. Appl. Phys.* **83**, 1049 (1998).
- 215 C. B. Fitzgerald, M. Venkatesan, L. S. Dorneles, R. Gunning, P. Steamenov, J. Coey, P. A. Stampe, R. J. Keendy, E. C. Moreira, and U. S. Sias, *Physical Review B* **74**, 115307 (2006).
- 216 A. Punnoose and J. Hays, *Journal of Applied Physics* **97**, 10D321 Part 2 (2005).
- 217 N. A. Theodoropoulou, A. F. Hebard, D. P. Norton, J. D. Budai, L. A. Boatner, J. S. Lee, Z. G. Khim, Y. D. Park, M. E. Overberg, S. J. Pearton, and R. G. Wilson, *Solid-State Electronics* **47**, 2231 (2003).

- 218 M. P. Ivill, S. J. Pearton, D. P. Norton, J. Kelly, and A. F. Hebard, *Journal of Applied Physics* **97**, 053904 (2005).
- 219 S. S. Park and J. D. Mackenzie, *Thin Solid Films* **258**, 268 (1995).
- 220 R. J. Choudhary, S. B. Ogale, S. R. Shinde, V. N. Kulkarni, T. Venkatesan, K. S. Harshavardhan, M. Strikovski, and B. Hannoyer, *Applied Physics Letters* **84**, 1483 (2004).
- 221 R. E. Cavicchi, S. Semancik, M. D. Antonik, and R. J. Lad, *Applied Physics Letters* **61**, 1921 (1992).
- 222 M. Kojima, H. Kato, A. Imai, and A. Yoshida, *J. Appl. Phys.* **64**, 1902 (1988).
- 223 D. Liu, Q. Wang, H. L. M. Chang, and H. Chen, *J. Mater. Res.* **10** (1995).
- 224 Y. R. Park and K. J. Kim, *J. Appl. Phys.* **94**, 6401 (2003).
- 225 X. Q. Pan and L. Fu, *J. Appl. Phys.* **89**, 6048 (2001).
- 226 D. H. Lowndes, D. K. Christen, C. E. Klabunde, Z. L. Wang, D. M. Kroeger, J. D. Budai, S. Zhu, and D. P. Norton, *Phys. Rev. Lett.* **74**, 2355 (1995).
- 227 J. D. Budai, W. G. Yang, N. Tamura, J. S. Chung, J. Z. Tischler, B. C. Larson, G. E. Ice, C. Park, and D. P. Norton, *Nature Materials* **2**, 487 (2003).
- 228 D. P. Norton, B. C. Chakoumakos, J. D. Budai, D. H. Lowndes, B. C. Sales, J. R. Thompson, and D. K. Christen, *Science* **265**, 2074 (1994).
- 229 H.-M. Christen, E. D. Specht, D. P. Norton, M. F. Chisholm, and L. A. Boatner, *Appl. Phys. Lett.* **72**, 2535 (1998).
- 230 Z. Ji, Z. Y. He, Y. Song, K. S. Liu, and Y. Xiang, *Thin Solid Films* **460**, 324 (2004).
- 231 M. Bagheri-Mohagheghi and M. Shokooh-Saremi, *Semiconductor Science and Technology* **19**, 764 (2004).
- 232 Z. Ji, Z. He, Y. Song, K. Liu, and Z. Ye, *J. Cryst. Growth* **259**, 282 (2003).
- 233 Y. Huang, Z. Ji, and C. Chen, *Appl. Surf. Sci.* **253**, 4819 (2007).
- 234 Z. Ji, L. Zhao, Z. He, Q. Zhou, and C. Chen, *Materials Letters* **60**, 1387 (2006).
- 235 G.-H. Rue, D. H. Yoo, Y. H. Hwang, and H.-K. Kim, *J. Mater. Res.* **17** (2002).

## BIOGRAPHICAL SKETCH

Li-Chia Tien was born in Taipei, Taiwan, in 1976. He grew up in Taipei city until he finished his high school education. With enthusiasm and great interest in Chemistry, he enrolled at the Department of Chemistry at National Tsing Hua University (NTHU), Hsinchu, Taiwan in 1995. He received the B.S in chemistry in 1999, and continued graduate study in Department of Materials Science and Engineering at the same institution. During the master program, he spent two years working on surface science with Dr. Jenn-Chang Hwang and Dr. Tun-Wen Pi in National Synchrotron Radiation Center (NSRRC) where he learned synchrotron photoemission techniques and concepts of scientific research. During his MS, he published 4 journal articles in the photoemission study of silicon surface. He received the M.S. degree in materials science and engineering from National Tsing Hua University in 2001. After 20 weeks of military training, mental and physical, he was commissioned second lieutenant in the army. From 2001 to 2003, he served as a platoon leader in the military police corp. During this period, he learned discipline, management and leadership.

From 2003, he began pursuing a doctoral degree in the Department of Materials Science and Engineering at University of Florida. He was fortunate to join Dr. Norton's group in 2004 and begin research on semiconductor oxide materials. During his PhD, he was able to learn different techniques including synthesis, processing and characterization of semiconductor materials. He was involved in different projects such as, synthesis/characterization of metal oxide nanowires, developing ZnO nanowires devices and synthesis/characterization epitaxial oxide thin films by pulsed laser deposition (PLD) and molecular beam epitaxy (MBE). He also developed a new catalyst-free method to synthesize metal oxide nanowires by pulsed laser deposition. The results were published in approximately 24 journal articles and were presented in 7 international conferences. His future plan is to continue research in academia.